THE DYNAMICS OF TWO-DIMENSIONAL PROPAGATING JUMPS AND DENSITY CURRENTS

by

Damon Wai Kwan So

Atmospheric Physics Group,

Imperial College of Science and Technology

A thesis submitted for the degree of

Doctor of Philosophy in the University of London

and for the

Diploma of Membership of the Imperial College

April 1986

To my parents

and my brothers

給我的父母親、哥哥、弟弟。

The dynamics of two-dimensional propagating jumps and density currents

by Damon So

ABSTRACT

The dynamics of density currents intruding into a lighter fluid is studied in the context of a purely hydrodynamical flow and a stratified flow. The internal motion within the density current is taken into account in contrast with conventional models. The solution to the steady energy conserving flow of Benjamin's model is derived and the unsteady dissipative model is discussed. A generalised hydrodynamical model is formulated including internal motion within the current and a second density current at the top boundary. Behaviour of this model with varying parameters is discussed. Stratified models are used to study density current phenomena in the atmosphere. Classification of two-dimensional squall lines based on neutrally stratified models is suggested . The free boundary problems associated with one density current interface are solved numerically.

Generalisation of the stratified models is made by allowing the potential temperature lapse rate of a parcel to vary with height. The two-dimensional vorticity equation is re-interpreted and some insights into the dynamical and thermodynamical structures of analytical cloud models are gained. The quantity $\left(\frac{\Upsilon - B}{u_0}\right)_{z_0}$ rather than CAPE is identified as fundamental in controlling convection and this has implications on the parameterisation of heat and momentum transport by convective systems in global numerical models. Solutions to analytic models with non-zero inflow shear are obtained. The vorticity

equation in pressure coordinates is derived thereby incorporating the variation of mean density with height in the atmosphere.

A squall line observed in West Africa in the French COPT81 experiment exhibited a two-dimensional structure where a cold density current lifted warm and moist boundary layer air aloft. The squall line is simulated with a numerical model and the results compare well with the observations. The relationship between the cold convective scale and warm meso-scale downdraughts is explained in terms of vorticity. A simulation with an idealised wind profile shows that the wind shear at mid-troposphere influences the mature regime. Strong mid-level inflow is shown to be associated with active multicellular systems and weak mid-level inflow is associated with deep unicellular system. It is suggested that this is also true of three-dimensional convective systems.

CONTENTS

"God is exalted in his power.
Who is a teacher like him?
Who has prescribed his ways for him,
or said to him, 'You have done wrong?'
Remember to extol his work,
which men have praised in song.
All mankind has seen it;
men gaze on it from afar.
How great is God-beyond our understanding!
The number of his years is past finding out.

He draws up the drops of water,
which distil as rain to the streams;
the clouds pour down their moisture
and abundant showers fall on mankind.
Who can understand how he spreads out the clouds,
how he thunders from his pavilion?"

Job 36: 22 to 29
(New International Version)

CHAPTER 1

INTRODUCTION

Intense organised convective phenomena in the atmosphere, or cumulonimbus convection, are not only inherently interesting for study but the understanding of their dynamics and thermodynamics and the associated transport properties is essential for consistent parameterisation of the effect of convective disturbances on the large scale motion in a global numerical weather prediction model.

Recent detailed observations of these phenomena in GATE(Global Atmospheric Research Programme's Atlantic Tropical Experiment, June-September 1974), VIMHEX (Venezuelan International Meteorological and Hydrological Experiment, June-September 1974) and ASECNA (Agence pour la Securité de la Navigation Aerienne) and earlier ones such as the Wokingham storm observation (Browning and Ludlam,1962) have provided data for conceptual model formulations and input for numerical simulations. Insight gained from such models and simulations have prompted theoretical analysis which seeks to isolate and elucidate some essential aspects of the dynamics and thermodynamics of cumulonimbus convection. Such analysis in turn helps to shape the observational methods and prompts further numerical investigation . Together, observation, simulation and theory form a useful set of interacting methods of investigation and they are employed in this study.

Intense organised convection under the scale of 1000 km can be classified into squall lines and non-squall systems. A squall line is either a two-dimensional convective line or it is a formation of individual three-dimensional convective cells organised as a line (or an arc); and it propagates relative to the ground (Bluestein and Jain (1985)). Non-squall systems can be further classified into supercells (Browning 1977) and multi-cell systems. In a supercell system, only one convective cell can be identified at any time whereas for multi-cell systems, cells at the growing and decaying stages can be identified at the same instance. Non-squall systems are by definition necessarily three-dimensional and therefore not conveniently amenable to theoretical analysis. However, results from two-dimensional studies may throw some light onto the organisation of three-dimensional storms as shown in chapter four and five; and numerical simulations (Miller and Pearce,1974, Thorpe and Miller,1978, Moncrieff and Miller,1976, Miller,1978, Dudhia,1984, Steiner,1973 and Schlesinger,1975) also give qualitative insights. A comprehensive review of organised convection can be found in Bolton(1981).

The initiation of intense organised convection is not well understood but it seems that potentially warm air trapped under a stable layer is one of the favourable conditions because the moisture content and temperature of the trapped air increase in time by diabatic processes. The eventual breaking out of severe convection may be triggered off by solar heating, orographic forcing or synoptic disturbances. The maintenance of organised convection , by contrast, is comparatively better understood. Two essential features identified in organised convections are the updraught and the evaporatively cooled and water laden downdraught. The edge of the cold downdraught is a region of high pressure which forces moist and warm boundary layer air aloft into the updraught where latent heat is released and rain formation takes place. Rain from the updraught falls into the downdraught causing rain water drag and evaporative cooling to the downdraught, thereby lowering the effective buoyancy of the downdraught air and maintaining the high pressure at the downdraught front. This maintenance mechanism is common to all well-organised long-lasting storms, in particular the mid-latitude and tropical squall lines.

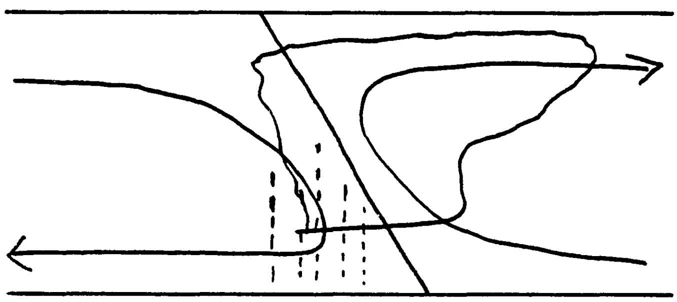

fig 1a Conceptual model of a mid-latitude squall line

Figure 1a shows a stationary streamline, cloud and rain pattern of a mid-latitude squall line. It is a two-dimensional idealisation of the Wokingham storm observed by Browning and Ludlam (1962). It shows that the interface between the updraught and the downdraught tilts upshear so that rain from the updraught can fall into the downdraught and the mechanism mentioned in the last paragraph can operate to maintain a quasi-steady system. The squall line propagates from left to right with a speed close to the mean tropospheric wind speed and the anvil extends forward ahead of the squall line. This model is the subject of theoretical study by Green and Pearce(1962). Pearce, assuming the shape of the interface as depicted here, deduced that a low level heat sink and a heat source at higher level within the updraught is necessary. This is confirmed by Moncrieff (1970) in his search for a heating pattern which would produce a backward-sloping (or upshear) interface. However, in the cases where the updraught is always buoyant, the interfaces were found by Moncrieff to be forward-sloping (or downshear) which implies that the rain falls into the updraught instead of the downdraught, making the model thermodynamically inconsistent. Since observation suggests a backward-sloping interface, we have to conclude that either the two-dimensional model is an oversimplification or the updraught air is not always buoyant. The second possibility is supported by observational evidence that the updraught air is negatively buoyant in the first three kilometres in the Wokingham storm which is consistent with the necessary heat sink condition in Pearce's analysis. A generalised theory in chapter four which allows updraught air to be buoyant and negatively buoyant may clarify this issue.

A distinction between tropical squall lines and mid-latitude squall lines is that the former propagate relative to the ground with a speed close to the maximum tropospheric wind and the latter propagate at the mean wind speed. A consequence of this is that as there is inflow ahead of a tropical squall line at every level, there is no forward anvil and the anvil trails behind the squall line covering an extensive area sometimes as large as 250-350 km (Zipser 1977 and Houze 1977). Figure 1b shows a conceptual model of a tropical squall line from House(1977). Potentially warm air from the boundary layer ascends in the updraught to feed new and mature cells which moves rearward relative to the gust front into the anvil region. The downdraught is identified below the anvil but the source of the downdraught air is not shown. The downdraught motion is classified into two scales. The convective scale downdraught occurs within 20-30 km behind the squall front and it is a result of evaporative cooling and water loading operating beneath growing and mature cells close to the front. The air parcels within the convective downdraught are therefore cooled and saturated and they end up in the lowest layer at the rear of the squall line. The meso-scale downdraught occurs behind the convective downdraught and covers an area over 100 km wide. The mesoscale downdraught air has similar low values of wet-bulb potential temperature as the convective scale downdraught air but as the former has low relative humidity its temperature sometimes is higher than the surrounding`s. The reasons for the mesoscale downdraught, according to Zipser(1977) and House(1977), are evaporative cooling and water loading but the difficulty with this argument is that the downdraught air starts and continues to descend even though it is warmer than the environment. From the trajectory analysis of a three-dimensional numerical simulation of a Venezualan squall line, Miller and Betts(1977) identified a cell downdraught and a system downdraught. The cell downdraught is similar to the convective scale downdraught but it is of a smaller scale. The system downdraught which occurs in

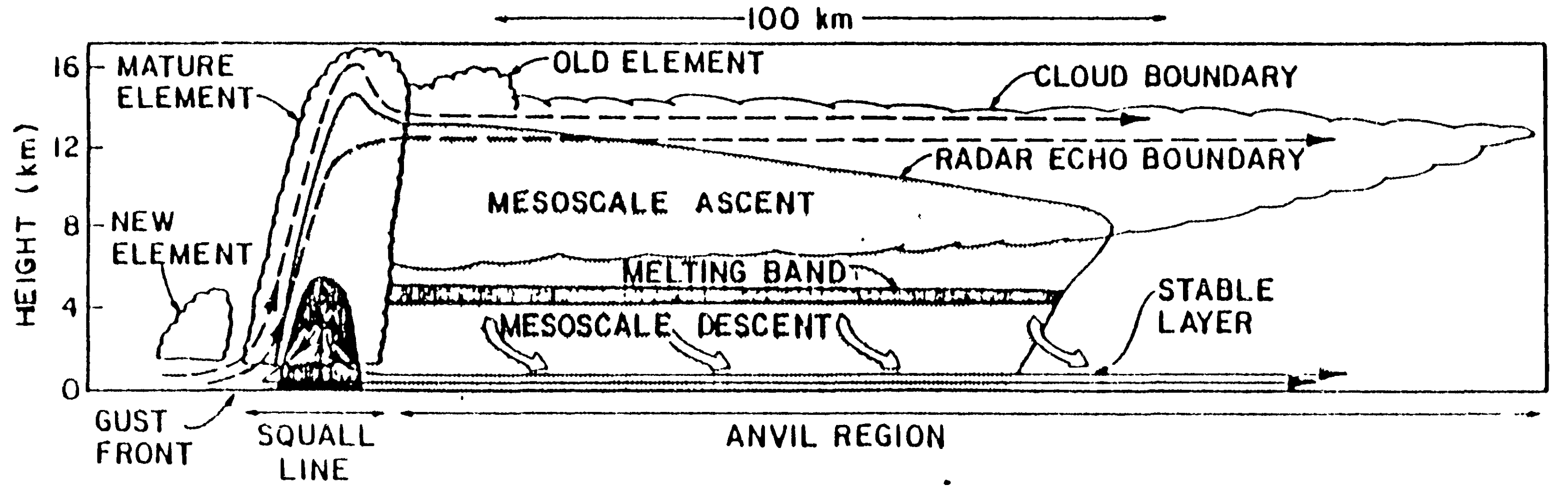

fig 1b

Schematic cross-section through squall-line system. Streamlines show flow relative to the squall-line. Dashed streamlines show updraft circulation, thin solid streamlines show convective-scale downdraft circulation associated with mature squall-line element, and wide arrows show mesoscale downdraft below the base of the anvil cloud. Dark shading shows strong radar echo in the melting band and in the heavy precipitation zone of the mature squall-line element. Light shading shows weaker radar echoes. Scalloped line indicates visible cloud boundaries (from Houze 1977).

the 30x30 km domain is fed with warm descending air from the sides. It is similar to the mesoscale downdraught but also of smaller scale. However, the mechanism suggested by Miller and Betts for the downward motion is not evaporative cooling since the simulated squall line did not have a large precipitating anvil. They suggested that the system downdraught is forced to descend as a dynamical response to the spreading density current. A two-dimensional numerical simulation by Thorpe,Miller and Moncrieff(1980) with a domain of 30kmx720mb, a dry atmosphere and a heat sink produced warming subsidence and therefore support Miller and Betts\` hypothesis that the system downdraught is forced dynamically. It seems that this hypothesis is better than Zipser\`s as Zipser\`s argument from a thermodynamical point of view cannot explain the warm subsidence. Similar subsidence occurs in a two-dimensional simulation of an African squall line as described in chapter five where explanation in terms of buoyancy and vorticity is given. A detailed review of tropical squall line downdraughts can be found in Fernandez(1982).

Some West African and Venezuelan squall lines have relative inflow from the rear and such can be identified as far as 100 km behind the front showing that downdraught air can originate from the front or the rear of the squall line or from both directions (Fernandez,1982). This is illustrated in fig 1c (from Ludlam 1980 , Betts,Grover and Moncrieff 1976).

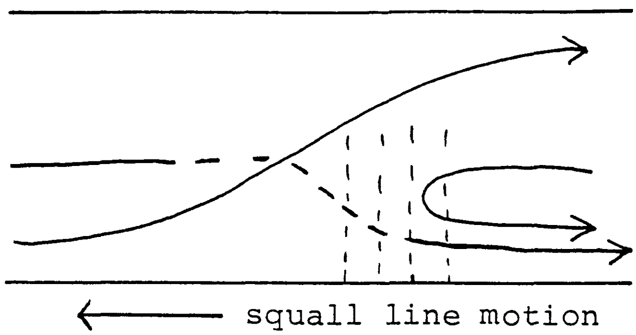

fig 1c Downdraught air originates from the front and rear of squall line

A model with no inflow from the rear, i.e. both updraught and downdraught derive their air supply from ahead of the front, was studied analytically and numerically by Moncrieff and Miller (1976). The squall line was an alignment of discrete three-dimensional cells. The propagation speed of the squall line was deduced as a function of CAPE (Convective Available Potential Energy) and the observed squall line was well represented by the numerical model. In our study, the other extreme case is investigated, i.e. the case where the downdraught from ahead of the squall line is absent and a two-dimensional configuration of a jump updraught and an overturning downdraught is left. Such a squall line was observed in the COPT81 experiment (Sommeria and Testud,1984). The overturning cold downdraught opposing incoming air from ahead of the squall line is in effect a density current which is a focus of this study.

Simpson (1969) and Simpson, Mansfield and Milford (1977) studied laboratary density currents and atmospheric density currents in the form of a sea-breeze front. Their work and that of Charba (1974) who observed the passage of a squall line in Oklahoma help to clarify the internal structure of density currents. At the front of a density current, a closed circulation or a cut-off vortex was identified by Simpson et al(1977). It is hypothesized that the sense of circulation is such that the shear between the ascending ambient fluid and the fluid inside the density current could be minimized , i.e. the fluid inside the density current, adjacent to the ascending ambient fluid, has to ascend as well. Behind this closed circulation, a downward overturning flow was observed in the squall line case (Charba,1974). Early theoretical study of density current was done by Von Karman (1940) who derived a formula, based on the density difference and density current depth, for predicting the propagation speed of density currents. A later more complete study by Benjamin (1968) showed that the formula was correct but the reasoning behind the derivation was unsound. In this study, it will be shown that this formula is in fact incomplete due to the fact that internal motion within the density current was omitted.

The dynamics of density currents and the associated jumps are analysed in chapter two in the context of hydrodynamical flow and stratified flow. A hierarchy of models with increasing complexity are developed and the behaviour of the models in the various parameter space is discussed. The approach of analysing steady non-linear models is adopted as in Moncrieff and Green (1972), Moncrieff and Miller (1976), Moncrieff (1978), Thorpe, Miller and Moncrieff (1980,1982) where a set of conserved quantities were derived and subsequently exploited. By assuming constant parcel lapse rate relative to the environment and some suitably simple shear at inflow, the conditions at outflow can be solved analytically and the asymptotic nature of the models are then known. In chapter four, the assumption of constant parcel lapse rate is found unnecessary and the implications of this concerning outflow thermodynamical profile, momentum balance and the role of CAPE in controlling convection are discussed.

Another theoretical investigation of squall line was made by Tepper (1950) who hypothesized that a pressure jump was initiated at a cold front and travelled ahead of the front under an inversion as a pressure jump line which became a region of convergence and cloud formation. This model suffers from the lack of energy source and energy dissipation would result in rapid decay. Other theoretical efforts were formulating linear gravity wave models of squall lines such as the wave-CISK (Lindzen 1974, Raymond 1976) models where the problem of lack of energy source is overcome by setting the heat source to be proportional to $\frac{dw}{dz}$ at some level. The shortcoming of linear models is that only the initial growth of a perturbation is considered and the theory becomes inadequate when the displacements of air parcels are large as is the case in organised convections. Fernandez and Thorpe (1979) found that predictions of tropical convection using wave-CISK models are poor. Therefore, the full non-linear approach employed in this theoretical study is more favourable although the initial growth aspect is not considered.

In chapter three, the difficult problem of solving the free boundary problem involving density current and a jump updraught is attempted. The method of solution is an iterative and relaxational one where the error resulted from each iteration is minimised by relaxing some variables. Not a great deal of insight is gained from the solutions but they show that the internal solutions to the non-linear analytic models often exist and in this sense the models in chapter two are realistic.

Chapter five deals with the simulation of a two-dimensional squall line observed in Ivory Coast in the COPT81 experiment. With a suitable initialisation, the numerical model reproduces much of the observed features such as the density current, the cellular nature of the updraught and the propagation speed. With a suitable change of initial wind profile above 750 mb, another simulation produces a more steady and deep single cell system. The interpretation of the two simulations suggests a mechanism for multicell formation which may be applicable to three-dimensional storms. The convective scale downdraught and the warm mesoscale downdraught are identified in the first simulation and their relation is explained in terms of vorticity generation. A formula for predicting squall line speed, utilising data from one ground station, is derived by considering the kinetic energy and pressure (or height perturbation) before and after the passage of a squall line.

Finally, in chapter six the conclusions of this study are given and some future work is suggested.

CHAPTER 2

DENSITY CURRENT MODELS IN TWO DIMENSIONS

To study the structure and dynamics of a density current and the associated jump, we define an idealised model which incorporates the important features of the density current and jump but we leave out the relatively unimportant processes such as diffusion which would otherwise complicate the mathematics and render the problem intractable. Therefore, the model is not a perfect representation of reality but it serves as a stepping stone for our understanding. Regarding the governing equations of the model, we must choose the form which is most useful for our purpose. For example, it is not easy to study stratified flow using the Navier-Stokes equation - the Boussinesq approximation is preferred; neither is it necessary to include the Coriolis parameter in the study of convection on a small scale.

Benjamin's density current models (1968) and some generalised models will be studied in the context of hydrodynamics where the fluid is incompressible and inviscid. The behaviour of the models with varying parameters such as density and density current depth will be discussed. Stratified models of density currents will be developed for understanding density current phenomena in the atmosphere. The case of uniform density or neutral stratification turns out to be the common limit of these two sets of models. The physical interpretation of total depth of the model, the inflow velocity and the Froude number will be given. Throughout this chapter, an important theorem of two-dimensional flow is used, viz: the flow force $\int_0^H u^2 + \frac{P}{\rho}\, dz$ or $\int_0^H u^2 + \frac{\delta P}{\rho}\, dz$ is invariant at any vertical section of the domain.

2.1 HYDRODYNAMICAL MODELS

In this set of models, the fluid is incompressible and inviscid (perfect fluid); and density is uniform within each flow branch although density can vary between various flow branches.

2.1.1 Benjamin's Model

In an important study of density current dynamics, Benjamin(1968) considered a steady energy-conserving model and an unsteady dissipative model. Some of his results will be derived in a manner different from Benjamin's before generalisation of his conservative model is presented.

2.1.1.1 Steady Energy-conserving Model -

This model features a stationary density current of uniform density ρ_a on the bottom boundary and a lighter fluid of uniform density ρ_b above the density current.

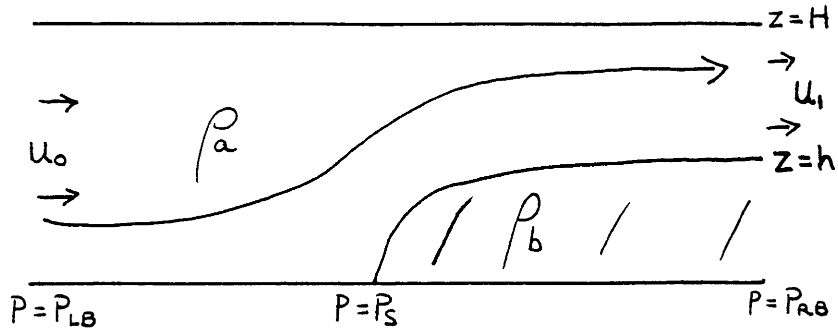

fig 2.1.1.1a Schema of Benjamin's steady conservative model

There is no internal motion within the density current so that it is completely stagnant. The inflow velocity of the lighter fluid, u_0, is independent of height so the shear at inflow is zero. This system is equivalent to one where the density current is moving bodily at a speed of u_0 into a lighter fluid which is stationary far ahead of the current. Any energy loss due to turbulent mixing and diffusion is excluded from this analysis.

Assuming this model is mathematically possible, i.e. all the mathematical constraints can be satisfied, we derive the necessary condition. Since the density of the lighter fluid is uniform, the inviscid Navier-Stokes equation can be written as

$$\frac{D\underset{\sim}{v}}{Dt} + \nabla\left(\frac{P}{\rho}\right) + g\underset{\sim}{k} = \underset{\sim}{0}$$

Taking the curl of this equation gives

$$\frac{D\eta}{Dt} = 0$$

where $\eta = (\mathrm{curl}\,\underset{\sim}{v})\cdot\underset{\sim}{j}$. Therefore, the vorticity of a fluid parcel is conserved and its value is the inflow value which is zero (irrotational). If we assume the flow far downstream ($x=\infty$) to be horizontal, then zero vorticity implies the outflow speed is also uniform, u_1, say. The conditions of mass continuity

$$U_0 H = U_1 (H - h)$$

and the balance of flow forces between far upstream and far downstream must be satisfied. Define

$$m_1 = \int_0^H \rho_a u_0^2 + P \, dz \quad_{x=-\infty}$$

$$m_2 = \int_h^H \rho_a u_1^2 + P \, dz \quad_{x=\infty}$$

$$m_3 = \int_0^h P \, dz \quad_{x=\infty}$$

Flow force balance, or momentum budget as it is sometimes called, requires that $m_1 = m_2 + m_3$. In addition to these two constraints, Bernoulli's equation applied at the bottom boundary and the density current interface gives

$$U_1^2 = gH \frac{\rho_b - \rho_a}{\rho_a} = \hat{g} H$$

where $\hat{g} \equiv g\frac{\rho_b - \rho_a}{\rho_a}$. Since the density current is stagnant, $\frac{Du}{Dt} = -\frac{1}{\rho_b}\frac{\partial P}{\partial x} = 0$ and this implies that the pressure on the bottom boundary of the density current is constant and $P_S = P_{RB}$. This gives a second expression for u_1^2 :

$$u_1^2 = 2\hat{g} h$$

Equating the two expressions for u_1^2 gives $h = \frac{H}{2}$. Hence, the height of the density current has to be exactly half of the total depth. By mass continuity,

$$u_1(H - h) = u_0 H \implies u_0 = \frac{u_1}{2}$$

so $U_0^2 = \frac{1}{4}\hat{g}H$. (2.1.1.1a)

The same result was obtained by Benjamin who considered an upside down model with a stagnant lighter fluid above a moving denser fluid. He studied the extreme case of zero density of the lighter fluid. This represents a stationary bubble and is mathematically equivalent to the model here. The mathematics is the same if $\hat{g}$ is replaced by g .

For any given densities ρ_a , ρ_b and total depth H, eqn 2.1.1.1a shows that U_0 , the inflow speed, must be of the right magnitude for the flow to be steady and non-dissipative. Also, since $U_0^2 > 0$, eqn 2.1.1.1a shows that $\hat{g} > 0$ which means that the underlying fluid must be more dense which is consistent with the model assumption.

To investigate the pressure change across the system at a certain level (i.e. from upstream to downstream at the same level), the upstream pressure $P_0(z) = P_{LB} - \rho_a g z$ is used as the reference pressure. Pressure far downstream for 0<z<H/2 is given by $P_R(z) = P_S - \rho_b g z$. The pressure change, δP is

$$\begin{aligned}
\delta P &\equiv P_R(z) - P_0(z) \\
&= P_S - P_{LB} - gz(\rho_b - \rho_a) \\
&= \frac{1}{2}\rho_a U_0^2 - gz(\rho_b - \rho_a) \\
&= \frac{1}{2}\rho_a U_0^2 - 4\rho_a U_0 \frac{z}{H} \qquad \text{by eqn } 2.1.1.1a \\
&= \rho_a U_0^2 \left(\frac{1}{2} - 4\frac{z}{H}\right)
\end{aligned}$$

Across the bottom boundary where z=0, pressure increases by $\frac{1}{2}\rho_a U_0^2$, δP drops linearly with height until it reaches the zero value at

$z=H/8$, a quarter of the depth of the density current. Above that, δp becomes negative reaching the lowest value of $-\frac{3}{2}\rho_a u_o^2$ at the top of the density current where $z=H/2$. Above the density current, the pressure drop has the same value, $-\frac{3}{2}\rho_a u_o^2$, independent of height as the pressure is hydrostatic far upstream and far downstream and the density is the same. Hence, the fluid far upstream with horizontal velocity u_o is accelerated by the pressure gradient to a velocity of $2u_o$ far downstream.

One of the definitions of the model is that outflow far downstream is horizontal. It is reasonable to speculate the possibility of outflow in the form of a wave train where amplitude either approaches a constant value or decays to zero far downstream. After lengthy analysis, Benjamin concluded that this is not possible in both the case of finite or infinite total depth if no energy loss is allowed. Thus the case of $h=H/2$ is the unique solution to the problem of steady conservative flow in the presence of a stagnant density current.

In the discussion so far the internal structure of the flow has not been mentioned,specifically the shape of the boundary (called the interface) between the lighter fluid and the density current. We have very little information about the interface except that it passes through the stagnation point on the lower boundary and that it reaches a height of $H/2$ far downstream. Finding the position of the interface is a nontrivial problem which will be dealt with in chapter three in a slightly different context. However, Von Karman (1940) showed that the interface makes an angle of 60° with the lower boundary. His argument is elaborated as follows. The pressure at the interface at a certain height is the same as that within the density current at the same height since the density current is stagnant. Thus the hydrostatic pressure at that height gives the pressure on the interface. Using Bernoulli's equation on the lower boundary and interface streamlines, the speed at the interface is given by

$$v^2 = 2gz\frac{\rho_b-\rho_a}{\rho_a} = 2\hat{g}z \qquad (2.1.1.1b)$$

The complex velocity potential for the irrotational flow of the lighter flow in the neighbourhood of the stagnation point Y=x+iz=0 has the form $\omega = CY^{\alpha}$ where α and C are real positive constants.

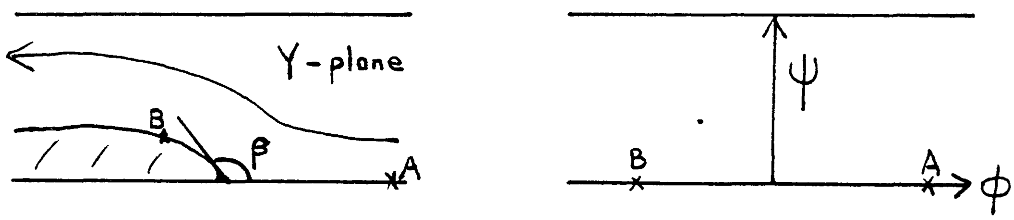

fig 2.2.1.1b Mapping from the (x,z) plane to (ϕ,ψ) plane

Near to Y=0, the interface is assumed to be straight and is mapped onto the negative portion of the ϕ-axis at a constant ψ while the lower boundary is mapped onto the positive ϕ -axis of the same ψ . The value of α determines the angle of inclination, β , of the tangent to the interface at the stagnation point.

Write ω as $\omega = r_\omega e^{i\beta_\omega}$ and Y as $Y = re^{i\beta}$.

$$\log\omega = \log C + \alpha\log r + i\alpha\beta$$

Also, $$\log\omega = \log r_\omega + i\beta_\omega$$

$$\therefore \alpha\beta = \beta_\omega$$

when $\beta_\omega = \pi$, $\beta = \frac{\pi}{\alpha}$. The next step is to find α.

$$V = \left|\frac{dW}{dz}\right| = C\alpha \left|z^{\alpha-1}\right|$$

$$= C\alpha r^{\alpha-1}$$

$$= C\alpha (x^2+z^2)^{(\alpha-1)/2}$$

$$= C\alpha \left[z^2 (1+\cot^2\beta)\right]^{(\alpha-1)/2}$$

But from eqn 2.1.1.1b , $V^2 \propto z$, (V^2 proportional to z),

$$\Rightarrow 2(\alpha-1)=1 \qquad \Rightarrow \alpha = 3/2$$

$$\therefore \beta = \pi/\alpha = \frac{2\pi}{3} = 120^\circ$$

It is expected that this analysis will still be valid in a stratified flow provided the vorticity is close to zero near the stagnation point and the fluid within the front of the density current is nearly stagnant.

2.1.1.2 Dissipative Model Of Great Depth -

As density currents are rarely observed to occupy half of the total depth, the existence of only one solution to the steady conservative model suggests that some other models have to be sought. One possibility is to relax the constraint of energy conservation. Benjamin did this by assuming a uniform energy loss by streamlines at outflow and he found that the density current depth could fall into the range of zero and H/2 according to the magnitude of dissipation. However, the assumption of uniform head loss at outflow is unrealistic especially with a shallow density current. Nevertheless, a more realistic unsteady dissipative model of great depth was proposed and the inflow velocity of the lighter fluid, or equivalently the propagation speed of the density current into the still fluid, was estimated. This model has been widely used to estimate propagation of density currents though sometimes in a rather inappropriate context as will be shown later.

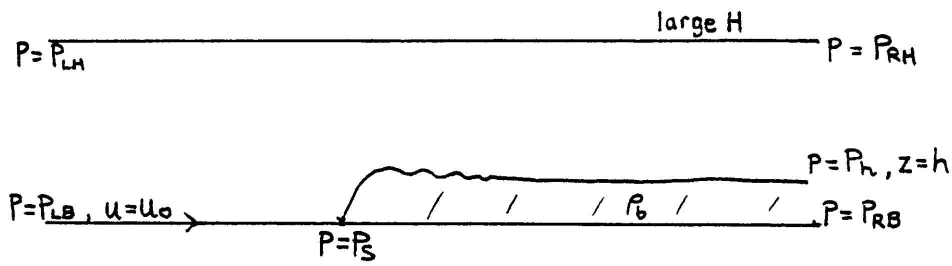

fig 2.2.1.2a Schema of Benjamin's dissipative model of great depth

A relation between the depth of density current, h, and the inflow speed u_0 is established as follows. Consider a fluid parcel originating from far upstream on the bottom boundary with pressure P_{LB} and travelling towards the stagnation point with increasing pressure. It is assumed that the flow along this section is steady which is reasonable, so that Bernoulli's equation holds, thus

$$P_S = \frac{1}{2}\rho_a u_0^2 + P_{LB}$$

Since the density current is stagnant, $P_{RB} = P_S$.

The pressure at the interface far downstream is expressed as

$$P_h = P_{RB} - \rho_b g h = \frac{1}{2}\rho_a u_0^2 + P_{LB} - \rho_b g h$$

Another expression for P_h is obtained via another consideration. Far upstream, pressure drops hydrostatically from P_{LB} to P_{LH} at great height within the lighter fluid. At this high level, fluid flow would not be affected much by the density current far below and $\frac{Du}{Dt} \sim 0$, i.e. $\frac{\partial P}{\partial x} = 0$ is almost exact, so that the pressure far downstream at the same height remains the same $P_{LH} = P_{RH}$. Far downstream , pressure also drops hydrostatically from P_{RH} to P_h at the interface. Thus the pressure at z=h far <u>upstream</u> equals P_h , i.e. $P_h = P_{LB} - \rho_a g h$. Equating the two expressions for P_h ,

$$\frac{1}{2}\rho_a u_0^2 + P_{LB} - \rho_b g h = P_{LB} - \rho_a g h$$

$$u_0^2 = 2\frac{\rho_b - \rho_a}{\rho_a} g h$$

$$u_0 = \sqrt{2\hat{g}h} \qquad (2.1.1.2a)$$

The derivation above does not require the flow to be steady at all regions or energy conserving and makes no reference to the speed downstream or the head loss! It is likely that the interface streamline would suffer the greatest energy loss whereas the streamlines further above the interface would suffer less.

One of the defects of this model is that it ignores the internal motion within the density current which is observed (Benjamin (1968) p243). In particular, knowledge of the fluid velocity, u_s, at the lower boundary of the density current would help to improve the formula for speed estimation which would then be $u_0 = \sqrt{2\hat{g}h + \frac{\rho_b}{\rho_a} u_s^2}$. Another crucial assumption of the model, that the pressure at the interface far downstream is the same as that far upstream at height h, might not be true if the total depth is not large or the density at outflow is different from its inflow value as is the case in the atmosphere. If a change in pressure at z=h across the system, ΔP, is included, then the constraint of great depth is not necessary and formula 2.1.1.2a can be further improved to

$$u_0 = \sqrt{2\hat{g}h + \frac{\rho_b}{\rho_a} u_s^2 + \frac{2\Delta P}{\rho_a}}$$

This formula involves two more parameters, u_s and ΔP, but it should be more accurate. Note that $\frac{1}{2}\rho_a u_0^2 = \frac{1}{2}\rho_a u_1^2$ +dissipation where u_1 is the velocity at the interface downstream. Therefore,

$\Delta P = -\frac{1}{2}\rho_a(u_1^2 - u_0^2)$ −dissipation so ΔP is probably negative. Eqn 2.1.1.2b is only a diagnostic equation in the sense that if an unsteady dissipative flow exists satisfying all the necessary pre-conditions, then it is an estimate of the propagation speed but no mention is made of the pre-conditions such as the momentum budget constraint.

2.1.2 Generalised Models With Non-trivial Flow Within Density Current And Forward Outflow

As pointed out in the last section, a stagnant density current with no internal flow does not really exist so that a more complete model necessarily incorporates internal dynamics within the current. In such models, the question of the existence of steady conservative flow arises again and is the theme of the following analysis. A generalised model is defined with a second 'density current' of smaller density at the top boundary and a simple overturning within each of the currents. The sense of overturning, upward or downward, is immaterial to the mathematics so it can be defined as either. However, in reality the sense of overturning affects the turbulence properties of the flow which have been neglected here.

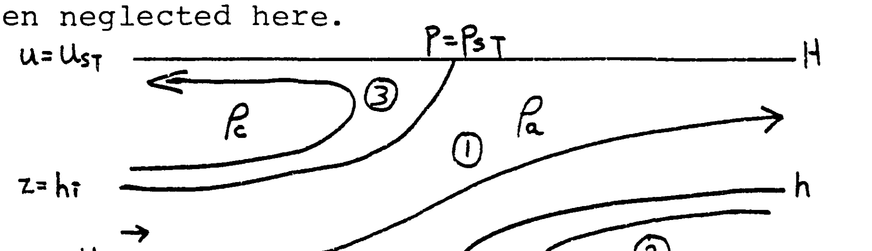

fig 2.1.2a Schema of generalised model

h, h_i heights of interfaces of density currents

ρ_a, ρ_b, ρ_c densities of fluid 1,2 and 3 respectively

P_{LB}, P_S, P_{ST} pressure

U_{ST}, U_S inflow and outflow velocities of upper and lower density currents respectively

U_0, U_1 inflow and outflow velocities of ambient fluid of density ρ_a

Since density distribution in each of the three flow regions is uniform, vorticity is conserved by fluid parcels. In 2 and 3, the velocity profile at infinity is linear and by mass continuity velocity is zero at the midpoints of the density currents

2.1.2.1 Conditions For Steady And Conservative Flow -

Define
$$m_1 = \int_0^{h_i} \rho_a u_0^2 + P \, dz \quad (x = -\infty)$$

$$m_2 = \int_h^H \rho_a U_1^2 + P \, dz \quad (x = \infty)$$

$$m_3 = \int_0^h \rho_b u^2 + P \, dz \quad (x = \infty)$$

$$m_4 = \int_{hi}^H \rho_c U^2 + P \, dz \quad (x = -\infty)$$

Applying Bernoulli's equation on top and bottom boundaries and the two interface streamlines gives

$$\rho_b u_s^2 = \rho_a u_1^2 - 2gh(\rho_b - \rho_a) \qquad (2.1.2.1a)$$

$$\rho_c U_{ST}^2 = \rho_a U_0^2 - 2(H - hi)(\rho_a - \rho_c) \qquad (2.1.2.1b)$$

Using eqns 2.1.2.1a,b and the momentum budget constraint, $m_4 + m_1 = m_2 + m_3$, gives after some algebra

$$u_o^2\left(\tfrac{2}{3}h_i - \tfrac{H}{6}\right) - \tfrac{1}{6}\hat{g}_c\,(H-h_i)^2 = u_1^2\left(\tfrac{H}{2} - \tfrac{2}{3}h\right) - \tfrac{1}{6}\hat{g}\,h^2 \qquad (2.1.2.1c)$$

where $\hat{g} = g\frac{\rho_b-\rho_a}{\rho_a}$ and $\hat{g}_c = g\frac{\rho_a-\rho_c}{\rho_a}$. The left-hand-side (LHS) of eqn 2.1.2.1c involves speed, density current depth and scaled density on the upstream side of the domain whereas the right-hand-side (RHS) involves the corresponding quantities on the downstream side. By noting $(H-h_i)$ as the LHS density current depth, the two sides of eqn 2.1.2.1c are totally symmetric. Normalising eqn 2.1.2.1c by dividing by $u_o^2 H$, using mass continuity condition, $h_i u_o = u_1(H-h)$, defining $K = \frac{\hat{g}H}{u_o^2}$ and $K_c = \frac{\hat{g}_c H}{u_o^2}$, we have

$$\left(\frac{h_i}{H}\right)^2\left(\frac{K_c}{6} + f\left(\tfrac{h}{H}\right)\right) - \frac{h_i}{H}\left(\tfrac{1}{3}K_c + \tfrac{2}{3}\right) + \tfrac{1}{6}\left(1 + K_c - K\left(\tfrac{h}{H}\right)^2\right) = 0 \qquad (2.1.2.1d)$$

where $f\left(\frac{h}{H}\right) = \frac{\frac{1}{2} - \frac{2}{3}\frac{h}{H}}{(1-\frac{h}{H})^2}$. This is a quadratic in h_i but an equivalent quadratic in h could be derived. In this form, the parameters of the equation are K, K_c and h/H. The conditions of positive discriminant and $0 \le \frac{h_i}{H} \le 1$ limit the possible choice of these parameters. Apart from these constraints which are inherent to eqns 2.1.2.1d, eqns 2.1.2.1a,b provide two more important constraints: for real u_s and u_{ST},

$$u_s^2 > 0 \;\Rightarrow\; u_1^2 \ge 2\hat{g}h \;\Rightarrow\; \left(\frac{h_i}{H}\right)^2 \ge 2K\frac{h}{H}\left(1-\frac{h}{H}\right)^2 \qquad (2.1.2.1e)$$

$$u_{ST}^2 > 0 \;\Rightarrow\; u_o^2 \ge 2\hat{g}_c(H-h_i) \;\Rightarrow\; \frac{h_i}{H} \ge 1 - \frac{1}{2K_c} \qquad (2.1.2.1f)$$

Eqn 2.1.2.1.d with all its constraints is rather difficult to analyse. First, the special case of $h_i = H$ will be investigated and compared to Benjamin's steady conservative model. Further investigation with $h_i < H$ will be discussed in a later section.

2.1.2.2 Full Depth Inflow Model -

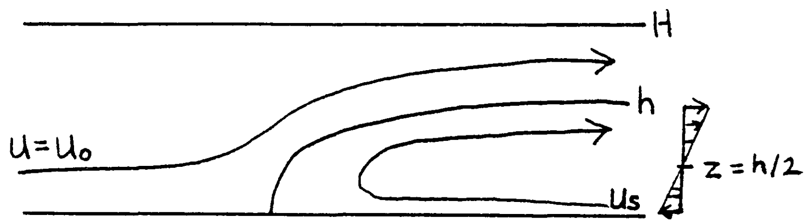

ΔP_H =pressure difference across the domain at z=H

ΔP_B =pressure difference across the domain at z=0

fig 2.1.2.2 Schema of full depth inflow model

This model is qualitatively similar to Benjamin's steady conservative model and the difference is that an overturning flow is introduced within the density current. It is interesting to see what possible values h can take. On setting $h_i = H$, eqn 2.1.2.1d simplifies to

$$\frac{h}{H} = \frac{2}{3} - \frac{1}{3} K \frac{h}{H} \left(1 - \frac{h}{H}\right)^2 \qquad (2.1.2.2a)$$

It can be shown that given K, the parameter of the model, there exists only one value of h/H which satisfies eqn 2.1.2.2a. For positive K, $\frac{h}{H} < \frac{2}{3}$ which is the upper limit of $\frac{h}{H}$. The lower limit is given by eqns 2.1.2.1e, 2.1.2.2a,

$$2K\left(\frac{h}{H}\right)\left(1-\frac{h}{H}\right)^2 = 4 - 6\frac{h}{H} \leq 1 \quad \Rightarrow \quad \frac{h}{H} \geq \frac{1}{2}$$

Hence the valid range for $\frac{h}{H}$ is $\left[\frac{1}{2}, \frac{2}{3}\right]$. This is interesting because there is more than one solution to the steady conservative problem whereas there is only one in Benjamin's model. To understand the behaviour of the model as $\frac{h}{H}$ varies from 1/2 to 2/3, $\frac{\rho_b}{\rho_a} \frac{U_s^2}{U_o^2}$, K, $\frac{\Delta P_B}{\frac{1}{2}\rho_a U_o^2}$ and $\frac{\Delta P_H}{\frac{1}{2}\rho_a U_o^2}$ are evaluated at both limits and their derivatives with respect to $\frac{h}{H}$ are found.

	$\frac{\rho_b}{\rho_a}\frac{u_s^2}{u_o^2} = \frac{6\,h/H - 3}{(1-h/H)^2}$	K	$\frac{\Delta P_B}{\frac{1}{2}\rho_a u_o^2} = \frac{(h/H)^2 - 8\,h/H + 4}{(1-h/H)^2}$	$\frac{\Delta P_H}{\frac{1}{2}\rho_a u_o^2} = 1-(1-\frac{h}{H})^{-2}$
h/H=0.5	0	4	1	-3
h/H=2/3	9	0	-8	-8

$$2\frac{u_s}{u_o}\frac{\rho_b}{\rho_a}\frac{du_s}{d\,h/H} = \frac{6\,h/H}{(1-h/H)^3} > 0 \quad \Rightarrow \quad \frac{du_s}{d\,h/H} > 0$$

$$\frac{dK}{d\,h/H} = \frac{K(3\,h/H - 1)(1-h/H)}{h/H\,(1-h/H)^2} < 0 \qquad \text{by eqn 2.1.2.2a}$$

$$\frac{d\,(\Delta P_H/\frac{1}{2}\rho_a u_o^2)}{d\,h/H} = -2\,(1-h/H)^{-3} < 0$$

Immediately, the case of h/H=0.5 is seen to be exactly the same as Benjamin's model with a stagnant density current ($u_s=0$) and $u_o^2=4\hat{g}H$. From 1/2, h/H increases, as surface inflow velocity of density current increases, as the density difference between the fluids decreases and as the pressure across the system drops at the upper and lower boundaries until h/H reaches the maximum value of 2/3 whence density difference is zero and pressure far downstream drops to its minimum. By mass continuity, large h/H implies a high outflow velocity of the lighter fluid and this is effected by a large pressure drop downstream.

2.1.2.3 Fractional Inflow Models -

Having considered the simpler case of full depth inflow with some qualitative interpretation, it is interesting to see how the more general models with fractional inflow (i.e. with two density currents in fig 2.1.2a) behave although the interpretation may well be complicated and difficult. The three important constraints of the models as derived in 2.1.2.1 are eqns 2.1.2.1d,e,f. To look at the simple limiting case of full depth outflow, $\frac{h}{H}$ is set to zero and eqn 2.1.2.1d becomes

$$\left(\frac{h_i}{H}\right)^2\left(\frac{K_c}{6}+\frac{1}{2}\right)-\frac{h_i}{H}\left(\frac{K_c}{3}+\frac{2}{3}\right)+\frac{1}{6}(1+K_c)=0 \qquad (2.1.2.3a)$$

$\frac{h_i}{H}=\frac{1}{2}$ and $K_c=1$ can be substituted into eqn 2.1.2.3a and shown to be a solution. This in fact is the inverted version of Benjamin's conservative model but in this case the density current has fluid of smaller density. Similarly, $\frac{h_i}{H}=\frac{1}{3}$ and $K_c=0$ can be shown to be solution of eqn 2.1.2.3a and this is the inverted version of the case $h_i=0, \frac{h}{H}=\frac{2}{3}$ and $K=0$ of 2.1.2.2.

So far models with one density current have been considered. To investigate the two density currents models, eqn 2.1.2.3a is solved numerically to give $\frac{h_i}{H}$ as a function of $\frac{h}{H}$, given K and K_c. A variety of values are assigned to K and K_c and it is found that there are solutions only if K and K_c are less than or very near to 4 and 1 respectively. Note that $K=4$ and $K_c=1$ correspond to the stagnant density current models with $u_s=0$ and $u_{sT}=0$. Four sets of solutions corresponding to $\{K, K_c\}$ taking the values of {0.5,0.5},{2,0.5},{3,1} and {4.1,1.1} are chosen as they cover the different class of behaviour of the system.

(A) $K=0.5$ $K_c=0.5$

	First solution			Second solution		
$\frac{h}{H}$	$\frac{h_i}{H}$	$\frac{U_{ST}^2}{U_o^2}$	$\frac{U_S^2}{U_o^2}$	$\frac{h_i}{H}$	$\frac{U_{ST}^2}{U_o^2}$	$\frac{U_S^2}{U_o^2}$
0	1			0.43	0.43	
0.1	0.9	0.9	0.9	0.45	0.45	0.15
0.2	0.8	0.8	0.8	0.47	0.47	0.15
0.3	0.7	0.7	0.7	0.5	0.5	0.21
0.4	0.6	0.6	0.6	0.54	0.54	0.41
0.5	0.61	0.61	0.99	0.5	0.5	0.5
0.6	0.78	0.78	3.17	0.4	0.4	0.4
0.7	0.3	0.3	0.3			
0.8	0.2	0.2	0.2			
0.9	0.1	0.1	0.1			

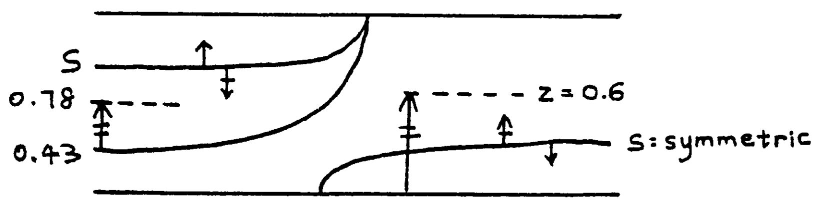

fig 2.1.2.3a Variation of $\frac{h_i}{H}$ with $\frac{h}{H}$, $K=0.5$ $K_c=0.5$

The three pairs of arrows schematically show how the heights of the density interfaces vary with one another.

(B) $K=2$ $K_c=0.5$

	First solution			Second solution	
$\frac{h}{H}$	$\frac{h_i}{H}$	$\frac{U_{ST}^2}{U_o^2}$	$\frac{U_S^2}{U_o^2}$	$\frac{h_i}{H}$	$\frac{U_{ST}^2}{U_o^2}$
0	1			0.43	0.43
0.1	0.91	0.91	0.62		
0.2	0.84	0.84	0.31		
0.3	0.81	0.81	0.12		

DENSITY CURRENT MODELS IN TWO DIMENSIONS

$\frac{h}{H}$	$\frac{h_i}{H}$	$\frac{U_{ST}^2}{U_o^2}$	$\frac{U_S^2}{U_o^2}$
0.4	0.81	0.81	0.2
0.5	0.85	0.85	0.89
0.6	0.99	0.99	3.74

fig 2.1.2.3b Variation of $\frac{h_i}{H}$ with $\frac{h}{H}$ K=2 K_c=0.5 no symmetric solution

(C) K=3 K_c=1

	First solution			Second solution	
$\frac{h}{H}$	$\frac{h_i}{H}$	$\frac{U_{ST}^2}{U_o^2}$	$\frac{U_S^2}{U_o^2}$	$\frac{h_i}{H}$	$\frac{U_{ST}^2}{U_o^2}$
0	1			0.5	0
0.1	0.91	0.82	0.43		
0.5	0.93	0.86	0.47		

fig 2.1.2.3c Variation of $\frac{h_i}{H}$ with $\frac{h}{H}$, K=3 K_c=1

(D) K=4.1 K_c=1.1

	First solution			Second solution
$\frac{h}{H}$	$\frac{h_i}{H}$	$\frac{U_{ST}^2}{U_o^2}$	$\frac{U_S^2}{U_o^2}$	
0	1			
0.1	0.92	0.82	0.22	

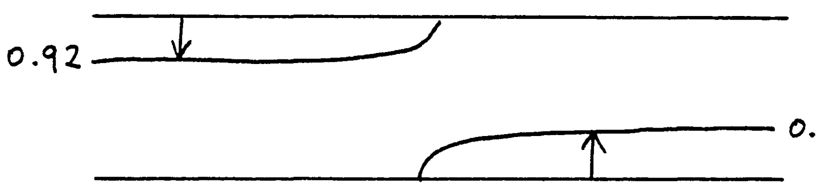

fig 2.1.2.3d Variation of $\frac{h_i}{H}$ with $\frac{h}{H}$, K=4.1 K_c=1.1

DENSITY CURRENT MODELS IN TWO DIMENSIONS

The models have three ways in which the heights of the interfaces vary with each other for given K and K_c. Firstly, it begins with $h_i=H$ and $h=0$ and the interfaces 'grows' towards one another until a limiting depth of the density current is obtained (type 1). The density currents have the same depth if $K=K_c$, representing the symmetric cases. Secondly, if K is small in the sense that K<4, then a solution corresponding to $h_i=H$ exists.

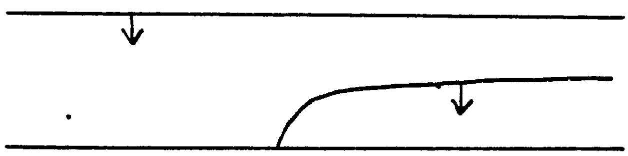

fig 2.1.2.3e Variation of $\frac{h_i}{H}$ with $\frac{h}{H}$: type 2

The top density current 'grows' as the lower density current 'shrinks'. Thirdly, there is the inverted analogue of the second type of behaviour, i.e. if K <1 then a solution corresponding to $h=0$ exists and the top density current 'shrinks' as the lower one grows.

It is seen that if K and K_c are suitably small, the second and third types of behaviour combine to give a continuous range of solution for $\frac{h_i}{H}$ and $\frac{h}{H}$ e.g. $K=K_c=0.5$. Otherwise, there are gaps between the ranges of solution e.g. K=2, $K_c=0.5$ and K=3,$K_c=1$. The behaviour of the models are summarised in the following figure.

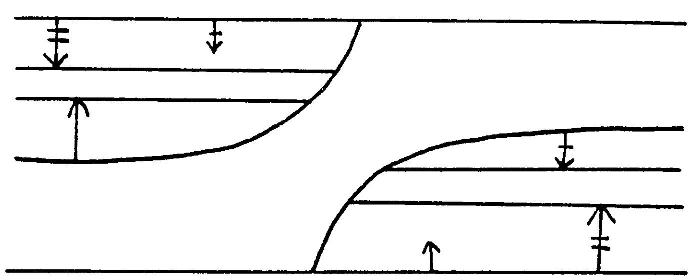

fig 2.1.2.3f Summary of variation of $\frac{h_i}{H}$ with $\frac{h}{H}$

For K>4 or K_c>1, the solutions indicated by ↨ and ↑ respectively do not exist e.g. the case of $K=4.1, K_c=1.1$, and the only possible type of solution left is ⇞ which means that only shallow density currents can exist. The fact that the models prefer shallow density currents at large K and K_c can be explained by a simple analysis.

1. From eqn 2.1.2.1f, $1-\frac{h_i}{H} < \frac{1}{2K_c}$ which shows that large K_c would require shallow top density current.

2. From eqn 2.1.2.1e, $\frac{h_i}{H} \geqslant 2K\frac{h}{H}(1-\frac{h}{H})^2$ which implies large K would also require shallow top density and since $h_i < H$, K cannot exceed a critical maximum value.

3. From eqn 2.1.2.1e, $\frac{h}{H}(1-\frac{h}{H})^2 \leqslant \frac{h_i/H}{2K}$ which has to be satisfied. The cubic $\frac{h}{H}(1-\frac{h}{H})^2$ attains its maximum at h/H=1/3 and its minimum at h/H=1.

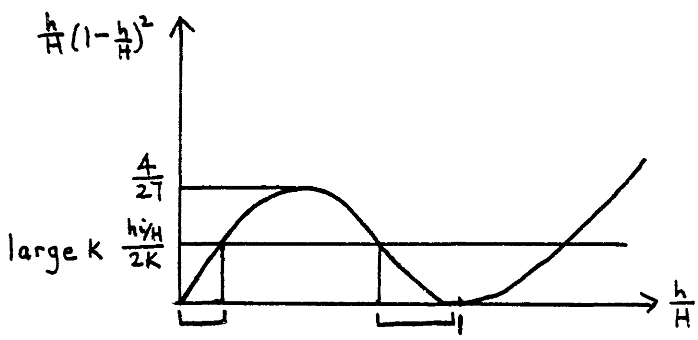

fig 2.1.2.3g Possible range of solution for large K, indicated by ⊔

If K is small such that $\frac{h_i}{H}/2K > \frac{4}{27}$ (i.e. $K < 3\frac{3}{8}\frac{h_i}{H}$), then eqn 2.1.2.1e is satisfied in the range $0 \leq \frac{h}{H} \leq 1$. If K is large such that $\frac{h_i}{H}/2K < \frac{4}{27}$,i.e. $K > 3\frac{3}{8}\frac{h_i}{H}$, then eqn 2.1.2.1e is satisfied only at two discrete intervals around h/H=0 and h/H=1 respectively. This accounts for the gap between the two ranges of solution as indicated in fig 2.1.2.3f and this situation definitely arises if K is large in the sense $K > 3\frac{3}{8} > 3\frac{3}{8}\frac{h_i}{H}$.

(1) and (2) all suggest a shallow upper density current for large K and K and (3) suggests a shallow lower density current. Since the model is symmetric in h/H and (1-h/H), similar arguments would also suggest a shallow lower and upper density currents.

The ranges of solution are further constrained by eqn 2.1.2.1d in that the discriminant must be positive and $0 \leq \frac{h_i}{H} \leq 1$ for given K, K_c and h/H. Expressing $\frac{h_i}{H}$ by using the standard formula for roots of a quadratic does not give any more insight due to the complicated nature of the expression. Further investigation into the hydrodynamical models of density currents is not justified as the primary purpose of this study is towards understanding density current phenomena in a stratified atmosphere. However, the case of $K=K_c=0$, i.e. the uniform density model, is relevant to this study as it represents a neutrally stratified flow about which the different cases of stably and unstably stratified flow vary.

2.1.2.4 Uniform Density Models -

With $K=K_c=0$, i.e. $\rho_a = \rho_b = \rho_c$, this is the simplest model incorporating two density currents and more detailed analysis is possible because the equations are mathematically tractable. Eqn 2.1.2.1d reduces to

$$\frac{h_i}{H}\left(\frac{\frac{1}{2} - \frac{2}{3}\,h/H}{(1-h/H)^2}\right) - \frac{2}{3}\frac{h_i}{H} + \frac{1}{6} = 0 \qquad (2.1.2.4a)$$

It can be shown that eqn 2.1.2.4a has the following two roots.

$$\frac{h_i}{H} = \begin{cases} 1 - \frac{h}{H} & \text{symmetric} \\ \frac{1 - h/H}{3 - 4h/H} & \text{asymmetric} \end{cases}$$

Also, the pressure change across the system, $\Delta P = \frac{1}{2}\rho(u_0^2 - u_1^2)$, which is independent of height , can be shown to satisfy

$$\frac{\Delta P}{\frac{1}{2}\rho u_0^2} = \begin{cases} 0 & \text{symmetric} \\ 1 - (3 - 4h/H)^{-2} & \text{asymmetric} \end{cases}$$

From eqns 2.1.2.1a,b, $u_s = u_1$ and $u_0 = u_{ST}$ which show that velocity is continuous at the two density interfaces. Therefore, this model has two solutions one of which is symmetric in the sense that both density currents have the same depth and there is no pressure change across the system. In the asymmetric case, for $\frac{1}{2} < \frac{h_i}{H} < 1$, $\frac{h_i}{H}$ is a rapidly varying function of $\frac{h}{H}$ and likewise $\frac{h}{H}$ is a rapidly function of $\frac{h_i}{H}$ for $0 < \frac{h}{H} < \frac{1}{2}$. The solution $\frac{h}{H} = \frac{h_i}{H} = \frac{1}{2}$ coincides with the symmetric solution.

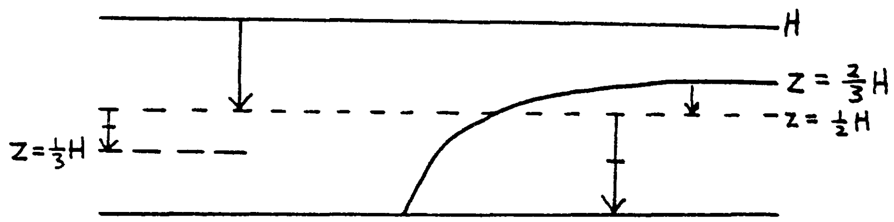

fig 2.1.24a Variation of $\frac{h_i}{H}$ with $\frac{h}{H}$ in uniform density model

The pressure changes for the asymmetric cases are

$$\frac{\Delta P}{\frac{1}{2}\rho u_0^2} = \begin{cases} -8 & , \frac{h}{H} = \frac{2}{3} , u_s = u_1 = 3u_0 \\ 0 & , \frac{h}{H} = \frac{1}{2} , u_s = u_1 = u_0 \\ \frac{8}{9} & , \frac{h}{H} = 0 \end{cases}$$

When the lower density current depth exceeds half of the total depth, there is a net pressure drop across the system and the lower density current is maintained by a faster inflow velocity. When $\frac{h}{H} < \frac{1}{2}$, there is a corresponding pressure jump and a decrease in U_s. Thus a shallow density current requires high pressure at the rear with relatively weak inflow in the asymmetric case.

2.2 STRATIFIED MODELS

The atmosphere is stratified (fluid density varies with height) and any realistic model must take this fact into account. The previous hydrodynamical models which assumed $\nabla \rho = \underset{\sim}{0}$ is inadequate in representing density current phenomena in the atmosphere. The Boussinesq approximation to the Navier-Stokes equation which will be used in the following analysis can incorporate stratification in density current models. It exploits the fact that local pressure and density do not differ much from the suitably chosen static values of pressure and density at a given level in the atmosphere. The value of pressure or density (or equivalently the potential temperature) at a point is written as the sum of the corresponding static value for that height and the departure from the static value.

$$P(x,y,z,t) = P_0(z) + \delta P(x,y,z,t)$$

$$\rho(x,y,z,t) = \rho_0(z) + \delta\rho(x,y,z,t)$$

$$\theta(x,y,z,t) = \theta_0(z) + \delta\theta(x,y,z,t)$$

where $\theta \equiv T\left(P_s/p\right)^{R/c_p}$, the potential temperature. Define $\phi \equiv \log_e \theta$ and it can be shown that $\phi = \frac{1}{\gamma}\log_e P_0 - \log_e \rho$ where $\gamma = c_p/c_v$. The basic static state is related by $\phi_o = \log_e P_o - \log_e \rho_o$ and $\frac{dP_o}{dz} = -\rho_o g$. With this chosen basic state, an approximate form of the Navier-Stokes equation can be derived:

$$\frac{D\underset{\sim}{v}}{Dt} + \nabla\left(\frac{\delta P}{\rho_o}\right) - g\delta\phi \underset{\sim}{k} = \underset{\sim}{0} \qquad (2.2a)$$

which is called quasi-Boussinesq when ρ_o is a function of height. ρ_o can be treated as a constant if the scale of vertical motion is less than the density scale height $\left(\frac{1}{\rho_o}\frac{d\rho_o}{dz}\right)^{-1}$ which is about 7km in the atmosphere. For cumulonimbus convection where the vertical motion extends up to 10km, this requirement is not satisfied. Nevertheless, the qualitative result is retained and in this sense eqn 2.2a is useful. The problem of gross variation of density with height can be overcome by deriving an equation analogous to eqn 2.2a in pressure coordinates. This will discussed in chapter four. For the present purpose, ρ_o is treated as a constant $, \rho$. The approximate mass continuity equation $\mathrm{div}\,\rho_o \underset{\sim}{v} = 0$ is replaced by $\mathrm{div}\,\underset{\sim}{v} = 0$ and the equation set becomes the Boussinesq approximation. As a consequence of the mass continuity equation, in two-dimensional motion a streamfunction, ψ , can be defined such that $u = \frac{\partial\psi}{\partial z}$, $w = -\frac{\partial\psi}{\partial x}$.

The thermodynamic equation is

$$\frac{D\phi}{Dt} = \frac{Q}{C_p T}$$

where Q is the rate of heating per unit mass. If the rate of log potential temperature increase following a parcel is written as proportional to the vertical velocity then the thermodynamic equation becomes $\frac{D\phi}{Dt} = \gamma w$

Since $\phi = \phi_o(z) + \delta\phi$, we can write

$$\frac{D\delta\phi}{Dt} = (\gamma - B)w \qquad (2.2b)$$

where $B \equiv \frac{d\phi_o}{dz}$ is the static stability. Furthermore, since $w(\gamma - B) = \frac{D}{Dt}\int_{z_o}^{z}(\gamma - B)dz$ eqn 2.2b becomes

$$\frac{D}{Dt}\left\{\delta\phi - \int_{z_o}^{z}(\gamma - B)\,dz\right\} = 0$$

$$\Rightarrow \quad \delta\phi = \int_{z_o}^{z}(\gamma - B)\,dz \qquad (2.2c)$$

where the boundary condition of $\delta\phi(z_o) = 0$ has been used. An energy equation is obtained by operating $\underset{\sim}{V}\cdot$ on eqn 2.2a.

$$\frac{D}{Dt}\left(\frac{1}{2}V^2\right) + \frac{D}{Dt}\left(\frac{\delta P}{\rho}\right) - g w \delta\phi = \frac{\partial}{\partial t}\left(\frac{\delta P}{\rho}\right)$$

Noting, $g w \delta\phi = \frac{D}{Dt}\int_{z_o}^{z} g\delta\phi\, dz = \frac{D}{Dt}\left\{g\int_{z_o}^{z}\int_{z_o}^{z}(\gamma - B)\,dz\right\}$

if $(\gamma - B)$ is assumed constant and the system in steady state, then the energy equation becomes

$$\frac{D}{Dt}\left\{\frac{1}{2}V^2 + \frac{\delta P}{\rho} - \frac{g(\gamma - B)(z - z_o)^2}{2}\right\} = 0 \qquad (2.2d)$$

Eqn 2.2d states that the quantity within the bracket is conserved following the parcel. It is an extension of Bernoulli's equation which is applicable in steady hydrodynamic flow but the term $g\int_{z_o}^{z}\delta\phi dz$, called the integrated buoyancy, represents available potential energy source or sink which is absent in hydrodynamical flow. In a two-dimensional regime with $\frac{\partial}{\partial y} = 0$, the y-component of the vorticity equation is, after taking the curl of eqn 2.2a

$$\frac{D\eta}{Dt} = -g\frac{\partial\delta\phi}{\partial x} \qquad \text{where} \quad \eta = \frac{\partial u}{\partial z} - \frac{\partial w}{\partial x} = \nabla^2\psi$$

Since $(\gamma\text{-}B)$ is constant, $\delta\phi = (\gamma - B)(z - z_0)$ and

$$\frac{\partial\delta\phi}{\partial x} = -(\gamma - B)\frac{\partial z_0}{\partial x} = \omega(\gamma - B)\frac{\partial z_0}{\partial \psi_z} \qquad \text{using} \quad \omega = -\frac{\partial\psi}{\partial x}$$

$$= \omega\left(\frac{\gamma - B}{u_0}\right) \qquad \text{using} \quad \frac{\partial\psi}{\partial z_0} = u_0$$

$$= \frac{D}{Dt}\int_{z_0}^{z}\frac{\gamma - B}{u_0}\,dz = \frac{D}{Dt}\left(\frac{(\gamma - B)(z - z_0)}{u_0}\right)$$

The two-dimensional vorticity equation can be written as

$$\frac{D}{Dt}\left\{\eta + \frac{g(\gamma - B)(z - z_0)}{u_0}\right\} = 0$$

The quantity inside the bracket is the original vorticity of the parcel at inflow and it is obvious that this, being a fact of history, is not going to change in time. The vorticity at height **z** is

$$\nabla^2\psi = \eta = \eta_0 - \frac{g(\gamma - B)(z - z_0)}{u_0} \tag{2.2e}$$

where η_0 is the initial vorticity at z_0 and the term $-\frac{g(\gamma - B)(z - z_0)}{u_0}$ represents the baroclinic generation of vorticity.

To summarise, the momentum, thermodynamics, energy and vorticity of a steady two-dimensional flow are governed respectively by eqns 2.2a,2.2c,2.2d and 2.2e. In the case where $(\gamma - B) = 0$, the flow is said to be neutral as there is no potential energy available for conversion to kinetic energy or work against the pressure field. This is an interesting case because it is equivalent to a hydrodynamical system of uniform density where Bernoulli's equation applies and there is no density gradient to generate vorticity. Hence, the model described in 2.1.2.4 is a specific case of the stratified models, being neutrally stratified.

The momentum constraint for a two-dimensional flow requires that the quantity $\int_{z=0}^{H} (u^2 + \frac{P}{\rho})\,dz$ has the same value evaluated at any vertical column. By subtracting $\int_{z=0}^{H} \frac{P_0(z)}{\rho}\,dz$ from this quantity, it is seen that $\int_{z=0}^{H} (u^2 + \frac{\delta P}{\rho})\,dz$ is also invariant at any column.

2.2.1 Buoyant Updraught Models

2.2.1.1 Flow Description -

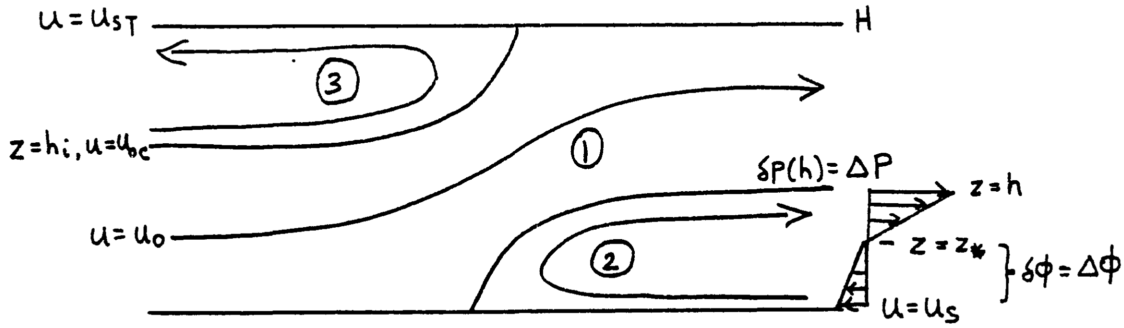

fig 2.2.1.1a Schema of stratified model with two density currents.

The flow configuration is qualitatively similar to that of 2.1.2 of the hydrodynamical models with two density currents and a jump updraught. However , the density differences are not represented explicitly but via the potential temperature differences. The static atmosphere which is used as the reference state in the Boussinesq approximation is chosen to be the inflow to the left-hand-side (LHS) of the domain and the static stability is extrapolated to the top of the domain. Parcels in region 1, 2 and 3 have lapse rates γ_1 , γ_2 and γ_3 respectively, representing the different moisture contents and releases of latent heat in the three regions. The jump updraught region (1) through which the moist boundary layer air ascends would have the largest latent heat release and hence a high γ_1 such that

$(\gamma_1 - B)$ is positive. With the updraught leaving above the lower density current, rainfall from the updraught would fall into the lower density current , thus cooling it by evaporation. If the flow within the lower density current overturns in the opposite sense(downward), then a parcel would experience a decrease in potential temperature while descending. Thus γ_2 is positive. An upward overturning with positive γ_2, which will be used in this study, has the same effect. The greater density of the lower density current is further represented by a log potential temperature deficit, $\Delta\phi$, in the inflow air to the density current. The upper density current would have lower γ_3 as the inflow air originates from a drier layer of the atmosphere.

Conservation of $\frac{1}{2}v^2 + \frac{\delta p}{\rho} - g\int_{z_0}^{z} \delta\phi \, dz$ on the density current interfaces means that if $g\int_{z_0}^{z} \delta\phi \, dz$ has different values on two sides of an interface then, since δp is the same on either side, the velocity must be discontinuous across the interface. In these circumstances, the interfaces become vortex sheets, and in reality, will be distorted by diffusion and instabilities. Such distortions are ignored in the present study, and we shall seek analytic solutions to the flow.

As vorticity is not in general conserved in the stratified models, the outflow conditions are not determined in a straightforward manner as in the hydrodynamical models. Nevertheless, analytic solutions can be obtained with simplified inflow profiles of zero or constant vorticity. The following list of symbols are used below:

H = total depth of domain,

h_i = height of the upper density current interface,

h = height of the lower density current interface,

u_o = inflow speed of the updraught parcel,

u_{oc} = inflow speed at $z=h_i$ of the upper density current,

u_{ST} = outflow speed at z=H of the upper density current,

u_S = inflow speed at z=0 of the lower density current,

$2A_c$ = constant inflow vorticity of upper density current,

$2A$ = constant inflow vorticity of lower density current,

z_* = level of stagnation in the lower density current,

z_o = inflow height of parcel,

z_1 = outflow height of parcel,

ψ_o = streamfunction at inflow,

ψ_1 = streamfunction at outflow,

$$F^2 \equiv \frac{u_o^2}{g(\gamma_1 - B)H^2}$$

$$E \equiv \left(\frac{\delta p}{\rho}\right)_h \Big/ \tfrac{1}{2} u_o^2$$

$$R_c \equiv \frac{g(\gamma_3 - B)}{4A_c^2}$$

$$R_B \equiv \frac{g(\gamma_2 - B)}{4A^2}$$

The vorticity equation is

$$\nabla^2 \psi = \eta_o - \frac{g(\gamma_i - B)(z - z_o)}{u(z_o)} \qquad i = 1,2,3 \qquad (2.2.1.1a)$$

which reduces to a second order ordinary differential equation at outflow where $\frac{\partial}{\partial x} = 0$. For the updraught region 1, η_o , the inflow vorticity is taken to be zero so that u_o is not a function of z_o and $\psi(z_o) = u_o z_o$. Eqn 2.2.1.1a is linear and has the solution, as given by Thorpe,Miller and Moncrieff(1982),

$$\psi_1 = u_o \left(z_1 - \epsilon F H \sinh \frac{z_1 - h}{FH} - h \cosh \frac{z_1 - h}{FH} \right) \qquad (2.2.1.1b)$$

$$\epsilon = 1 - \sqrt{1 - E + (h/FH)^2}$$

$$E \equiv \left(\frac{\delta P}{\rho}\right)_h \Big/ \tfrac{1}{2} u_0^2$$

where $\psi = 0$ on the lower boundary has been used.

For region 2 of overturning updraught, with constant inflow vorticity 2A, eqn 2.2.1.1a is non-linear but the solution was found by Moncrieff and Green (1972) to be

$$Z_* - Z_0 = \beta\,(Z_1 - Z_*) \qquad (2.2.1.1c)$$

$$Z_* = \beta h/(1+\beta)$$

$$\beta(\beta - 1) = R_B \equiv \frac{g(\gamma_2 - B)}{4A^2}$$

Note the outflow shear is also constant. Similarly for region 3

$$Z_{*c} - Z_0 = \beta_c\,(Z_1 - Z_{*c})$$

$$Z_{*c} = h_i + \beta_c (H - h_i)/(1+\beta_c) = \frac{h_i + \beta_c H}{1+\beta_c}$$

$$\beta_c(\beta_c - 1) = R_c \equiv \frac{g(\gamma_3 - B)}{4A_c^2}$$

2.2.1.2 Momentum Balance -

The momentum budget is an overall bulk constraint on the whole convective system. It relates the momentum flux, ρu^2, and the pressure perturbation on one side of a two-dimensional domain to those on the other side:

$$\int_0^H \left[u^2 + \frac{\delta P}{\rho} \right]_{-\infty}^{\infty} dz = 0$$

In fact, the vertical integration need not be carried out at infinity but, since u^2 and $\frac{\delta P}{\rho}$ are only known asymptotically, the constraint can only be applied well away from the convective system. Evaluation of the integral at inflow is easy since u and $\frac{\delta P}{\rho}$ are known, but on outflow u and $\frac{\delta P}{\rho}$ are deduced from the solutions to the vorticity equation and the integration has to be laboriously carried out. On the LHS of the domain, we define

$$M_1 \equiv \int_0^{h_i} u^2 + \frac{\delta P}{\rho}\, dz$$

$$M_4 \equiv \int_{h_i}^{H} u^2 + \frac{\delta P}{\rho}\, dz$$

On the right-hand-side (RHS),

$$M_2 \equiv \int_h^{H} u^2 + \frac{\delta P}{\rho}\, dz$$

$$M_3 \equiv \int_0^{h} u^2 + \frac{\delta P}{\rho}\, dz$$

Since there is no shear at the inflow to the jump updraught branch, u_o is constant with height and since the static reference thermodynamic profile is taken at this inflow, $\frac{\delta P}{\rho}$ is zero. Therefore, $M_1 = h_i u_o^2$. By the energy equation 2.2d, we can write the integrand of M_2 as

$$u_1^2 + \frac{\delta P}{\rho} = u_o^2 + g(\gamma_1 - B)(z_1 - z_o)^2 - \left(\frac{\delta P}{\rho}\right)_{z_1}$$

At outflow $\frac{Dw}{Dt} = 0$ and therefore the pressure is hydrostatic:

$$\frac{\partial}{\partial z_1}\left(\frac{\delta P}{\rho}\right) = g\delta\phi = g(\gamma_1 - B)(z_1 - z_o(z_1))$$

Integration of this equation with respect to z_1 gives $\left(\frac{\delta P}{\rho}\right)_{z_1}$, implying

$$M_2 = \int_h^H u_o^2\, dz_1 + \int_h^H g(\gamma_1 - B)(z_1 - z_o(z_1))^2\, dz_1$$
$$- \int_h^H \left(\frac{\delta P}{\rho}\right)_h dz_1 - \int_h^H \left[\int_h^{z_1} g(\gamma_1 - B)(z_1 - z_o(z_1))\, dz_1\right] dz_1$$

The integrands of the first and third terms are constant but the integrands of the second and fourth terms involve Z_0 as a function of Z_1 which complicates the algebra. Z_0 is found as a function Z_1 by eqn 2.2.1.1b and after lengthy algebra,

$$m_2 = (H-h)\left(u_0^2 - \left(\frac{\delta P}{\rho}\right)_h\right) + g(\gamma_1 - B)\Big\{ \tfrac{1}{4} FH \sinh 2\alpha \left[(\epsilon FH)^2 + h^2 \right] + \epsilon h (FH \sinh\alpha)^2 + (H-h)\left[\tfrac{1}{2}h^2 - \tfrac{1}{2}(\epsilon FH)^2 + \epsilon (FH)^2\right] - \epsilon \sinh\alpha (FH)^3 - h\cosh\alpha (FH)^2 + h(FH)^2 \Big\}$$

where $\alpha = \dfrac{H-h}{FH}$. The momentum budget contribution from the lower density current can be written as

$$m_3 = \int_0^{Z*} u^2(z_0)\,dz_0 + \int_{Z*}^{h} u^2(z_1)\,dz_1 + \int_0^{Z*} \left(\frac{\delta P}{\rho}\right)_{z_0} dz_0 + \int_{Z*}^{h} \left(\frac{\delta P}{\rho}\right)_{z_1} dz_1$$

$u(z_0)$ and $u(z_1)$ are both functions of Z and they can be deduced from eqn 2.2.1.1c. $\left(\frac{\delta P}{\rho}\right)_{z_0}$ is non-zero at inflow and is complicated by a non-zero log potential temperature perturbation there. The sum of the first two terms of m_3 is

$$\int_0^h u^2\,dz = \frac{4A^2}{3}\frac{(\beta h)^3}{(1+\beta)^2}$$

The sum of the last two terms is

$$\int_0^h \frac{\delta P}{\rho}\,dz = h\left(\frac{\delta P}{\rho}\right)_{Z*} + \frac{1}{2}\Delta\phi\, g h^2 \frac{(1-\beta)}{(1+\beta)} + \frac{g(\gamma_2 - B)h^3}{6(1+\beta)^2}$$

with $\left(\frac{\delta P}{\rho}\right)_{Z*}$ being a function of $E \equiv \dfrac{\left(\frac{\delta P}{\rho}\right)_h}{\frac{1}{2}u_0^2}$, $\Delta\phi$, β, $g(\gamma_2 - B)$ and h ; m_3 is a function of A, β, h, E, $\Delta\phi$ and $g(\gamma_2 - B)$. Since $g(\gamma_2 - B) = 4A^2\beta(\beta-1)$, $g(\gamma_2 - B)$ can be eliminated in the expression of m_3. A can be expressed in terms of E, $\Delta\phi$, h and β by considering the energy equation applied at the bottom boundary it can be shown that $M_3 = M_3(\beta, h, E, \Delta\phi)$. After considerable algebra

$$M_3 = \frac{1}{2}\frac{h}{H} + \frac{1}{6}\frac{h}{H}\frac{2\beta^2 - 2\beta - 1}{1+\beta-\beta^2}\left(1 + \frac{h}{H}G - E\right) + \frac{1}{4}G\left(\frac{h}{H}\right)^2$$

$$G \equiv \frac{g\Delta\phi H}{\frac{1}{2}u_o^2} \quad , \quad E = 1 + \left(\frac{h}{FH}\right)^2 - \left[\frac{1 - \frac{h_i}{H} - \frac{h}{H}\cosh\alpha}{F\sinh\alpha} - 1\right]^2$$

The calculations for the upper density current are similar but without the complication of non-zero $\delta\phi$ and $\frac{\delta P}{\rho}$ at inflow; the normalised budget contribution is therefore

$$\frac{M_4}{Hu_o^2} = \frac{1}{3}\left(1 - \frac{h_i}{H}\right)\left[1 - \frac{1}{F^2}\left(1 - \frac{h_i}{H}\right)^2\right]\frac{\beta_c + \frac{1}{2}(\beta_c - 1)}{\beta_c + (1+\beta_c)^2(\beta_c - 1)}$$

The momentum budget $M_1 + M_4 = M_2 + M_3$ is already a powerful constraint on the system but two further constraints analogous to eqns 2.1.2.1e,f of the hydrodynamical models are

$$\left(\frac{u_s}{u_o}\right)^2 = \frac{1 + \frac{h}{H}G - E}{1 - (\beta^2 - 1)/\beta} > 0 \qquad (2.2.1.2a)$$

$$\left(\frac{u_{oc}}{u_o}\right)^2 = \frac{1 + \left(1 - \frac{h_i}{H}\right)^2/F^2}{1 + (\beta_c^2 - 1)(\beta_c + 1)/\beta_c} > 0 \qquad (2.2.1.2b)$$

Eqn 2.2.1.2b is satisfied if $\beta_c^3 + \beta_c^2 - 1 > 0$, i.e. if $\beta_c > 0.755$, i.e. $R_c > -0.185$.

The normalised momentum budget equation obtained by dividing the original equation by Hu_o^2 is a transcendental equation in $\frac{h}{H}$, $\frac{h_i}{H}$, β, β_c, F, G. With the specification of four parameters, we can show how the other two parameters vary with each other.

2.2.1.3 Full Depth Inflow Model -

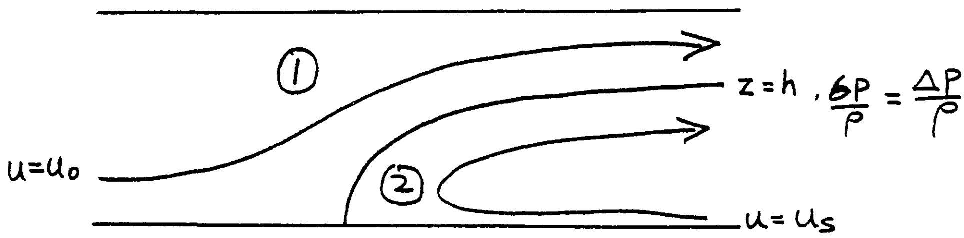

fig 2.2.1.3a Schema of stratified full depth inflow model

In region 1 with zero inflow vorticity , $\psi_0 = u_0 z_0$ and the vorticity equation reduces to

$$\nabla^2\psi = \frac{g(\gamma_1 - B)}{u_0}\left(z - \frac{\psi}{u_0}\right)$$

with boundary condition of $\psi = 0$ and $\psi = u_0 H$ at the lower and upper boundary respectively. The solution far downstream in this case is particularly simple:

$$\psi_1 = u_0\left(z_1 - \frac{h\sinh\frac{H-z_1}{FH}}{\sinh\alpha}\right)$$

where $\alpha = \frac{H-h}{FH}$ and $F^2 = \frac{u_0^2}{g(\gamma_1 - B)H^2}$. Consideration of the conserved quantity $\frac{1}{2}v^2 + \frac{\delta P}{\rho} - g\int_{z_0}^{z}\delta\phi\, dz$ along the lower boundary and interfacial streamline leads to the relation

$$\frac{h}{FH}\operatorname{cotanh}^2\alpha + 2\frac{h}{FH}\operatorname{cotanh}\alpha + E - \left(\frac{h}{FH}\right)^2 = 0$$

This quadratic equation has only one physically meaningful root:

$$\tanh\alpha = \frac{h}{FH}\left(\sqrt{1 - \left[E - (h/FH)^2\right]} - 1\right)^{-1}$$

The condition of $\tanh\alpha \leq 1$ in turn requires

$$E \leq -2\frac{h}{FH}$$

so there must be a pressure drop across the system at z=h.

DENSITY CURRENT MODELS IN TWO DIMENSIONS

There are only four variable parameters, $\frac{h}{H}$, F, G and β, in the momentum balance equation as $\frac{h_i}{H} = 1$ and β_c is not relevant. The momentum balance equation is

$$\left(1-h/H\right)\left(1-E/2\right) + \frac{(h/H)^2}{2F\sinh^2\alpha}\left(\frac{1}{2}\sinh 2\alpha - \alpha\right) + \frac{h}{H}\left(1-\alpha\,\mathrm{cotanh}\,\alpha\right)$$

$$+ \frac{1}{2}\frac{h}{H} + \frac{1}{6}\frac{h}{H}\left(\frac{2\beta^2-2\beta-1}{1+\beta-\beta^2}\right)\left(1+\frac{h}{H}G - E\right) + \frac{1}{4}G\left(\frac{h}{H}\right)^2 - 1 = 0$$

where $E = E(F, \frac{h}{H})$.

G and β are prescribed the values 0 and 1 respectively and the variation of F with $\frac{h}{H}$ is plotted on fig 2.2.1.3a, together with the deduced quantities E and $(u_s/u_o)^2$. $\beta = 1$ means that the overturning flow is neutral. As $\frac{h}{H}$ approaches 2/3 from above, F tends to infinity and there is no solution for $\frac{h}{H} < \frac{2}{3}$. Since $F^2 = \frac{u_o^2}{g(\gamma_1 - B)H^2}$, large F corresponds to small $(\gamma_1 - B)$ or nearly neutral flow and the extreme case of infinite F corresponds to the case of neutral flow which is described in 2.1.2.2 of the hydrodynamical models where the same limiting value of 2/3 is derived for the uniform density case. As $(\gamma_1 - B)$ increases (or u_o decreases), F decreases and $\frac{h}{H}$ increases from 2/3 to 1. In other words, the depth of the density current increases with buoyancy in the updraught or with decreasing inflow speed. The E-$\frac{h}{H}$ curve shows E is always negative with an asymptotic value E=-8 and its magnitude is generally alarmingly large. E in other models is of much smaller magnitude, e.g. about 1 in Moncrieff and Miller(1976) and Thorpe, Miller and Moncrieff(198o,1982).

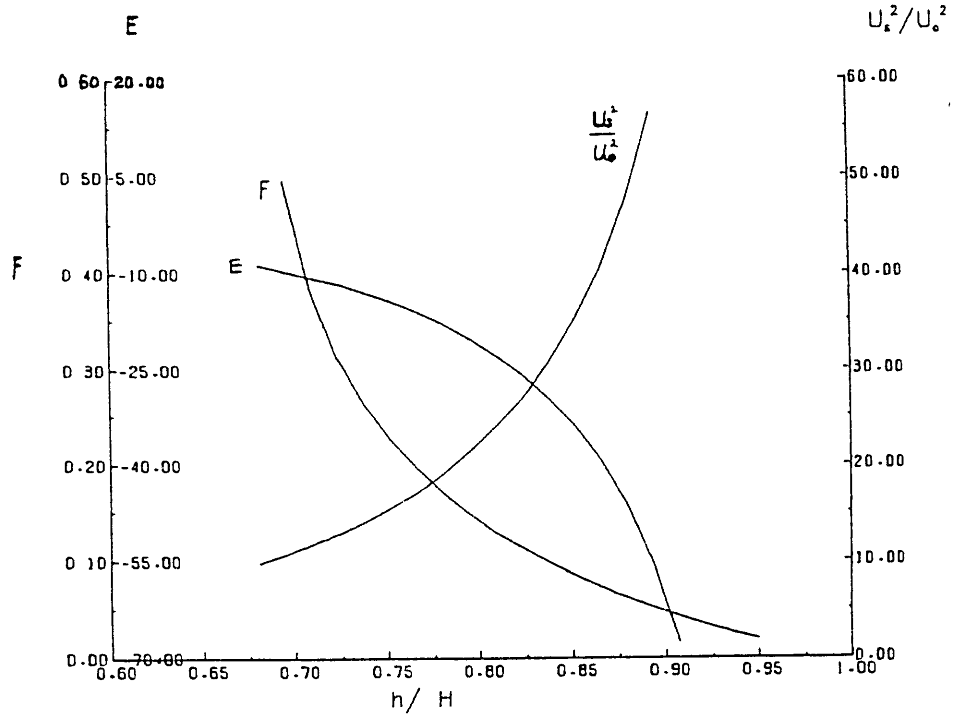

h_i=H,G=0,β=1

fig 2.2.1.3a Variations of F,E and $\left(\frac{U_s}{U_o}\right)^2$ with $\frac{h}{H}$ CAPE > O

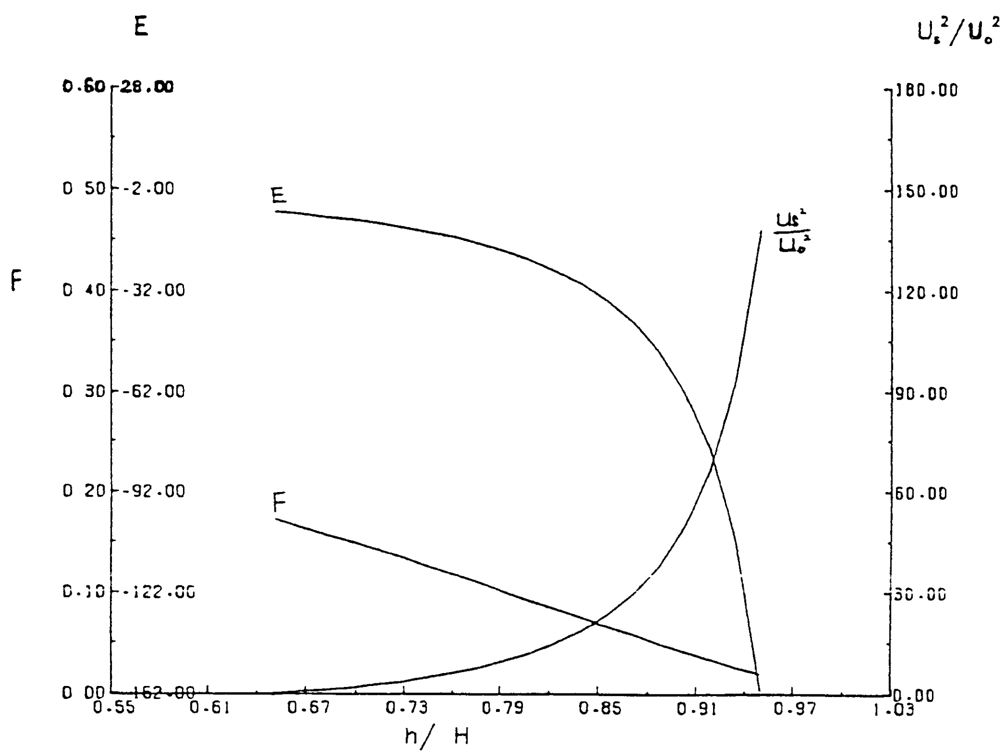

h_i=H,G=−15,β=1

fig 2.2.1.3b (as fig 2.2.1.3a)

$\frac{h}{H}$	E	F	$\left(\frac{u_s}{u_o}\right)^2$	u_o	u_s	$g(\gamma_1-B)H^2$ $= 2\,CAPE$
2/3	-8	∞	9	3.19	9.58	0
0.7	-10.04	0.44	11.04	2.85	9.47	41.54
0.8	-21.26	0.14	22.26	1.96	9.25	196.84
0.9	-60.88	0.05	61.88	1.16	9.11	604

Table 2.2.1.3a Variation of parameters,given ΔP=-50 Pa, G=0 and β=1.

The surface inflow speed of the density current, u_s , is considerably larger than the inflow speed of the updraught, u_o . As $\frac{h}{H}$ increases u_o and u_s decreases and the system becomes less active. For constant $\frac{h}{H}$, E , $\frac{u_s}{u_o}$ and F are constant also and

$$u_s = \left(\frac{u_s}{u_o}\right) u_o = \left(\frac{u_s}{u_o}\right) \sqrt{\frac{\Delta P}{\frac{1}{2}\rho E}} .$$

Therefore, u_s and u_o are proportional to the square root of the magnitude of the pressure drop. And since

$$CAPE \equiv \frac{g(\gamma_1-B)H^2}{2} = \frac{1}{2}\left(\frac{u_o}{F}\right)^2 = \frac{1}{2F^2}\frac{\Delta P}{\frac{1}{2}\rho E} = \frac{\Delta P}{\rho E F^2}$$

for a given $\frac{h}{H}$, $|\Delta P|$ is proportional to CAPE . It can be shown that for reasonable u_s such as $u_s < 15\,m/s$, $|\Delta P|$ is confined below 1mb and CAPE < 600 J/kg. This model represent a class of flow which is dominated by a fast neutral overturning flow within a deep density current which propagates slowly (<6 m/s) through a still environment with CAPE < 600 J/kg and induces a small drop in pressure (<1 mb) downstream.

{G,β } are assigned the values {-15,1}, {-5,1}, {-10,1}, {0,0.8} and {0,1.25} and the graphs are shown in figs 2.2.1.3b-f. The solution range for h/H extends from a lower limit (corresponding to a neutral updraught) to h/H=1. Negative G and β <1 decrease this lower

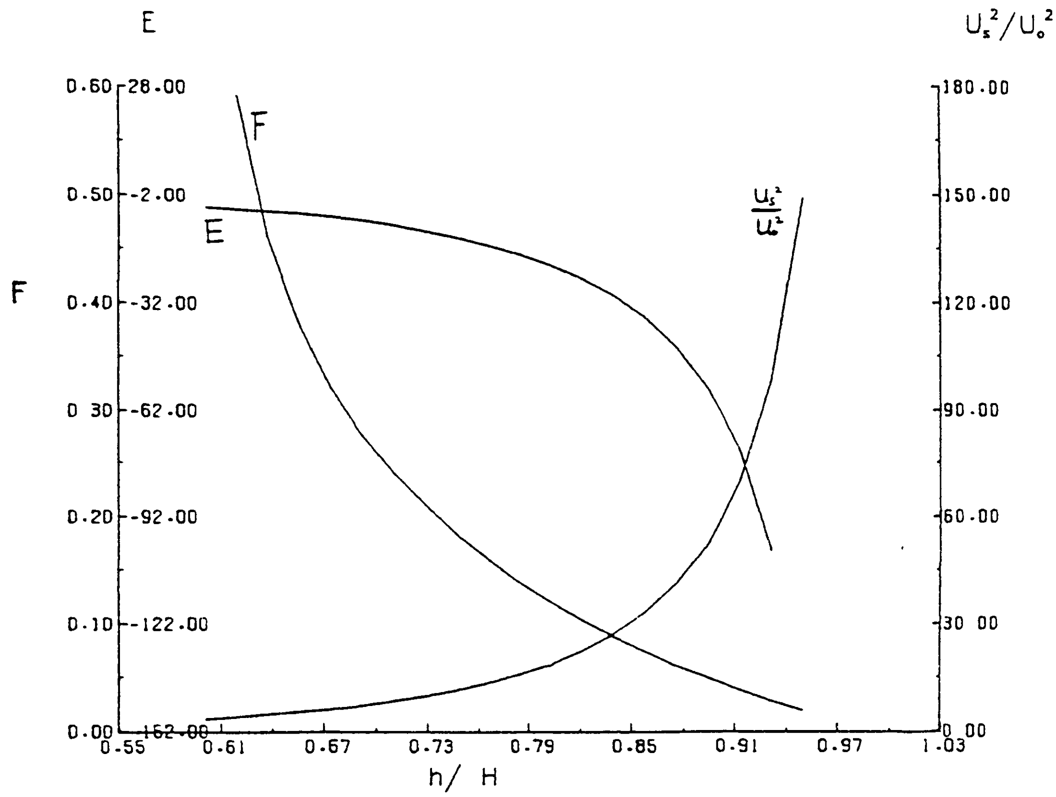

h_i=H,G=−5,β=1

fig 2.2.1.3c (as fig 2.2.1.3a)

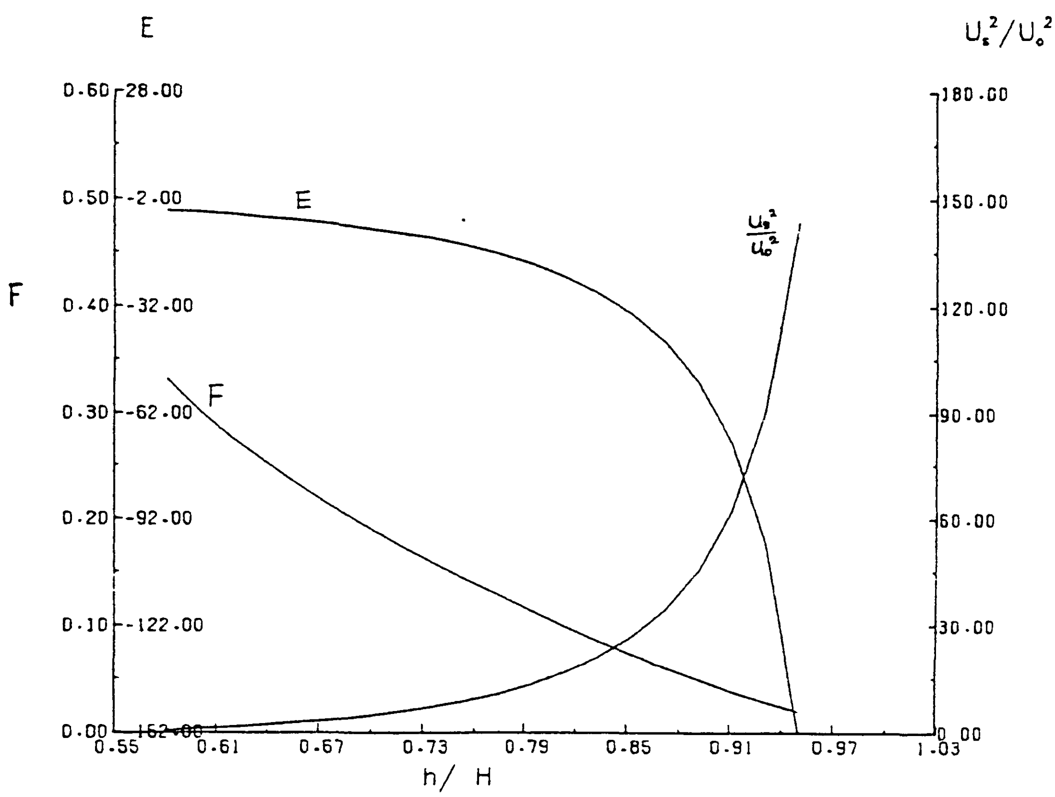

h_i=H,G=−10,β=1

fig 2.2.1.3d (as fig 2.2.1.3a)

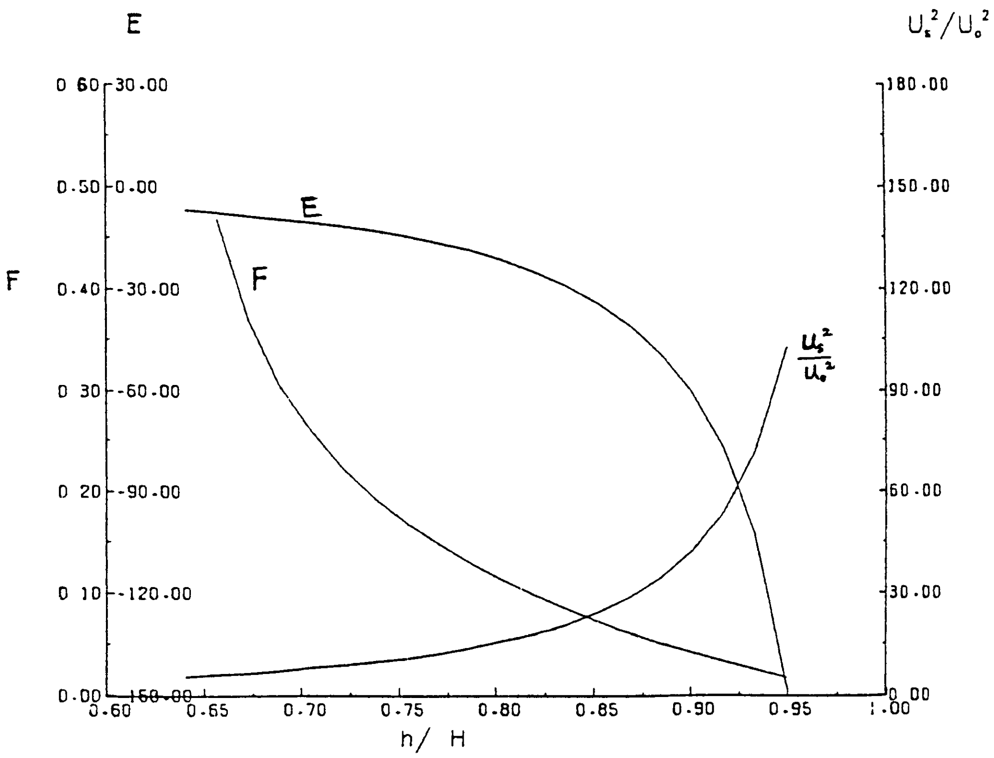

h_i=H,G=0,β=0.8

fig 2.2.1.3e (as fig 2.2.1.3a)

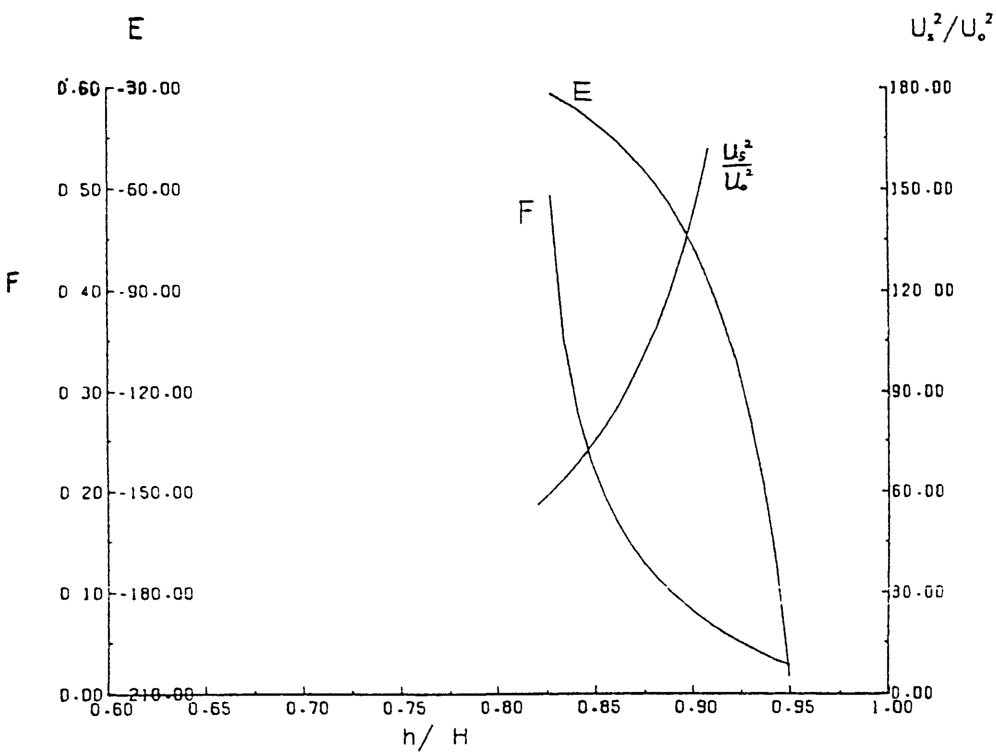

h_i=H,G=0,β=1.25

fig 2.2.1.3f (as fig 2.2.1.3a)

limit while β >1 raises this limit narrowing the solution range. The models with the above parameter values have similar behaviour and the common properties are that the system is dominated by a slowly propagating overturning current and becomes less active as $\frac{h}{H}$ increases towards 1. The outflow layer of the jump updraught is much shallower than the inflow layer implying, by mass continuity, a higher velocity at outflow. This is effected by a large drop in pressure, hence the large magnitude of the negative quantity, E. The low pressure induced at the base of the density current far downstream means that the surface inflow speed of the overturning flow has to be large to maintain the stagnation point, hence the large magnitude of $\left(\frac{U_s}{U_0}\right)^2$. Because of the large magnitude of E and $\frac{U_s}{U_0}$, for reasonable pressure drop and surface inflow speed, U_0 has to be small.

In a real situation, only CAPE and H (the zero buoyancy level) are known as environmental parameters and the system has to choose a suitable value for $\frac{h}{H}$ such that $F(\frac{h}{H})$, $U_0(F, CAPE)$, $E(F, \frac{h}{H})$ and U_S can satisfy the momentum constraint and the requirement imposed by the larger scale.

2.2.1.4 Fractional Model -

In this model, on the LHS there are two branches of flow - one is the jump updraught and the other overturns and exits on the LHS in the form of a forward outflow. From the analysis of all neutral flows in the system, i.e. $F=\infty$, G=0, $\beta=1$ and $\beta_c=1$ in 2.1.2.4, for a given $\frac{h_i}{H}$ there exist two solutions for $\frac{h}{H}$ and they are $1-\frac{h_i}{H}$ and $\frac{3\,h_i/H - 1}{4\,h_i/H - 1}$. $\frac{h_2}{H}$ is defined as the larger of the two and $\frac{h_1}{H}$ is defined as the other. It is found that the solution ranges for the stratified models are $[0, \frac{h_1}{H}]$ and $[\frac{h_2}{H}, 1)$. The values of 0.75, 0.417 and 0.17 are chosen for $\frac{h_i}{H}$ in plotting the curves in fig 2.2.1.4a-q as they are the midpoints of [0.5,1],[1/3,0.5] and [0,1/3] respectively. The significance of $\frac{h_i}{H} = 0.5$ and $\frac{h_i}{H} = \frac{1}{3}$ is explained in 2.1.2.4.

The properties of the models in the solution range $[\frac{h_2}{H}, 1)$ are similar to the full depth inflow model of 2.2.1.3 where negative E of large magnitude forces u_0 to be small. The parameters vary in a similar way - as h/H, $\left(\frac{u_s}{u_0}\right)^2$ and $\left(\frac{u_{oc}}{u_0}\right)^2$ increase, F and E decrease.

The lower solution range is characterised by a deep jump outflow as the density current is shallow. By mass continuity, this means that the normalised outflow velocity is small compared to that of the upper solution range and this in turn requires relatively large pressure downstream, hence E has positive value or negative value of small magnitude.

$$E = \left(\frac{\Delta P}{\rho}\right) \Big/ \tfrac{1}{2} u_0^2 \quad \Rightarrow \quad u_0^2 \propto \frac{1}{|E|}$$

so for the lower range u_0 can be large and this model represents a class of fast propagating squall lines. Also, $u_s < u_0$ in this case whereas in the full depth inflow model $u_s > u_0$ is always true. The variation of parameters is also different - as h/H, F and $\left(\frac{u_s}{u_0}\right)^2$ increase, E and $\left(\frac{u_{oc}}{u_0}\right)^2$ decrease.

The graphs also show that the limiting case of $\frac{h}{H} = 0$ is a possible solution with F and E taking finite values. In this configuration, there is no lower density current and the model consequently does not represent any squall line.

$\frac{h_2}{H}$ and $\frac{h_1}{H}$ are both functions of G, β and β_c and their values corresponding to the special case of $G=0$ and $\beta=\beta_c=1$ have been given above. The graphs of fig 2.2.1.4a-q indicate $\frac{h_1}{H}$ and $\frac{h_2}{H}$ vary in the following way: G decreasing from zero, β and β_c decreasing from 1 lower the upper limit $\frac{h_2}{H}$ and raise the lower limit $\frac{h_1}{H}$ thereby extending the solution ranges ; β and β_c increasing from 1 raise the upper limit and lower the lower limit thereby contracting the solution ranges. The extension of the two solutions ranges sometimes results in merging and one continuous range [0,1) exists as in fig 2.2.1.4b,f,,i,k. In fig 2.2.1.4h, the lower range is annihilated by the positive u_s^2 constraint given by eqn 2.2.1.2a which is also responsible for the gaps in what would have been continuous curves in fig 2.2.1.4p.

It is evident from the graphs that a single value of F may correspond to two values of $\frac{h}{H}$ belonging to the upper and the lower ranges. However, the two systems are quite distinct. Large $\frac{h}{H}$ is associated with slow moving systems and small $\frac{h}{H}$ is associated with a fast moving systems. Since $F^2 = \frac{u_0^2}{g(\gamma_1-B)H^2} = \frac{\frac{1}{2}u_0^2}{CAPE}$ and F is the same in both system, it follows that CAPE has to be larger in the fast moving system. In this sense, the fast moving system is much more active.

It is tentatively suggested that a deep upper density current and a deep lower density current could model a mid-latitude squall line.

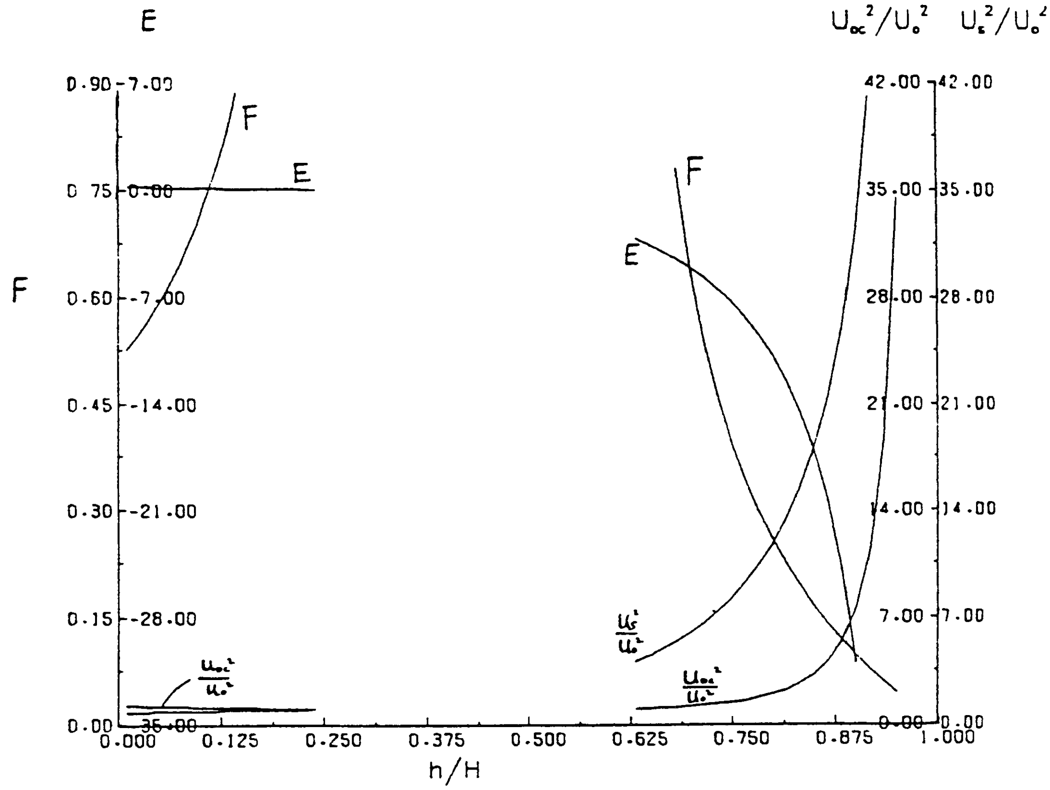

h_i=0 75H,G=0,β=1,β_c=1

fig 2.2.1.4a Variations of F,E,$\frac{u_s^2}{u_o^2}$,and $\frac{u_{oc}^2}{u_o^2}$ with $\frac{h}{H}$

CAPE > O

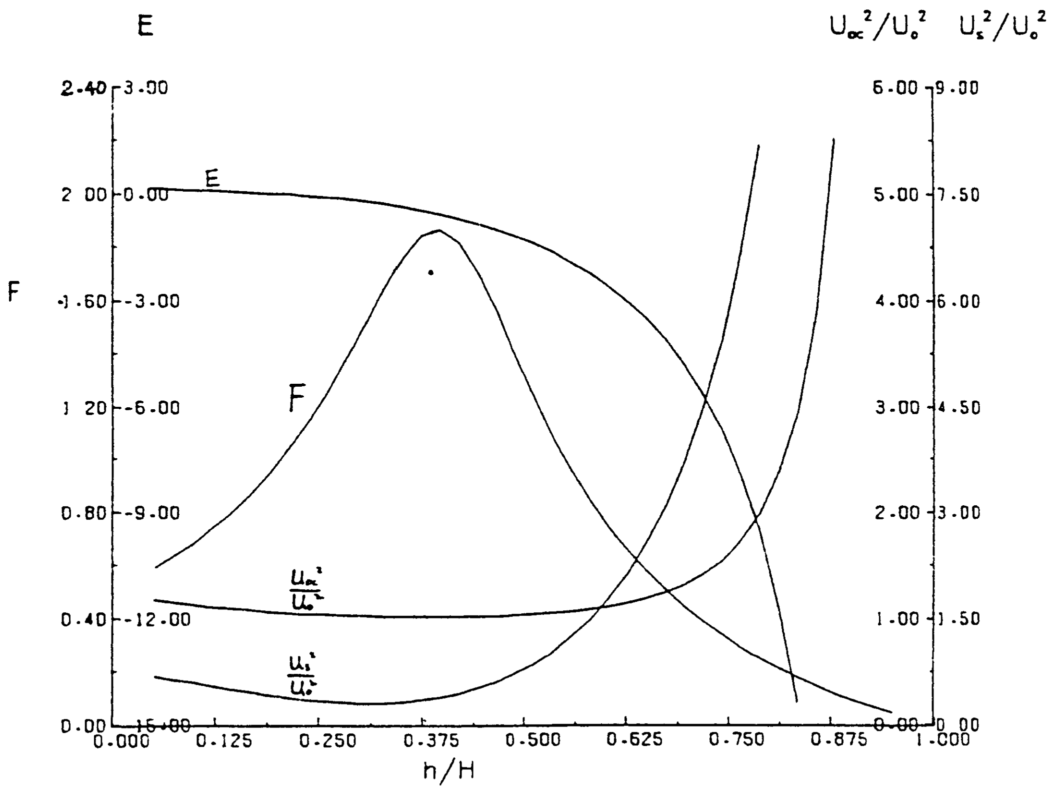

h_i=0.75H,G=−3,β=1,β_c=1

fig 2.2.1.4b (as fig 2.2.1.4a)

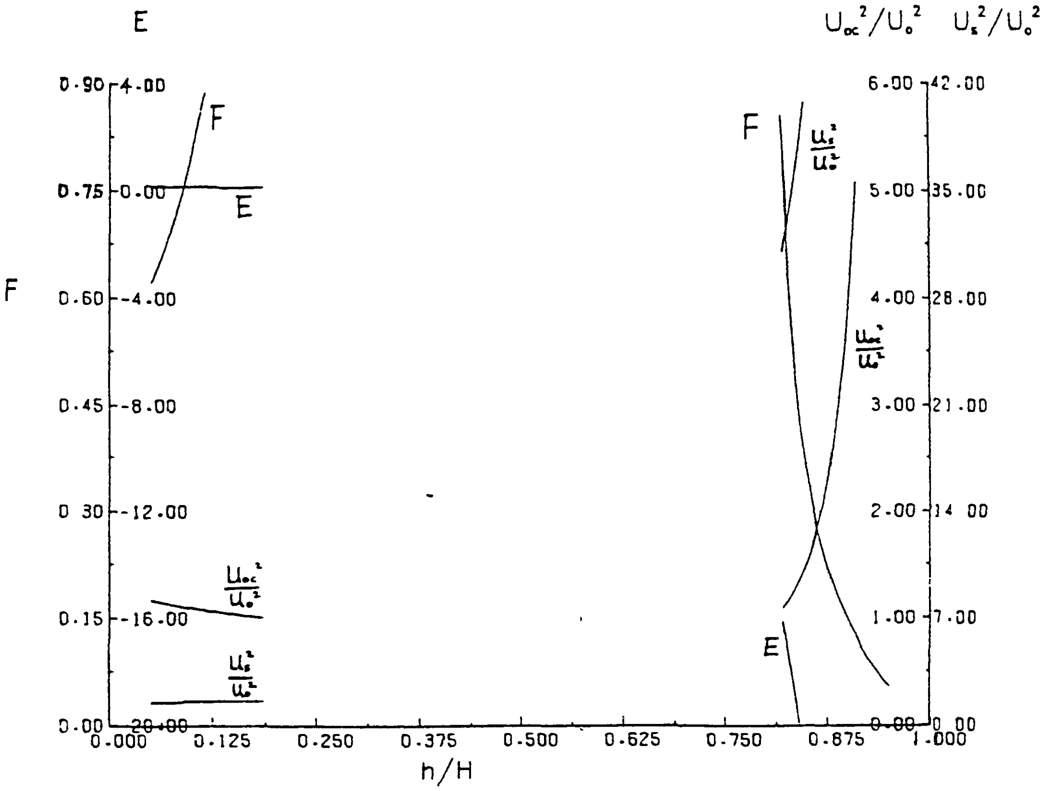

h_i=0.75H,G=0,β=1.25,β_c=1

fig 2.2.1.4c (as fig 2.2.1.4a)

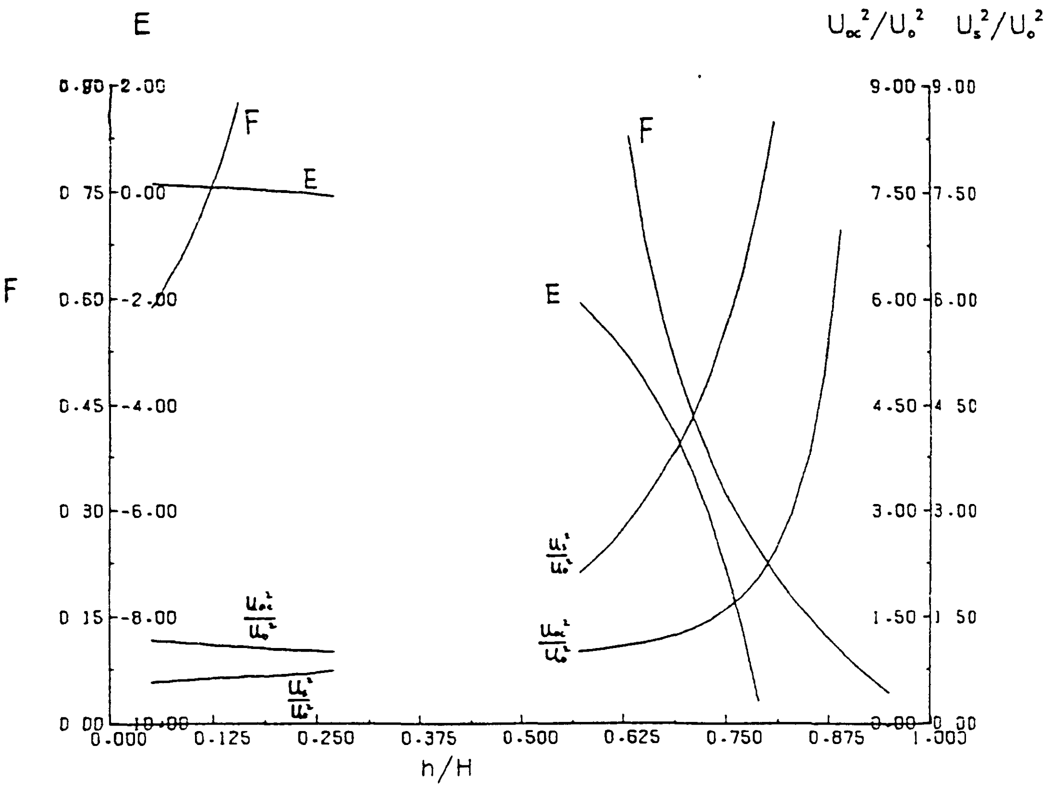

h_i=0 75H,G=0,β=0 8,β_c=1

fig 2.2.1.4d (as fig 2.2.1.4a)

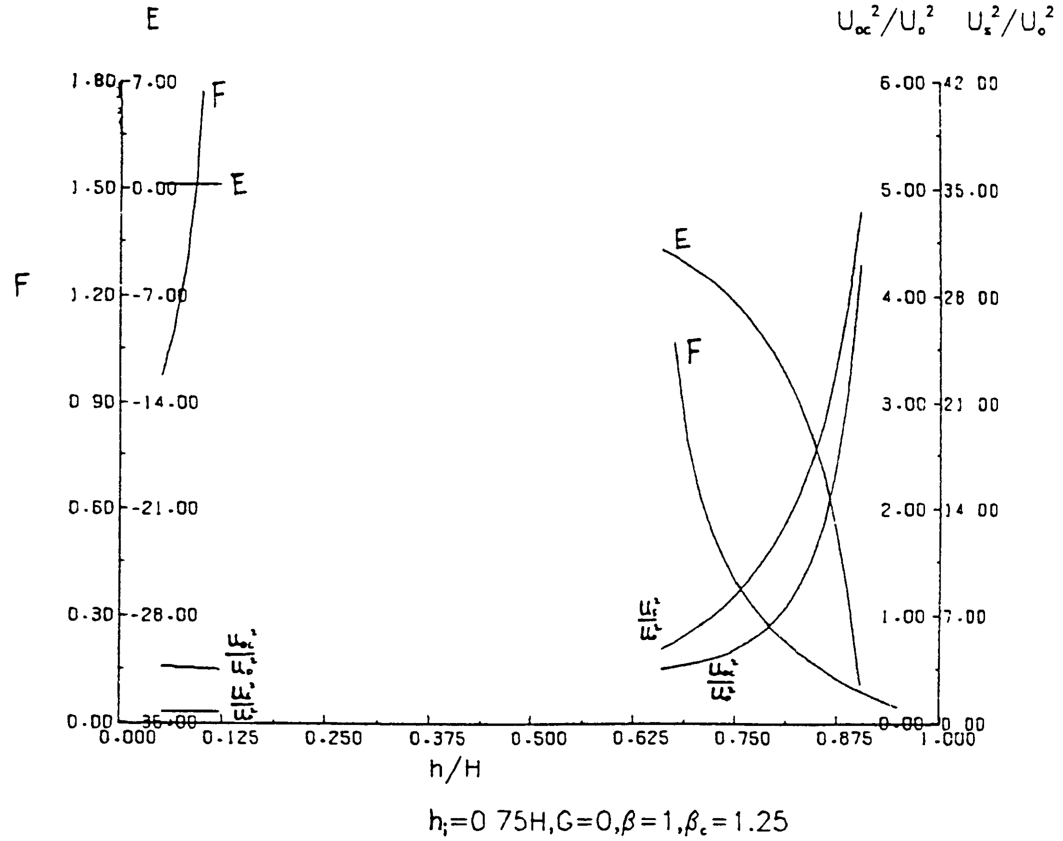

fig 2.2.1.4e (as fig 2.2.1.4a)

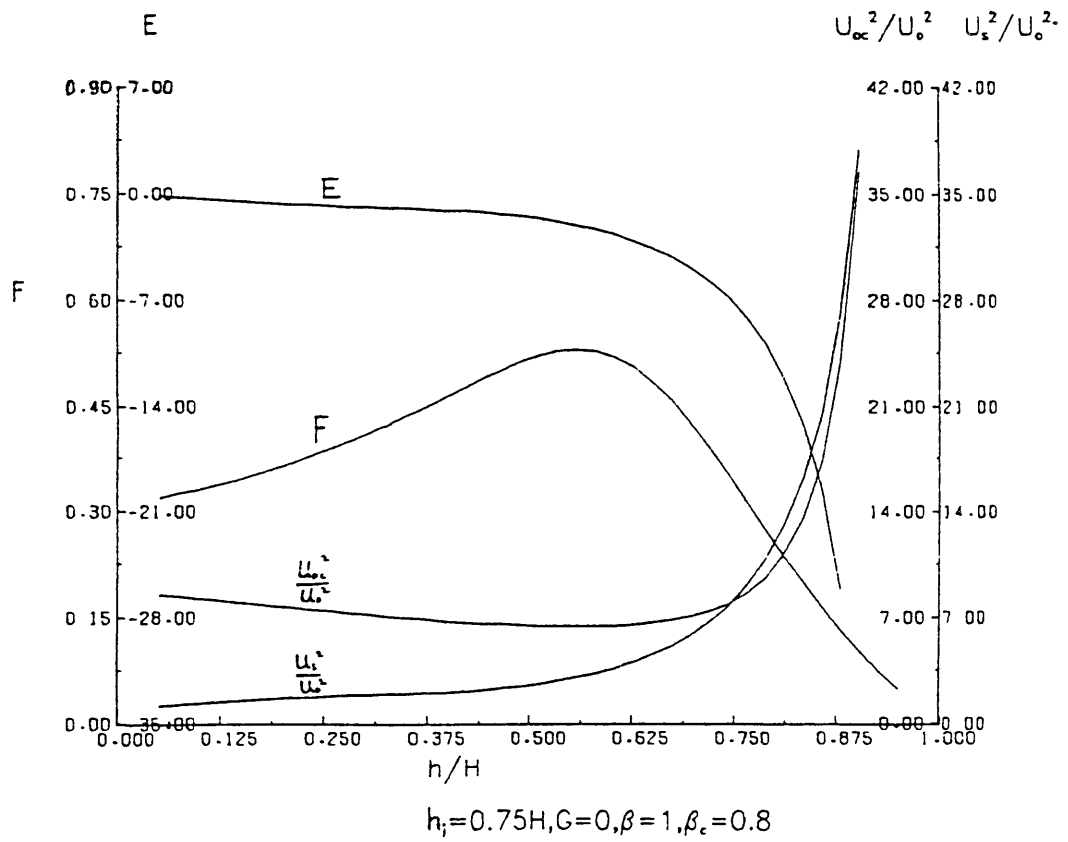

fig 2.2.1.4f (as fig 2.2.1.4a)

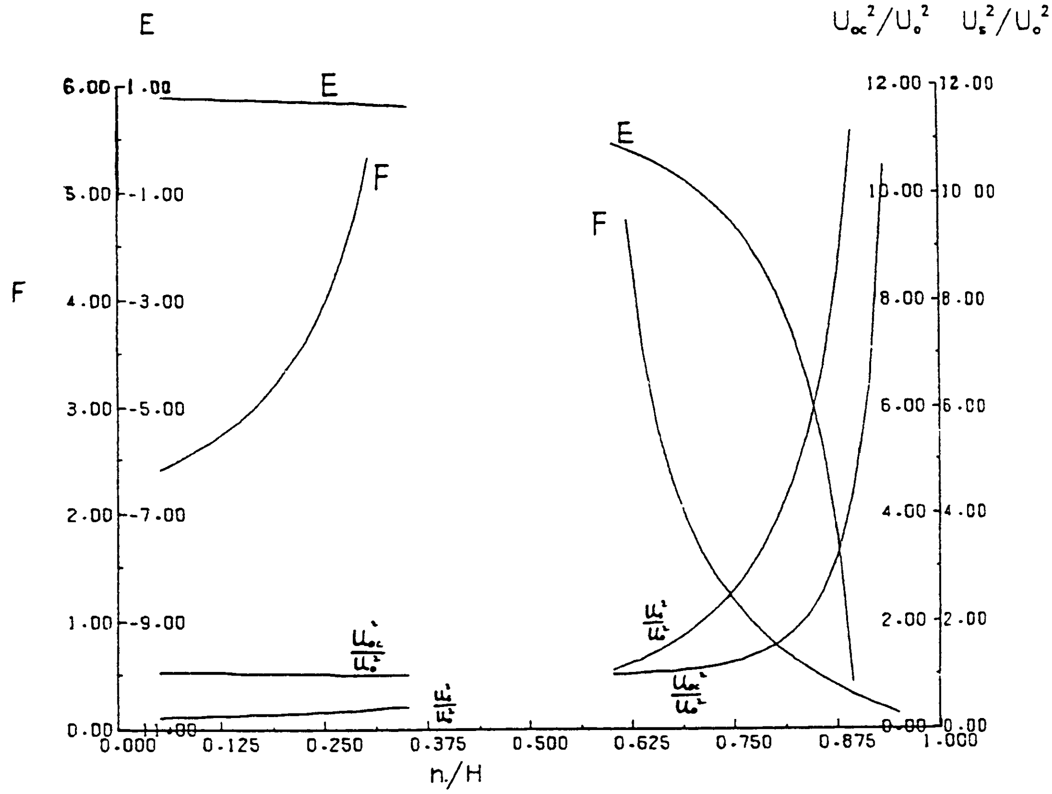

h_i=0 417H,G=0,β=1,β_c=1

fig 2.2.1.4g (as fig 2.2.1.4a)

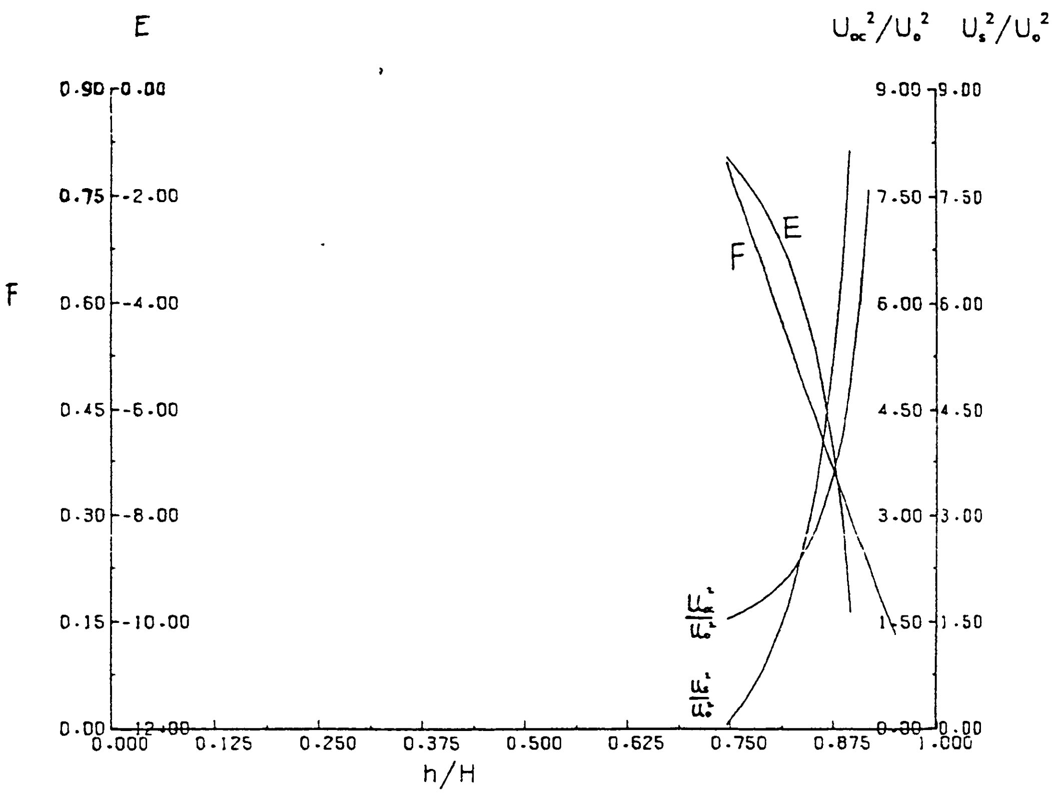

h_i=0.417H,G=−3,β=1,β_c=1

fig 2.2.1.4h (as fig 2.2.1.4a)

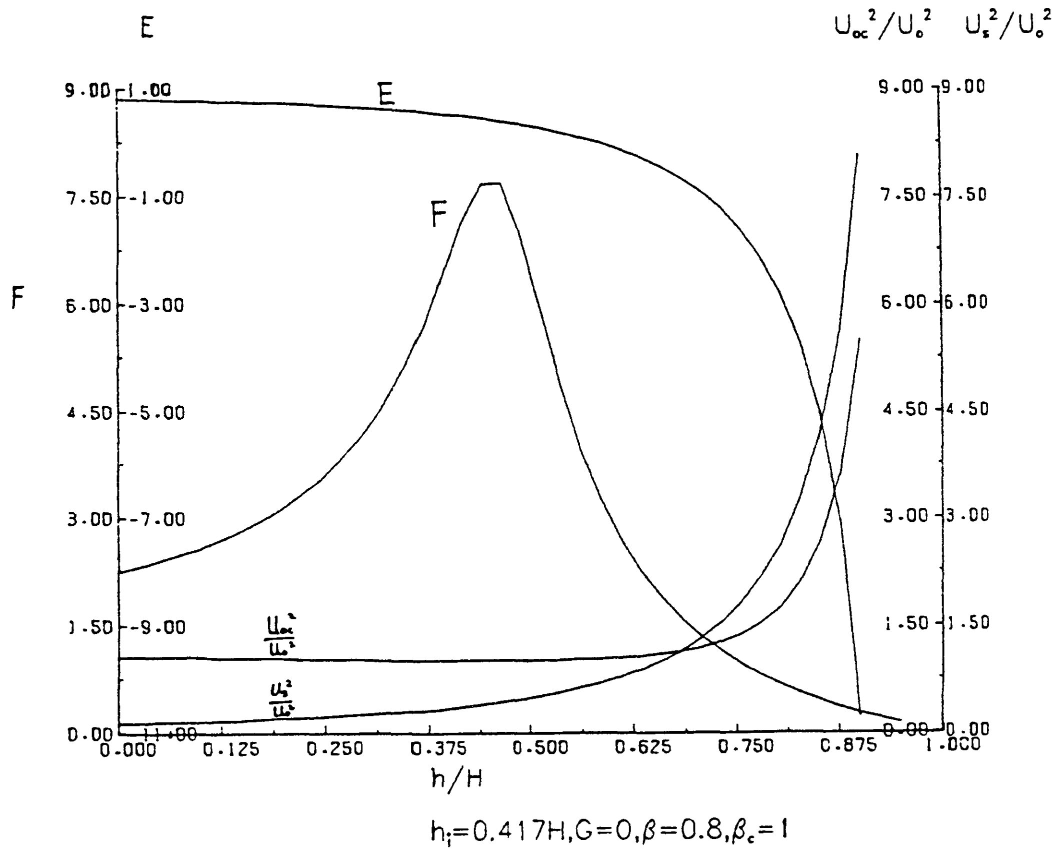

fig 2.2.1.4i (as fig 2.2.1.4a)

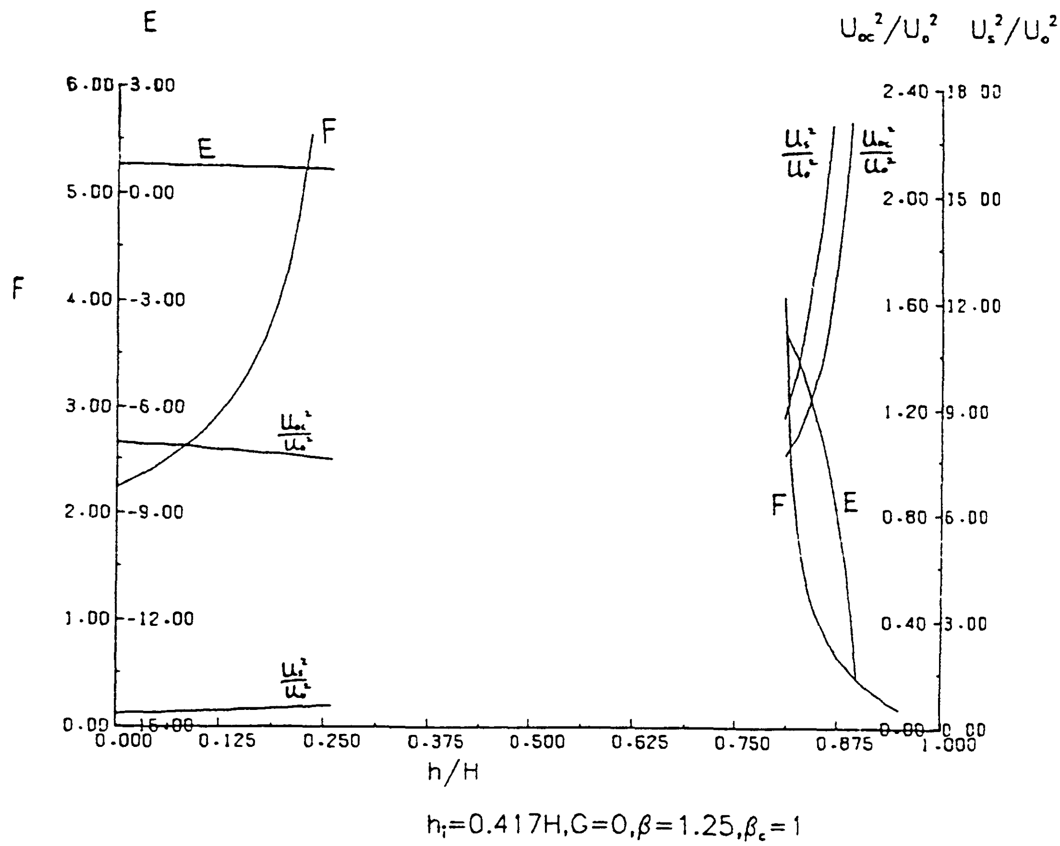

fig 2.2.1.4j (as fig 2.2.1.4a)

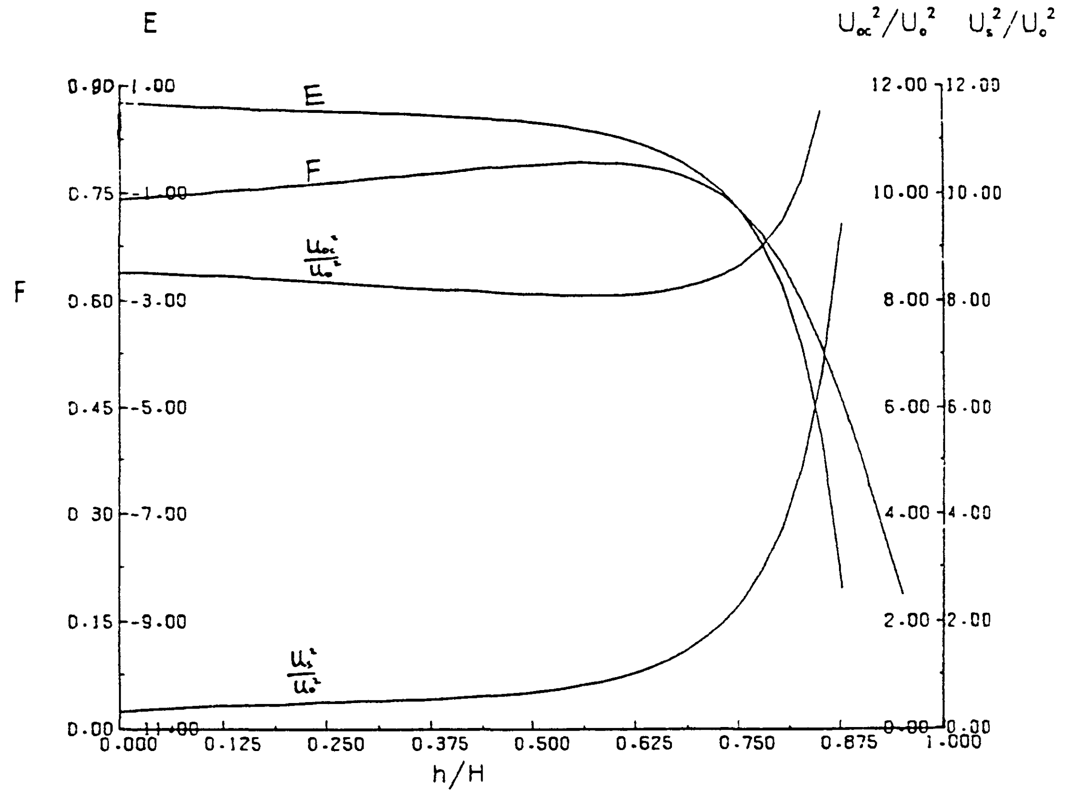

h_i=0.417H,G=0,β=1,β_c=0.8

fig 2.2.1.4k (as fig 2.2.1.4a)

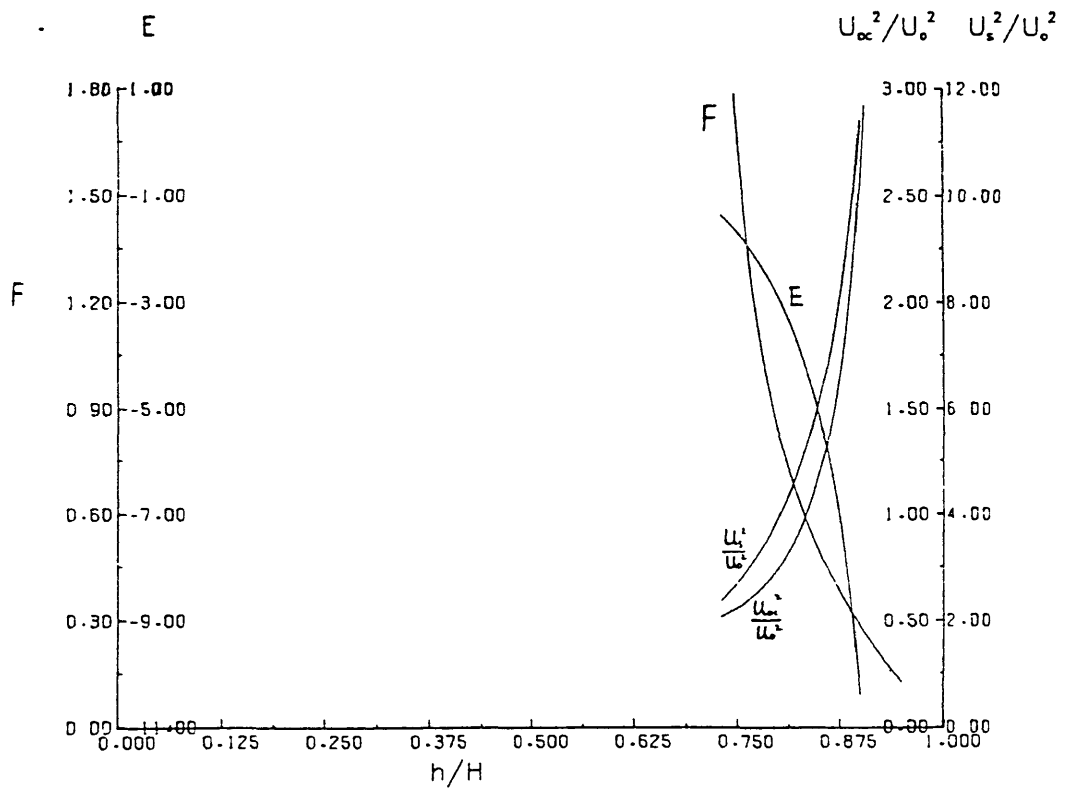

h_i=0.417H,G=0,β=1,β_c=1.25

fig 2.2.1.4l (as fig 2.2.1.4a)

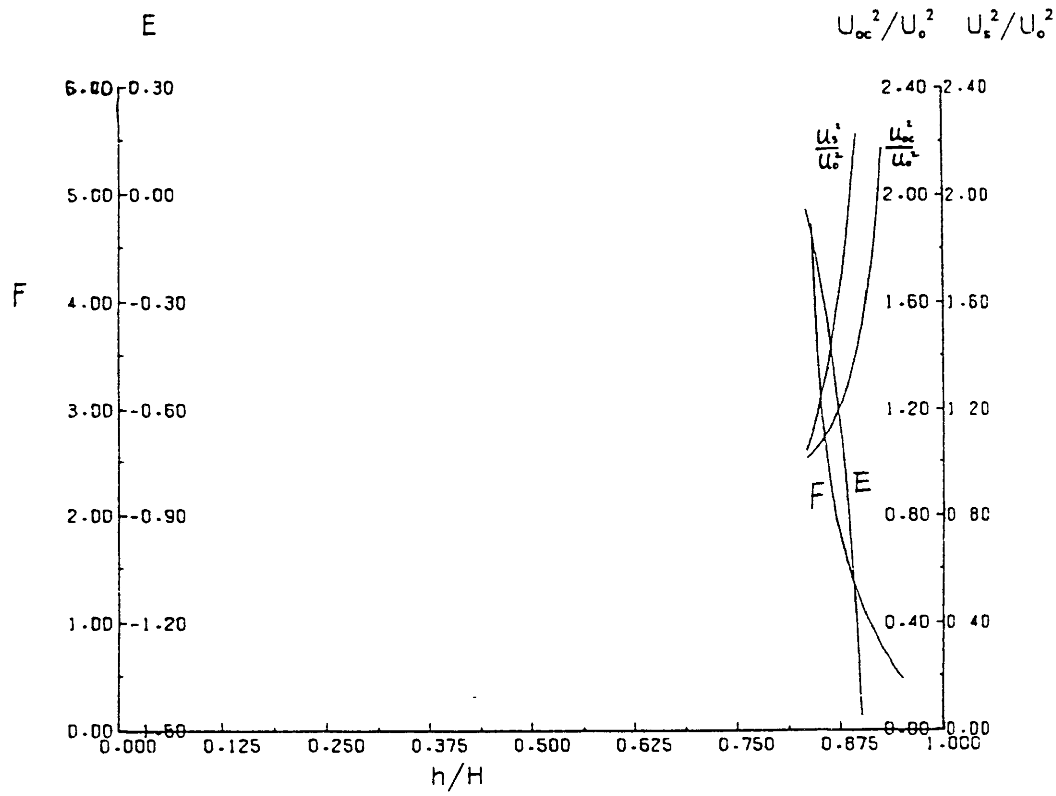

h_i=0.17H,G=0,β=1,β_c=1

fig 2.2.1.4m (as fig 2.2.1.4a)

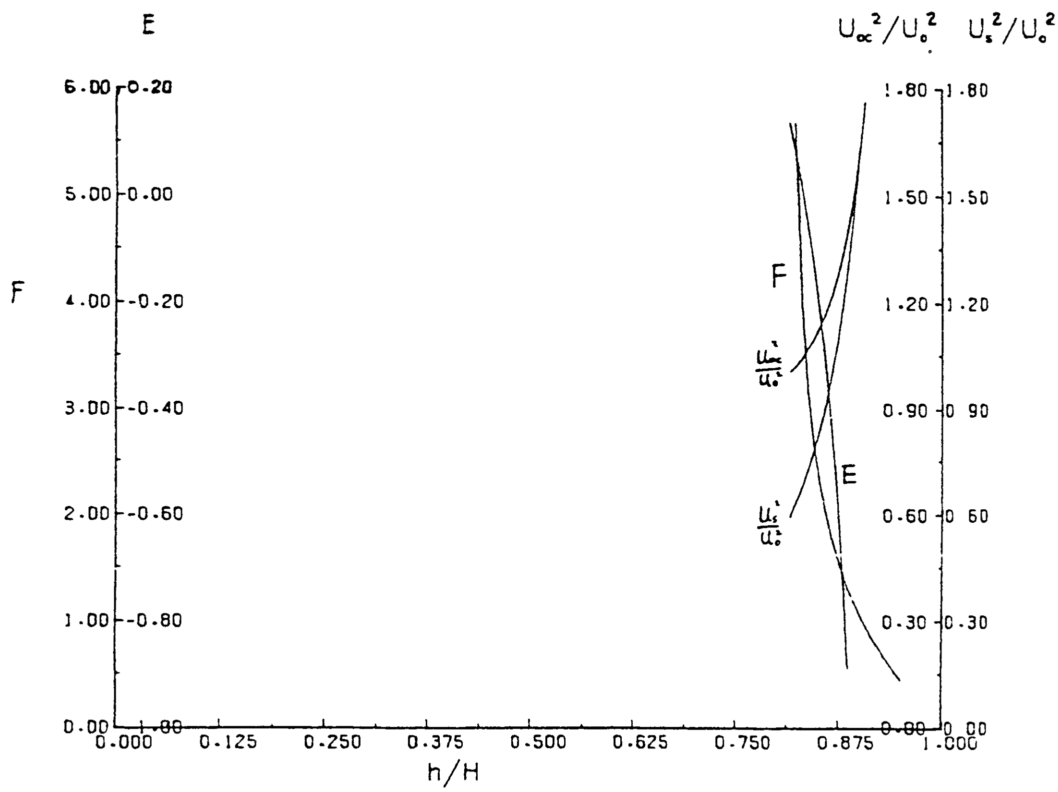

h_i=0 17H,G=0,β=0.8,β_c=1

fig 2.2.1.4n (as fig 2.2.1.4a)

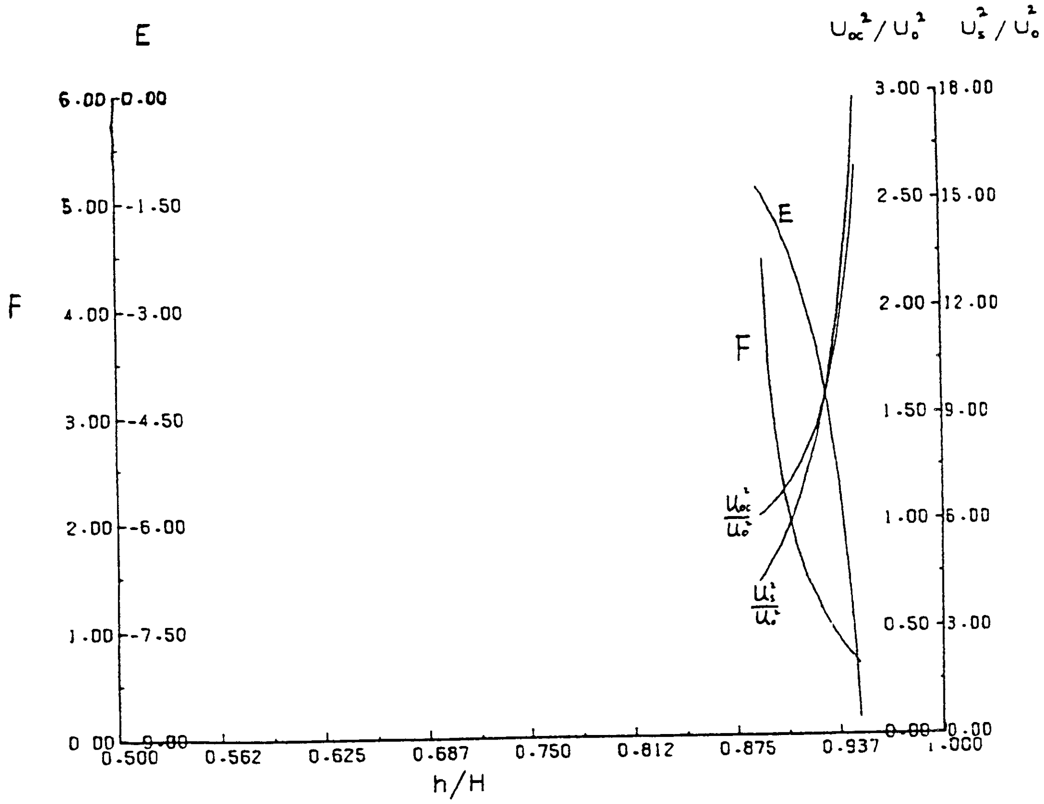

h_i=0.17H,G=0,β=1.25,β_c=1

fig 2.2.1.4o (as fig 2.2.1.4a)

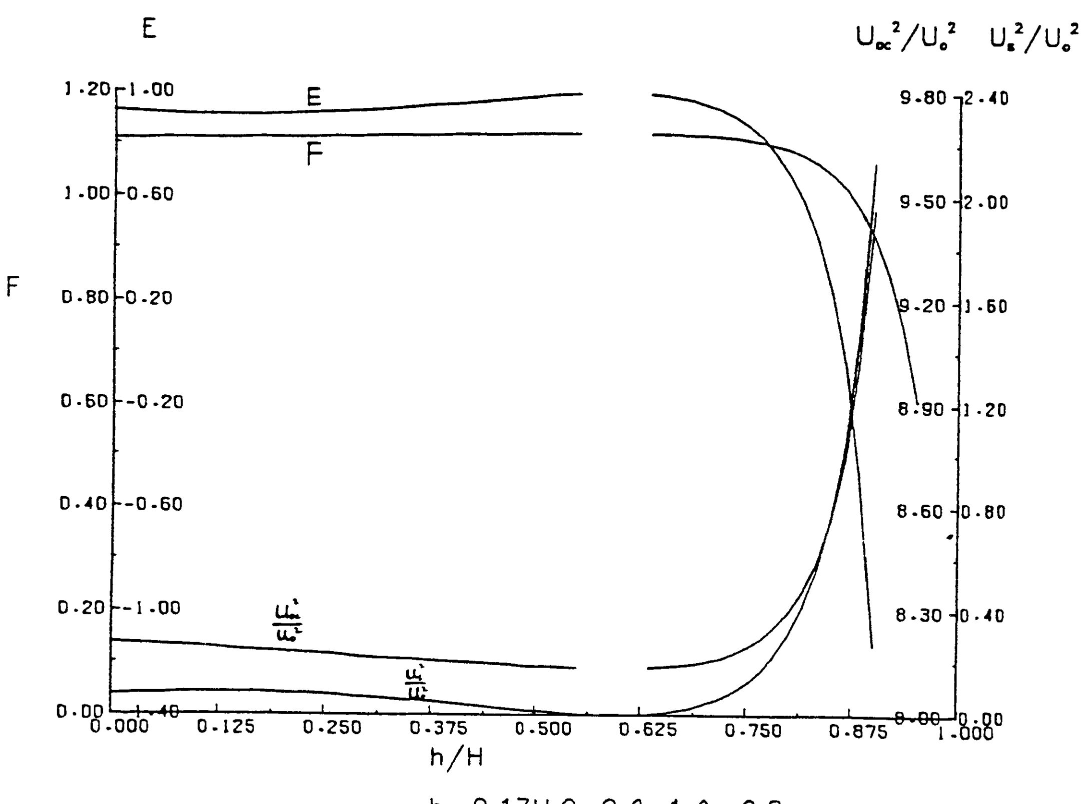

h_i=0.17H,G=0,β=1,β_c=0.8

fig 2.2.1.4p (as fig 2.2.1.4a)

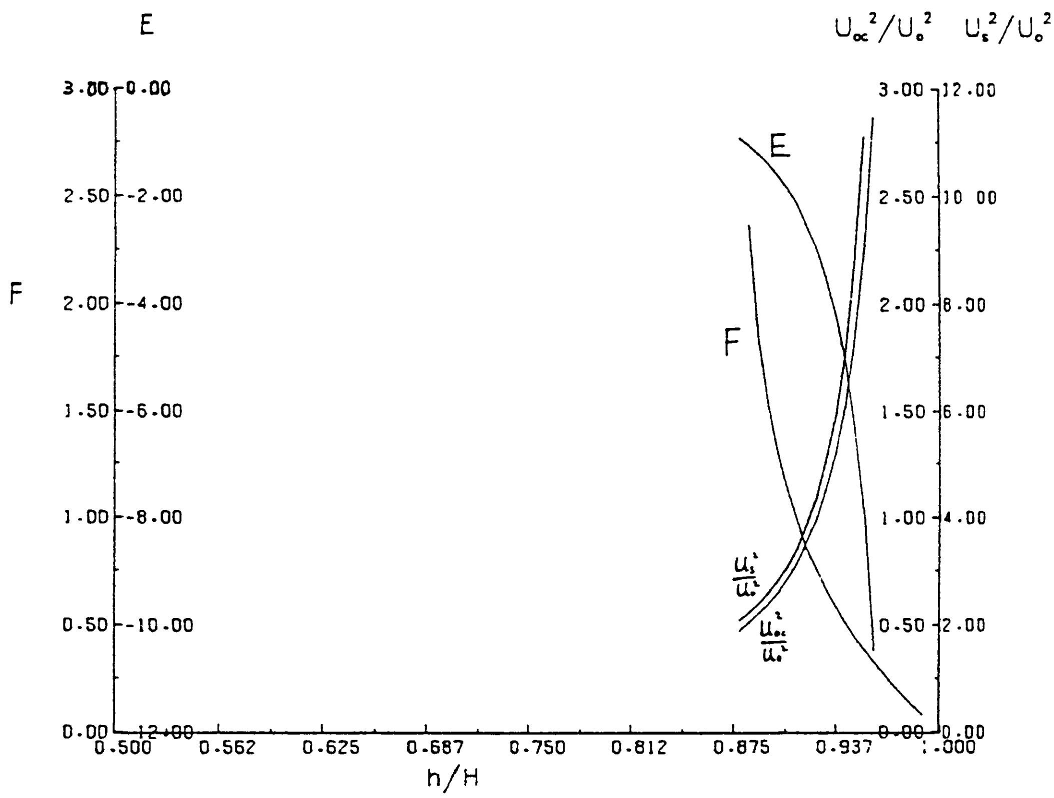

h_j=0.17H,G=0,β=1,β_c=1.25

fig 2.2.1.4q (as fig 2.2.1.4a)

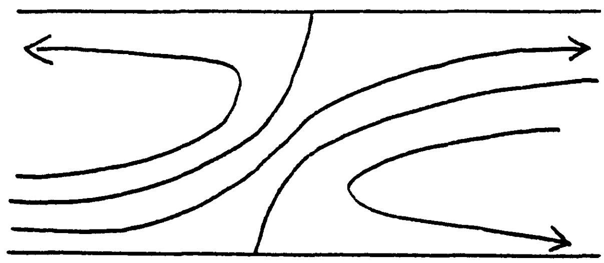

fig 2.2.1.4a An almost symmetric model of mid-latitude squall line

This is a perturbation of the symmetric model of neutral stratification. Also, the shallow lower density model can represent tropical squall line with small or large $\frac{h_i}{H}$.

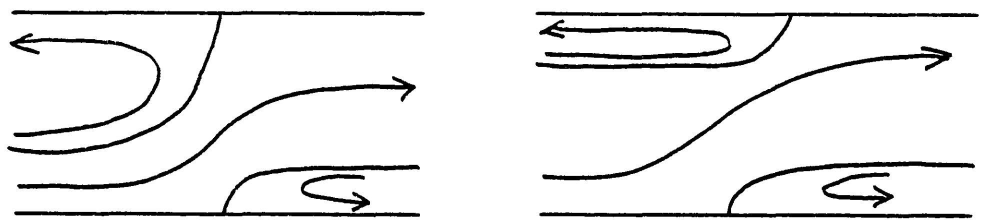

fig 2.2.1.4b Shallow density current models of tropical squall line, perturbations of neutrally stratified models.

2.2.2 Negatively Buoyant Updraught Models

2.2.2.1 Flow Description -

The models are essentially the same as those in 2.2.1 except that the parcel lapse rate in the updraught region is less than the environmental lapse rate, i.e. $\gamma_1 < B$. With uniform inflow to the updraught region, the streamfunction is solved as

at inflow $\psi = u_0 z_0$,

at outflow $$\psi = u_0 \left(z_1 - \epsilon F H \sin \frac{z_1 - h}{FH} - h \cos \frac{z_1 - h}{FH} \right),$$

$$\epsilon = (1 - h_i/H - h/H \cos\alpha)/(F \sin\alpha),$$

$$\alpha \equiv \frac{H-h}{FH}, \quad F^2 \equiv \frac{u_0^2}{-g(\gamma_1 - B) H^2}$$

To find E, the energy equation is applied on the streamline $\psi = 0$,

$$\tfrac{1}{2}u_0^2 = \tfrac{1}{2}u_1^2(h) + \left(\frac{\delta P}{\rho}\right)_h + \frac{g(B-\gamma_1)h^2}{2}$$

$$\Rightarrow \quad E = 1 - \left(\frac{h}{FH}\right)^2 - (1-\epsilon)^2$$

Again E is a function of F and $\frac{h}{H}$. Notice F^2 is defined in a different way

$$F^2 \equiv \frac{\frac{1}{2}u_0^2}{-\text{CAPE}} \quad , \qquad \text{CAPE} = \tfrac{1}{2}H^2 g(\gamma_1 - B)$$

2.2.2.2 Momentum Balance -

The expression for m_1, m_3 and m_4 as defined in 2.2.1.2 remain unchanged and $m_2 \equiv \int_h^H u^2 + \frac{\delta P}{\rho}\,dz \Big|_{x=\infty}$ is found to be

$$\frac{m_2}{Hu_0^2} = \left(1-\frac{h}{H}\right) - \tfrac{1}{2}E\left(1-\frac{h}{H}\right) + \left(1-\frac{h}{H}\right)\left(\epsilon - \epsilon^2/2\right) - \epsilon\frac{h}{H}\sin^2\alpha$$
$$- F\epsilon\sin\alpha - \frac{h}{H}(\cos\alpha - 1) - \frac{1}{F^2}\left[\tfrac{1}{2}\left(1-\frac{h}{H}\right)\left(\frac{h}{H}\right)^2 + \frac{F}{4}\sin 2\alpha\left[\left(\frac{h}{H}\right)^2 - (\epsilon F)^2\right]\right]$$

2.2.2.3 Full Depth Inflow Model -

The solution for ψ at outflow is

$$\psi_1 = u_0\left(z_1 - \frac{h\sin\frac{H-z_1}{FH}}{\sin\alpha}\right)$$

Conservation of $\frac{1}{2}v^2 + \frac{\delta P}{\rho} - g\int_{z_0}^{z}\delta\phi\,dz$ along the bottom boundary and interface leads to

$$\left(\frac{h}{FH}\cot\alpha\right)^2 + 2\frac{h}{H}\cot\alpha + E + \left(\frac{h}{FH}\right)^2 = 0$$

which for real $\cot\alpha$ requires $E \leq 1 - \left(\frac{h}{FH}\right)^2$.

The parameter set $\{G, \beta\}$ are given the values of {0,1}, {-3,1}, {0,0.8} and {0,1.25} and the graphs are shown in fig 2.2.2.3a-d. The variation of parameters is as $\frac{h}{H}$, F and $\left(\frac{u_s}{u_o}\right)^2$ increase E decreases. For {0,1}, the solution range is [0,2/3] and it is noted that for h/H>2/3 CAPE is required to be positive. When h/H is near to zero, $u_s << u_o$ and E is positive which is different from the full depth inflow model with positive CAPE where $u_s >> u_o$ implies the density current is the dominant flow. It is also interesting to note that when h/H=0, E and F attain finite values of 1 and $\frac{1}{\pi}$ =0.3183 respectively. This value of F is one of the allowable values given by Thorpe,Miller and Moncrieff(1980). However, they showed that E is arbitrary in the sense that E can be any value within the interval [-3,1].

Again for G<0 and β <1, the upper limit of the solution range is depressed below 2/3 and β >1 raises this limit.

2.2.2.4 Fractional Inflow Model -

As seen in fig 2.2.2.4a-g, the solution range for $\frac{h}{H}$ occupies a continuous interval . F and $\left(\frac{u_{oc}}{u_o}\right)^2$ attain their minimums simultaneously. $\left(\frac{u_s}{u_o}\right)^2$ and E increase and decrease respectively as $\frac{h}{H}$ increases. Again a single F correspond to two configurations of flow. The two cases of neutral flow are approached as F tends to infinity and $\frac{h}{H}$ tends to its two critical values.

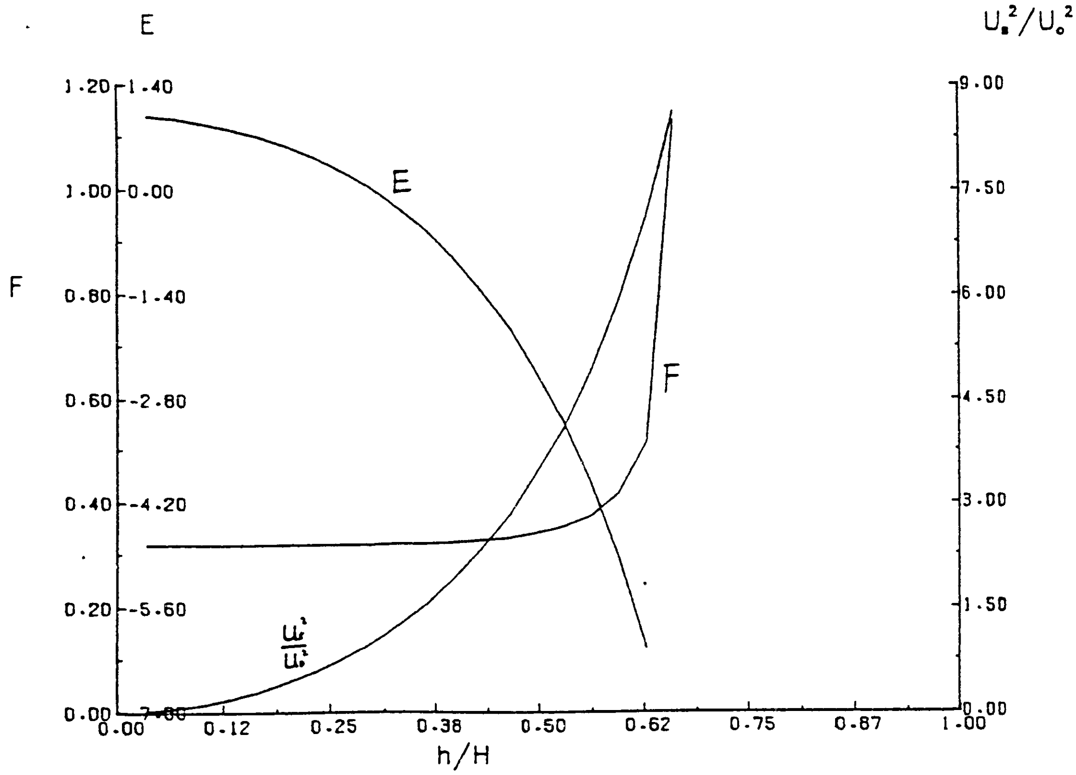

$h_i = H, G = 0, \beta = 1$

fig 2.2.2.3a Variations of F,E and $\frac{U_s^2}{U_o^2}$ with $\frac{h}{H}$

CAPE < 0

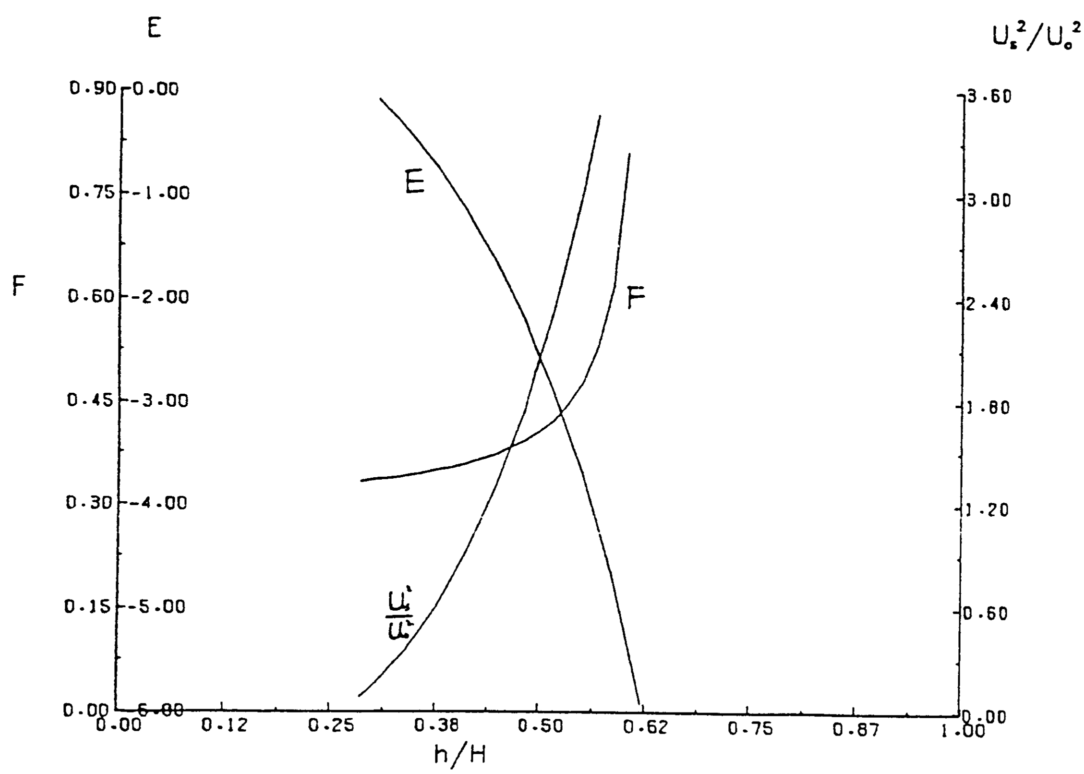

$h_i = H, G = -3, \beta = 1$

fig 2.2.2.3b (as fig 2.2.2.3a)

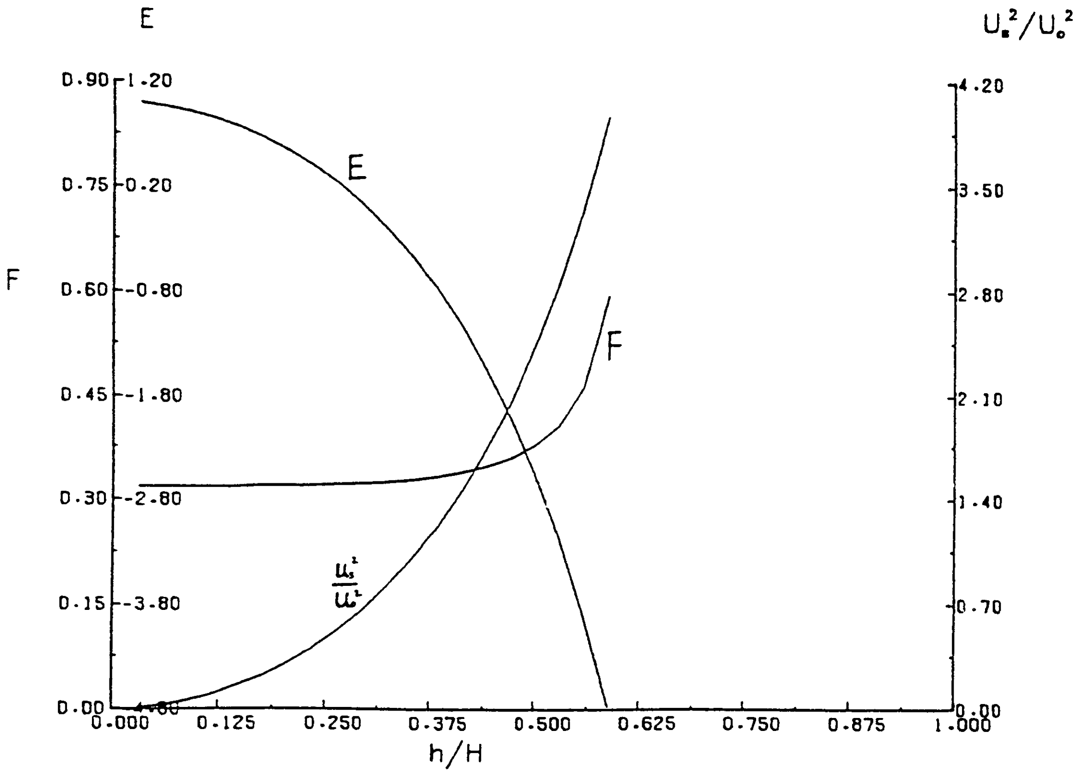

h_1=H,G=0,β=0.8

fig 2.2.2.3c (as fig 2.2.2.3a)

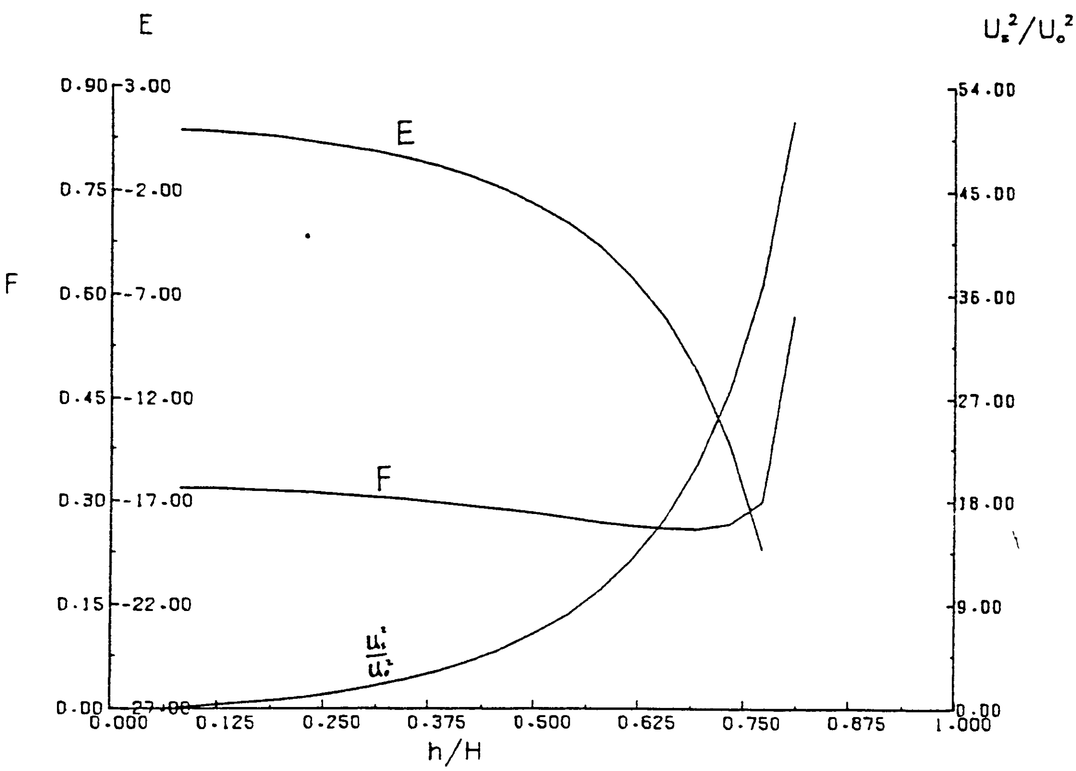

h_1=H,G=0,β=1.25

fig 2.2.2.3d (as fig 2.2.2.3a)

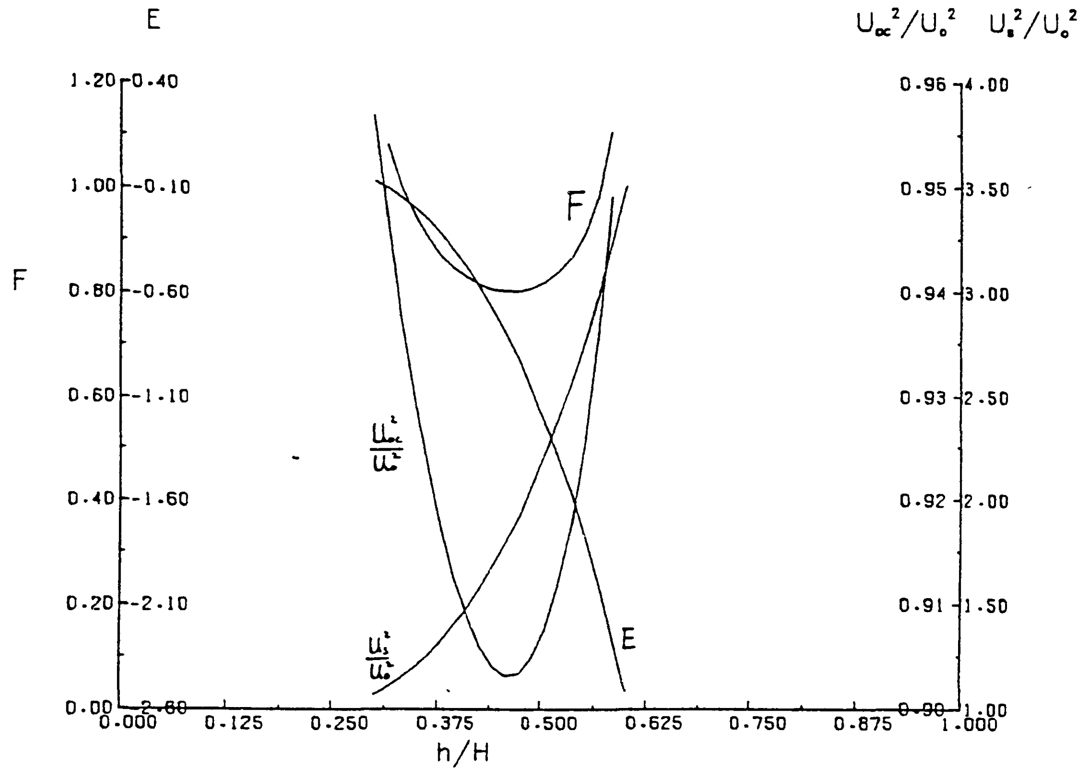

$h_1=0.75H, G=0, \beta=1, \beta_c=1$

fig 2.2.2.4a Variations of F,E, $\frac{u_s^2}{u_o^2}$ and $\frac{u_{oc}^2}{u_o^2}$ with $\frac{h}{H}$

CAPE < 0

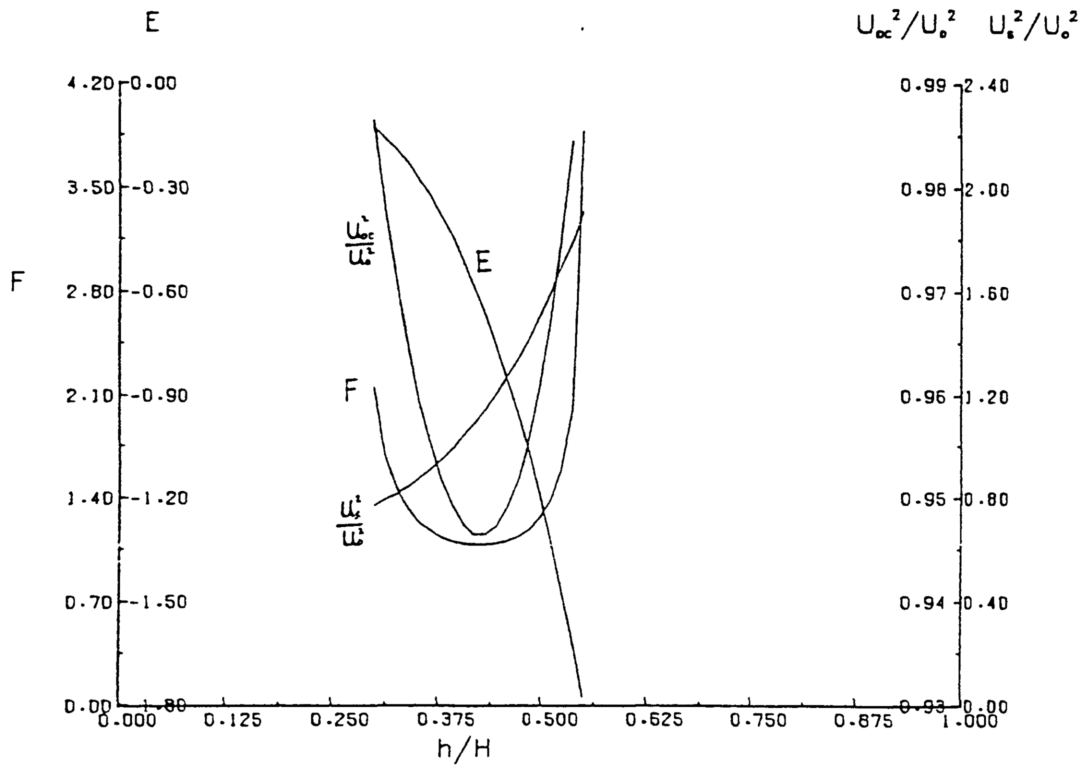

$h_1=0.75H, G=0, \beta=0.8, \beta_c=1$

fig 2.2.2.4b (as fig 2.2.2.4a)

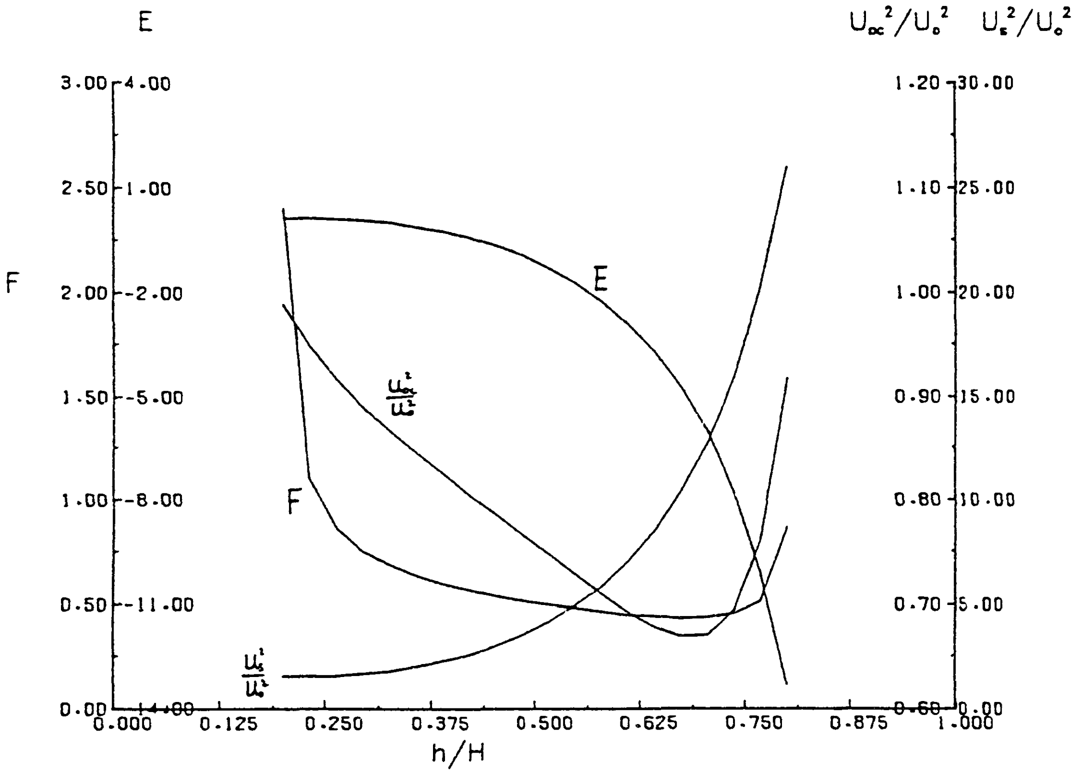

h_1=0.75H,G=0,β=1.25,β_c=1

fig 2.2.2.4c (as fig 2.2.2.4a)

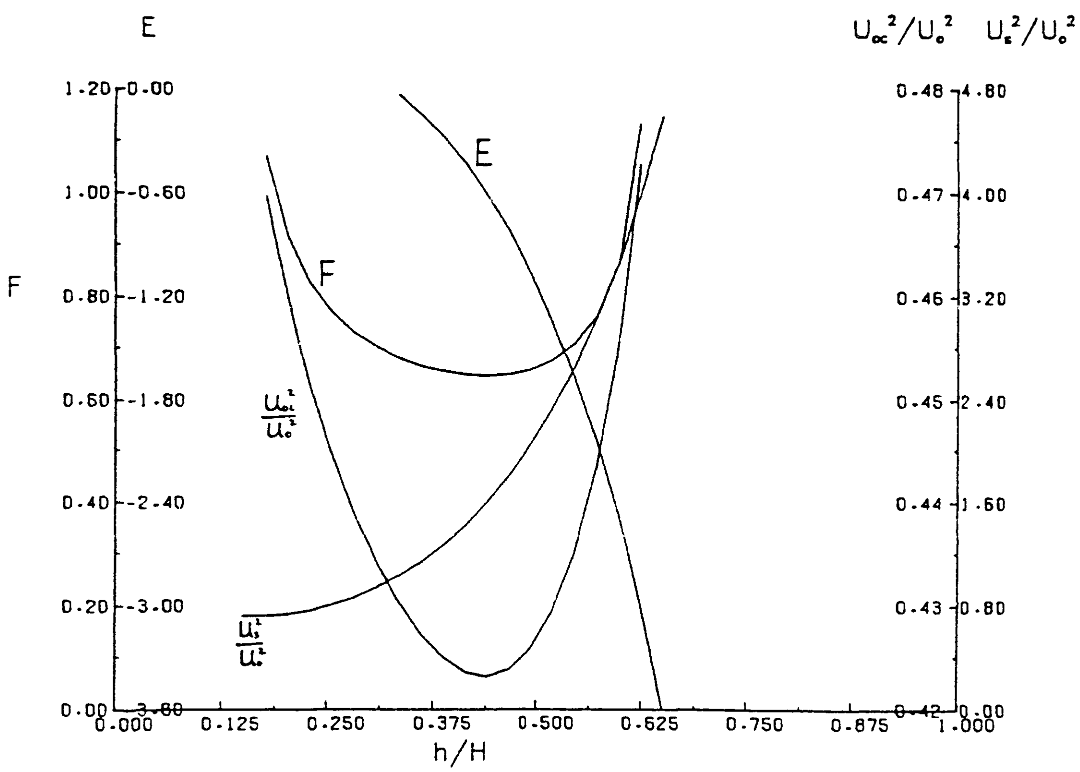

h_1=0.75H,G=0,β=1,β_c=1.25

fig 2.2.2.4d (as fig 2.2.2.4a)

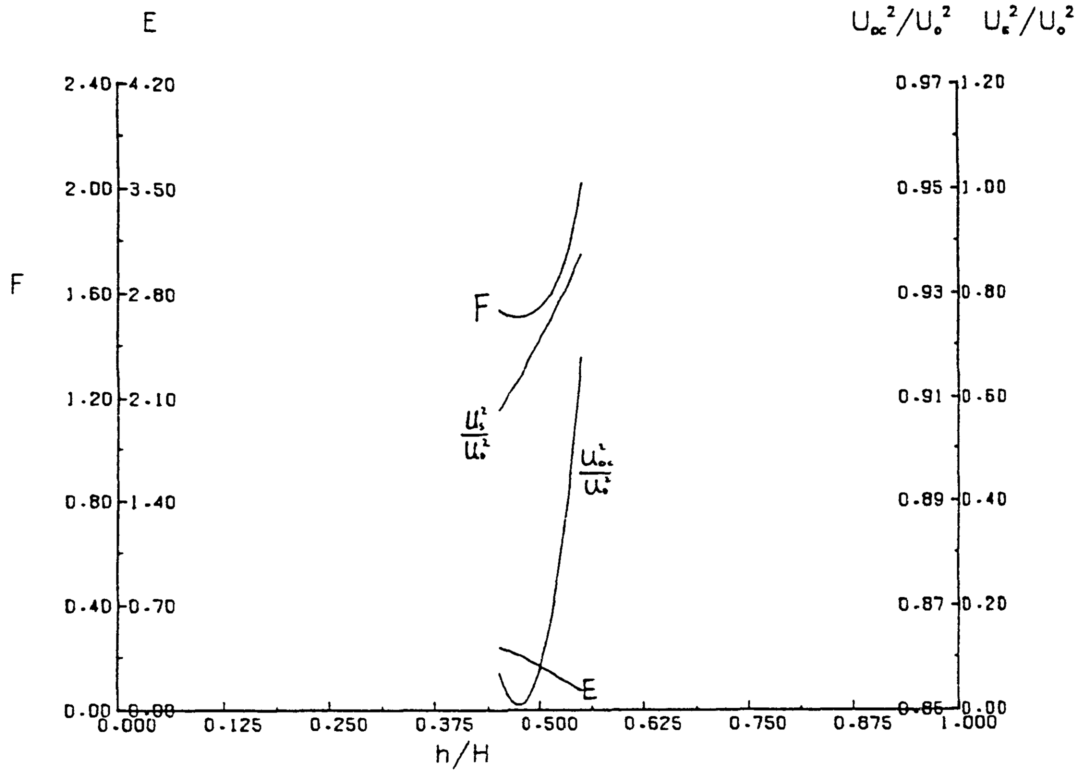

h_1=0.417H,G=0,β=1,β_c=1

fig 2.2.2.4e (as fig 2.2.2.4a)

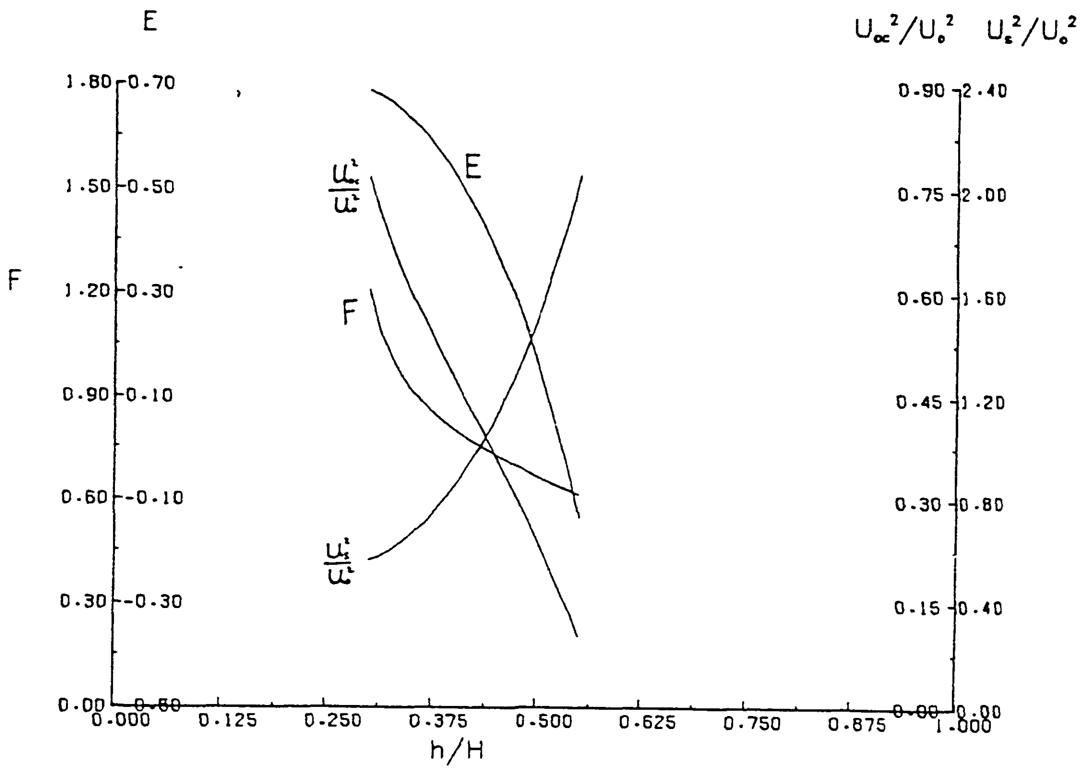

h_1=0.417H,G=0,β=1.25,β_c=1

fig 2.2.2.4f (as fig 2.2.2.4a)

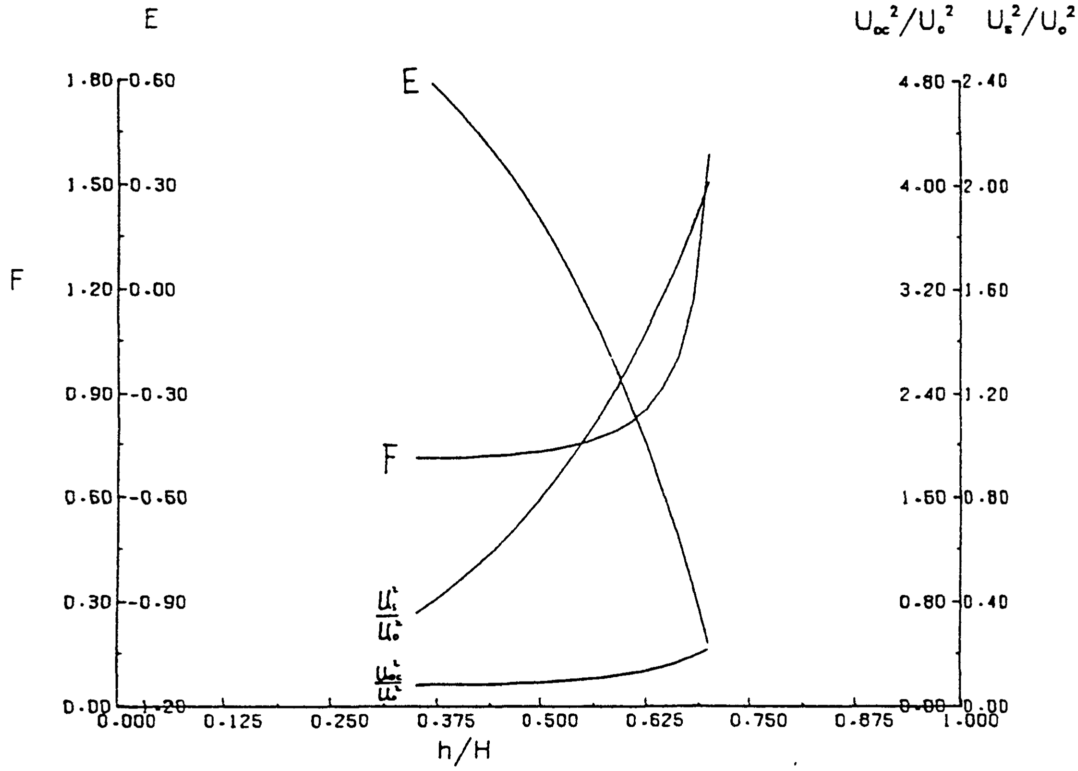

fig 2.2.2.4g (as fig 2.2.2.4a)

2.2.3 Overall Behaviour Of Stratified Models

For $\frac{1}{3} < \frac{h_i}{H} < 1$ and G=0 and $\beta = \beta_c = 1$, there exist two critical values $\frac{h_1}{H}$, $\frac{h_2}{H}$ with $h_2 > h_1$ such that the buoyant updraught models occupy the upper and the lower solution ranges $[0, h_1/H]$ and $[h_2/H, 1)$; and the negatively buoyant updraught models occupy the range $[h_1/H, h_2/H]$. $\frac{h_1}{H}$ and $\frac{h_2}{H}$ are the two values which correspond to the two neutrally stratified cases for that particular $\frac{h_i}{H}$. For $\frac{h_i}{H} < \frac{1}{3}$, $\frac{h_1}{H}$ and $[h_1/H, h_2/H]$ do not exist and thus there is no solution for the negatively buoyant updraught models. The variations of G about 0, β and β_c about 1 influence $\frac{h_2}{H}$ and $\frac{h_1}{H}$ in the following way: as G, β and β_c decrease, $\frac{h_2}{H}$ decreases and $\frac{h_1}{H}$ increases; as β and β_c increase, $\frac{h_2}{H}$ increases and $\frac{h_1}{H}$ decreases. Where $\frac{h_2}{H}$ and $\frac{h_1}{H}$ merge together, only solutions for buoyant updraught models exist. Finally, the constraint of $U_s^2 > 0$ sometimes is not satisfied and invalidate some part of what would otherwise have been valid solution.

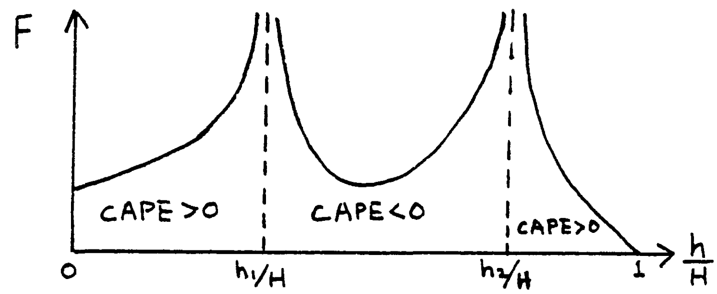

fig 2.2.3 Solution ranges for CAPE>0 and CAPE<0

2.2.4 Physical Interpretation Of F, U_0, H And E

Out of the various parameters of the models, only CAPE and H are known a priori. CAPE $= \int_0^H g\delta\phi\, dz$ and H is the highest zero buoyancy level attained by some parcel entering the system. Strictly speaking with $(\gamma_1 - B)$ a constant for each streamline, a finite value for H is not possible but in reality $(\gamma_1 - B)$ is not a constant and H can be identified on $T-\phi$ gram.

u_0 is not really known as it does not only depend on the environmental wind profile but it also depends on the system propagation speed relative to the ground. Moreover, the level of no motion of the upper overturning flow on the LHS depends on u_0 and this in turn causes h_i to be dependent on u_0 .

Given a wind profile relative to the ground, the system has to choose a 'suitable' propagation speed such that the relative wind profile has an appropriate u_0 which then determines the following parameters in the written order, $\frac{h_i}{H}$, $F^2 \equiv \frac{\frac{1}{2}u_0^2}{CAPE}$, $\frac{h}{H}$ (either of the two possible values), E, $\left(\frac{\delta P}{\rho}\right)_h$. Notice that the larger scale situation influences the possible values of h and $\left(\frac{\delta P}{\rho}\right)_h$ hence the suitable propagation speed is required if steady two-dimensional motion is to occur.

CHAPTER 3

FREE BOUNDARY PROBLEM

Only the asymptotic problems of density currents models have been considered so far. The existence of solutions to the asymptotic problem does not necessarily mean that complete solutions describing the internal dynamics/thermodynamics can be found. It is the purpose of this chapter to investigate if internal solutions to the simplest stratified models considered in chapter two exist. If indeed an internal solution can be found, then we are able to describe the distribution of the important field variables such as streamfunction,pressure and temperature over the whole domain of the model. The internal structure can then be interpreted to see whether it is physically realistic and consistent with other physical constraints which have so far been excluded from the model. For example, in Browning and Ludlam's conceptual model based on observation of the Wokingham storm (fig 1a), the interface slopes upshear with the updraught leaning over the downdraught and therefore the rain from the updraught falls into the downdraught which is then evaporatively cooled. The conceptual model is thermodynamically consistent. Moncrieff(1978) studied analytically the dynamical structure of two-dimensional steady convection in constant vertical shear which is based on the conceptual model and corresponds to some mid-latitude squall lines. The internal solutions of his analytic models show that the interface between the updraught and downdraught slopes downshear so that the downdraught leans above the updraught. Therefore, the internal solutions show that this two-dimensional analytic model is not thermodynamically consistent and Moncrieff suggested that quasi-steady storms are not adequately described by two-dimensional dynamics. However, Thorpe, Miller and Moncrieff 1982(TMM) stressed that steady two-dimensional mid-latitude squall lines were possible if the shear varies suitably with height.

In the present study, the internal solutions of the full-depth inflow models will be studied since they have simpler internal structures than those with two density currents. The asymptotic values of the streamfunctions are known and they are prescribed as boundary values at $x=\pm\infty$. The domain is divided by the interface into two regions governed by two different vorticity equations. The difficulty of solving the vorticity equations is significantly increased because the position of the interface is unknown. The apparently indeterminate nature of the problem is removed by introducing a necessary boundary condition on the interface, that of pressure continuity. This means that the pressure should approaches to the same limit on the interface from either side of the interface. This particular problem involving an unknown free boundary belongs to a much wider class of free boundary problems. Three other examples of free boundary problems will now be presented.

FREE BOUNDARY PROBLEM

3.1 EXAMPLES OF FREE BOUNDARY PROBLEMS

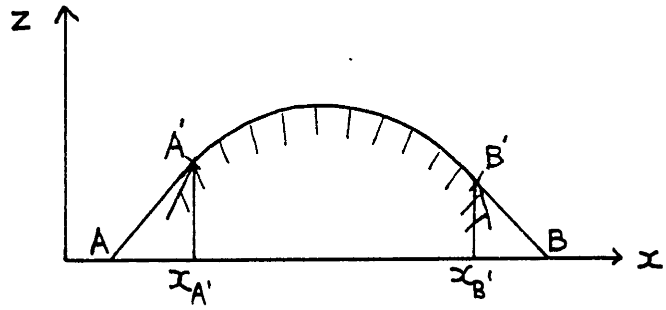

fig 3.1a Taut string on a known obstacle–a free boundary problem

In the example shown in fig 3.1a (Elliot and Ockendon,1982), a taut string wraps round a fixed obstacle. The string is fixed at the end points, A and B. However, the two points at which the string leaves the obstacle, A' and B', are not known. A' and B' therefore are the unknown boundary points in this one-dimensional free boundary problem.

Since the shape of the obstacle is known, its gradient at every point is also known as a function of x . The section AA' is taut and therefore it has a constant gradient. The extra static boundary condition required is that the gradient of AA' be the same as the gradient of the obstacle at A'. The problem can be solved by assuming $x_{A'}$ as the x-coordinate of the correct boundary A' and solve for $x_{A'}$ using the static boundary condition. The same can be done for the other unknown boundary point B'. In this problem, the gradients at the unknown boundary points can be expressed as function of $x_{A'}$ and $x_{B'}$ whereas in our problem velocity(streamfunction gradient) at the interface cannot be expressed analytically as a function of space.

FREE BOUNDARY PROBLEM

The second example is that of water seepage through a porous dam.

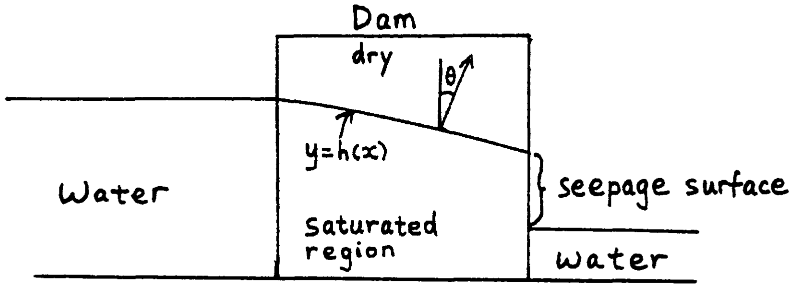

fig 3.1b Water seepage through a porous dam

The upper boundary of the saturated region , $y=h(x)$, is not known. The governing equation for the flow within the saturated region is

$$\nabla^2 P = 0$$

where P is the pressure and the boundary condition at the unknown boundary h(x) is

$$P = 0 = \frac{\partial P}{\partial n} + \rho g \cos\theta$$

This problem can be reformulated by making the transformation

$$u(x,y) = \begin{cases} \int_y^{h(x)} P(x,y')\,dy' & , \; y < h(x) \\ 0 & , \; y > h(x) \end{cases}$$

to

$$\nabla^2 u = \rho g \;, \quad y<h(x) \quad ; \qquad u = 0 \;, \quad y > h(x)$$

with boundary condition at y=h(x) as $u = \frac{\partial u}{\partial n} = 0$. If analytic solution can be found for the Poisson equation over a region bounded by any given smooth boundary h(x), then application of the extra boundary condition $\frac{\partial u}{\partial n} = 0$ determines the ideal boundary. Unfortunately, an analytic solution is not possible and so another method of solution has to be employed(Elliot and Ockendon 1982).

The third example is the problem of Benjamin's conservative density current model where the stagnant density current has to occupy half the total depth. The governing equation for the jump region is $\nabla^2\psi = 0$ since the flow is irrotational. The velocity at the interface, given by $\frac{\partial\psi}{\partial n}$, is known as a function of z, i.e. $\left(\frac{\partial\psi}{\partial n}\right)^2 = 2\hat{g}z$. An attempt to find the shape of the interface was made by Benjamin(1968) who employed some complicated complex transformations. However,only an approximate shape of the interface was obtained.

In each of these three examples, once the positions and shapes of the unknown boundary have been assumed, the solution on one side of the boundary is known, i.e. z is known on section $A'B'$ of taut string, u=0 for y>h(x) and ψ =constant within the density current. Furthermore, the gradient of the unknown variable at the assumed boundary is also known. Free boundary problems of this type are called 'one-phase' problems in the literature. Our problem of non-stagnant density current is more complicated since the solution and the gradient of the variable is not known on both sides of the interface and the gradient on one side is dependent on the gradient on the other side. Such problems which involve solving for the variable on both sides of an unknown boundary are called 'two-phase' problems. There are no general methods available for solving such problems and so a numerical approach will be presented in 3.3. First, the governing equations and dynamical boundary conditions are presented in normalised forms.

3.2 NORMALISED VORTICITY EQUATIONS AND DYNAMICAL BOUNDARY CONDITIONS

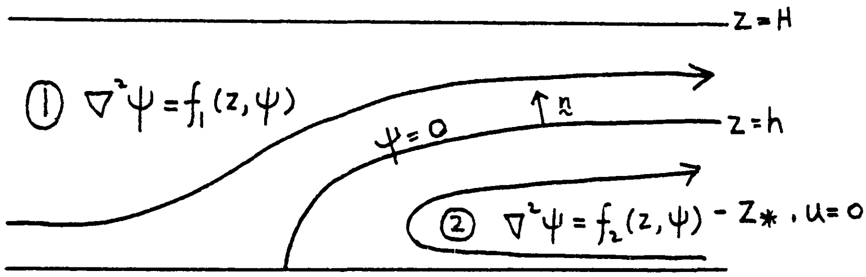

fig 3.2a Different vorticity equations on two adjacent sub-domains

The vorticity equation is a complete description of the dynamics of the problem because if it is solved over the whole domain then, $u = \frac{\partial\psi}{\partial z}$, $w = -\frac{\partial\psi}{\partial x}$ and the temperature field can be obtained and subsequently the pressure field can be deduced by considering the conserved quantity $\frac{1}{2}v^2 + \frac{\delta P}{\rho} - g\int_{z_0}^{z}\delta\phi\, dz$. Thus the crux of the problem is to find the interface position and solve the vorticity equations. Before attempting to solve the problem, it is advisable to normalise the vorticity equations and the boundary conditions so that a minimum number of parameters are carried in the model.

3.2.1 Overturning Updraught

For region 2, the original form of the vorticity equation is

$$\nabla^2\psi = \frac{-g(\gamma_2 - B)}{U(z_0)}(z - z_0) + 2A$$

This is normalised by making the following transformations

$$\psi_{norm} \equiv \frac{\psi}{U_0 H} \quad , \quad Z_{norm} \equiv \frac{z}{H} \quad , \quad U_{norm} \equiv \frac{u}{U_0}$$

where U_0 is the inflow speed in region 1, giving

FREE BOUNDARY PROBLEM

$$\nabla^2\psi = \frac{2}{C}\left\{\frac{R(z - Z_*)}{\sqrt{Z_*^2 + c\psi}} + (1+R)\right\} \qquad (3.2.1a)$$

where the subscript norm has been dropped and

$$Z_* \equiv \frac{\beta\, h/H}{1+\beta} \quad , \qquad C \equiv 2Z_*/\left(\frac{u_s}{u_0}\right) \quad , \quad R \equiv \frac{g(\gamma_2 - B)}{4A^2}$$

The boundary conditions at $x = \pm\infty$ are

$$\psi = \frac{1}{C}\left[z_0^2 - 2z_0 Z_*\right], \; 0 < z_0 < Z_* \qquad \text{at inflow}$$

$$\psi = \frac{\beta^2}{C}\left(z_1 - 2Z_* + \frac{h}{H}\right)\left(z_1 - \frac{h}{H}\right), \; Z_* < z_1 < \frac{h}{H} \qquad \text{at outflow}$$

where $R = \beta(\beta - 1)$.

The pressure of a parcel originating from z_0 and arriving at height z is , after normalising with respect to $\frac{1}{2}u_0^2$,

$$\left(\frac{\delta P}{\rho}\right)\Big/\tfrac{1}{2}u_0^2 = \frac{4}{C^2}(z_0 - Z_*)^2 - V^2 - G\left(\frac{h}{H} - z\right) - \frac{4R}{C^2}\left[\frac{\left(\frac{h}{H}\right)^2}{1+\beta} - (z - z_0)^2\right] + E \qquad (3.2.1b)$$

where V is the speed of the parcel normalised with respect to u_0 .

3.2.2 Buoyant Updraught

The original vorticity equation of the buoyant updraught region

$$\nabla^2\psi = \frac{-g(\gamma_1 - B)}{u_0}\left(z - \frac{\psi}{u_0}\right)$$

is transformed by $\psi_{norm} \equiv \dfrac{\psi}{u_0 H}$, $z_{norm} \equiv \dfrac{z}{H}$ to

$$\nabla^2\psi = -\frac{1}{F^2}(z - \psi) \qquad (3.2.2a)$$

where $F^2 = \frac{u_0^2}{g(\gamma_1 - B)H^2}$. The boundary conditions are

$$\psi = z_0 \qquad \text{at inflow}$$

$$\psi = z_1 - \frac{h/H \sinh((1-z_1)/F)}{\sinh((1-h/H)/F)} \quad \text{at outflow.}$$

The normalised pressure perturbation at the interface at the normalised height z is

$$\left(\frac{\delta p}{\rho}\right) \Big/ \tfrac{1}{2}u_0^2 = 1 - v^2 + z^2/F^2 \qquad (3.2.2b)$$

3.2.3 Negatively Buoyant Updraught

The normalised vorticity equation is

$$\nabla^2 \psi = \frac{1}{F^2}(z - \psi) \qquad (3.2.3a)$$

where $F^2 = \frac{u_0^2}{-g(\gamma_1 - B)H^2}$. The boundary conditions are

$$\psi = z_0 \qquad \text{at inflow}$$

$$\psi = z_1 - \frac{h/H \sin((1-z_1)/F)}{\sin((1-h/H)/F)} \quad \text{at outflow.}$$

The normalised pressure perturbation at the interface at normalised height z is

$$\left(\frac{\delta p}{\rho}\right) \Big/ \tfrac{1}{2}u_0^2 = 1 - v^2 - z^2/F^2 \qquad (3.2.3b)$$

3.2.4 Normalised Dynamical Boundary Condition At The Interface

The dynamical boundary condition is that the pressure perturbation on the jump updraught side and the overturning side are equal at the interface. This is mathematically described by equating the expression in eqn 3.2.1b ($z_0=0$) with that of eqn 3.2.2b or eqn 3.2.3b. The fluid speed at the interface is $\frac{\partial\psi}{\partial n}$ which in general takes different values on different sides of the interface. At any given z, all the parameters in the expressions are fixed except the speeds of the parcels on the two sides of the interface. Therefore, the pressure continuity condition is satisfied only when the fluid speeds are of the correct magnitudes. When an inappropriate interface is assumed , the pressure on one side is greater than the other. One way to increase the lower pressure to satisfy the pressure continuity condition is to slow down the fluid speed on the low pressure side since the quantity $\frac{1}{2}V^2 + \frac{\delta P}{\rho} - g\int_{z_0}^{z}\delta\phi\, dz$ is conserved. Slow fluid speeds implies small $\frac{\partial\psi}{\partial n}$ which means that the streamlines are wide apart. One way to achieve sparse streamlines is to extend the area containing these streamlines. This is done by moving the interface away from the low pressure side towards the higher pressure side. This is effectively the approach employed in the numerical method of solution in section 3.3.

3.3 METHOD OF SOLUTION

Although the theory of existence and uniqueness of solution to one-phase free boundary problems involving irrotational flow is advanced(p391 Encyclopedia of Physics vol IX), no such theory has been developed for two-phase problems involving rotational flow such as the problems tackled in this chapter. It was thought unfruitful to pursue such theory and it is better to make bold attempts to seek solutions to our two-phase problems.

The method employed here is numerical and the finite difference scheme is used. A finite box is used to approximate the infinite strip in the analytic theory.

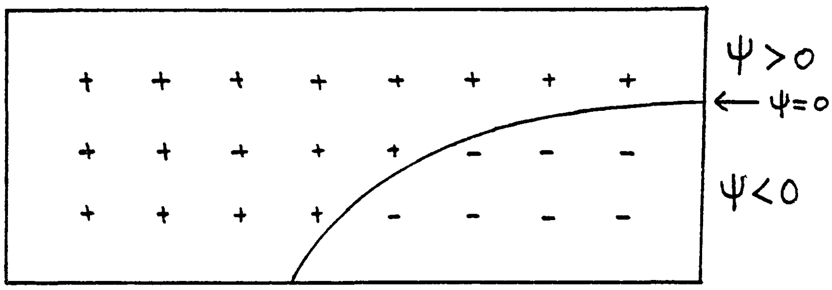

fig 3.3a Finite difference mesh and an interface position

As the position of the interface is represented explicitly without crossing any grid point, the finite difference forms of the first and second order derivatives at points next to the interface (called pivot points) are slightly more complicated than those at other grid points. At,non-pivot point (i,j),

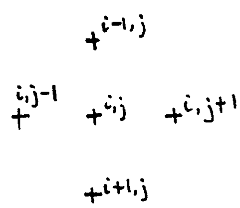

fig 3.3b Derivatives at non-pivot point (i,j)

$$\nabla^2\psi \sim (\psi_{i,j+1} + \psi_{i,j-1} + \psi_{i-1,j} + \psi_{i+1,j})/\Delta s^2 - 4\psi_{i,j}/\Delta s^2$$

where Δs is the grid length,

$$\frac{\partial \psi}{\partial x} \sim (\psi_{i,j+1} - \psi_{i,j-1})/(2\Delta s)$$

$$\frac{\partial \psi}{\partial z} \sim (\psi_{i-1,j} - \psi_{i+1,j})/(2\Delta s)$$

are second order finite difference representations. At pivot points in the jump updraught region for example,

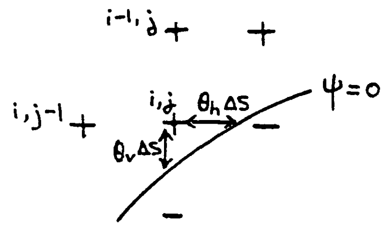

fig 3.3b Derivatives at pivot points

$$\frac{\partial^2 \psi}{\partial x^2} \sim 2\left(\psi_{i,j-1}/(1+\theta_h) - \psi_{i,j}/\theta_h\right)/\Delta s^2$$

$$\frac{\partial^2 \psi}{\partial z^2} \sim 2\left(\psi_{i-1,j}/(1+\theta_v) - \psi_{i,j}/\theta_v\right)/\Delta s^2$$

where $\psi = 0$ on the interface has been used, are finite difference representations accurate to the first order. When considering pressure continuity at the interface , fluid speed and hence $\frac{\partial \psi}{\partial x}$ or $\frac{\partial \psi}{\partial z}$ are required. The expressions

$$\frac{\partial \psi}{\partial x}_{\text{interface}} \sim \left(\psi_{i,j-1}\frac{\theta_h}{1+\theta_h} - \psi_{i,j}\frac{(1+\theta_h)}{\theta_h}\right)/\Delta s$$

$$\frac{\partial \psi}{\partial z}_{\text{interface}} \sim \left(\psi_{i,j}\frac{(1+\theta_v)}{\theta_v} - \psi_{i-1,j}\frac{\theta_v}{1+\theta_v}\right)/\Delta s$$

are second order finite difference representations of the vertical and horizontal speeds at the interface.

FREE BOUNDARY PROBLEM

Our method to find the perfect interface is iterative and is consistent in the sense that given the perfect interface as the initial guess, the iterative procedure should not alter the shape of the interface at all. There are three steps in the algorithm.

1. Initiate the boundary values of ψ at the left and right lateral boundaries according to section 3.2 and the top and bottom horizontal boundaries. Make an initial guess of the shape of the interface whose asymptotic height, h/H is prescribed. Figure 3.3a shows a typical initial guess with a steep front.

2. Given the latest guess of the position of the present interface, the finite difference forms of the vorticity equations of the overturning branch, eqn 3.2.1a and eqn 3.2.2a or 3.2.3a of the jump branch are solved separately by using the SOR method. Continuity of pressure at the interface is not considered at this stage. SOR is an iterative method and $\psi_{i,j}$ is updated, for example in a non-pivot point in the convective jump region, according to the algorithm

$$\psi_{i,j}^{new} = \psi_{i,j} + R/(\text{SOR factor})$$

where

$$R = (\psi_{i-1,j} + \psi_{i+1,j} + \psi_{i,j-1} + \psi_{i,j+1} - 4\psi_{i,j}) + \frac{\Delta s^2}{F^2}(z - \psi_{i,j})$$

FIG 3.3a

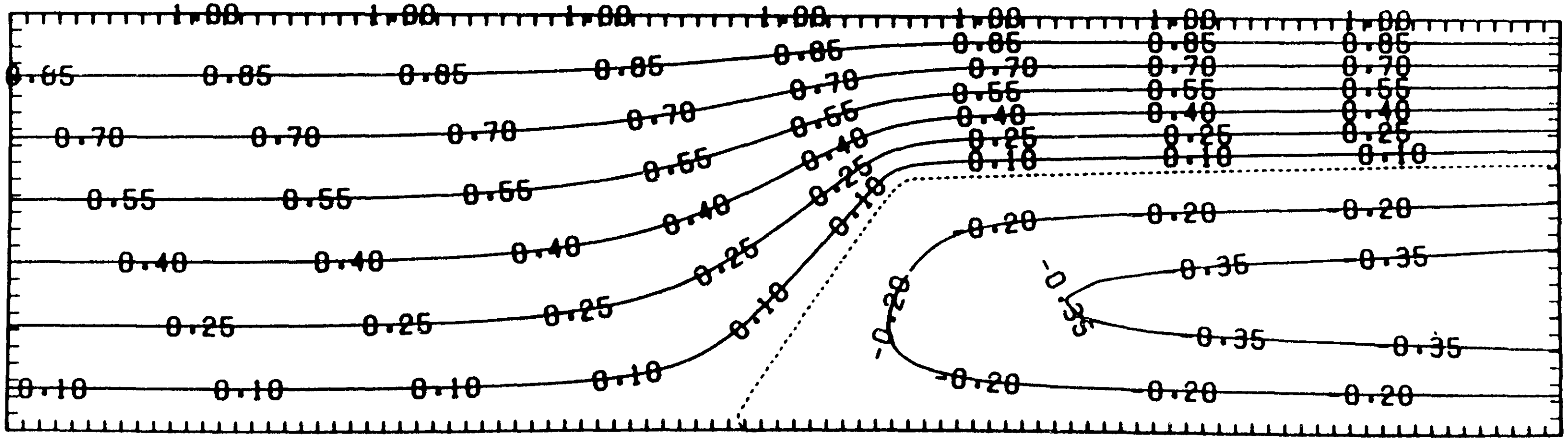

STREAMLINES $h = .65H$ $F = .60$ $G = -3$ $\beta = 1$ CAPE > 0

FIG 3.3b

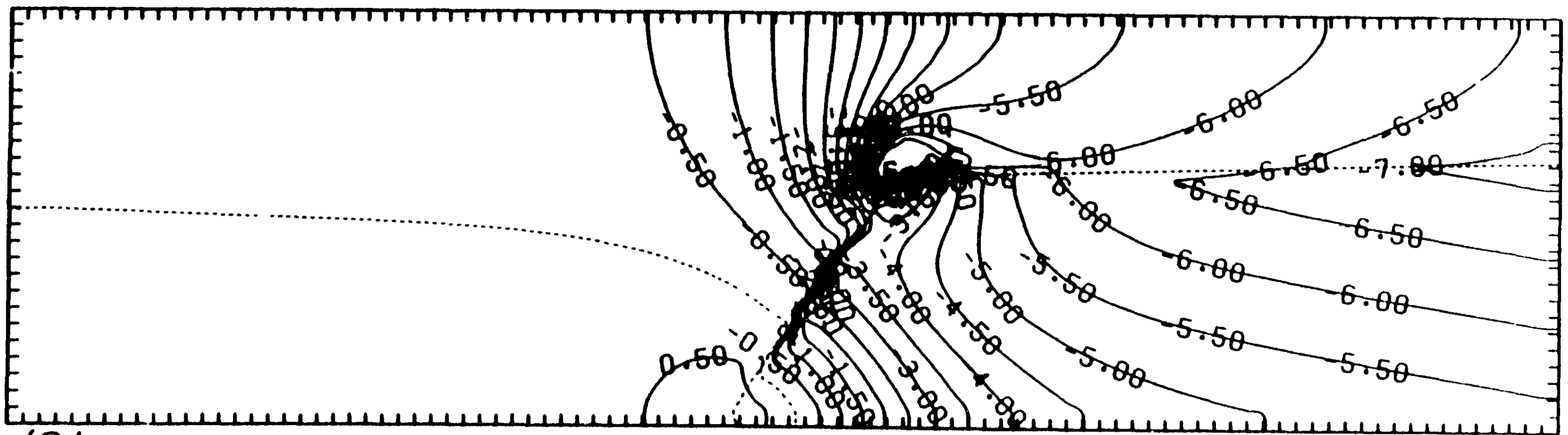

$\frac{\delta P}{\rho} \Big/ \frac{1}{2}u_0^2$ $h = .65H$ $F = .60$ $G = -3$ $\beta = 1$

i.e. R is the residue of the corresponding vorticity equation. Essentially, ψ is updated to try to nullify the residue. The SOR factor controls the iterative convergence rate but it has to be near 4 to ensure convergence. The values of ψ are adjusted in a similar way in the overturning region and at pivot points.

The pressure $\frac{\delta P}{\rho}/\frac{1}{2}u_0^2$ can be calculated (by considering the conserved quantity $\frac{1}{2}v^2+\frac{\delta P}{\rho}-\int_{z_0}^{z} g\,\delta\phi\,dz$) once the streamfunction values have been obtained through the SOR method. With a poor approximation of the interface such as the initial guess in fig. 3.3a, discontinuity of pressure is evident at the interface in fig. 3.3b. This leads on the pressure adjustment process which is step 3.

3.

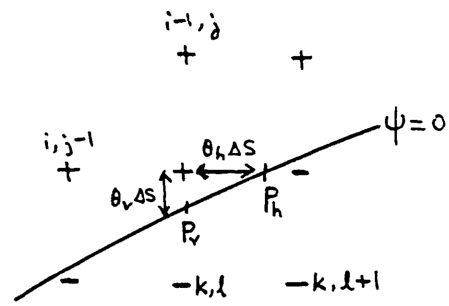

fig 3.3d Pressure continuity at P_v and P_h

The pressure continuity condition at P_v on the interface can be expressed in terms of velocities and the parameters of the system and hence can be written in the following form:

$$f\left(\theta_h, \theta_v, \psi_{i,j}, \psi_{i-1,j}, \cdots, \psi_{k,l}, \psi_{k,l+1}, \cdots\right) = 0$$

With an imperfect interface, the value of this function will not be zero. However, if we keep all the variables of this function constant except θ_v , we can solve for θ_v numerically such that the value of the function indeed becomes zero. In physical terms, this means shifting the interface locally up or down to satisfy the pressure continuity requirement, as qualitatively described in section 3.2.4. Similarly, for local horizontal displacement of the interface, θ_h can be treated as the variable to be solved. This procedure of solving θ_v and θ_h works well as long as the interface does not attempt to migrate over a grid point. In fact, a solution for θ_v or θ_h cannot be found in this circumstance:

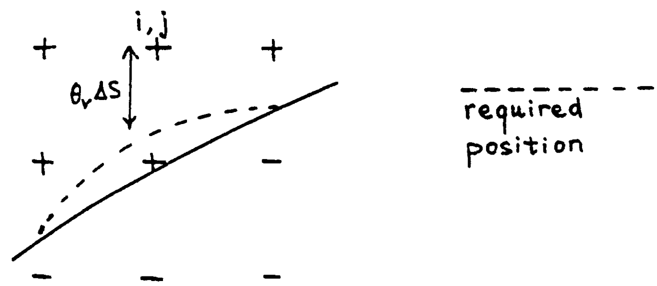

fig 3.3e Migration of interface over a grid point

When this situation does arise, the grid point (i,j) immediately above the original pivot point is chosen as the pivot point and θ_v can then be solved in the same way. The value of θ_v then gives the position of the interface which has now crossed the original pivot point. In a similar way, the interface is allowed to migrate horizontally over a grid point.

Since the interface shifts relative to the pivot points, the vorticity equations are not satisfied at these points and step 2 must be repeated to solve for the streamfunction values. Step 2 and 3 are repeated until the maximum local interface displacement is below a certain chosen error limit.

3.4 COMMENT ON SOLUTIONS TO FREE BOUNDARY PROBLEMS

The method outlined above had been applied successfully to solve several two-phase problems of a jump updraught coexisting with an overturning flow as described in section 2.3.2.3 and 2.3.3.3. There are four parameters in such a system-- $\frac{h}{H}$, F , G and β . One parameter, e.g. F , is a function of the other three which can be prescribed. The cases of a convective jump updraught with CAPE>0 and a negatively buoyant jump updraught with CAPE<0 will be considered separately.

3.4.1 Convective Updraught Models

Four cases had been studied and their corresponding parameters are

$\frac{h}{H}$	F	G	β	u_s/u_0	E
0.65	0.60	-3	1	2.50	-7.21

FREE BOUNDARY PROBLEM

$\frac{h}{H}$	F	G	β	u_s/u_o	E
0.70	0.27	0	0.8	2.77	-10.11
0.67	1.97	0	1	3.02	-8.11
0.85	0.22	0	1.25	8.69	-40.51

The streamline plots and $\left(\frac{\delta P}{\rho}\right)/\frac{1}{2}u_o^2$ contour plots are shown in fig 3.4.1a to fig 3.4.1d. All streamline plots show a convex-shaped interface whose tangent at the stagnation point makes an angle of 60° to 70° with the horizontal bottom boundary. This angle range is close to the analytic result of 60° obtained by Von Karman(1940) in his stagnant density current model with irrotational updraught. This is not coincidental and is understandable since near to the stagnation point the fluid in the updraught has gone through little ascent to generate negative vorticity and therefore the flow is very nearly irrotational;and the fluid in the overturning flow near to the stagnation point is nearly stagnant, i.e. the local situation at the stagnation point is similar to Von Karman's model. Starting with an angle of 60° to 70° at the stagnation point, the interface quickly turns to be nearly horizontal over a short horizontal distance-about twice the depth of the overturning flow. This, in addition to the fact that the updraught parcels ahead of the stagnation point experience very little ascent imply that the parcels go through a rapid ascent in a short time interval over a short horizontal distance.

The pressure $\frac{\delta P}{\rho}/\frac{1}{2}u_o^2$ contour plots generally show a local high pressure region around the stagnation point which retards low level inflow air and accelerates air upward along the interface. The initial ascent in the updraught is followed by large horizontal acceleration along the more gentle section of the interface where the

FIG 3.4.1a

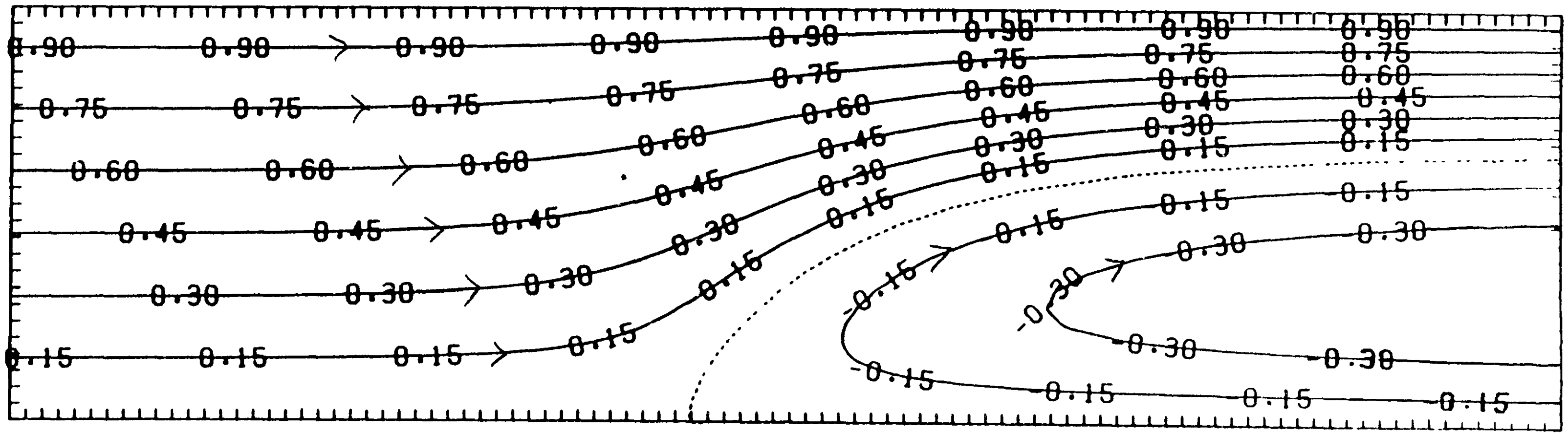

STREAMLINES h=.65H F=.60 G=-3 β=1 **CAPE > O**

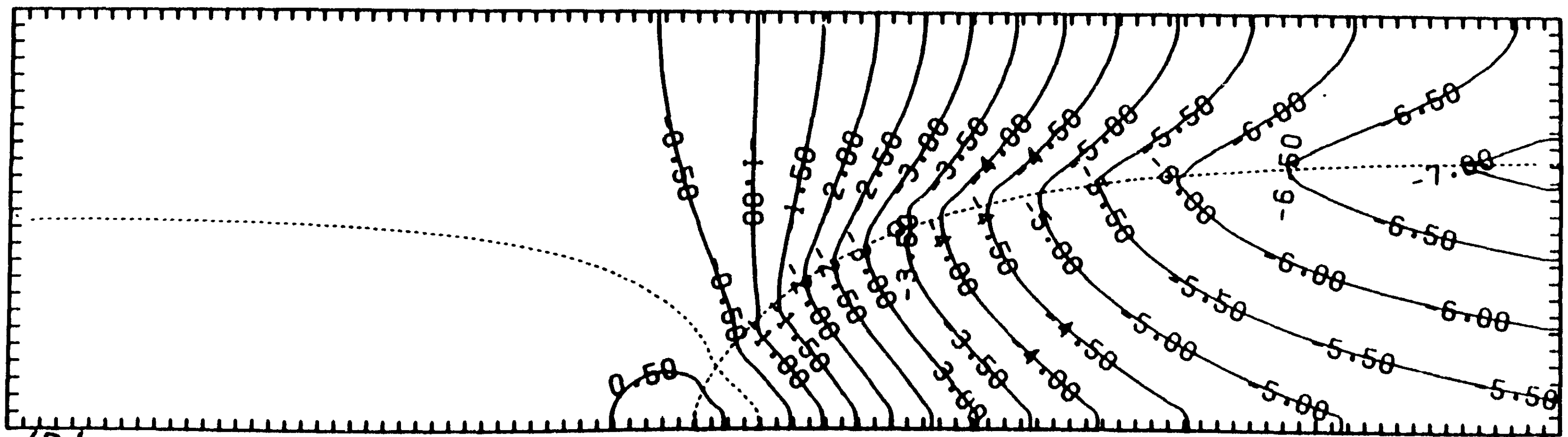

$\frac{\delta P}{\rho} / \frac{1}{2} u_0^2$ h=.65H F=.60 G=-3 β=1

FIG 3.4.1b

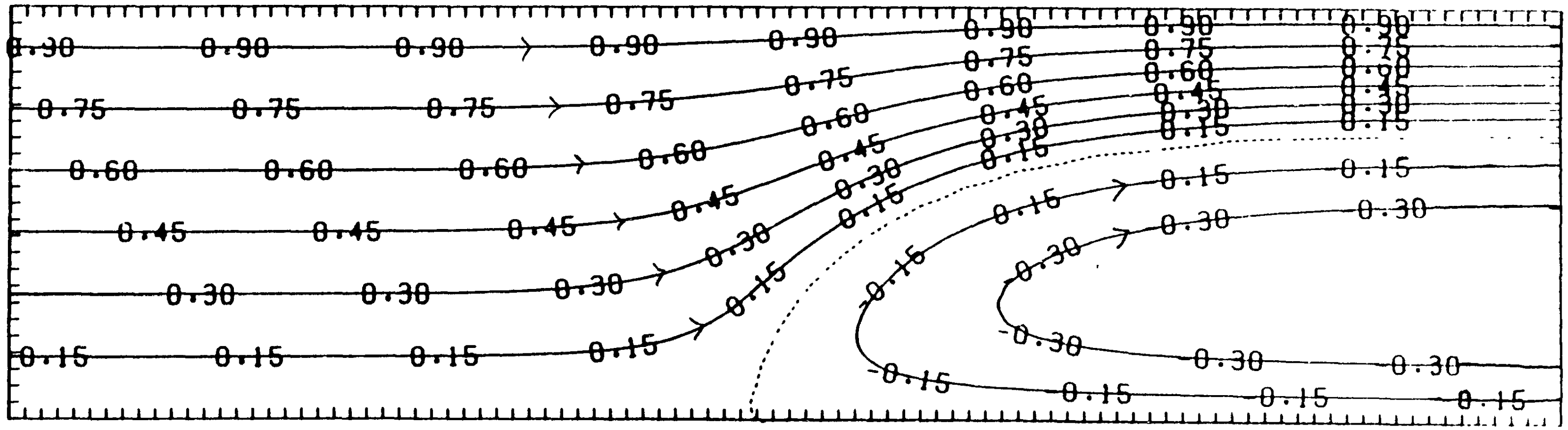

STREAMLINES h=.7H F=.27 G=0 β=.8 **CAPE > O**

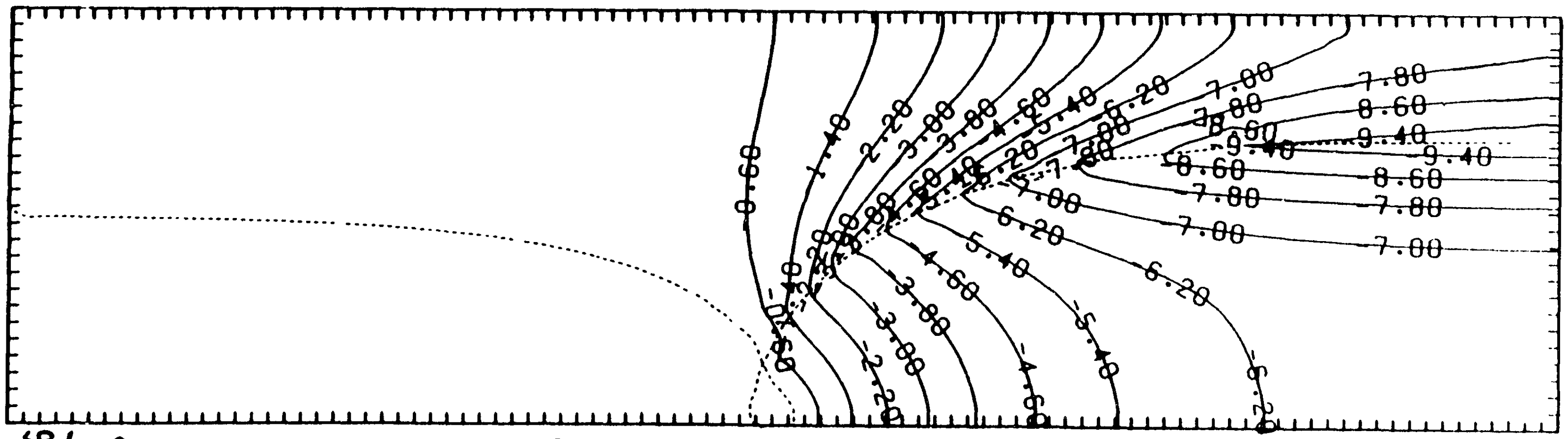

$\frac{\delta P}{\rho} / \frac{1}{2}u_0^2$ h=.7H F=.27 G=0 β=.8

FIG 3.4.1c

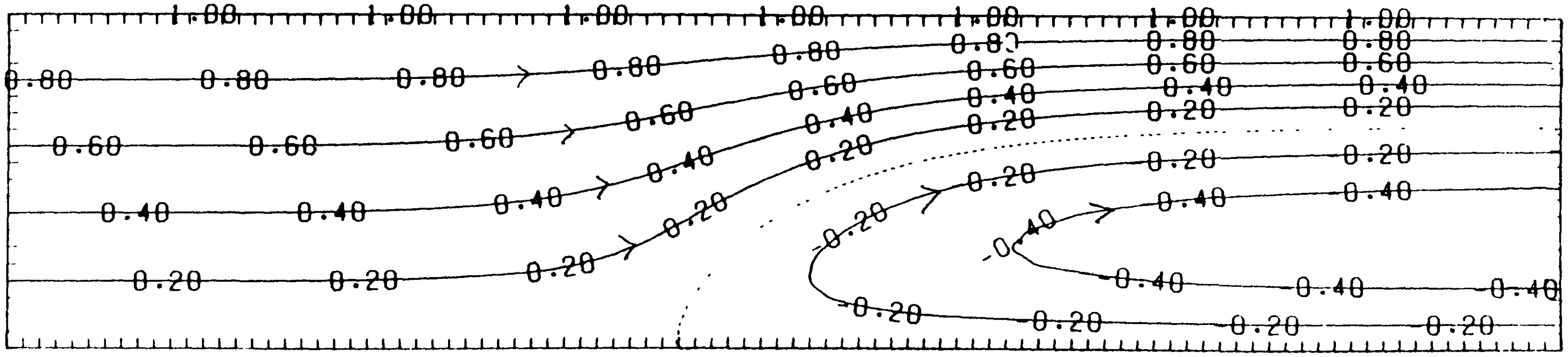

STREAMLINES h=.67H F=1.97 G=0 β=1.00 CAPE > O

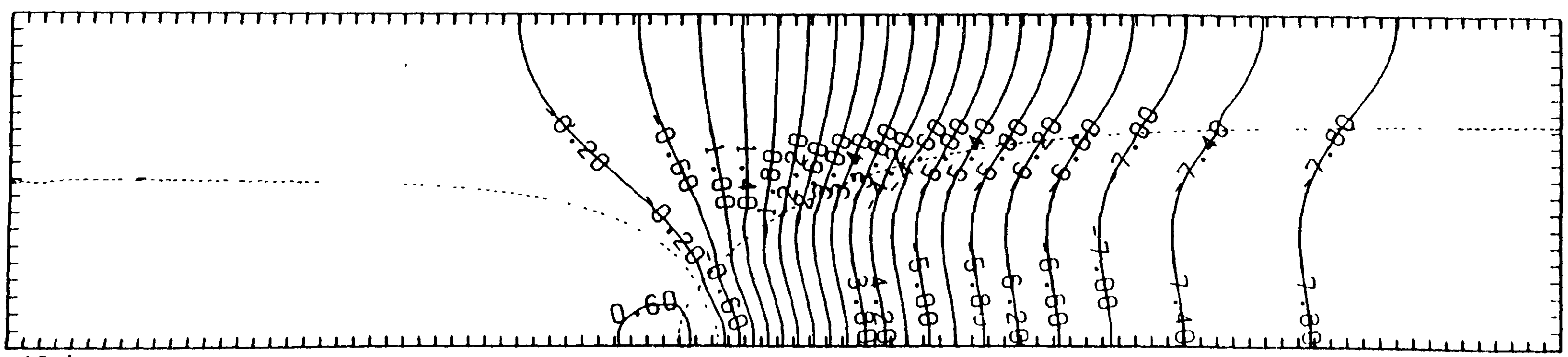

$\frac{\delta P}{\rho} / \frac{1}{2} u_0^2$ h=.67H F=1.97 G=0 β=1.00

FIG 3.4.1d

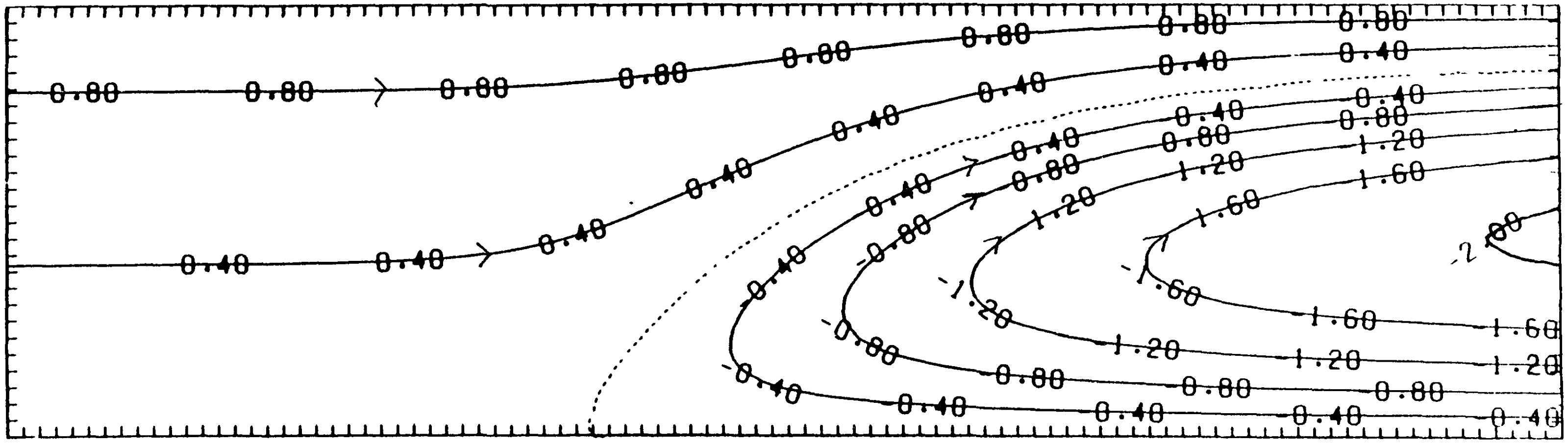

STREAMLINES **h**=.85H F=.22 G=0 β=1.25 **CAPE > 0**

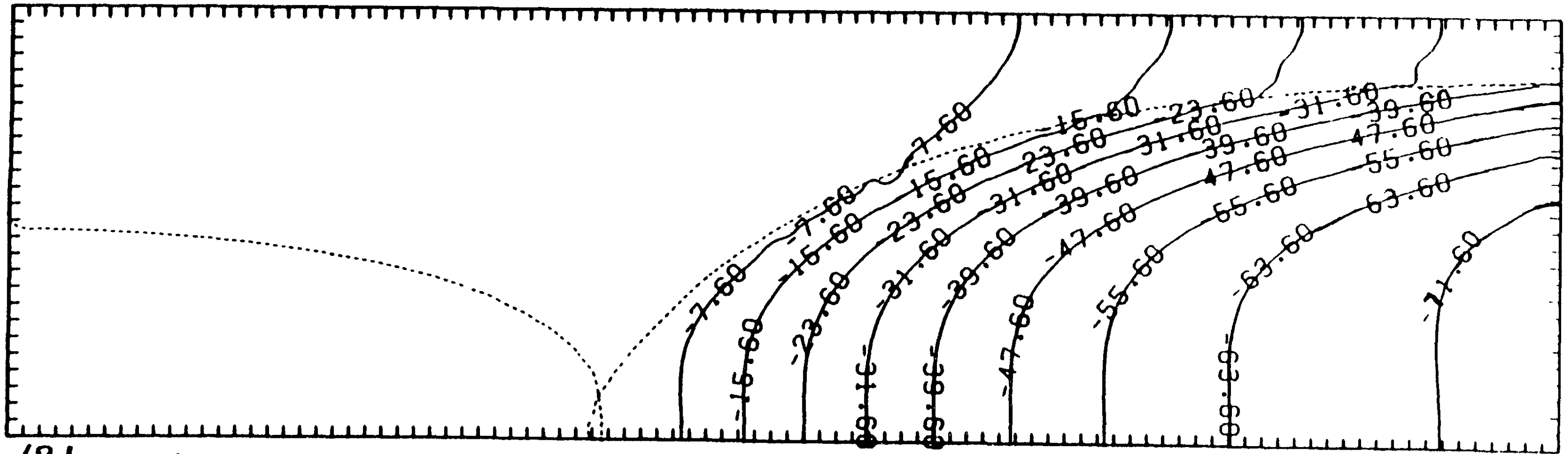

$\frac{\delta P}{\rho} / \frac{1}{2} u_0^2$ **h**=.85H F=.22 G= 0 β=1.25

horizontal pressure is most intense. Further to the rear of the interface where it is nearly horizontal, the pressure force is acting downward to keep buoyant updraught air on a horizontal trajectory. In fact, where the interface is horizontal at $x = \infty$ the horizontal pressure gradient should be zero and this is nearly achieved even in finite domain. Consequently, the low pressure area of a buoyant updraught region is always located at the horizontal section of the interface.

Near the RHS boundary of the upward overturning flow, the pressure contours are also nearly horizontal so that the pressure force counteracts the buoyancy force to keep vertical acceleration near to zero. In the case of negative buoyancy at outflow when $G=-3$ or $\beta=0.8$, the pressure force acts upward whereas in the case of positive buoyancy at outflow when $\beta=1.25$, the pressure force act downward. In the case of neutral-buoyancy at outflow when G=0 and $\beta=1$, no pressure force is at work at the RHS boundary.

The quantity $\frac{D\underset{\sim}{v}}{Dt} - g\delta\phi\,\underset{\sim}{k}$ in general has two values on the interface corresponding to fluid occupying the two regions. Therefore the pressure gradient is discontinuous at the interface and indeed kinks in the pressure contours can be identified there. However, pressure itself is continuous at the interface as shown by the pressure plots.

In the case of $\frac{h}{H}=0.85$, the pressure plot is not particularly smooth and this is probably due to our relatively short domain for such a deep overturning flow. A run with a longer domain is not worthwhile as the computing cost involved is very expensive.

3.4.2 Negatively Buoyant Updraught Models

Three cases were attempted with the following parameters.

$\frac{h}{H}$	F	G	β	u_s/u_o	E
0.40	0.32	0	1	1.39	-0.94
0.35	0.34	-3	1	0.65	-0.48
0.40	0.34	0	0.8	1.16	-0.97

The streamlines and pressure contour plots are shown in fig 3.4.2a to 3.4.2c. The pressure force is always acting upward throughout the jump updraught region as the negatively buoyant air parcels are either accelerated upward or kept on horizontal trajectories. The tangent to the interface at the stagnation point makes an angle of about 60° with the bottom boundary. This angle is closer to the result of Von Karman mentioned in section 3.4.1 possibly because a large section of the overturning flow near to the stagnation point is very nearly stagnant which makes the local condition very similar to his model. In general, the interface slopes more gently than those of the buoyant updraught models and this implies that starting with an angle of about 60° at the stagnation point the interface turns to be nearly horizontal over a longer horizontal distance--about three times the depth of the overturning flow. This, together with the fact that ascent of the inflow air to the jump updraught starts further in front of the stagnation point than in the buoyant updraught models means that the updraught parcels achieve

FIG 3.4.2 a

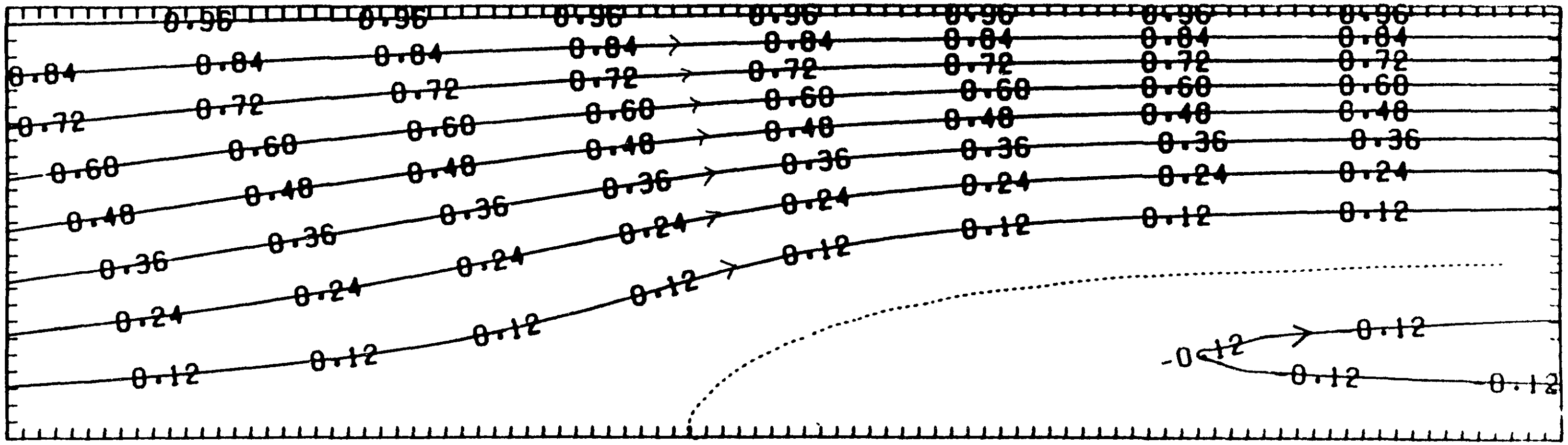

STREAMLINES h=.40H F=.32 G=0 β=1.00 **CAPE< 0**

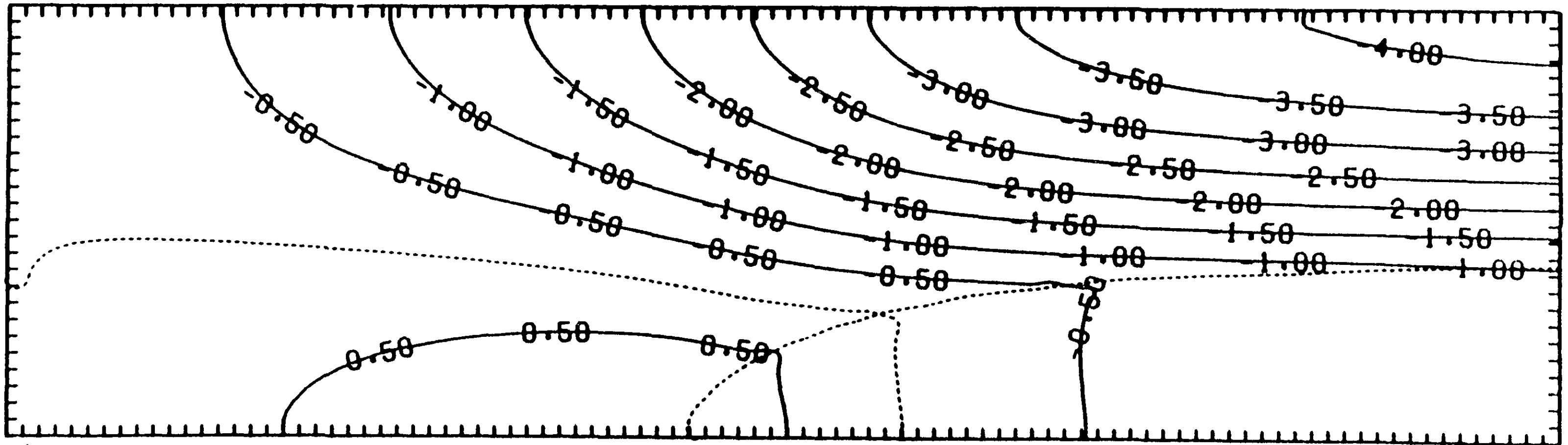

$\frac{\delta P}{P} / \frac{1}{2} u_0^2$ h=.40H F=.32 G=0 β=1.00

FIG 3.4.2b

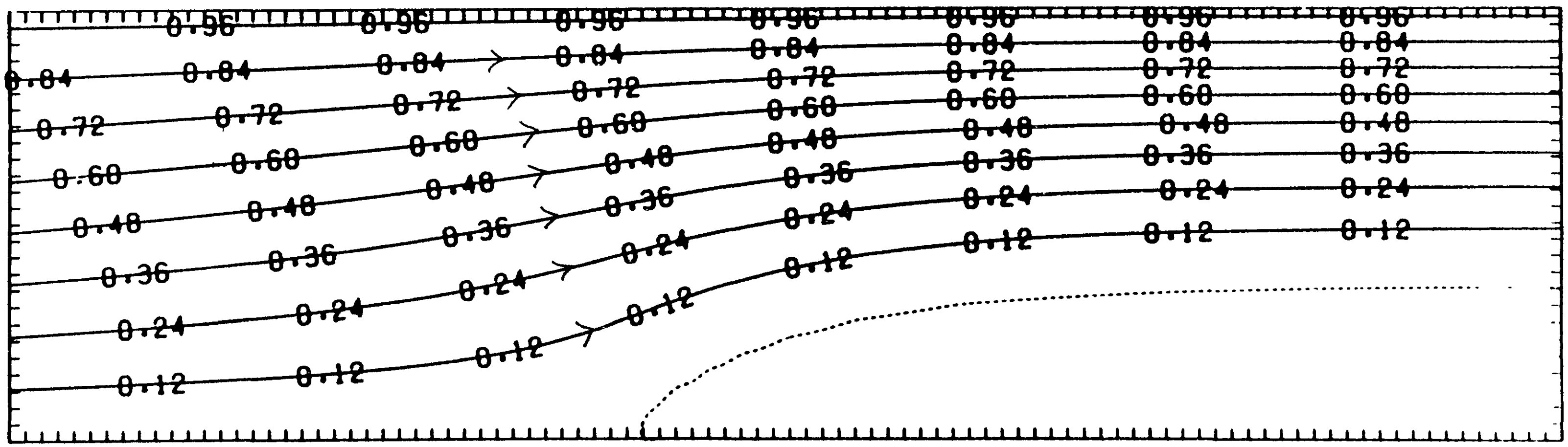

STREAMLINES h=.35H F=.34 G=-3 β=1.00 CAPE < 0

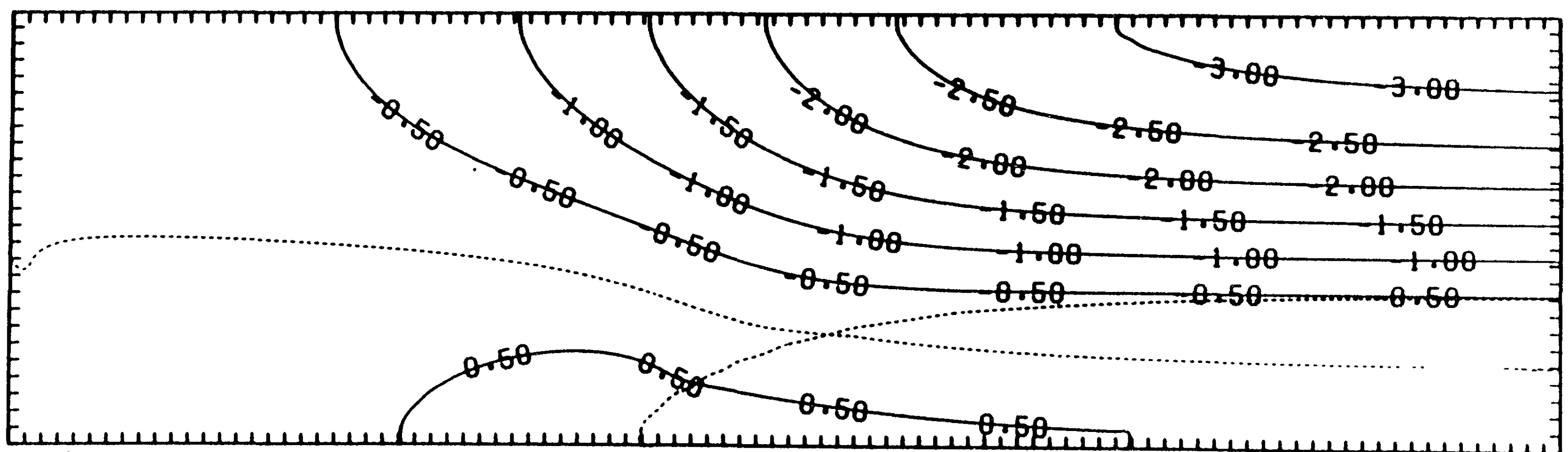

$\frac{\delta P}{\rho} \Big/ \frac{1}{2} u_0^2$ h=.35H F=.34 G=-3 β=1.00

FIG 3.4.2 c

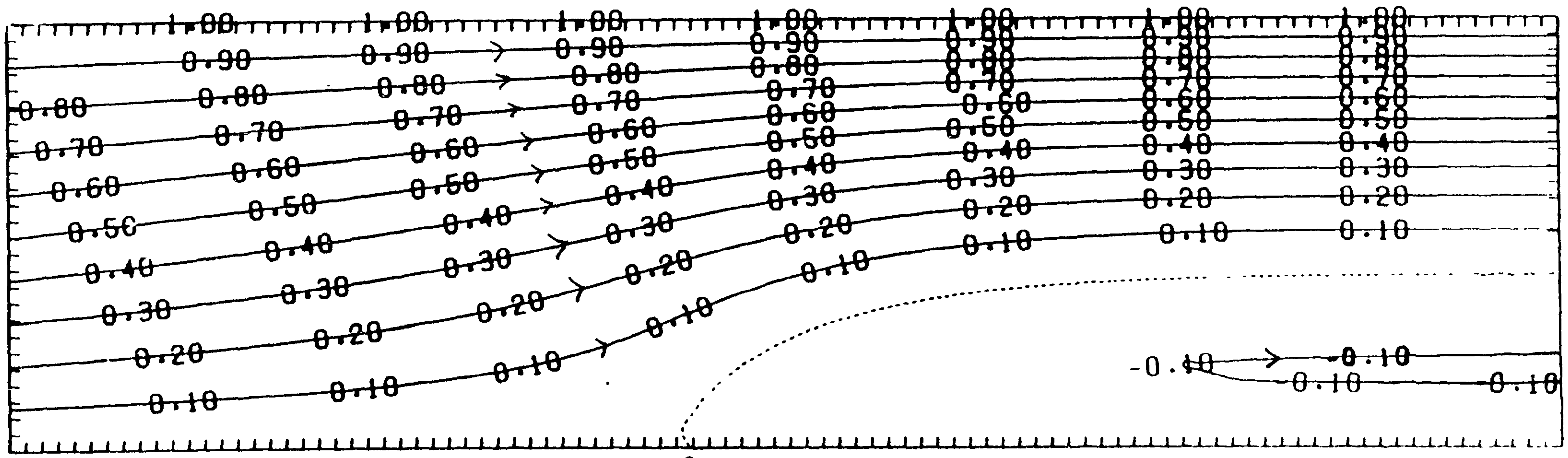

STREAMLINES h=.40H F=.34 G=0 β=0.80 **CAPE < O**

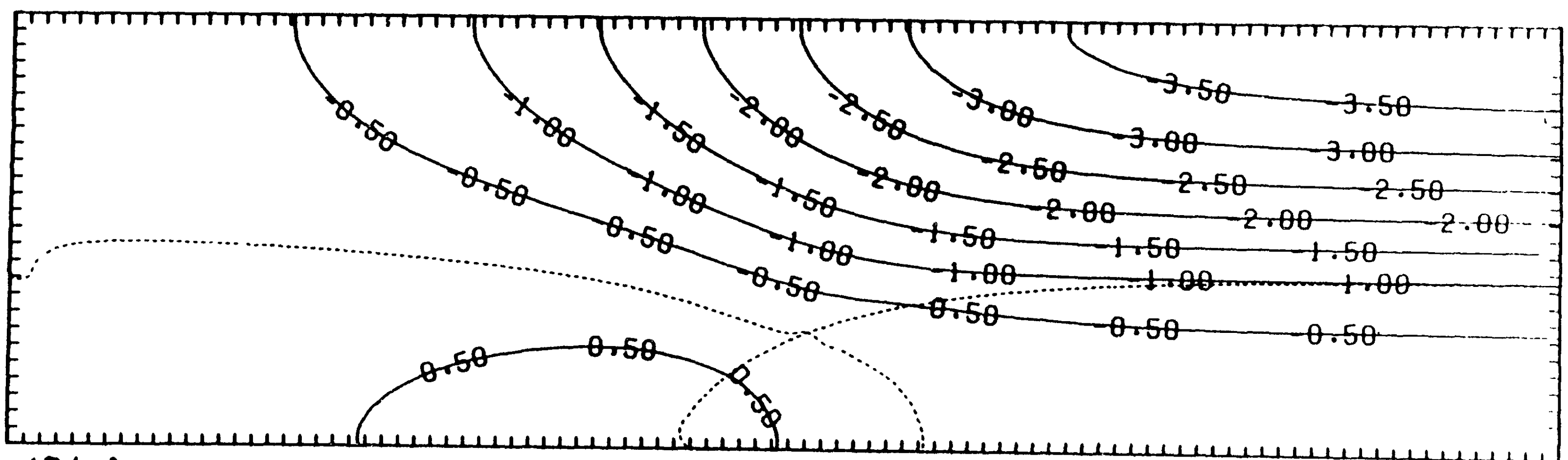

$\frac{\delta P}{\rho/2\, u_0^2}$ h=.40H F=.34 G= 0 β=0.80

their total ascent over a longer horizontal distance.

Cases with $\beta = 1.25$ which requires F<0.3183 had been attempted but no solution was found. This can be understood in terms of the radius of curvature of the section of the streamline ahead of the stagnation point. In natural coordinate the vorticity $\nabla^2\psi = -\frac{v}{R_s} + \frac{\partial v}{\partial n}$ where R_s is the radius of curvature of the streamline, v the fluid speed.

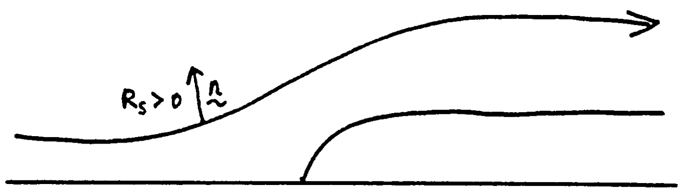

fig. 3.4.1a Radius of curvature of a streamline

Ahead of the stagnation point, $R_s > 0$. Since the updraught is negatively buoyant the vorticity is positive and this is satisfied only if $\frac{\partial v}{\partial n}$ is large enough. For large vorticity associated with small value of F, the value of $\frac{\partial v}{\partial n}$ required is so large that no physical flow pattern is possible. Therefore if F<0.3183 (the critical value) the vorticity equation cannot be satisfied in the jump updraught region and therefore no internal solution exists*.

3.5 CONCLUSIONS

Solutions to seven free boundary problems have been found and this suggests that internal solutions of more complicated models of chapter two exist and that these models are realistic in this sense. The angles of the tangents to the interface at the stagnation point are around 60° which is close to Von Karman's analytic result for a slightly different model. The shapes of the interfaces are shown to be always convex which will be confirmed by the simulation results in fig 5.2.3c,d of chapter five. Also, the low pressure area identified at the base of the rearward section of a buoyant updraught in the internal solutions will be confirmed by the simulation results in fig 5.2.3.2a of chapter five.

CHAPTER 4

GENERALISATION OF ANALYTIC MODELS

The analytic models of chapter two and the semi-analytic models of chapter three have three main limitations. Firstly, to obtain internal solutions to the free boundary problems in chapter three, it has been assumed that the internal structures consist of only two branches of flow. However, more complicated internal structures can be constructed such that the asymptotic lateral boundary conditions are unchanged. Secondly, a restriction on the models is that the difference between the parcel and environmental lapse rate, $(\gamma - \beta)$, has to be constant. In fact, we will show in this chapter that $(\gamma - \beta)$ can be allowed to vary with height above a certain level without affecting the flow patterns. The implications of this are quite far reaching. Steadiness has always been required in order to obtain useful information from the models but it will be shown that this is not strictly necessary. Thirdly, in the Boussinesq approximation the gross variation of mean density with height is neglected but this factor can be taken into account by deriving the equations of the models in pressure coordinates.

GENERALISATION OF ANALYTIC MODELS

4.1 INTERNAL CIRCULATION

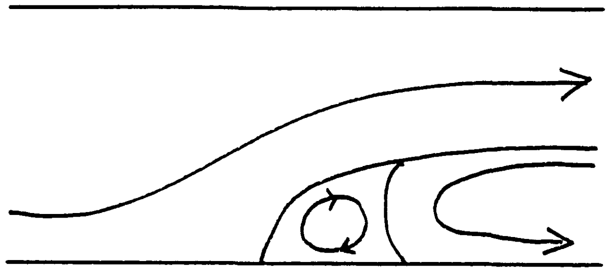

fig 4.1a Flow structure with closed circulation

It is clearly seen that a similar flow regime without the closed circulation, called the rotor, at the front of the density current can have the same lateral boundary conditions. In fact, the asymptotic analysis is completely identical. However, in fig 4.1a the internal dynamics are more complicated-the equations governing the motion within the rotor have to be derived and an extra free boundary separating the rotor from the internal flow of the density current introduces severe problems in obtaining the complete flow structure. In a similar way, closed circulations could be introduced into other analytic models without affecting the lateral boundary conditions.

4.2 NON-CONSTANT LAPSE RATE MODELS

In assuming $(\gamma - \beta)$ to be constant, the thermodynamics are crudely represented in the analytic models of chapter two with the consequence that the potential temperature perturbation of the parcel at the cloud-top outflow is non-zero. Also, the whole thermodynamic profile at outflow can be unrealistic since γ , the parcel lapse, is not given by the wet adiabats. It is found that $(\gamma - \beta)$ need not be assumed constant and yet the form of the vorticity equation remains unchanged.

This throws some light onto the thermodynamics of two-dimensional and perhaps three-dimensional convective cloud models and suggests that the role of CAPE in controlling convective activity be re-examined. Lastly, a model with suitably chosen inflow shear is investigated.

4.2.1 The Two-dimensional Vorticity Equation

Taking the curl of the momentum equation,

$$\frac{D\underset{\sim}{v}}{Dt} + \nabla\left(\frac{\delta P}{\rho}\right) - g\,\delta\phi\,\underset{\sim}{k} = \underset{\sim}{0}$$

and assuming $\frac{\partial}{\partial y} = 0$, the two-dimensional vorticity equation corresponding to the y-component of the vorticity vector is obtained:

$$\frac{D\eta}{Dt} = -g\frac{\partial\delta\phi}{\partial x} \qquad (4.2.1a)$$

where $\eta = \frac{\partial u}{\partial z} - \frac{\partial w}{\partial x}$ is the y-component of the vorticity.

Note that steadiness has not been assumed. Eqn 4.2.1a shows that the rate .of change of vorticity following a parcel is entirely due to the instantaneous horizontal potential temperature gradient. It is on this temperature gradient that we now focus our attention.

$$\frac{\partial\delta\phi}{\partial x} = \frac{\partial\psi}{\partial x}\frac{\partial\delta\phi}{\partial\psi_z} = -w\frac{\partial\delta\phi}{\partial\psi_z}$$ where definition of ψ is used,

$$= -\frac{D}{Dt}\left\{\int_{z_0}^{z}\frac{\partial\delta\phi}{\partial\psi_z}\,dz'\right\} \qquad (4.2.1b)$$

where it is understood that the integral inside the bracket is evaluated along a trajectory and the following rule of differentiation of an integral has been applied:

$$\frac{D}{Dt}\left\{\int_{z_0}^{z}f(z')\,dz'\right\} = \int_{z_0}^{z}\frac{Df(z')}{Dt}\,dz' + \frac{Dz}{Dt}f(z) - \frac{Dz_0}{Dt}f(z_0).$$

If $f(z')$ and z_0 do not change with time, then only the second term is non-zero. Now $\frac{\partial \delta\phi}{\partial \psi_z}$ is to be analysed further. The general expression for the log potential temperature perturbation is

$$\delta\phi = \int_{z_0}^{z} (\gamma - B)\, dz'$$

where $(\gamma - B)$, treated as a single variable, is a function of z and ψ_z (i.e. $(\gamma - B) \equiv (\gamma - B)(z, \psi_z)$) and the integral is evaluated along a trajectory.

$$\frac{\partial \delta\phi}{\partial \psi_z} = \frac{\partial}{\partial \psi_z}\int_{z_0}^{z} (\gamma - B)\, dz'$$

$$= \int_{z_0}^{z} \frac{\partial(\gamma - B)}{\partial \psi_z} dz' + \frac{\partial z}{\partial \psi_z}(\gamma - B)(z, \psi_z) - \frac{\partial z_0}{\partial \psi_z}(\gamma - B)(z_0, \psi_z)$$

$\frac{\partial z}{\partial \psi_z}$ is clearly zero and if $(\gamma - B)$ is a function of z only then the first term is also zero. For steady motion, ψ is constant along a trajectory and therefore $\frac{\partial z_0}{\partial \psi_z} = 1\Big/\frac{\partial \psi_0}{\partial z_0} = \frac{1}{u_0}$. The remaining term is

$$-\frac{\partial z_0}{\partial \psi_z}(\gamma - B)(z_0, \psi_0) = \frac{-(\gamma - B)(z_0, \psi_0)}{u_0} = -\left(\frac{\gamma - B}{u_0}\right)_{z_0}.$$

$$\therefore \quad \frac{\partial \delta\phi}{\partial \psi_z} = \left(\frac{\gamma - B}{u_0}\right)_{z_0} . \qquad (4.2.1c)$$

This implies that for steady motion the difference in $\delta\phi$ on a horizontal surface between two particular streamlines is independent of z . Since $\left(\frac{\gamma - B}{u_0}\right)_{z_0}$ is constant for a fixed ψ ,

$$\int_{z_0}^{z} \frac{\partial \delta\phi}{\partial \psi_z}\, dz' = \left(\frac{\gamma - B}{u_0}\right)_{z_0} (z - z_0). \qquad (4.2.1d)$$

Combining eqns 4.2.1a-c , we have

$$\frac{D\eta}{Dt} = -\frac{D}{Dt}\left\{ g\left(\frac{\gamma - B}{u_0}\right)_{z_0} (z - z_0)\right\}$$

which implies that the quantity $\left\{\eta + g\left(\frac{\gamma - B}{u_0}\right)_{z_0}(z - z_0)\right\}$ is conserved following a parcel in steady motion. The vorticity can therefore be written as

$$\eta = \nabla^2\psi = \eta_0 - g\left(\frac{\gamma - B}{u_0}\right)_{z_0}(z - z_0) \qquad (4.2.1e)$$

A similar vorticity equation was given by Thorpe, Miller and Moncrieff (1980) but $(\gamma - B)$ was not referred at inflow only but it has to be a constant throughout the domain. It should be noted that the change in vorticity is proportional to the change in height. This equation is general in the sense that there is no restriction on the values of $(\gamma - B)$ and u_0 but $\frac{\partial}{\partial t} = 0$ has been assumed. The surprising fact is that only the value of $(\gamma - B)$ at z_0 appears; $(\gamma - B)$ at other heights does not appear in the equation! Some physical interpretation is required.

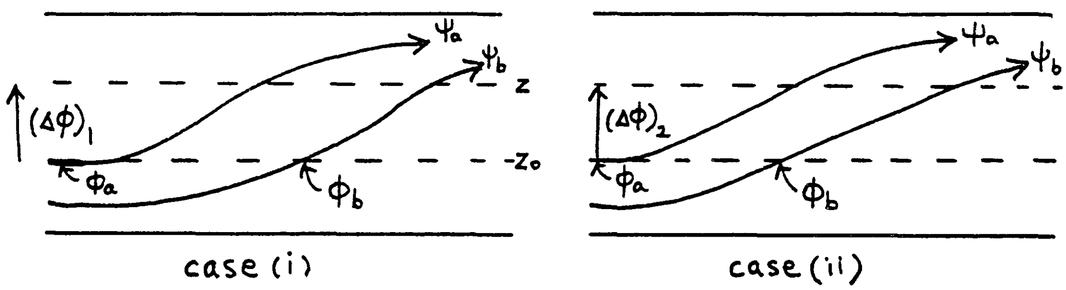

fig 4.2.1a Difference in ϕ as a function of z_0 only

Consider fig 4.2.1a, suppose in both cases that $\phi_b - \phi_a$ has the same value of $\Delta\phi$ at the inflow level of ψ_a, z_0. If $(\gamma - B)$ is a function of z only, then in (i) the two parcels on streamlines ψ_a and ψ_b undergo the same log potential temperature change, $(\Delta\phi)_1$, say, in ascending from z_0 to z. Similarly, in (ii) ϕ_a and ϕ_b change by the same amount, $(\Delta\phi)_2$ with $(\Delta\phi)_1 \neq (\Delta\phi)_2$.

In case (i), $\phi_b(z) - \phi_a(z) = [\phi_b(z_0) + (\Delta\phi)_1] - [\phi_a(z_0) + (\Delta\phi)_1]$

$$= \phi_b(z_0) - \phi_a(z_0) = \Delta\phi$$

Similarly for case (ii),

$$\phi_b(z) - \phi_a(z) = \Delta\phi$$

Therefore, $\phi_b - \phi_a$ is the same at z_1 as at z_0 in both case (i) and (ii) confirming the mathematical deduction from 4.2.1c. It is seen that the $(\gamma-B)$ above z_0 does not affect $\frac{\phi_b-\phi_a}{\psi_b-\psi_a} = \frac{\Delta\phi}{\Delta\psi}$ which is a constant. Furthermore, since $\frac{D\eta}{Dt} = g\omega\frac{\partial\delta\phi}{\partial\psi_z}$, $(\gamma-B)$ above z_0 has no part to play in determining the evolution of the vorticity. This result, that it is the value of $(\gamma-B)/u_0$ at inflow which determines the outflow vorticity, is a controversial one and further work is needed to examine its validity and implications for convective dynamics and modelling. Some further discussion of these points can be found in Moncrieff 1985.

4.2.2 Thermodynamic Profiles At Inflow And Outflow

In the analytic models of chapter two, $(\gamma-B)$ is constant and therefore $\delta\phi$ is proportional to the vertical displacement of the parcel. For $(\gamma-B)>0$, parcels following the top streamline of the system at outflow always attain positive $\delta\phi$ at outflow. Similarly for $(\gamma-B)<0$, $\delta\phi$ at outflow is always negative, However, a physically more realistic boundary condition for the top streamline is that $\delta\phi$ should be zero there. Now given the analysis of 4.2.1 we see that this is possible if we allow $(\gamma-B)$ to vary suitably with height. In fact, $(\gamma-B)$ can be adjusted to give any value of $\delta\phi$ at outflow!

Another implication of allowing $(\gamma-B)$ to vary with height is that $\delta\phi$ could be positive or negative on different sections of the same streamline. An initially buoyant ascent $(\delta\phi>0)$ can turn into a forced ascent $(\delta\phi<0)$ further above. An initially forced ascent can turn into a buoyant ascent as in the case of the Wokingham storm (Browning and Ludlam 1962) where the updraught was forced for the first three kilometres.

Figure 4.2.2a shows an updraught with the top of the inflow at Z_T and the outflow top at Z_H.

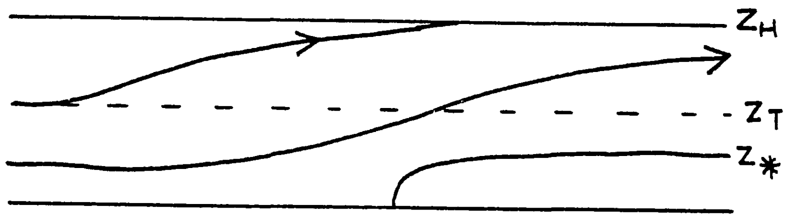

fig 4.2.2a Updraught with fractional inflow

Let us investigate two cases with identical inflow boundary conditions and identical Z_H but with $(\gamma - B)$ different above Z_T. The vorticity equation is exactly the same in both cases and, since the outflow bounded by the same Z_H and Z_* the asymptotic boundary conditions at outflow are identical. The difference between the two cases lies in the temperature fields which in turn give rise to differences in $\left(\frac{\delta P}{\rho}\right)$ fields. In the calculation of the flow force quantity $\int_0^{Z_H} u^2 + \frac{\delta P}{\rho}\,dz$, u^2 is identical in both cases but $\left(\frac{\delta P}{\rho}\right)$ is different. Therefore, the flow force has different values in the two cases and this would affect the solution to the asymptotic problem where the flow force has to be balanced at different vertical sections. The quantity $\frac{1}{2}u_0^2 = \frac{1}{2}u_1^2 + \left(\frac{\delta P}{\rho} - \int_{z_0}^{z_1} g\,\delta\phi\,dz\right)$ is conserved following the parcel in steady motion, and for the same streamline in the two cases this quantity is the same since u_0 is the same. Since u_1 is also the same in each case , because the outflow patterns are identical, it follows that the quantity $\left(\frac{\delta P}{\rho} - \int_{Z_0}^{Z_1} g\,\delta\phi\,dz\right)$ has the same value in both cases. Thus, this quantity is independent of $(\gamma - B)$ above Z_T implying that it has the same value irrespective of the static stability above Z_T. Also, altering γ but keeping B unchanged would change the pressure field within the flow but not the outflow structure.

$(\gamma - B)$ above top of inflow seems to be a free parameter of the problem but the questions of its actual form in reality and whether it is independent of streamlines still remain. In reality, B is given by the environmental atmosphere and γ is deduced from the wet adiabatic lapse rate with the condition that the parcels are always saturated. When the parcels are not saturated γ is known and is equal to zero. Thus $(\gamma - B)$ is in fact determinate and since the value of γ is almost independent of θ_ω (or θ_e) at a given height or pressure, $(\gamma - B)$ can be treated as streamline-independent to a good approximation. Therefore, realistic values of $(\gamma - B)$ can be used as input to the analytic models. The following example illustrates how this can be achieved.

4.2.2.1 A Two-dimensional Squall Line As An Example -

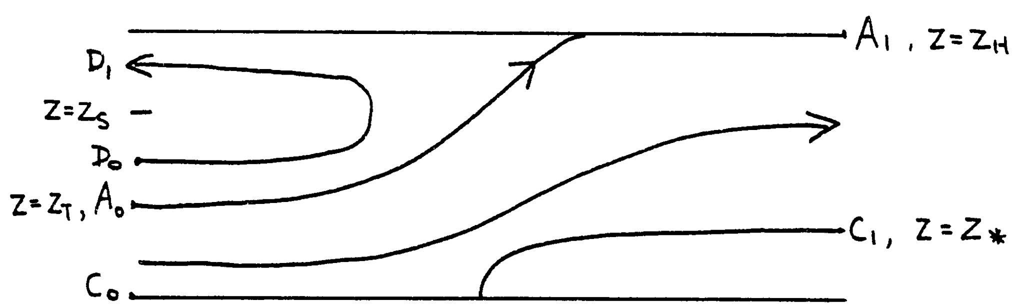

fig 4.2.2.1a Squall line flow structure

Only the updraught and the upward overturning branch will be considered to illustrate the thermodynamic profiles at inflow and outflow. The lower density current structure is not considered.

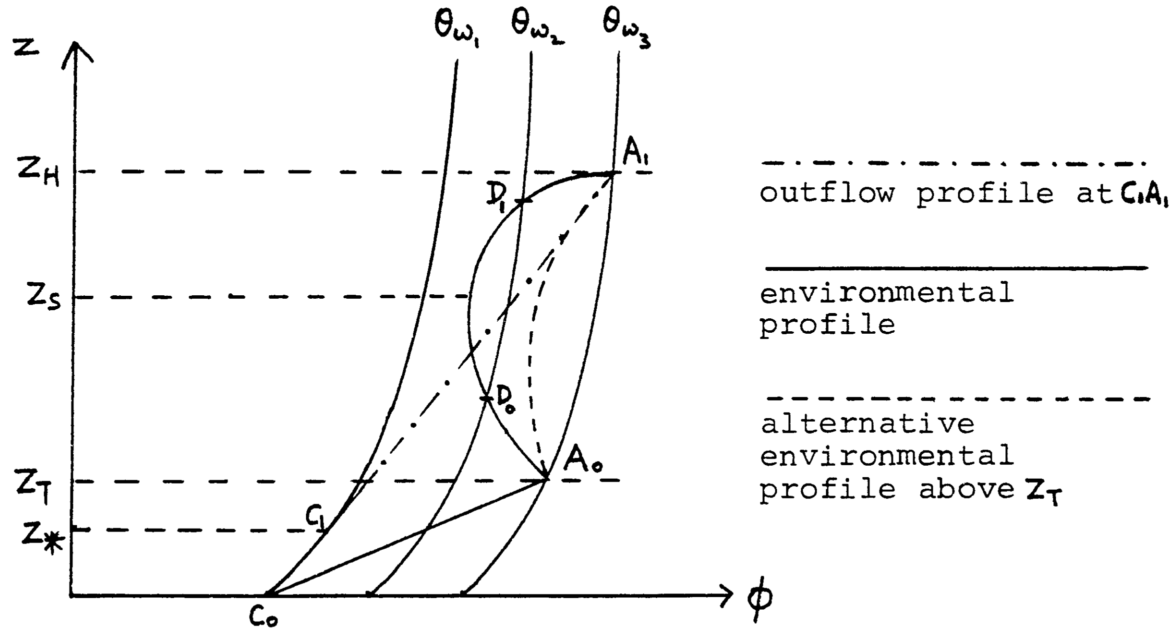

fig 4.2.2.1b Thermodynamic diagram of squall line.

The environment below Z_T is stable but between Z_T and Z_S it is unstable. The surface parcel starts from point C_0 and reaches C_1 following the wet adiabats for θ_{ω_1} on the thermodynamic diagram. Strictly speaking, initially the parcel below cloud base is not saturated so γ =0 and ϕ is conserved by the parcel. This could be taken into account by replacing the θ_ω curves below the cloud base by straight vertical lines but this is not included here for simplicity. Similarly the parcel starting from the top of the inflow to the updraught reaches A_1 following a different wet adiabats for θ_{ω_3}. The unstable section between Z_T and Z_S overturns and in fact part of the environment is the result of the flow. D_0 and D_1 denote the initial and final positions of a parcel within this flow. Z_S is the steering level of the overturning flow and is near to the level of minimum ϕ in the environmental profile.

In fig 4.2.2.1b, $\delta\phi$ at A_1 is zero and the thermodynamic profile at outflow of the updraught from C_1 to A_1 can be obtained(after the vertical displacements of parcels are calculated). An initially stable profile C_0A_0 near the ground gives rise to a stable outflow profile at C_1A_1 and an unstable inflow profile would give an unstable outflow profile. In the overturning flow, the unstable inflow profile gives rise to a stable outflow profile.

If the environmental thermodynamic profile above Z_T is replaced by the alternative profile, the inflow parameter $\left(\frac{\gamma-B}{u_0}\right)_{z_0}$ is unchanged for the jump updraught and the top boundary at Z_H remains the same. Thus the outflow streamline pattern and therefore the momentum transport by the jump updraught remain unchanged but the heat transport by the updraught would certainly be different. However, the structure of the overturning flow would be affected and a different steering level would correspond to the new minimum in ϕ. The two different profiles give different values for the flow force $\int_0^{z_H} u^2 + \frac{\delta p}{\rho}\, dz$.

One important question that arises is the role which CAPE $\equiv g\int_{z_0}^{z_1} \delta\phi\, dz$ plays in this height dependent lapse rate model. Each streamline corresponds to a different value of CAPE. In fact some parcels have negative CAPE and some have positive CAPE in the example shown in fig 4.2.2.1b. Furthermore, changing the environmental thermodynamic profile to the alternative one would inevitably change the CAPE values but the wind profile at the jump updraught outflow would remain the same. If the vorticity equation is made dependent on CAPE, then the outflow wind profile is also dependent on CAPE.

Consequently the momentum transport which depends on the outflow wind profile will change as CAPE changes. But as it has been shown in this example the outflow wind profile, and hence the momentum transport should remain unchanged while the heat transport will be different. In these respects, CAPE may not be a useful parameter for describing convection in two dimensions and possibly in three dimensions. Furthermore, a clear implication for the parameterisation of heat transport by a convective system is that the complete environmental thermodynamic profile has to be considered in detail.

In the study of two-dimensional convection, an upshear sloping interface between the updraught and downdraught was difficult to obtain (Moncrieff(1978)) although such a configuration is thermodynamically consistent. In view of the fact that vorticity generation depends essentially on the inflow characteristics and $(\gamma - B)$ need not be constant with height (varying $(\gamma - B)$ would affect the pressure at the interface and subsequently its shape and direction of tilt), the possibility of an upshear sloping interface for that model should not be entirely ignored.

4.2.3 Steady Stratified Models With Inflow Shear

Eqn 4.2.1e can be non-dimensionalised by multiplying by $\frac{Z_T}{u_S}$ where Z_T and u_S are the height and velocity scales respectively. For example, Z_T can be the top of the inflow and u_S the surface velocity.

$$\nabla^2\psi = \eta_0 - g\left(\frac{\gamma - B}{u_0}\right)_{z_0}\frac{Z_T^2}{u_S}(Z - Z_0)$$

where ψ, η_0, Z and Z_0 are non-dimensionalised variables.

GENERALISATION OF ANALYTIC MODELS

To solve the asymptotic problem with non-zero inflow shear analytically, we insist on a simple relationship between η_0 and Z_0 at inflow of the form

$$\eta_0 + K Z_0 = a - b\psi_0 \quad ,$$

where $K \equiv g\left(\frac{\gamma - B}{u_0}\right)_{Z_0} \frac{Z_T^2}{u_S}$ is required to be a constant.

Now since at inflow $\frac{\partial}{\partial x} = 0$ and $\eta_0 = \frac{d^2\psi_0}{dZ_0^2}$, we have a linear second order differential equation:

$$\frac{d^2\psi_0}{dZ_0^2} + b\psi_0 = a - kZ_0 \tag{4.2.3a}$$

For convex inflow profiles, $a<0$ and $b>0$, the solution is

$$\psi_0 = \frac{1}{\sqrt{b}}\left(1 + \frac{k}{b}\right)\sin\sqrt{b}\,Z_0 - \frac{a}{b}\cos\sqrt{b}\,Z_0 + \frac{1}{b}(a - kZ_0)$$

on applying the boundary condition $\psi_0(0)=0$ and $\left.\frac{d\psi_0}{dZ_0}\right|_{Z_0=0} = 1$. The inflow wind profile is given by

$$U_0 = \frac{d\psi_0}{dZ_0} = \left(1 + \frac{k}{b}\right)\cos\sqrt{b}\,Z_0 + \frac{a}{\sqrt{b}}\sin\sqrt{b}\,Z_0 - \frac{k}{b}$$

Given profiles of u_0 and $(\gamma - B)$ as input data, the most representative K could be chosen and a and b could be tuned to fit the inflow wind profile as closely as possibly. A typical value of $g\left(\frac{\gamma-B}{u_0}\right)_{Z_0}$ is of the order $10^{-5} m^{-1} s^{-1}$ with $Z_T \sim 10^3 m$, $u_S \sim 10 m/s$, K is of order 1.

At outflow, since the motion is steady $\psi_1 = \psi_0$, the differential equation describing the outflow vorticity is of the same form as eqn 4.2.3a:

$$\frac{d^2\psi_1}{dz_1^2} + b\psi_1 = a - kz_1$$

which has a slightly different solution as different boundary conditions are applied. For a concave wind profile, $b<0$ and the solution to eqn 4.2.3a is expressed in terms of hyperbolic functions.

4.3 TIME-DEPENDENT MODELS

Before the time-dependent vorticity equation is analysed, it is interesting to look at the form of the momentum budget equation for unsteady motion.

Integrating the mass continuity equation over the domain $AA'B'B$ of fig4.3a gives

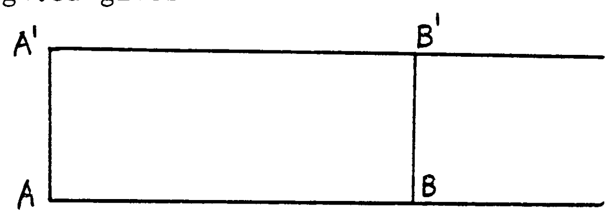

fig 4.3a Integration of mass continuity equation over a sub-domain

$$\int_{AA'B'B} \frac{\partial u}{\partial x} + \frac{\partial w}{\partial z}\, dx\, dz = 0 \qquad \Longrightarrow \qquad \int_{AA'} u\, dz = \int_{BB'} u\, dz$$

Let AA' be the lateral boundary and BB' be any vertical section within the domain. If the mass flux at the lateral boundary , $\int_{AA'} u\, dz$, remains constant with time, then the mass flux at any vertical section within the domain also remains constant with time , i.e. $\frac{\partial}{\partial t}\int_{BB'} u\, dz = 0$. It follows that

$$\int_{BB'} \frac{\partial u}{\partial t}\, dz = 0 \quad \Longrightarrow \quad \int_{AA'B'B} \frac{\partial u}{\partial t}\, dx\, dz = 0$$

Therefore on integrating the time-dependent momentum equation over

$A\acute{A}\acute{B}B$,

$$\int_{AA'B'B} \frac{\partial u}{\partial t} + \operatorname{div} u\underset{\sim}{v} + \frac{1}{\rho}\frac{\partial P}{\partial x}\, dx\, dz = 0 \Rightarrow \int_{AA'B'B} \operatorname{div} u\underset{\sim}{v} + \frac{1}{\rho}\frac{\partial P}{\partial x}\, dx\, dz = 0$$

which leads to the flow force theorem that the quantity $\int_{BB'} u^2 + \frac{P}{\rho}\, dz$ is invariant at any column BB. Hence, if the mass flux at a lateral boundary is constant with time, the flow force theorem still holds despite the possibility of unsteady motion within the domain.

The vorticity equation, however, is more complicated for the unsteady than the steady case. In the analysis of 4.2.1, $\frac{\partial \delta\phi}{\partial \psi_z} = -\frac{\partial z_0}{\partial \psi_z}(\gamma - B)_{z_0}$ where it has been assumed that $(\gamma - B)$ is a function of height only. In unsteady motion, ψ is not conserved following a parcel so $\frac{\partial z_0}{\partial \psi_z} \neq 1/\frac{\partial \psi_0}{\partial z_0} = u_0$ and

$$\int_{z_0}^{z} \frac{\partial \delta\phi}{\partial \psi_z}\, dz' = -(\gamma - B)_{z_0} \int_{z_0}^{z} \frac{\partial z_0}{\partial \psi_z}\, dz' \qquad (4.3a)$$

which is different from eqn 4.2.1d. Now,

$$\int_{z_0}^{z} \frac{\partial z_0}{\partial \psi_z}\, dz' = \int_{t(z_0)}^{t(z)} \frac{\partial z_0}{\partial \psi_z} \frac{Dz}{Dt}\, Dt$$

$$= \int_{t(z_0)}^{t(z)} \frac{\partial z_0}{\partial \psi_z}\, \omega\, Dt = \int_{t(z_0)}^{t(z)} -\frac{\partial z_0}{\partial \psi_z}\frac{\partial \psi}{\partial x}\, Dt$$

$$= -\int_{t(z_0)}^{t(z)} \frac{\partial z_0}{\partial x}\, Dt \qquad (4.3b)$$

Combining eqns 4.2.1a, 4.2.1b, 4.3a and 4.3b,

$$\frac{D\eta}{Dt} = \frac{D}{Dt}\left\{ g(\gamma - B)_{z_0} \int_{t(z_0)}^{t(z)} \frac{\partial z_0}{\partial x}\, Dt \right\} \qquad (4.3c)$$

$$= g(\gamma - B)_{z_0} \frac{\partial z_0}{\partial x} \qquad (4.3d)$$

A conserved quantity for unsteady motion can be derived from eqn 4.3c although it is difficult to evaluate. Eqn 4.3d indicates the sign of vorticity generation. For example, for a jump updraught with inflow from the left and $(\gamma - B)_{z_0} < 0$, $\frac{\partial z_0}{\partial x} < 0$ and therefore positive vorticity is generated. We will find this useful in interpreting the vorticity patterns produced by numerical models such as those described in chapter 5.

4.4 ANALYTIC MODELS IN PRESSURE COORDINATES

An analogue of eqn 4.2.1e can be derived in pressure coordinates. Following Moncrieff (1985), the momentum and mass continuity equation are

$$\frac{Du}{Dt} + g\frac{\partial h'}{\partial x} = 0 \ , \qquad (4.4a)$$

$$\frac{D}{Dt}\left(\frac{\omega}{\bar{\rho} g}\right) + g^2 \bar{\rho}\frac{\partial h'}{\partial p} + g\delta\phi = 0 \ , \qquad (4.4b)$$

$$\frac{\partial u}{\partial x} + \frac{\partial \omega}{\partial p} = 0 \ ,$$

where $\omega = \frac{Dp}{Dt}$, $\bar{\rho} = \bar{\rho}(p)$ is the mean density and h' is the displacement of the pressure surface from the reference pressure surface. ψ can be defined such that $u = \frac{\partial \psi}{\partial p}$ and $\omega = -\frac{\partial \psi}{\partial x}$.

Operating with $\bar{\rho} g \frac{\partial}{\partial p}$ on eqn 4.4a and with $\frac{\partial}{\partial x}$ on 4.4b and eliminating the terms involving h' gives , after some rearrangement

$$\frac{D\eta}{Dt} - \frac{\omega}{\bar{\rho} g}\frac{\partial}{\partial p}(\bar{\rho} g)\eta + g\frac{\partial \delta\phi}{\partial x} = 0 \ , \qquad (4.4c)$$

where $\eta \equiv \frac{1}{\bar{\rho} g}\frac{\partial \omega}{\partial x} - \bar{\rho} g \frac{\partial u}{\partial p}$ is analogous to the vorticity $\frac{\partial u}{\partial z} - \frac{\partial w}{\partial x}$. Eqn 4.4c can be rewritten as

$$\frac{D}{Dt}\left\{ \int_{p_0}^{p} \frac{D\eta}{Dp} - \frac{\partial}{\partial p}(\ln \bar{\rho} g)\, \eta \, dp \right\} + g\frac{\partial \delta\phi}{\partial x} = 0 \qquad (4.4d)$$

where $\frac{D\eta}{Dp}$ is a differentiation following a parcel. $(\gamma - B)$ is defined such that

$$\delta\phi = \int_{p_0}^{p} \bar{\rho}\,(\gamma - B)\, dp \;,$$

and following the analysis in 4.2.1 for steady models

$$\frac{\partial \delta\phi}{\partial x} = \frac{D}{Dt}\int_{p_0}^{p} \bar{\rho}\left(\frac{\gamma - B}{u_0}\right)_{p_0} dp \;,$$

assuming $(\gamma - B)$ is a function p only. Thus,eqn 4.4d becomes

$$\frac{D}{Dt}\left\{ \int_{p_0}^{p} \frac{D\eta}{Dp} - \frac{\partial}{\partial p}(\ln \bar{\rho} g)\,\eta + \bar{\rho} g \left(\frac{\gamma - B}{u_0}\right)_{p_0} dp \right\} = 0$$

This implies the integral inside the bracket is conserved and since the upper limit of the integral, p, is arbitrary, the integrand must be zero. Therefore,

$$\frac{D\eta}{Dp} - \frac{\partial(\ln \bar{\rho} g)}{\partial p}\,\eta + \bar{\rho} g \left(\frac{\gamma - B}{u_0}\right)_{p_0} = 0$$

and since $\frac{\partial(\ln \bar{\rho} g)}{\partial p} = \frac{D(\ln \bar{\rho} g)}{Dp}$ this equation becomes, after dividing by $\bar{\rho} g$

$$\frac{1}{\bar{\rho} g}\frac{D\eta}{Dp} - \frac{\eta}{\bar{\rho} g}\frac{D(\ln \bar{\rho} g)}{Dp} + g\left(\frac{\gamma - B}{u_0}\right)_{p_0} = 0$$

which can be re-arranged to give

$$\frac{D}{Dp}\left(\frac{\eta}{\bar{\rho} g}\right) + g\left(\frac{\gamma - B}{u_0}\right)_{p_0} = 0 \;.$$

Finally,

$$\left(\frac{\eta}{\bar{\rho}g}\right)_p = \left(\frac{\eta}{\bar{\rho}g}\right)_{p_0} - g\left(\frac{\gamma - B}{u_0}\right)_{p_0}(p - p_0) \qquad (4.4e)$$

which is the analogous vorticity equation in pressure coordinates to eqn 4.2.1e . The corresponding asymptotic problems can be solved in a similar way as eqn 4.2.1e with p replacing z. The fixed lid top boundary condition z=H is replaced by the free surface boundary condition $p = p_H$ =constant. The bottom boundary condition $p(z=0)$ =constant, however, is not realistic but only the surface pressures at $\pm\infty$ are required in the asymptotic analysis.

4.5 CONCLUSIONS

The two-dimensional vorticity equation has been re-interpreted in the light of the fact that $(\gamma - B)$ can be height-dependent. The solutions to the constant lapse rate models can be treated as solutions to the varying lapse rate models although the thermodynamics are quite different. Thermodynamic profiles at outflow can now be explicitly obtained so that their stabilities can be determined and the heat transport by the cloud systems can be deduced. The fact that the dynamical flow structure is not a function of CAPE has serious implication on parameterisation of momentum and heat transport in global numerical forecast models. The problem of finding the interfacial boundary between the updraught and the downdraught in the mid-latitude squall line model studied by Moncrieff and Green (1972) should be re-examined as the shape of the interface may depend on values of $(\gamma - B)$ at various heights. Finally, the results presented in this chapter can be re-derived in pressure coordinates and the difficulty in comparing observation with incompressible models can now be overcome.

CHAPTER 5

OBSERVATION OF A WEST AFRICAN SQUALL LINE AND SIMULATIONS

The study of density current and its associated jump updraught presented in chapters two to four is largely analytical and it is appropriate to use them to interpret the observation and numerical simulation of a West African squall line which is quasi two-dimensional, steady and exhibits a similar structure described by the analytic models. This squall line was observed in the French COPT 81 (Convection Profonde Tropicale 1981) experiment. The squall line was simulated using the meso-scale model of the Atmospheric Physics Group at Imperial College.

5.1 OBSERVATION OF AN AFRICAN SQUALL LINE

The COPT 81 experiment was a collaboration between several French research organisations, the University of Abidjan(Ivory Coast) and the Agency for Security of Aeronautical Navigation(ASECNA). The purpose was to observe the time evolution of dynamical and thermodynamical structure of deep convection and their associated electrical properties. The observational network covered the northern part of Ivory Coast which is a tropical savanna region at the southern edge of

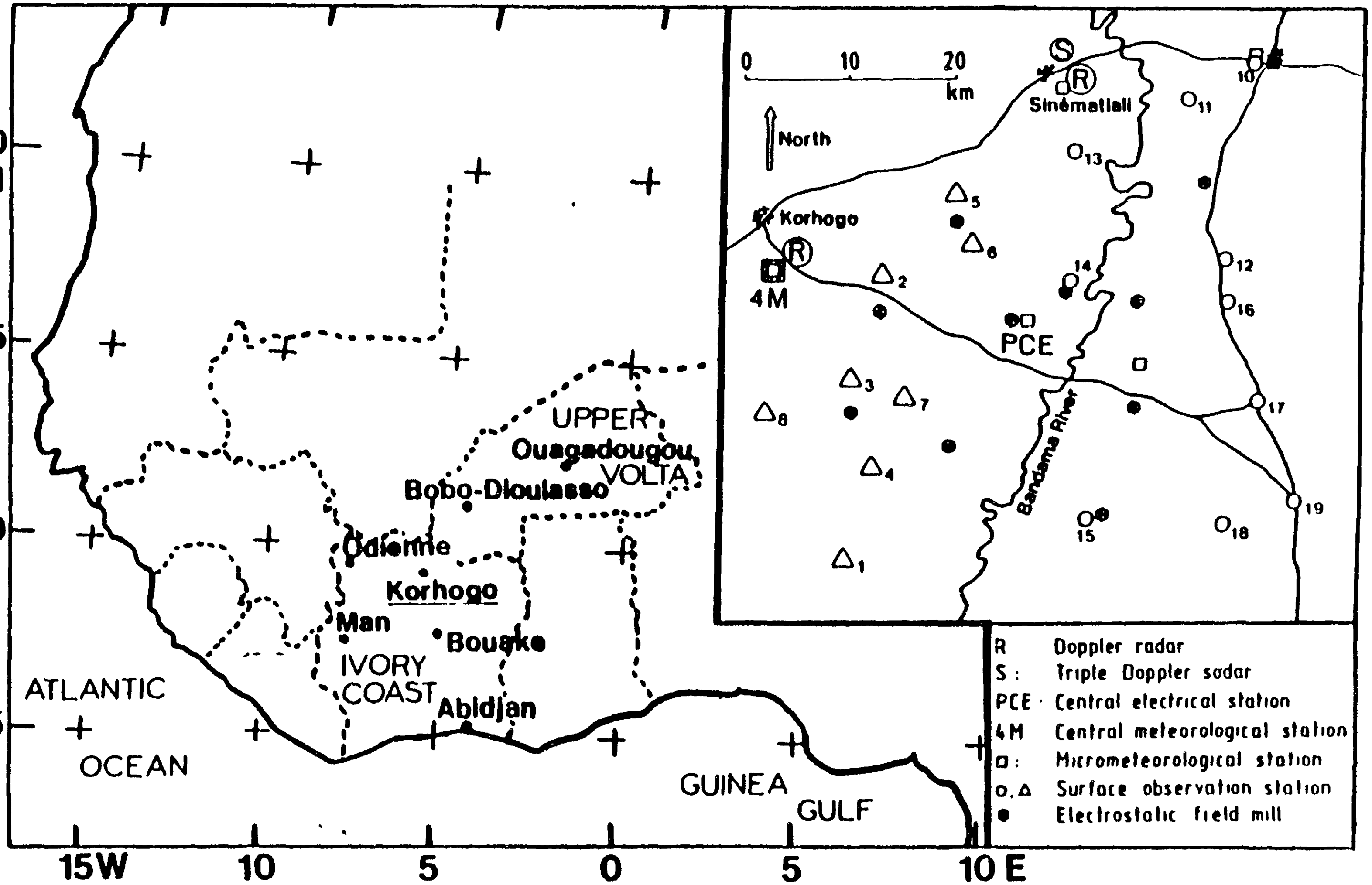

FIG 5.1 a The COPT81 observational network

the Sahel (fig 5.1a). The use of dual doppler radars for measuring precipitation velocity enables retrieval of the three-dimensional wind velocity field which is vital in understanding the dynamical structure. The ground network and the main meteorological station at Korhogo provided the measurement of wind,temperature, pressure, humidity and surface rainfall and the vertical structure of the atmosphere was regularly monitored by rawinsondes. In West Africa, deep convection organised in the form of squall lines several hundred kilometres long occur about once every three days, travelling westward with speed 10-20 m/s over thousands of kilometres. Two such squall lines were observed by the network on 22nd June and 23rd June1981. Their dynamical structures are very different as the former was essentially two-dimensional and the latter was three-dimensional. It is the case of 22nd June which will be discussed and simulated by the meso-scale model.

5.1.1 Structure Of The Squall Line Observed On 22nd June1981

Eight hours before the squall line hit the experimental site at Korhogo at 0415, it could be identified on an infra-red NOAA 6 satellite picture (fig 5.1.1a). The breakdown of the squall line occurred twelve hours after its passage over Korhogo. Fig 5.1.1b shows the squall line positions at four different times. The system was moving to the southwest at the speed of about 17m/s. The thermodynamic and wind profiles measured at Korhogo 30km ahead of the squall line are shown in fig 5.1.1c and 5.1.1d respectively. The pre-squall thermodynamic sounding has a typical continental nocturnal

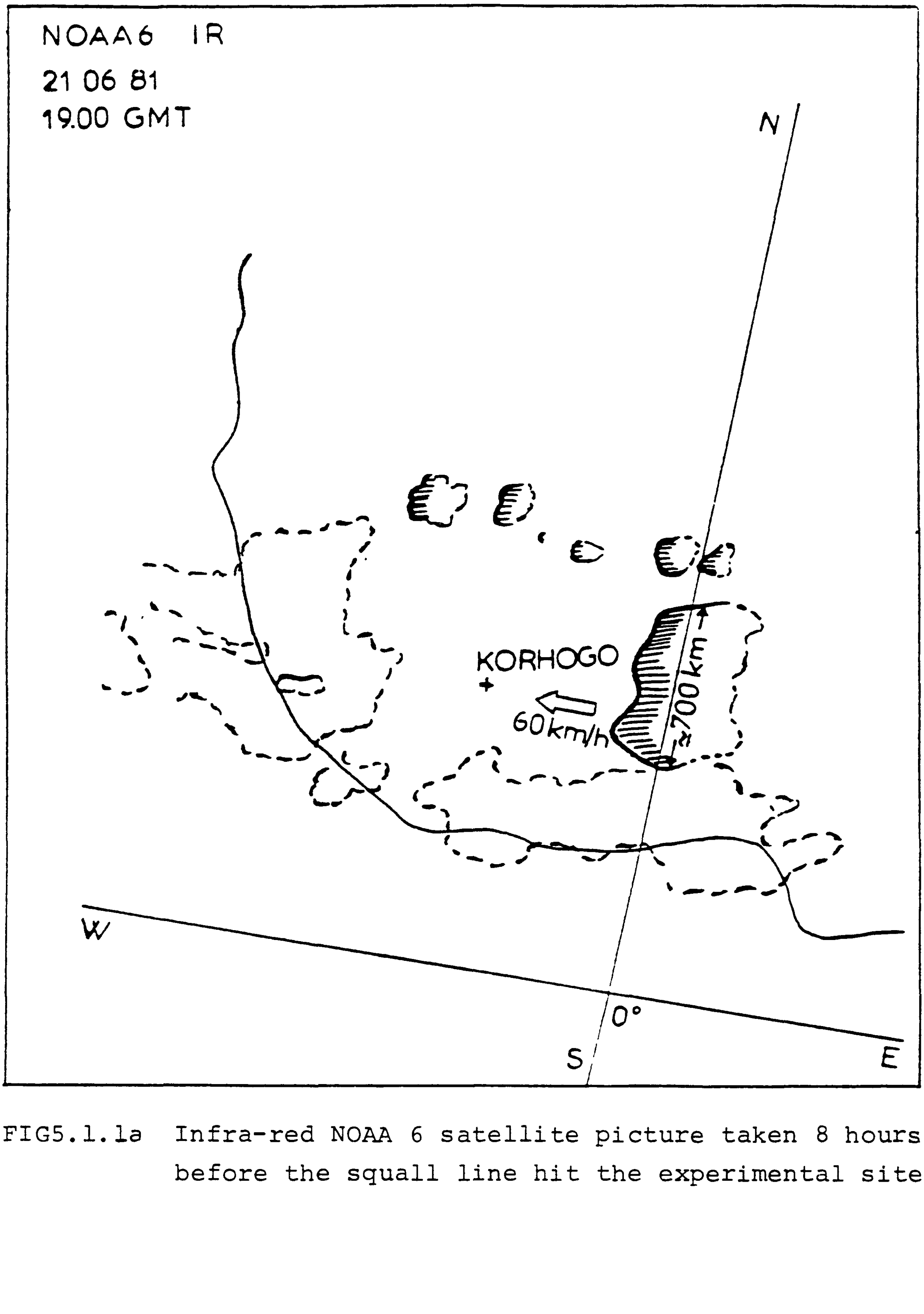

FIG5.1.1a Infra-red NOAA 6 satellite picture taken 8 hours before the squall line hit the experimental site

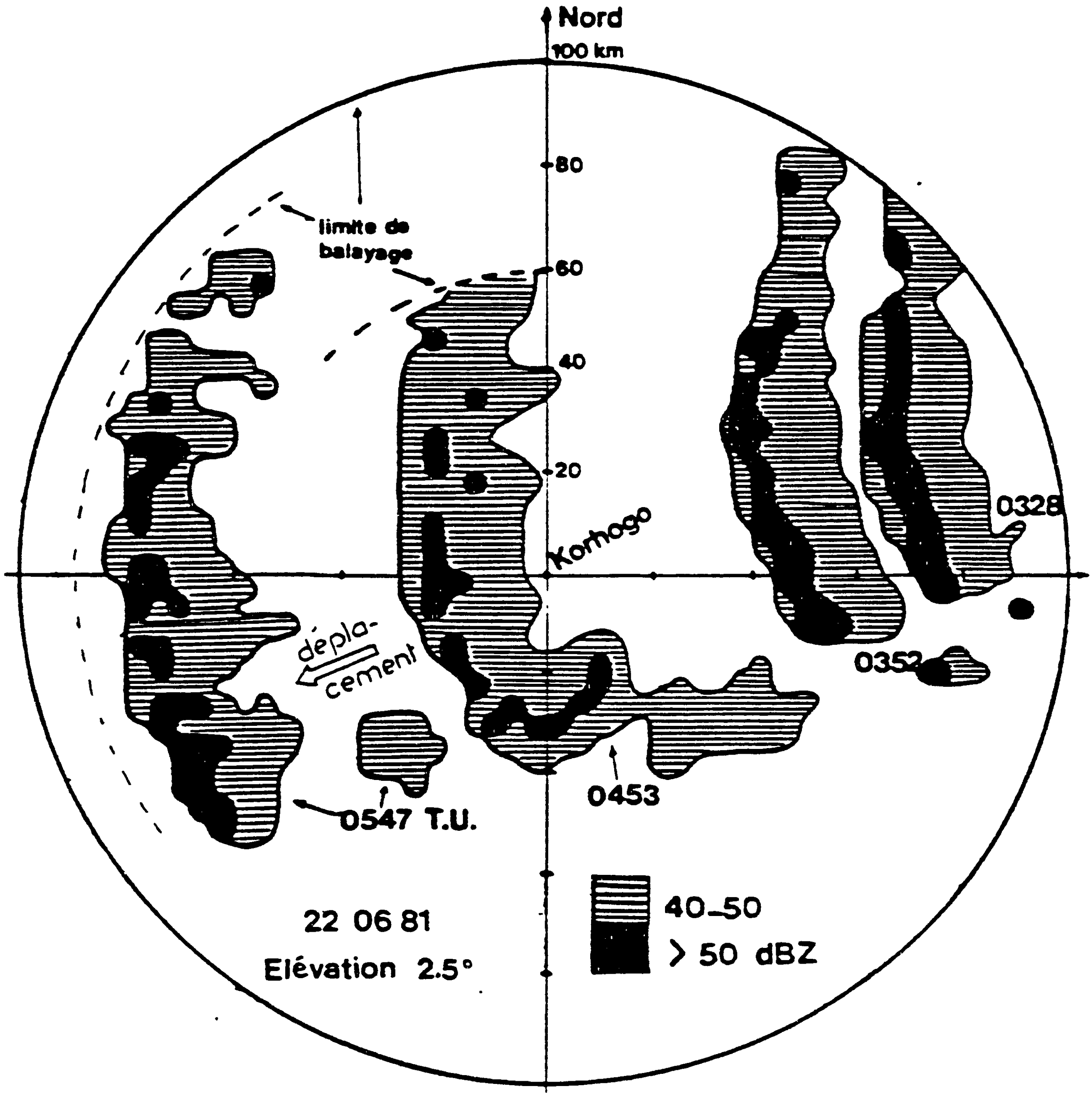

FIG 5.1.1b Radar reflectivity factor contours showing the positions of squall line at four instances

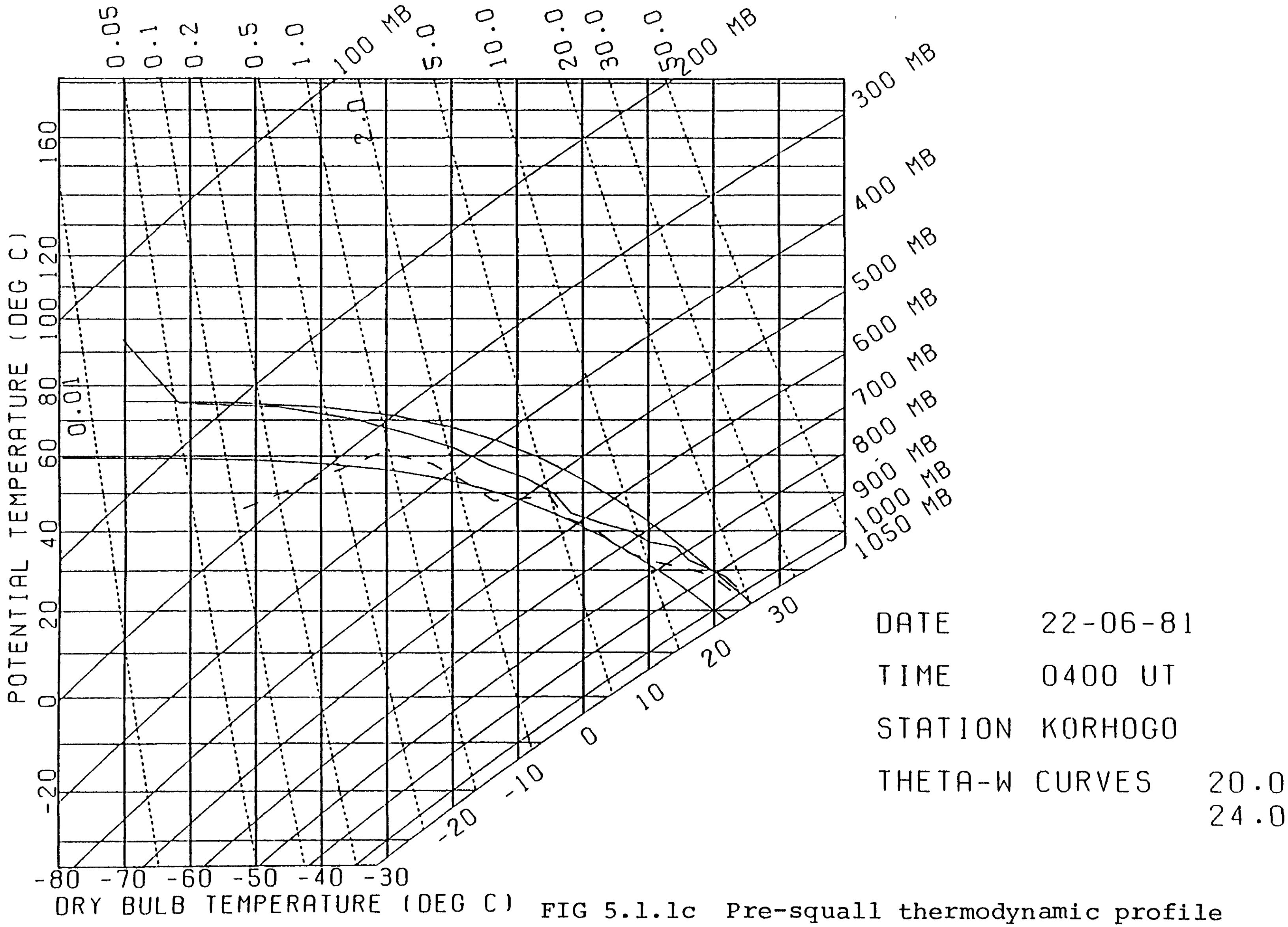

FIG 5.1.1c Pre-squall thermodynamic profile

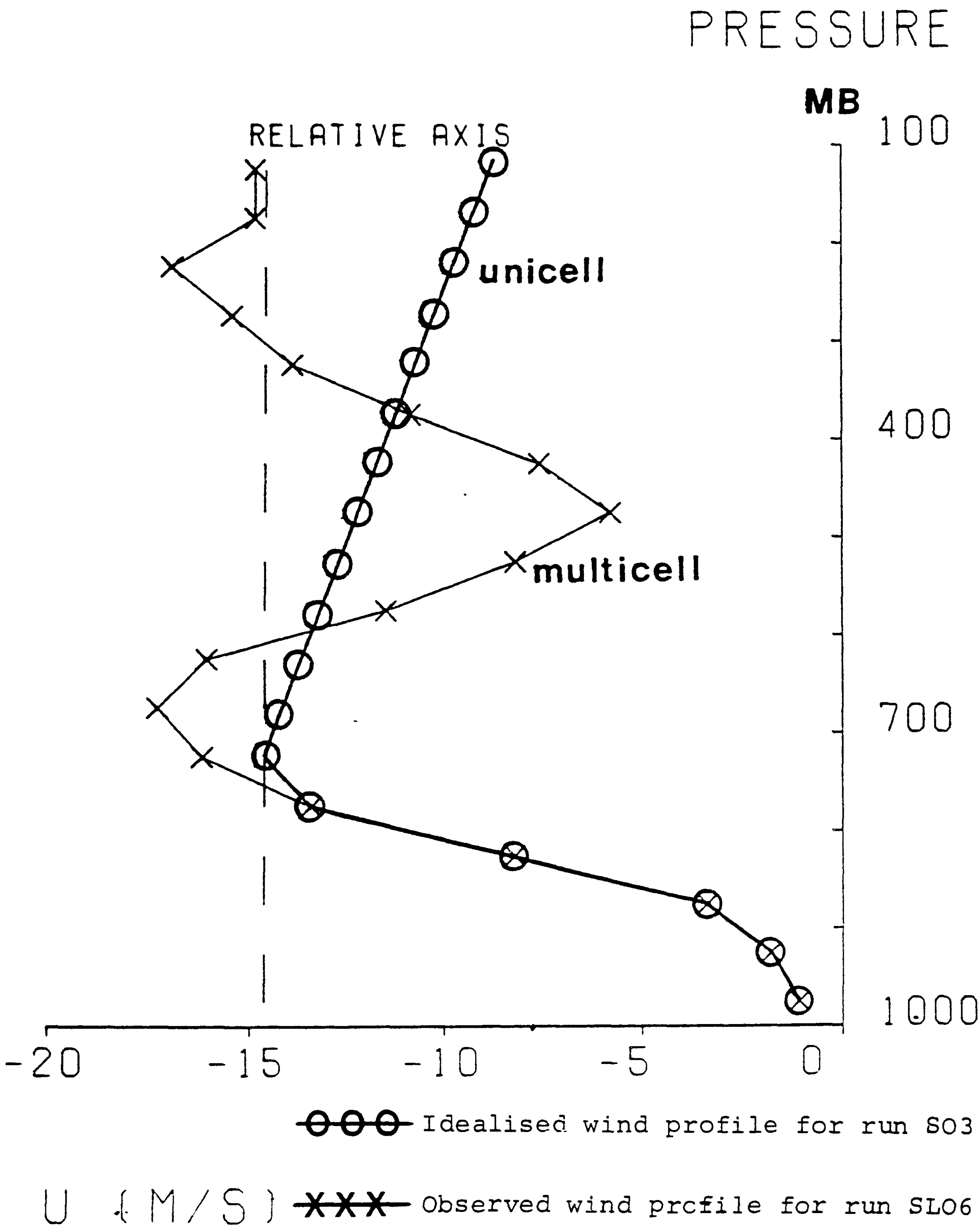

OOO Idealised wind profile for run SO3

XXX Observed wind prcfile for run SL06

FIG 5.1.1 d

boundary layer with the atmosphere being almost saturated in the lowest kilometre due to surface cooling. The boundary layer was stably stratified but convective available potential energy(CAPE) of the boundary layer air could be released if the air is subjected to forced ascent. The profile of the wind component in the system propagation direction shows the African Easterly Jet at 675mb and the Tropical Easterly Jet at 250mb with a easterly wind minimum at 450mb. The wind component perpendicular to the system propagation direction is light, suggesting a two-dimensional structure. The two-dimensional structure is confirmed by the similarity of the various vertical cross-sections of the wind fields taken perpendicular to the squall line. Fig 5.1.1e shows such four slices at the same time but at different section of the squall line. The propagation velocity of the system has been subtracted from the wind vectors so that the wind fields correspond to a stationary system. The front of the system is located near the 6km point at the ground(fig 5.1.1e) where the flow is almost stationary. This is the high pressure area where the downdraught from the east meets with the boundary layer air from the west. The downdraught air originates at about 4km high from the east and as it is evaporatively cooled, descends towards the front to feed a pool of cold air 3km deep and 4K cooler than the boundary layer air ahead of the squall line. The cold pool forces the boundary layer air ahead to ascend even though the boundary layer air is neutrally buoyant for the first 3km of the ascent. The lack of updraught buoyancy is partly explained by the rainwater loading on the air parcel. Above 3km the release of rainwater helps to increase the buoyancy of the updraught air some of which eventually reaches the

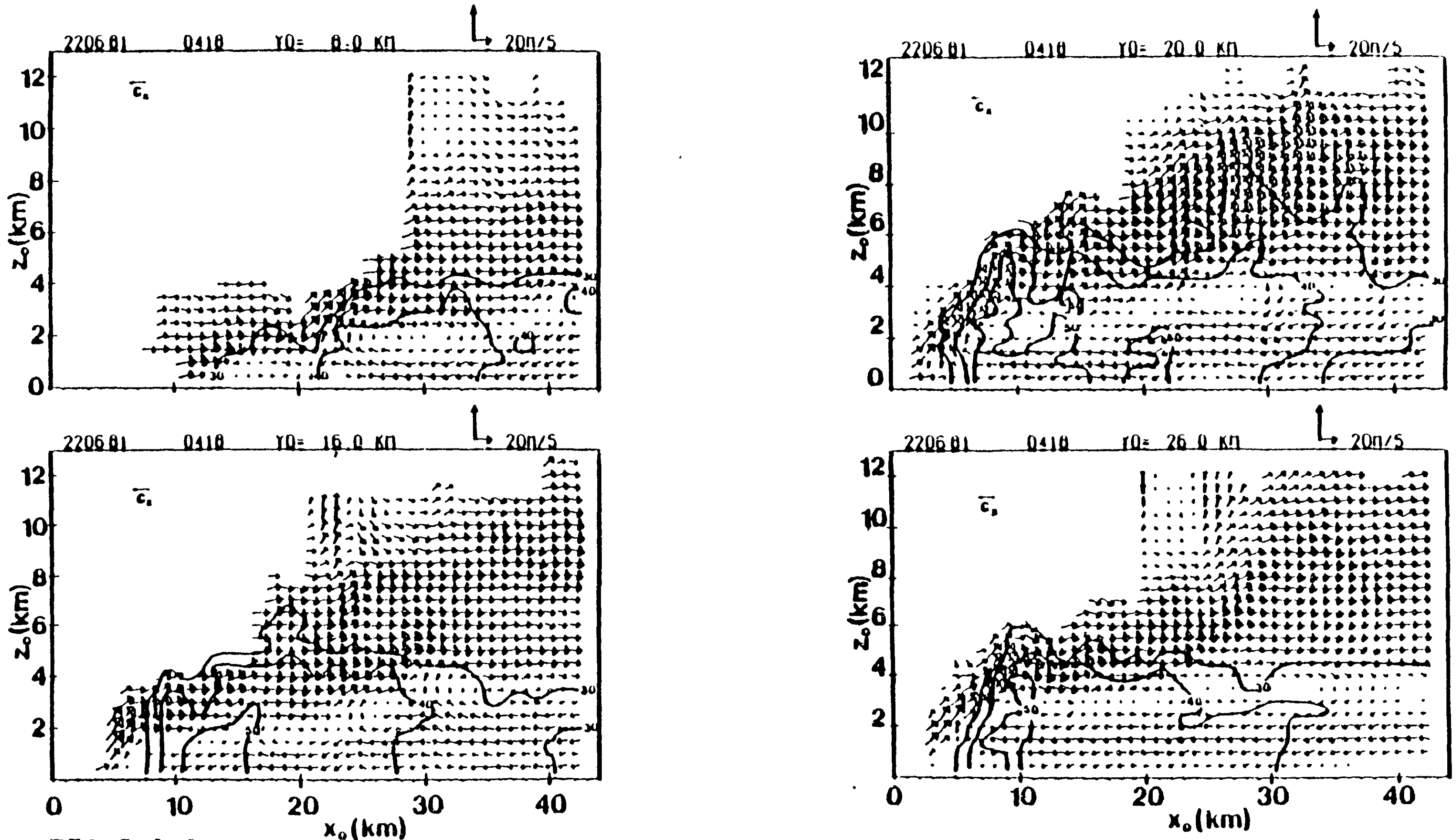

FIG 5.1.1e
Four vertical cross-sections of the squall line relative wind field taken at 0418

cloud-top height of 12km. The updraught and downdraught cooperate to maintain a steady system-the cold downdraught triggers the surface air to ascend into the updraught and the rain from the updraught helps to maintain the cold downdraught by evaporative cooling. The two-dimensional structure is different from the three-dimensional model of Moncrieff and Miller (1976) where the downdraught originates from the front of the system, whereas, in this case, it is from the rear. The precipitation pattern is illustrated by the radar reflectivity contour in fig 5.1.1f. Notice the heavy rainfall near the front and a continuous stratum of rain over a hundred kilometres to the rear of the system.

5.2 SIMULATION AND COMPARISON WITH OBSERVATION AND THEORY

It is interesting to see whether the features of the observed squall line can be reproduced in a numerical simulation. If indeed they can be, we have confidence in the results produced by the model and the entire structure of the squall line can be looked at more closely than the observation can afford.

5.2.1 The Numerical Model

The numerical model employed is a two-dimensional version of the non-hydrostatic meso-scale model of the Atmospheric Physics Group at Imperial College. The model uses pressure as the vertical coordinate and it is essentially an updated version of the Miller and Pearce(1974) model. The equations used are

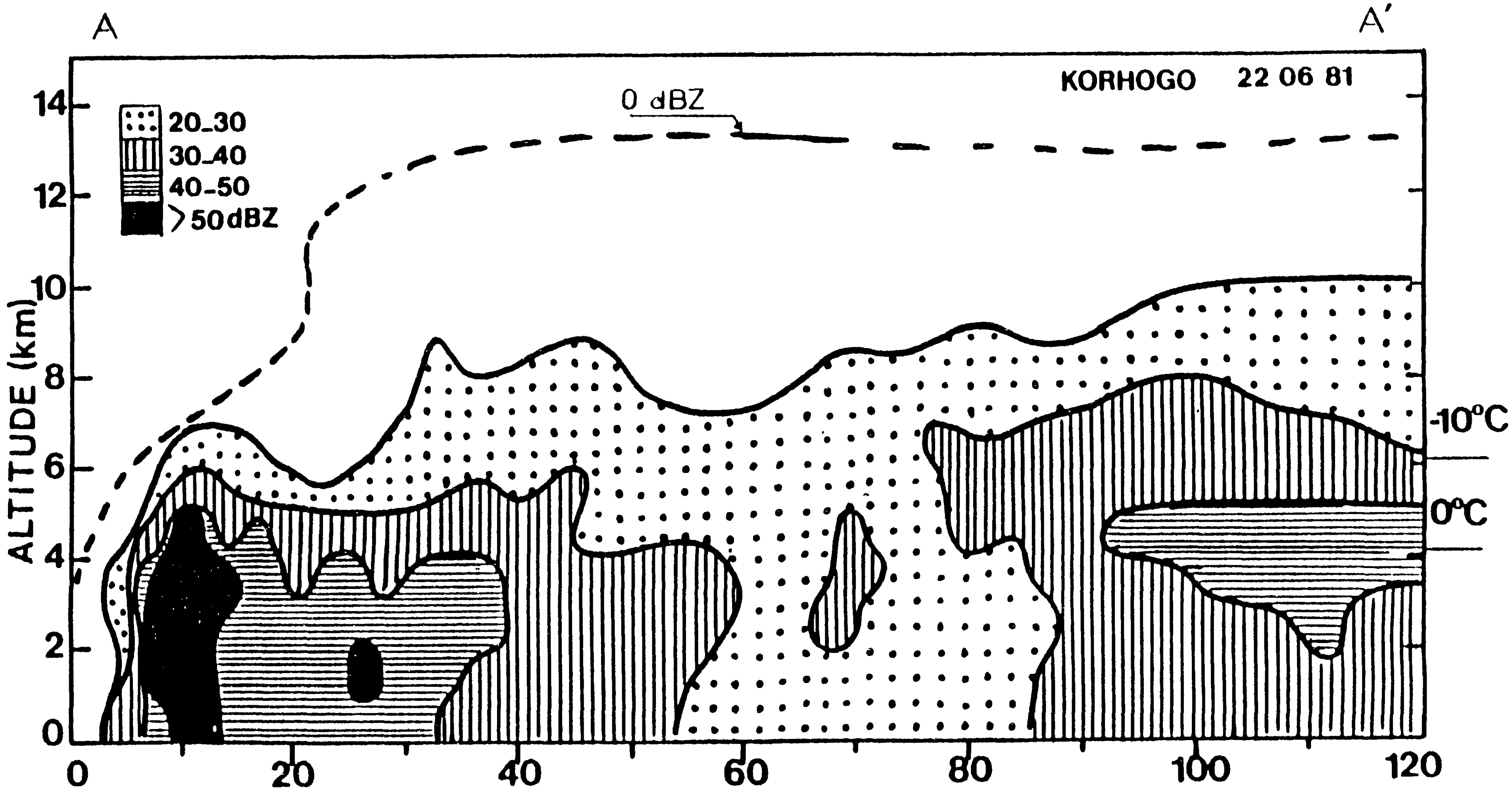

DISTANCE KM

FIG 5.1.1f Radar reflectivity factor contours showing a vertical cross-section of the precipitation pattern

$$\frac{\partial u}{\partial t} = -\nabla . u \underset{\sim}{v} - g \frac{\partial h'}{\partial x}$$ x-momentum

$$\frac{\partial \omega}{\partial t} = -\rho_o g \nabla . \left(\frac{\omega}{\rho_o g} \underset{\sim}{v} \right) - \rho_o g^2 \left(\frac{\theta_v'}{\theta_{vs}} - \ell \right) + \rho_o^2 g^3 \frac{\partial h'}{\partial p} = 0$$ p-momentum

$$\frac{\partial u}{\partial x} + \frac{\partial \omega}{\partial p} = 0$$ mass continuity

$$\frac{\partial \theta}{\partial t} = -\nabla . \theta \underset{\sim}{v} + \frac{\theta}{T} \left(\frac{LQ}{c_p} \right)$$ thermodynamics

$$\frac{Dq}{Dt} = -Q$$ moisture

where $\omega = \frac{DP}{Dt}$

h' is the perturbation from the referenced pressure surface

θ_v' is the virtual potential temperature perturbation

ℓ is the liquid water content

q is the specific humidity

Q is determined by the Kessler(1969) microphysical parametisation scheme.

The boundary condition of $\frac{DP}{Dt} = 0$ is applied at the top and bottom of the domain at 1000mb and 100mb. As the simulation domain is necessarily finite in the horizontal direction, waves inside the domain may travel across the lateral boundaries into the outside regions and this is made possible by the use of a radiation boundary condition as described in Miller and Thorpe(1981). The Euler backward and Euler forward scheme are used alternatively for time integration.

The scheme is slightly unstable but a 17-point filter, a 3-point filter and smoothing keep the scheme stable. The smoothing represents crudely the sub-grid scale mixing process. Given a set of consistent velocity field, h' field and temperature field, the right-hand-side (RHS) of the momentum and thermodynamical equations can be evaluated which can be used to update the velocity and temperature fields of the next time step. The h' field for the next time step is obtained by solving a poisson equation in h' which is the time derivative of the mass continuity equation.

5.2.2 Initialisation

The pre-squall thermodynamic and wind profiles in fig. 5.1.1b,c are used to initialise the simulation by setting the various variables as functions of pressure only. As the squall line moves roughly at the African Easterly Jet(AEJ) speed relative to the ground, 14.6m/s is added to the wind velocity at every level to produce an almost stationary system relative to the simulation frame. In this frame of reference, there are two maxima of westerly wind , one at the surface and the other at 500mb. Their magnitudes are 13.5m/s and 8.8m/s respectively. The minimum westerly is found at the AEJ level at 700mb.

An important feature of a long-lasting squall line is a cold downdraught. In this case, it is not easy to initialise and develop such a downdraught as the almost saturated boundary layer is not favourable for evaporative cooling. The 'warm bubble' approach as used by Moncrieff and Miller(1976) was tried but was found unsuccessful. This approach works for their Venezuelan squall line simulation because the rain from the initial cell evaporates into a dry lower layer, thereby initialising a cold downdraught which continues to drive the system. However, a different approach has to be used here. Instead of introducing a warm bubble, a fixed surface region of 10km long by 3km deep was cooled at a rate of 0.01k/s for 8 minutes. This represents a pool of cold air moving at 14.6m/s relative to the ground and simulates a cold density current intruding into the unperturbed pre-squall region. This is reasonable since by the time the squall line reached Korhogo, it was mature and a density current would have developed. In the initial stage of the simulation, the cold pool induces a local high pressure area near the surface which impedes the westerly (relative to the frame) on the west side of the pool and forces the boundary layer air to ascend. The precipitation produced with the ascent is advected downstream and falls into the dry layer between 700-800mb which is then evaporatively cooled. The dry easterly around 675mb on the eastern side of the cold pool is also impeded but helped by rainwater drag to descend to join the westerly flow at the surface. Thus this cold descending branch forms the downdraught on the eastern side of the original cold pool which is quickly advected eastward out of the domain, leaving the cold downdraught as the driving mechanism of the system.

The simulation domain is 128km long and 900mb deep. The horizontal grid-length is 1km and vertical grid-length is 50mb. The time-step used is 15 seconds and the total simulation time is 10 hours. This simulation run is named SL06 for future reference.

5.2.3 Structure Of Simulated Squall Line And Its Interpretation With Theory

As explained in the last section, a cold pool representing the front section of a density current initiates a local convergence and ascent of the boundary layer air. The rain produced in this ascent is advected downstream and some of which falls to the immediate east of the convergence region. There the rainwater drag, 4-5g/kg, is strong enough to initiate a downdraught of 3m/s even though the air is not significantly negatively buoyant (because at the beginning of the simulation the surface air is nearly saturated and evaporative cooling is not dominant in accounting for the net buoyancy). The descent of dry air from 600-800mb layer towards the front and the surface means that evaporative cooling can operate more to reduce the temperature of the downdraught. By 110 minutes, the surface temperature in the downdraught is 2K below the pre-squall temperature. In the first 100 minutes of the simulation, the updraught slope is steep as indicated in the streamline plot at 60 minutes (fig 5.2.3a). Consequently, the updraught rains into itself and some of its ascending air is dragged to the surface again. However, at about 110 minutes, the slope of the updraught was decreased to such an extent that all the boundary layer air is forced to ascend to release its potential energy, thus invigorating the activity of the system. From 120 minutes (fig 5.2.3b) to 180 minutes, the downdraught maximum recedes away from the front to the east while a clockwise circulation, alternatively called a rotor, grows in size between the front and the downdraught maximum. During this period, the temperature deficit from the pre-squall value

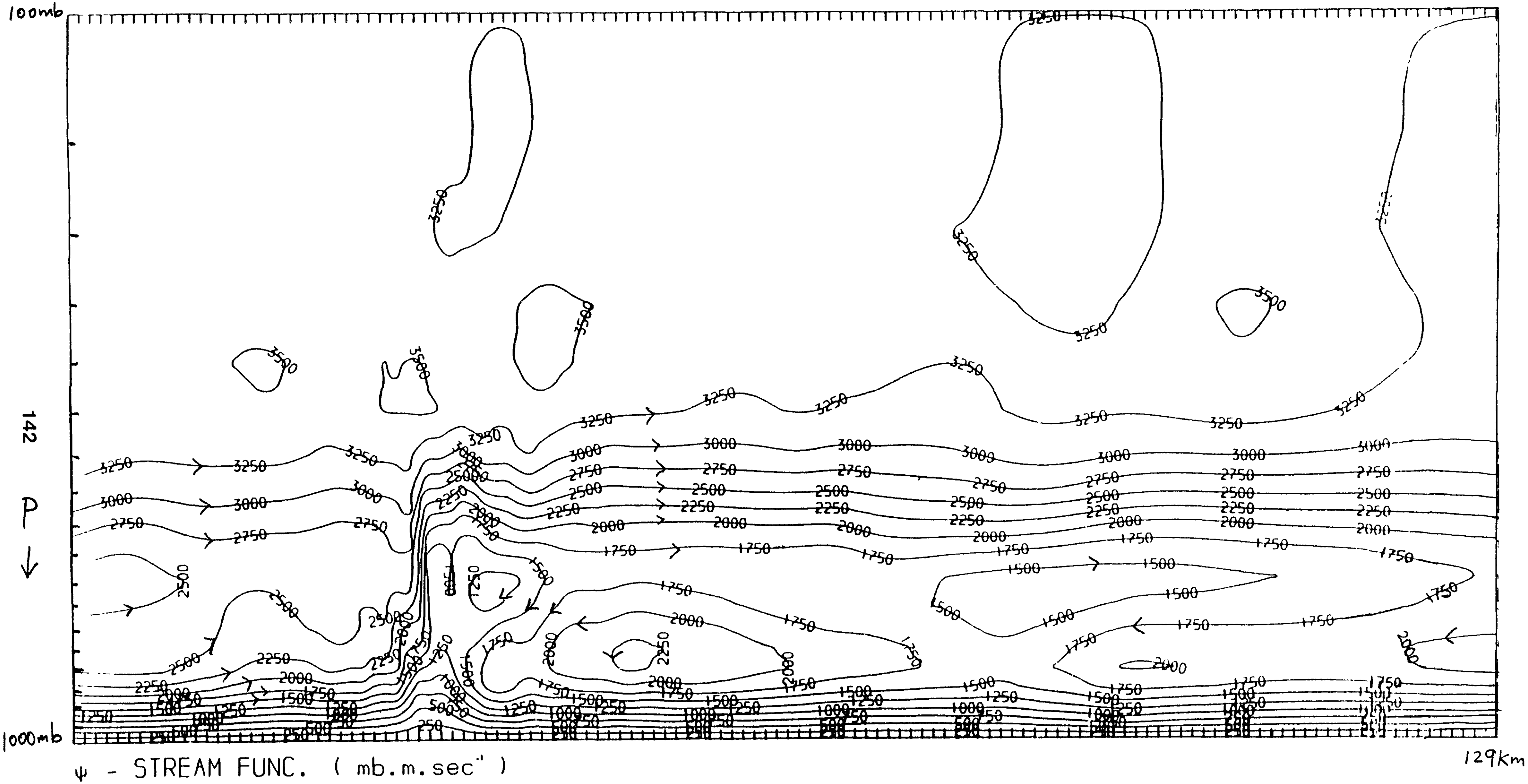

FIG 5.2.3a

RUN SL06 Time 60.0 min.

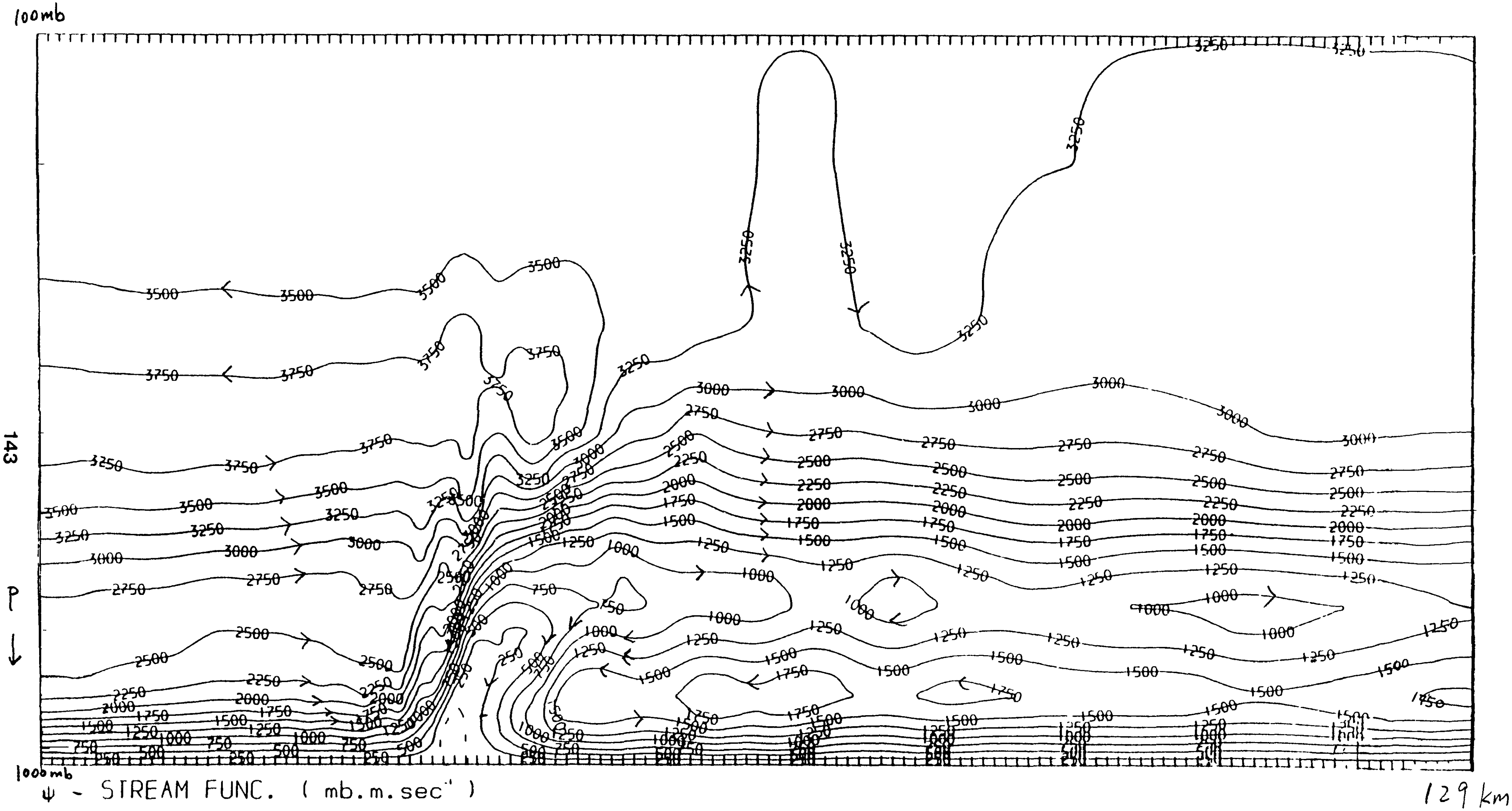

FIG 5.2.3b

RUN SLO6 Time120.0 min.

of the downdraught increases from 2K to 4K and the propagation speed of the squall line relative to the ground increases to 16m/s. The cold downdraught and the rotor structure is an example of a classical density current intruding into a fluid of smaller density. From 180 minute onward, the squall line remains quasi-steady and a typical streamline pattern is shown in fig 5.2.3c,d.

5.2.3.1 Updraught Structure -

The updraught is neutral or slightly negatively buoyant in the lowest 3km and therefore the air parcel is forced upward by the pressure field. Above 3km and several kilometres behind the front, the updraught becomes positively buoyant through the release of latent heat and overturning in convective cells occurs. The magnitudes of the maximum vertical velocity in the forced and convective updraughts are 9m/s and 6-9m/s respectively(fig 5.2.3.1a). There is a weak forward outflow ahead of the front in the form of a non-precipitating anvil at 300mb (fig 5.2.3c,d). The origin of this outflow is at around 750mb and the mass flux is small, suggesting that the forward outflow is dynamically unimportant although it shows up in satellite images as a region of high cloud. The more important anvil extends rearward and occupies the layer between 4-9km(300-600mb), above the density current. Rain from this anvil region falls into the downdraught and evaporative cooling operates over a long distance of about 100km, maintaining the low temperature of the downdraught. This picture is confirmed by the specific humidity contour plot at 360 minutes in fig 5.2.3.1b where the updraught air enters the system with

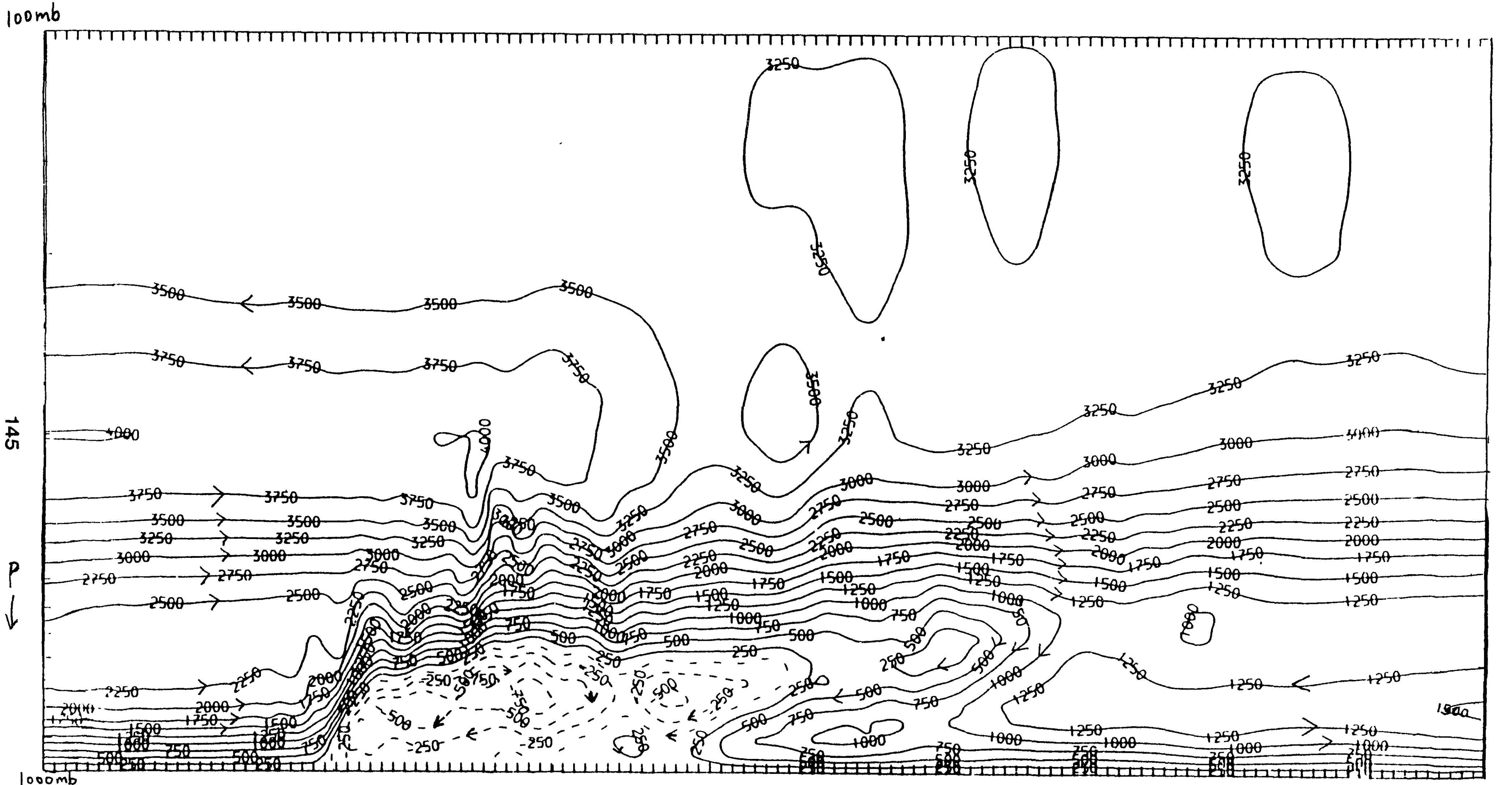

ψ - STREAM FUNC. (mb.m.sec⁻¹)

FIG 5.2.3c

RUN SL06 Time240.0 min.

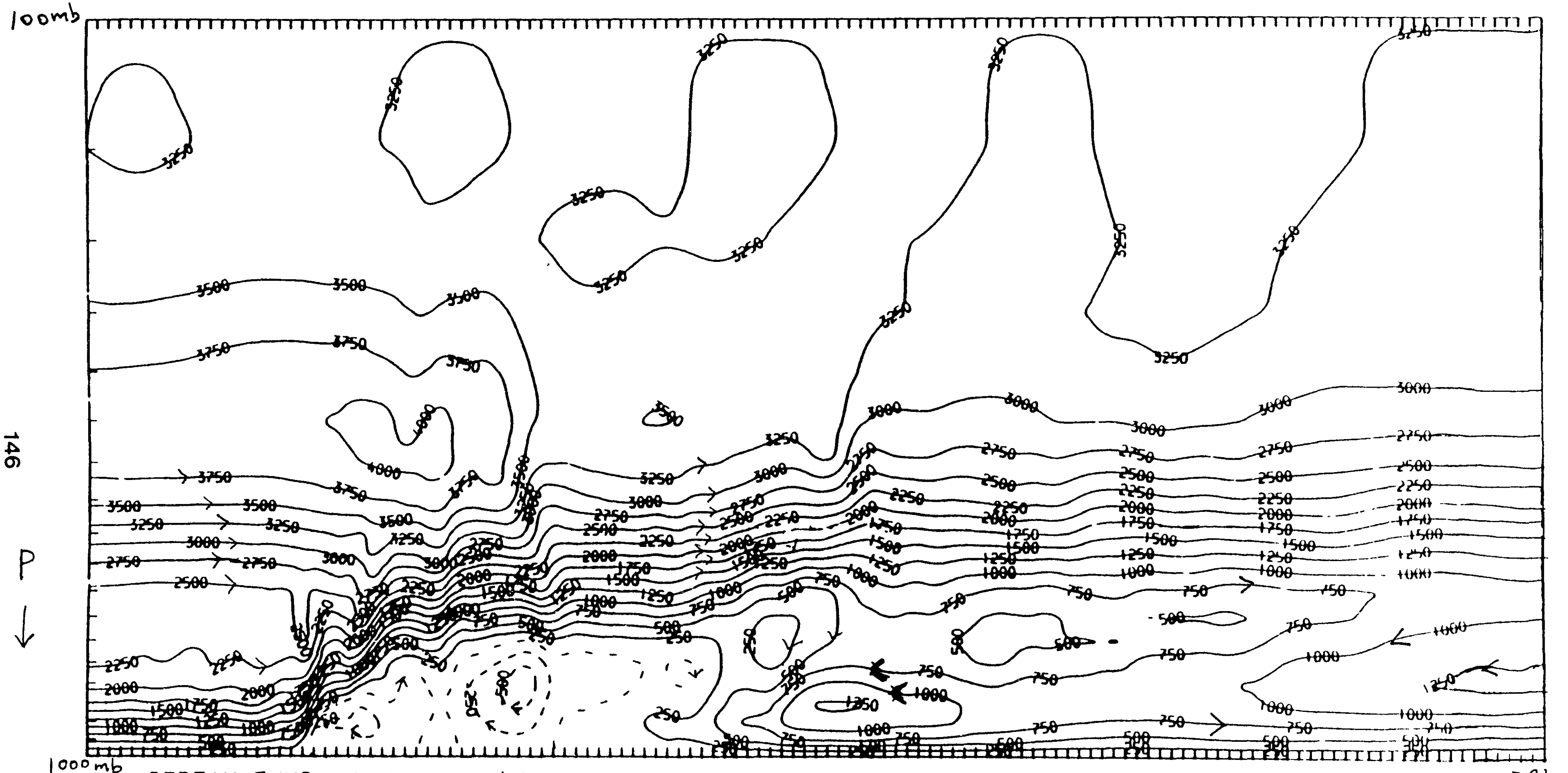

ψ - STREAM FUNC. (mb.m.sec^{-1})

FIG 5.2.3d

RUN SL06

Time360.0 min.

20km

45km

60km

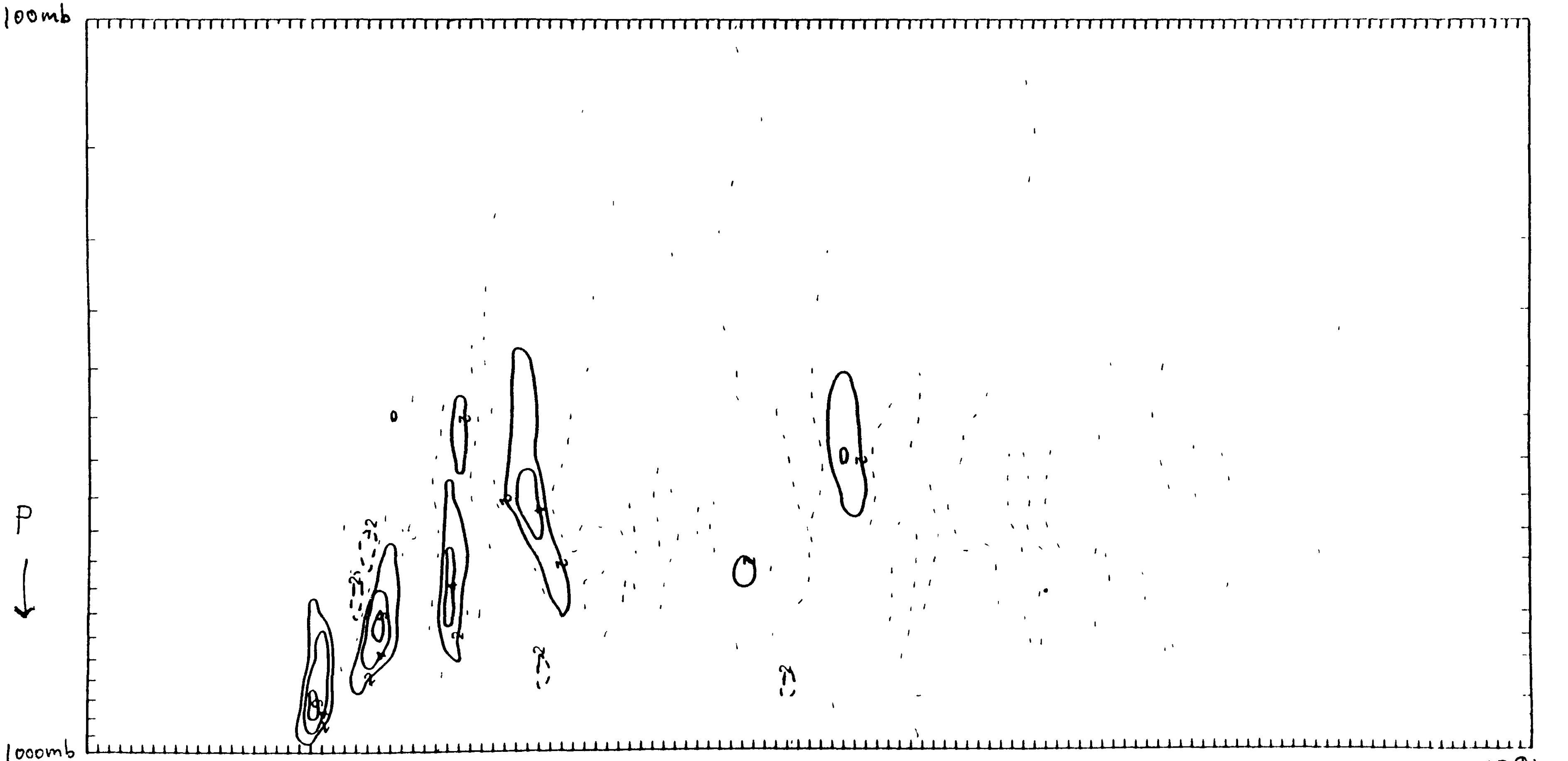

w - VERTICAL VELOCITY (m.s⁻¹)

RUN SL06 Time360.0 min.

FIG 5.2.3.1a

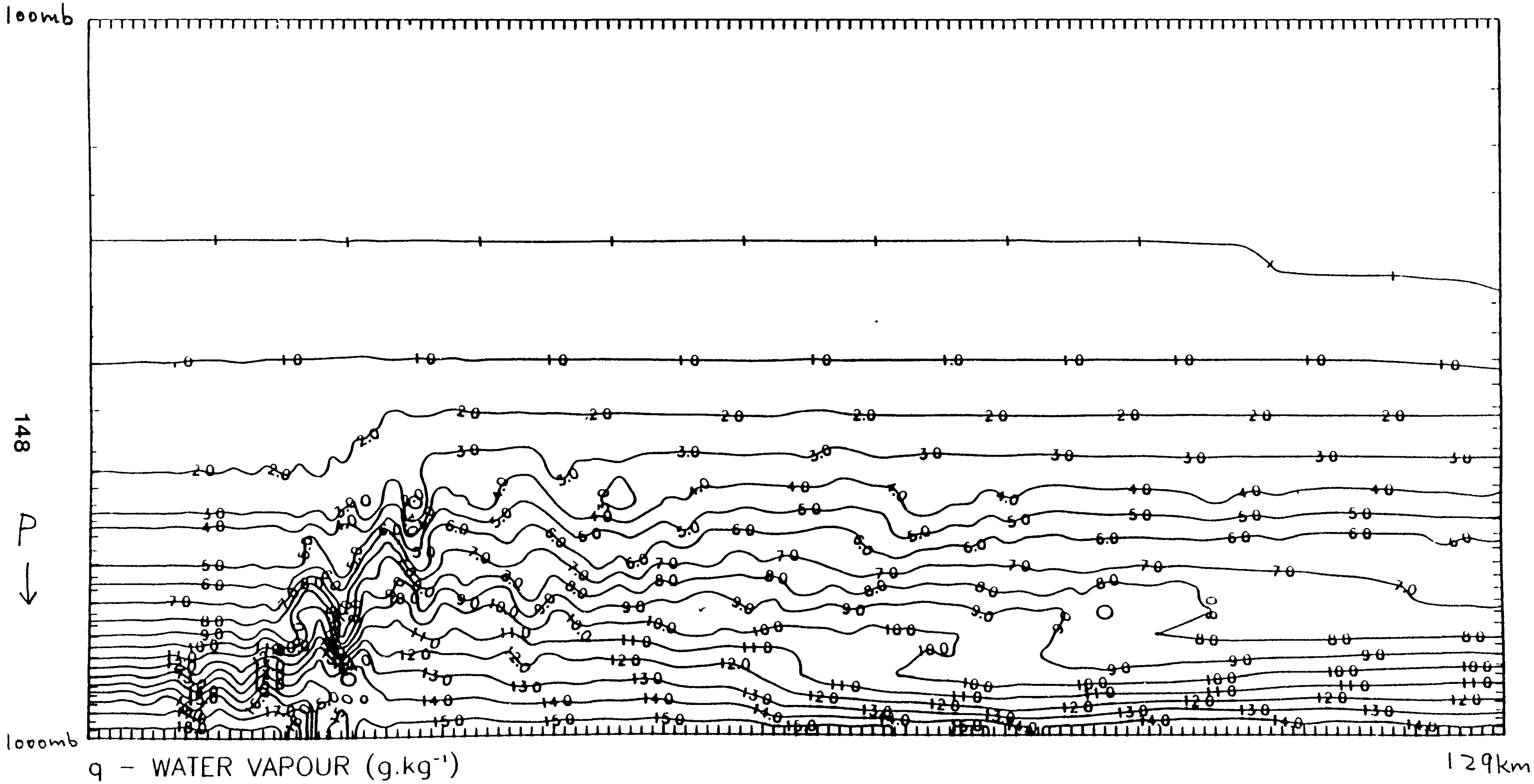

RUN SL06 Time360.0 min

FIG 5.2.3.1b

18 grams of water vapour per kilogram of moist air and exits with only 6 grams of water vapour whereas the downdraught air enters from the rear with a specific humidity of 8g/kg and attains a maximum value of 15g/kg.

Embedded in the updraught are a series of convective cells which propagate rearward relative to the front at about 9m/s. The cells start growing at the front and go through maturity to decay in a lifetime cycle of about one hour. The cell propagation speed apparently depends on the relative inflow speed of the 400-500mb layer. At 450mb, the inflow wind profile has a maximum value of 8.8m/s which is close to the average cell propagation speed of 9m/s. The spatial separation between consecutive cells is about 15-20km. Fig 5.2.3.1c is a streamline plot of the motion relative to the cells. At x=24km and x=37km, two growing cells can be identified whereas at x=50km and x=66km a mature cell and a decaying cell respectively are found and their bases are located at 600-700mb. Comparing with the rainwater contours in fig 5.2.3.1d the areas beneath the cells have greater rainfall rates as a result of the ascent and condensation in such cells. The cloud water contours in fig 5.2.3.1e confirms this picture. The surface rainfall pattern should also show regions of heavy rainfall associated with the travelling convective cells. This is in fact shown in fig 5.2.3.1f where the x-axis corresponds to time and the y-axis corresponds to the spatial dimension perpendicular to the squall line. At some given time, a pattern of maxima and minima in surface rainfall can be identified and this pattern moves rearward in time at a speed given by the slope of the contours. The heaviest

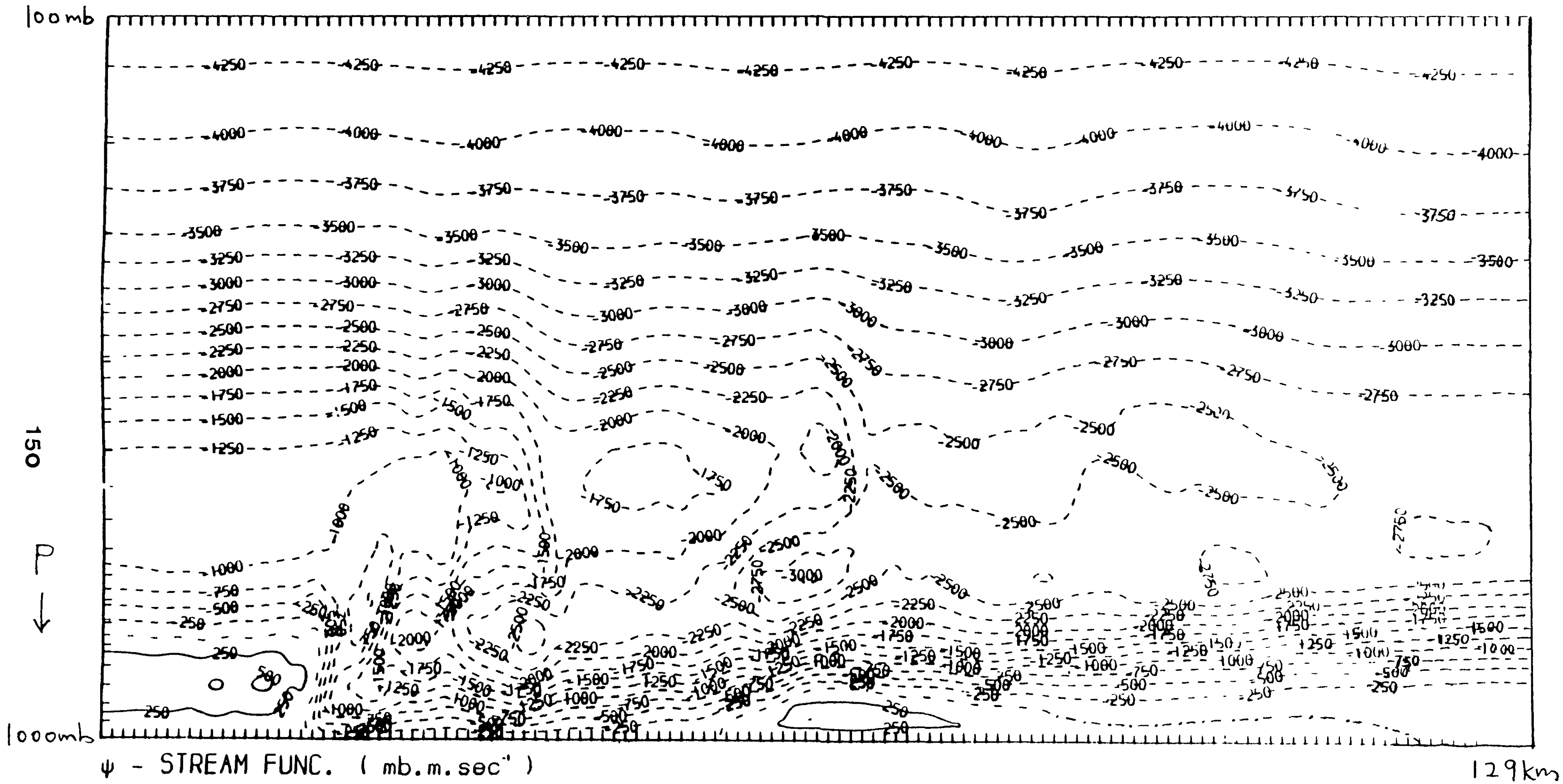

FIG 5.2.3.1c

RUN SL06 Time360.0 min.

↑ 24km ↑ 37km ↑ 50km ↑ 66km

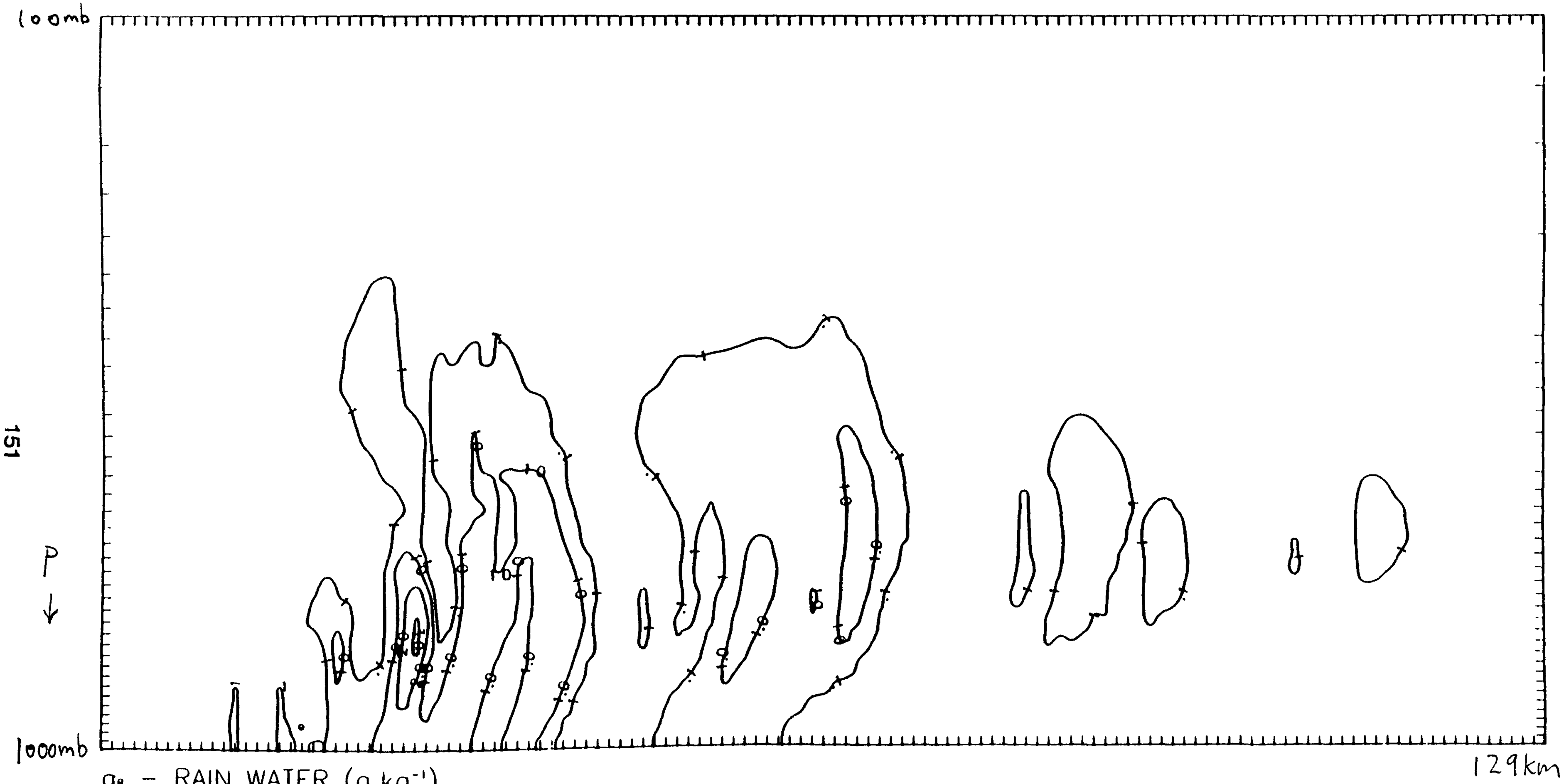

q_R – RAIN WATER (g kg^{-1})

FIG 5.2.3.1d RUN SLO6 Time 360 min.

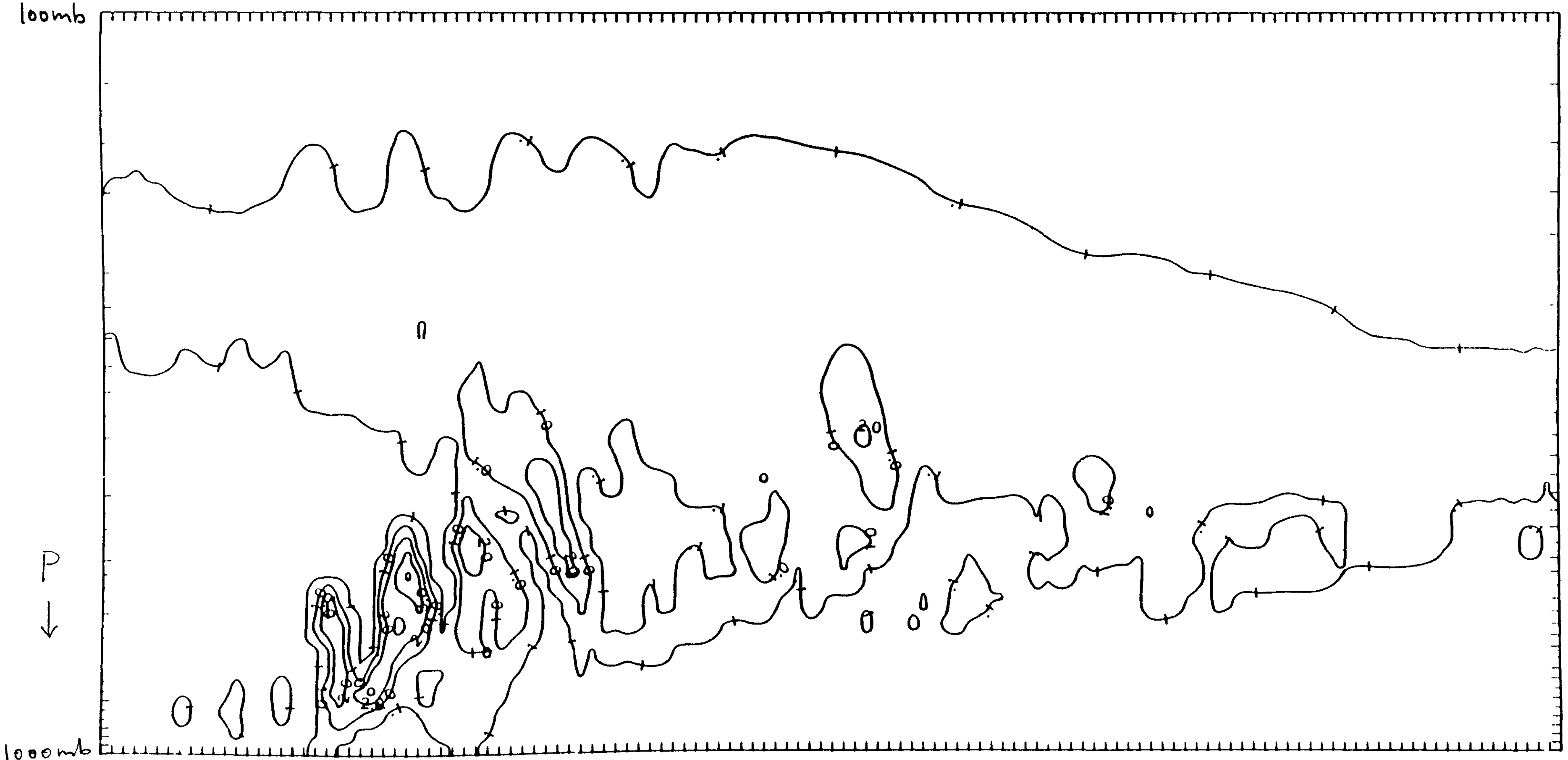

q_c - CLOUD WATER (g kg^{-1})

RUN SL06 Time360.0 min

FIG 5.2.3.1e

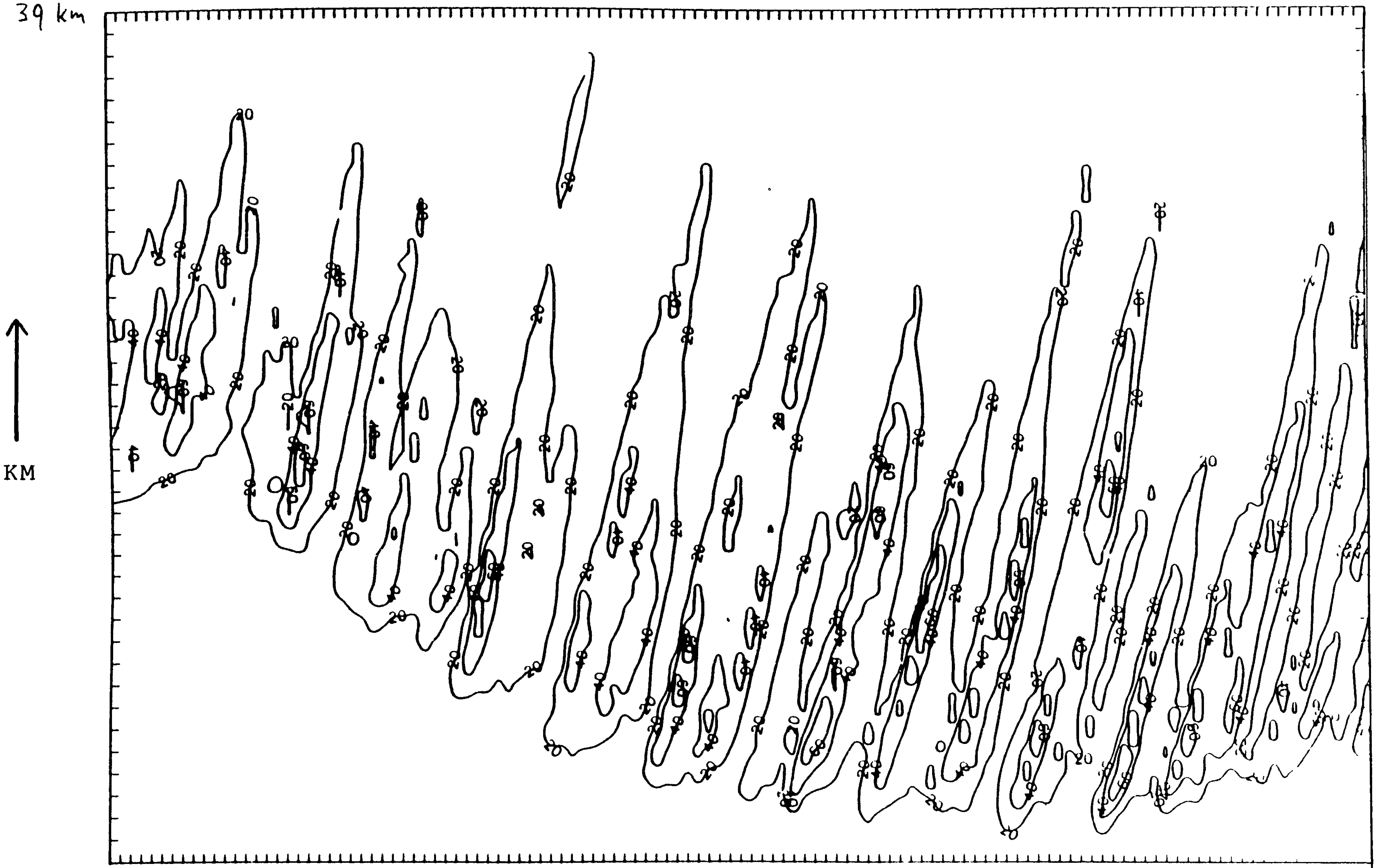

SURFACE RAINFALL (mm.hr⁻¹) 4- 8 **hour**

FIG 5.2.3.1f

Time

rainfall regions are found near to the front where the cells are particularly active. The occurrence of periodic convective cells is not clearly understood but a possible explanation is that, as rain falls from a new cell at the front, rain drag destroys some vertical momentum of the ascending boundary layer air and inhibits the formation of cells (and substantial rainfall at the front). As the growing cell and the associated rainfall pattern move rearward, the updraught at the front is free from rainwater loading and the situation becomes once again favourable for convective cell formation. This cellular structure is also found in the P(-5) and P(-1c) simulations of TMM.

As seen in the last chapter, the generation of vorticity is associated with horizontal temperature gradient in the following relationship: $\frac{D\eta}{Dt} = -\frac{g}{\theta}\frac{\partial\theta'}{\partial x}$. Therefore, the vorticity pattern in fig 5.2.3.1g can be explained in terms of vorticity at inflow and the subsequent temperature gradient. At first sight, convection seems to enhance negative vorticity(anti-clockwise sense) and with inflow vorticity of the updraught being negative($-5\times10^{-3}s^{-1}$), the outflow vorticity apparently should be negative. However,this is not the case as the outflow vorticity is nearly zero and a more detailed explanation should be sought.

In fig 5.2.3.1h, a θ' maximum on the 750mb pressure surface is found at x=21km and another maximum on the 550mb surface is found at x=27km. The maximum at 750mb shows that the lowest layer of the environment is slightly stably stratified and above this layer the environment is slightly unstably stratified. $\frac{\partial\theta'}{\partial x}$ is negative on the right of the maximum at 550mb and the cooler air on the right originates from the surface with negative vorticity $-5\times10^{-3}s^{-1}$. This

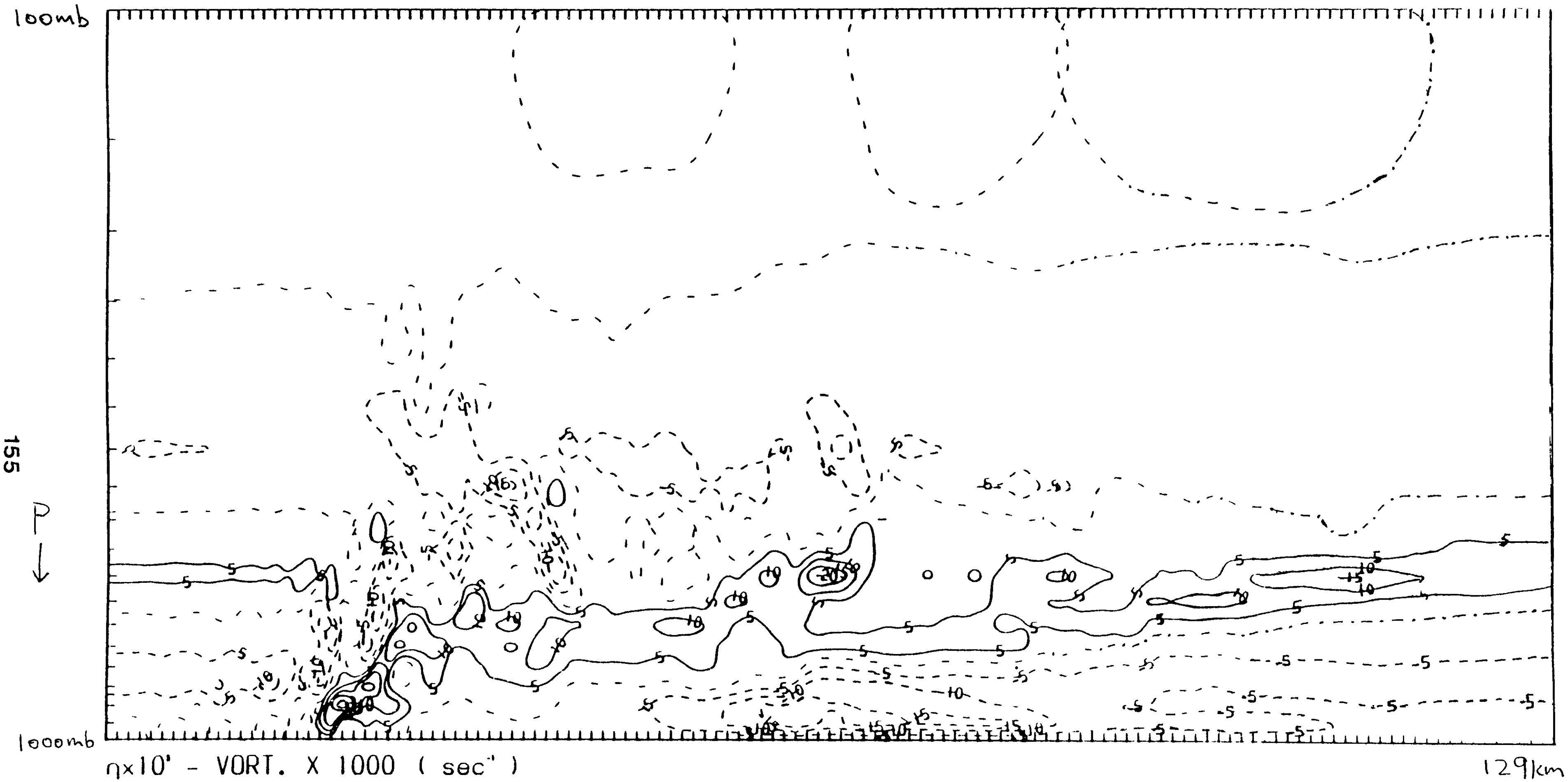

$\eta \times 10'$ - VORT. X 1000 (sec^{-1})

FIG 5.2.3.1g RUN SL06 Time360.0 min.

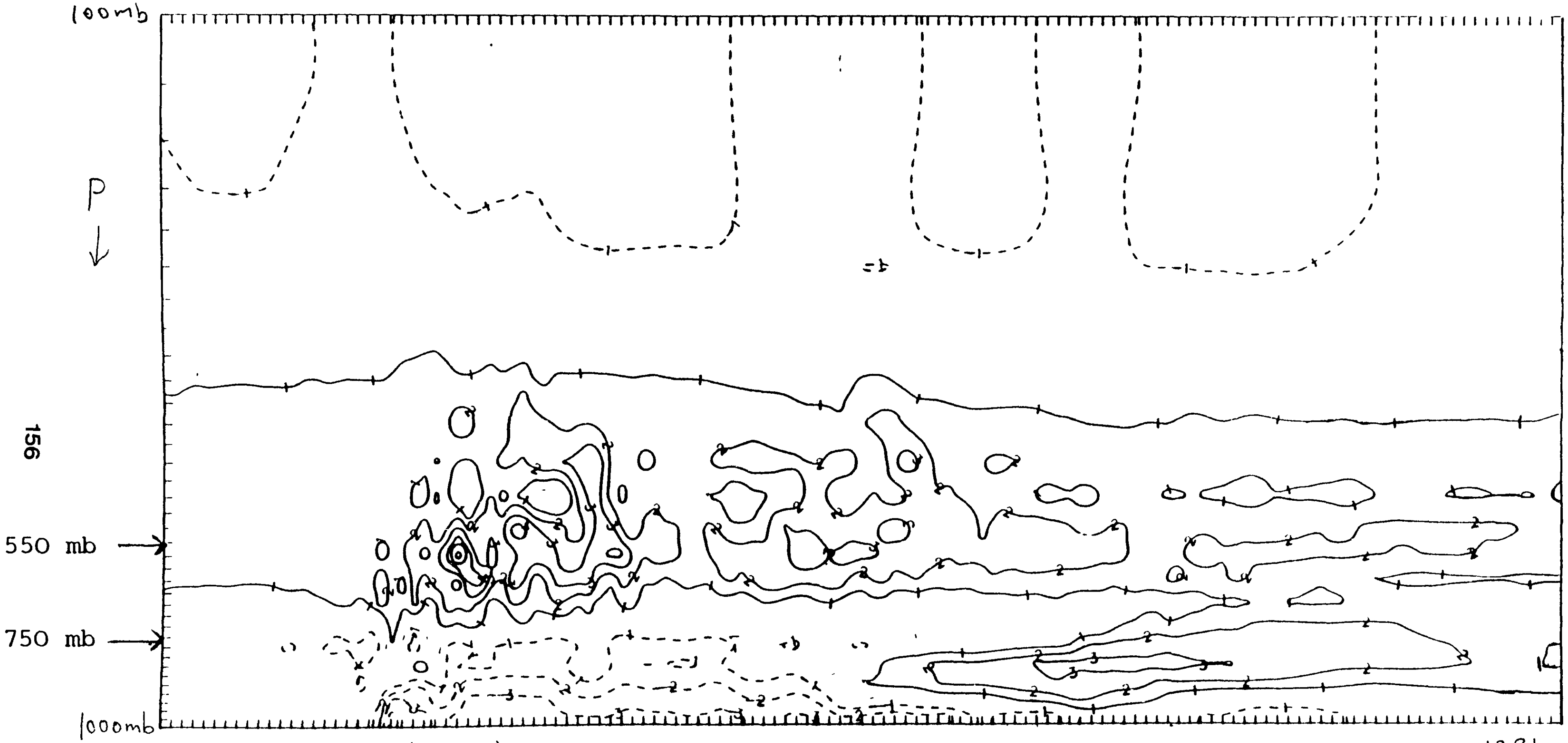

θ' - TEMP. DEVN (deg K)

FIG 5.2.3.1h

RUN SL06 Time360 0 min

21km 27km

negative vorticity is gradually destroyed by diffusion of momentum to the density current and more importantly the persistent negative temperature gradient which is a result of eqn 4.3d.

$$\frac{D\eta}{Dt} = g(\gamma - B)_{z_0} \frac{\partial z_0}{\partial x} = -\frac{g}{\theta} \frac{\partial \theta'}{\partial x}$$

and since $(\gamma - B)_{z_0} < 0$ and $\frac{\partial z_0}{\partial x} < 0$

$$\therefore \quad \frac{D\eta}{Dt} > 0$$

Hence, at the updraught outflow the vorticity is nearly zero.

5.2.3.2 Density Current Structure -

The density current could be divided into two regions, the rotor at the front and the downdraught at the rear. Within the downdraught region, an area of positive θ' and an area of negative θ' can be identified.

The easterly warm subsiding air of positive θ' within the downdraught originates from about 650mb where the atmosphere is stably stratified and dry. Its subsiding rate of 10-20cm/s cannot be accounted for by evaporative cooling as that is overwhelmed by subsidence warming (fig 5.2.3.1h). Thus the descent is caused by pressure gradient and therefore forced (fig 5.2.3.2a,b). The western limit of this warm subsidence area is at x=60km on fig 5.2.3.2b. This warm subsidence phenomena covering over 60km in the domain is an example of meso-scale warm subsidence behind squall line fronts(Zipser 1977). In this instance, rainfall drag and evaporative cooling cannot account for the subsidence but an explanation in terms of vorticity will be given later. Between x=45km and x=60km on the western side of

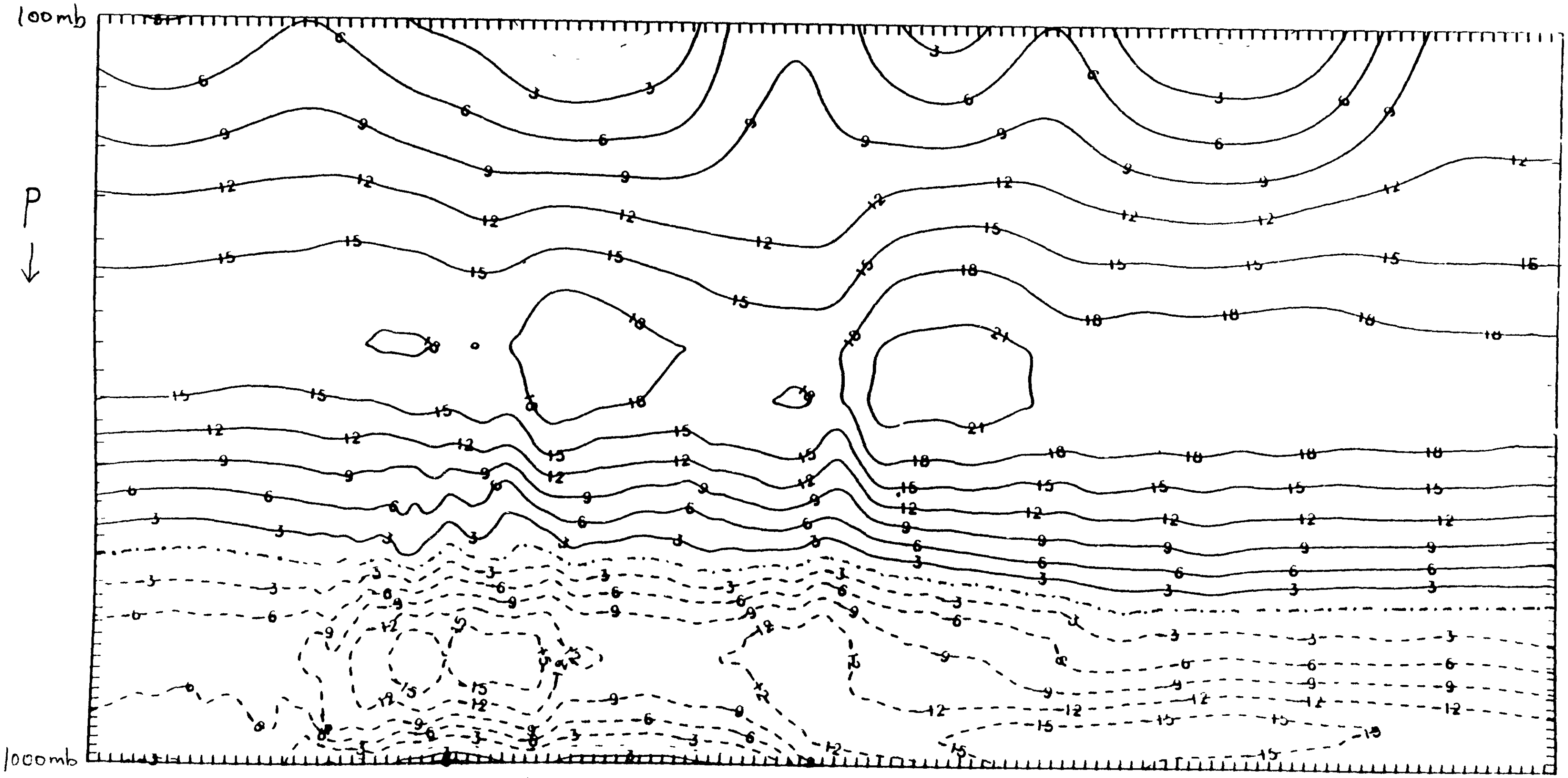

h' – HEIGHT DEVIATION (metres)

FIG 5.2.3.2a

RUN SL06 Time360.0 min

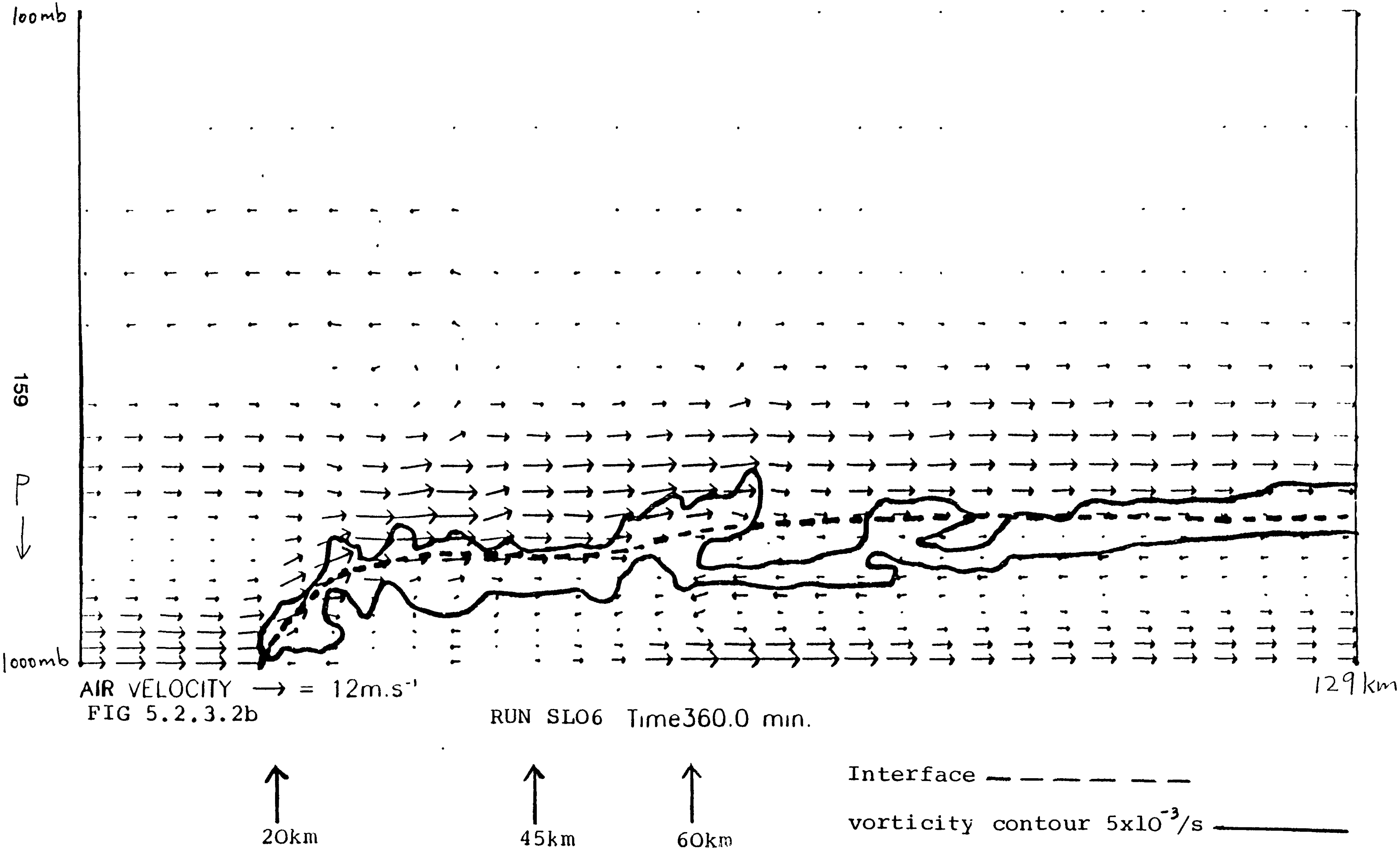

AIR VELOCITY → = 12m.s^{-1}

FIG 5.2.3.2b RUN SL06 Time360.0 min.

the warm subsidence area, rainfall is heavier as the convective cells are more active. The air arriving there has gone through a longer period of evaporative cooling so that θ' is negative and its effective buoyancy is further decreased by rainwater loading. This cold section of the downdraught is almost stagnant with respect to the front but still descending slowly. It is an example of the so called 'convective scale' downdraught (Zipser 1977). Therefore, examples of meso-scale and convective scale downdraughts are identified in this simulation.

Inflow to the downdraught from the east enters with the environmental vorticity of about $5 \times 10^{-3} s^{-1}$. This vorticity is conserved by the air parcel as it descends until it reaches the western limit of the warm pool at x=60km where greater evaporative cooling on the west results in positive horizontal temperature gradient and therefore generation of negative vorticity. The downdraught air exits to the east with a negative vorticity of $-5 \times 10^{-3} s^{-1}$. The meso-scale and convective scale downdraugahts in fact belong to the same downward overturning flow with the convective scale downdraught occupying the western (outer) section of the flow. As a consequence of the negatively buoyant descending convective scale downdraught and <u>negative vorticity generation</u> (due to horizontal differential in cooling and water loading), the warm air is forced to descend as the mesoscale downdraught. There has been disagreement on whether the meso-scale is evaporatively driven or forced by the pressure field (Zipser 1977, Miller and Betts 1977 and Thorpe, Miller and Moncrieff 1980). In the case where evaporative cooling indeed operates and accounts for part of the downward acceleration, the pressure field can account for the rest of the acceleration. Where the downdraught is warm, subsidence can only be explained by vorticity and pressure only and the mesoscale downdraught is a response to the convective scale downdraught.

The rotor region is found between x=20km and x=45km (fig 5.2.3d,fig 5.2.3.2b). It actually consists of two circulations and is about 2-3km deep. Its potential temperature is about 3-4K below the pre-squall value. The rotor is not completely closed but it `leaks` at its top and is replenished with cold air near the surface from the cold downdraught area. If the rotor had not existed between the overturning downdraught and updraught, the vorticity would have been very large at their interface, the flow would have been unstable and evolved into a stable regime like the present one. The sense of rotation of the rotor is clockwise and this reduces the sharp change of velocity at the squall line front

In fig 5.2.3.2b, a ribbon of high positive vorticity can be identified between the density current and the updraught. The diffusion of momentum from the updraught to the density current and the steep temperature gradient at the front between the boundary layer air and the cold rotor air causes a rapid generation of positive vorticity which is then advected with the fluid downstream to the east, forming the ribbon of positive vorticity.

Solutions to the free boundary problems in chapter three show that the density current is convex in shape which is confirmed by the streamline plots in fig 5.2.3c,d. Also, the solutions show a low pressure area at the base of the rearward section of a buoyant updraught which agrees with the h'-plot in fig 5.2.3.2a.

5.2.3.3 Post Squall Properties -

An area of about 100km in the simulation domain can be identified behind the squall front and the post-squall properties of momentum, temperature , moisture and pressure can be obtained. As seen in fig 5.2.3.3a, the westerly momentum below 650mb is decreased while above 650mb the westerly momentum is increased. This kind of momentum transport is typical of squall line as shown by studies by Zipser(1977) and Miller and Betts(1977). The decrease of westerly momentum near the surface is expected because the post-squall surface air originates from the African Easterly Jet where the westerly momentum is a minimum. Similarly, the increase of westerly momentum above 650mb is consistent with the fact that the air originates from near the surface where the westerly momentum is large. It is interesting to note that the post-squall wind profile is similar in shape to the pre-squall profile. The post-squall thermodynamic profile in fig 5.2.3.3b shows that the air above 600mb is nearly saturated, being the anvil outflow of the updraught. Below 600mb, the air has gone through dry subsidence within the meso-scale downdraught and this gives the high potential temperature and low moisture content in the lower atmosphere, thus forming a so-called 'onion' shape

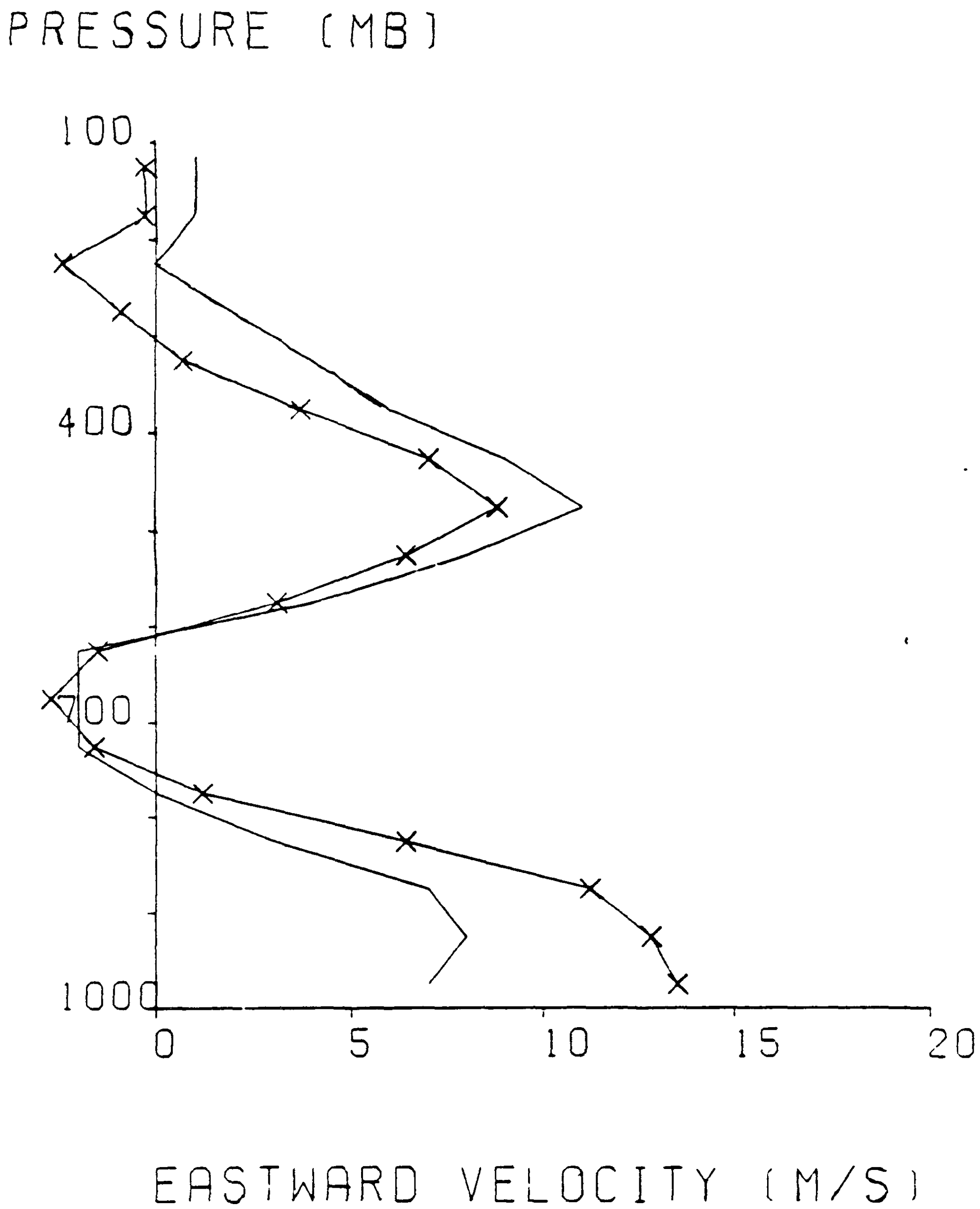

FIG 5.2.3.3a

pre-squall

post-squall

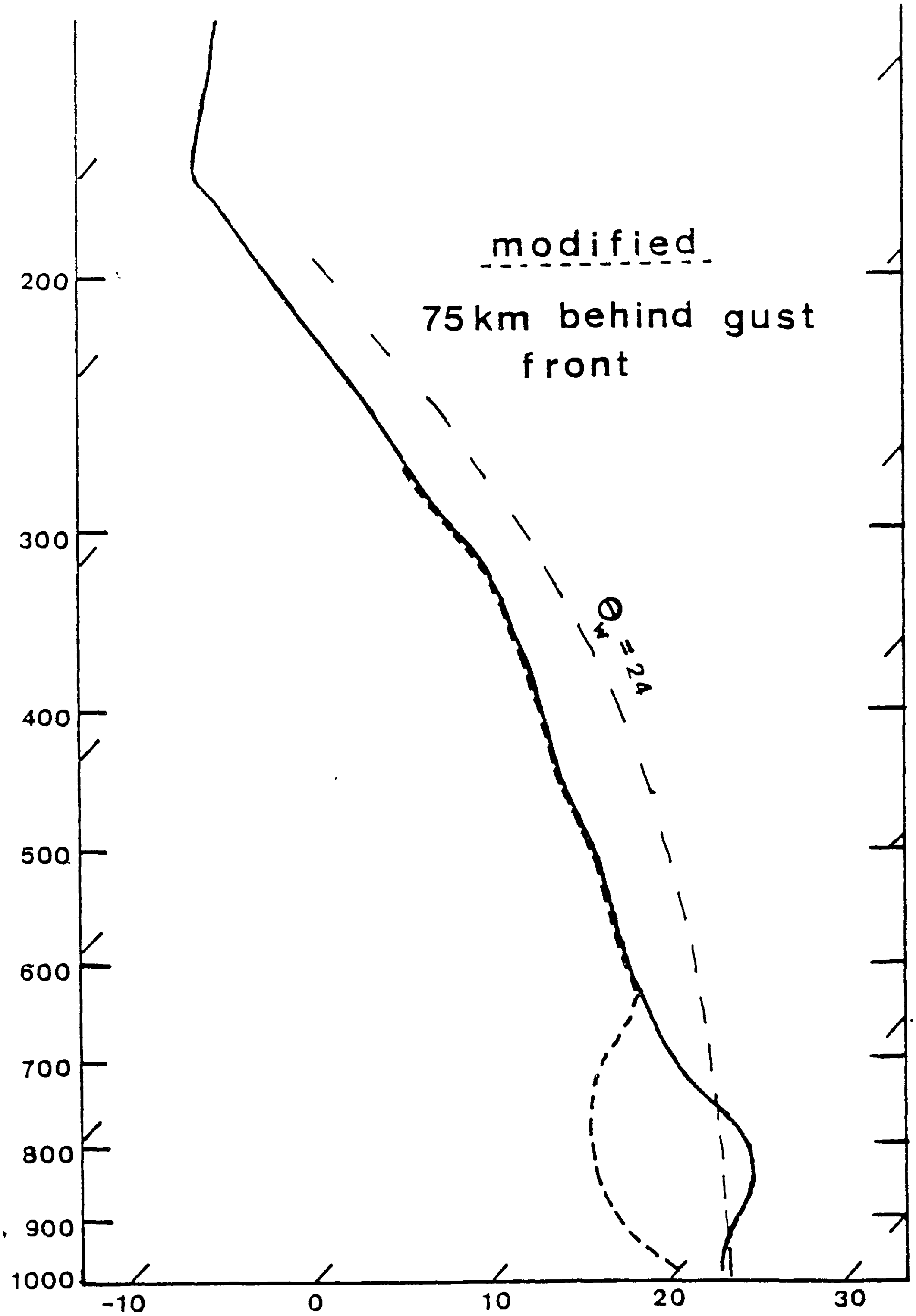

FIG 5.2.3.3b Post-squall thermodynamic profile

described by Zipser(1977). However, in the lowest kilometre, the air has gone through evaporative cooling for a longer period as it travels nearer to the front so that its potential temperature is lower and its moisture content is higher.

The moist static energy(MSE), defined as $c_pT + gz + Lq$ where Lq is the latent heat content, is quasi-conserved by a parcel in moist process and is therefore useful in tracing the origin of air parcels. The MSE profiles before and after the passage of the squall line are plotted in fig 5.2.3.3c. The MSE below 650mb decreases as the air originates from about 700mb and where the MSE is low. Similarly, the transport of boundary layer air of high equivalent potential temperature to the anvil region increase the MSE above 650mb. The passive passage of air at about 200mb through the system give similar profiles at that level.

The post-squall surface pressure is less than the pre-squall value due to the presence of the warm anvil outflow and a warm subsided layer. The pressure drop is about 1mb.

5.2.4 An Alternative Method Of Estimating Propagation Speed

The propagation speed of the simulated squall line relative to the frame of simulation can be calculated by identifying the positions of the front at different time (direct method). A different method which utilises the values of h' and u at some grid points on the bottom boundary is presented as follows.

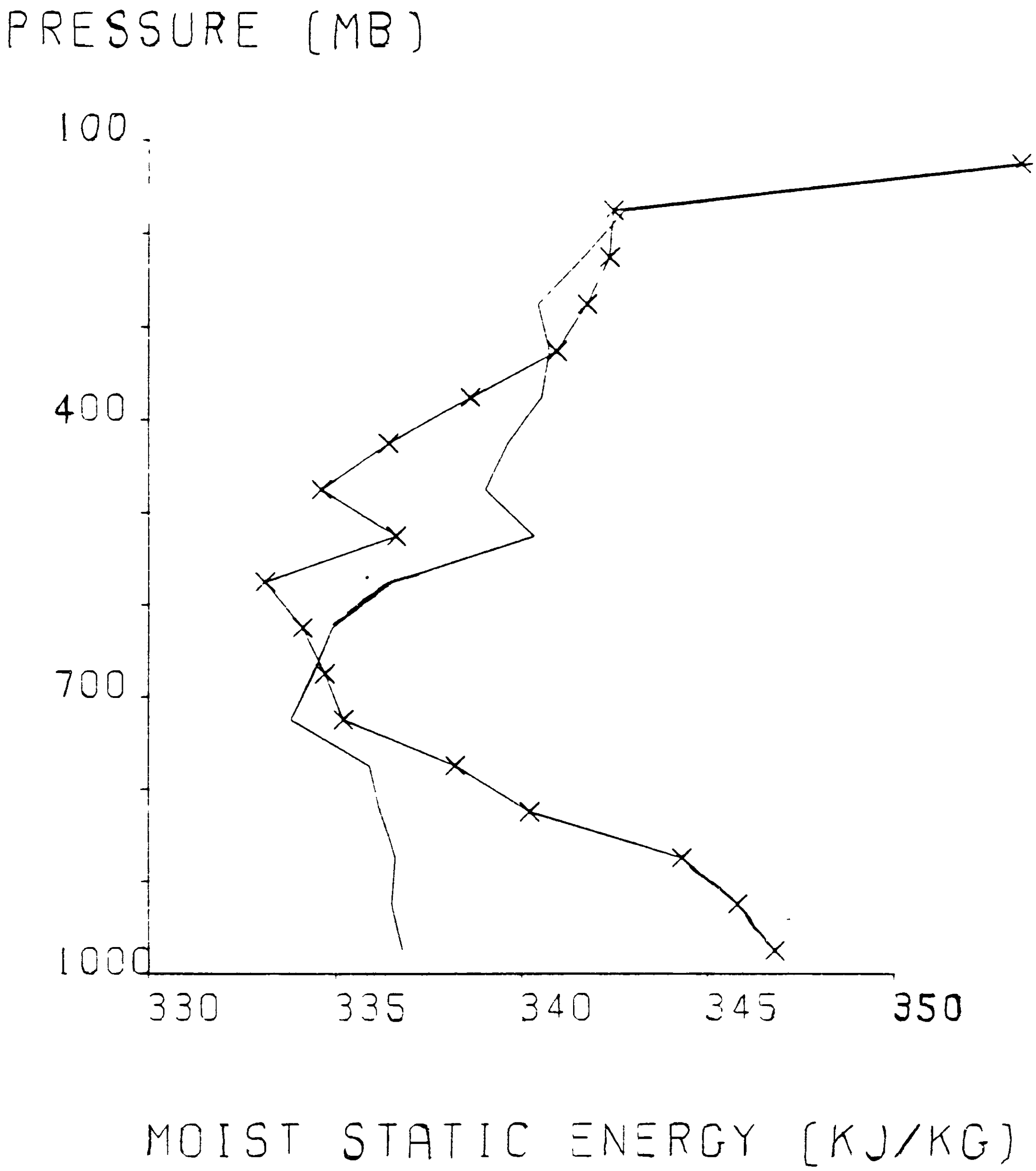

FIG 5.2.3.3c

pre-squall

post-squall

As the squall line propagates roughly at a constant speed C relative to the frame, the motion is made steady by subtracting C from the velocity field.

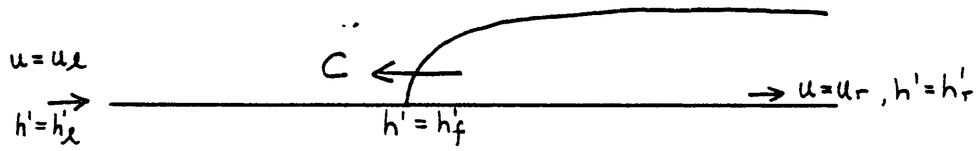

fig 5.2.4a Velocities relative to simulation frame

For steady motion along the bottom boundary, $\frac{1}{2}u^2 + gh'$ is conserved following a parcel on the boundary.

$$\therefore \quad \frac{1}{2}(u_l + c)^2 + g h'_l = g h'_f$$

$$\frac{1}{2}(u_r + c)^2 + g h'_r = g h'_f$$

Eliminating h'_f,

$$\left(c + \frac{u_l + u_r}{2}\right)(u_l - u_r) = g(h'_r - h'_l)$$

Since the motion cannot be truly steady relative to any moving frame, this relation involving a pair of points does not strictly hold but we can propose that it holds in an average sense over n pairs of points, i.e.,

$$\sum_1^n \left(c + \frac{u_l + u_r}{2}\right)(u_l - u_r) = \sum_1^n g(h'_r - h'_l)$$

$$\Rightarrow \quad C = \frac{g\left(\sum_1^n h'_r - \sum_1^n h'_l\right) - \frac{1}{2}\left(\sum_1^n u_l^2 - \sum_1^n u_r^2\right)}{\sum_1^n u_l - \sum_1^n u_r} \qquad (5.2.4a)$$

Therefore, the propagation speed can be estimated by merely obtaining

h' and u on the lower boundary. Using six pairs of points, this method give the squall line propagation at 240 minutes as 0.2m/s to the west relative to the frame which gives a speed of 14.8m/s relative to the ground. This is close to the observed value of 16.5-17m/s and it is even closer to the value of 16m/s obtained by using the direct method mentioned at the beginning. A modified version of this alternative method could provide estimation of squall line propagation speed using data from only one ground station.

5.2.5 Comparison Of Simulation With Observation

The close similarity between the simulation and observation is clearly seen in the wind vector fields in fig 5.2.5a (Sommeria and Testud,1984) and fig 5.2.3.2b. The updraught in the form of a jump is evident in both figures. The forced ascent of the boundary layer air up to 3km and free convection above are reproduced in the simulation. Furthermore, the cellular structure embedded in the updraught in the simulation agrees with that of the observation. The density current structure in the simulation which includes the cold rotor and the downdraught to the rear resembles very much that of the observation. Both have inflow to the density current from the rear at the African Easterly Jet level and upward overturning at the front of the rotor. Both have density current of about 3 km deep and a temperature deficit of 4K. The maximum surface rainfall rate of 60mm/hr in the model is close to that measured in the observation.

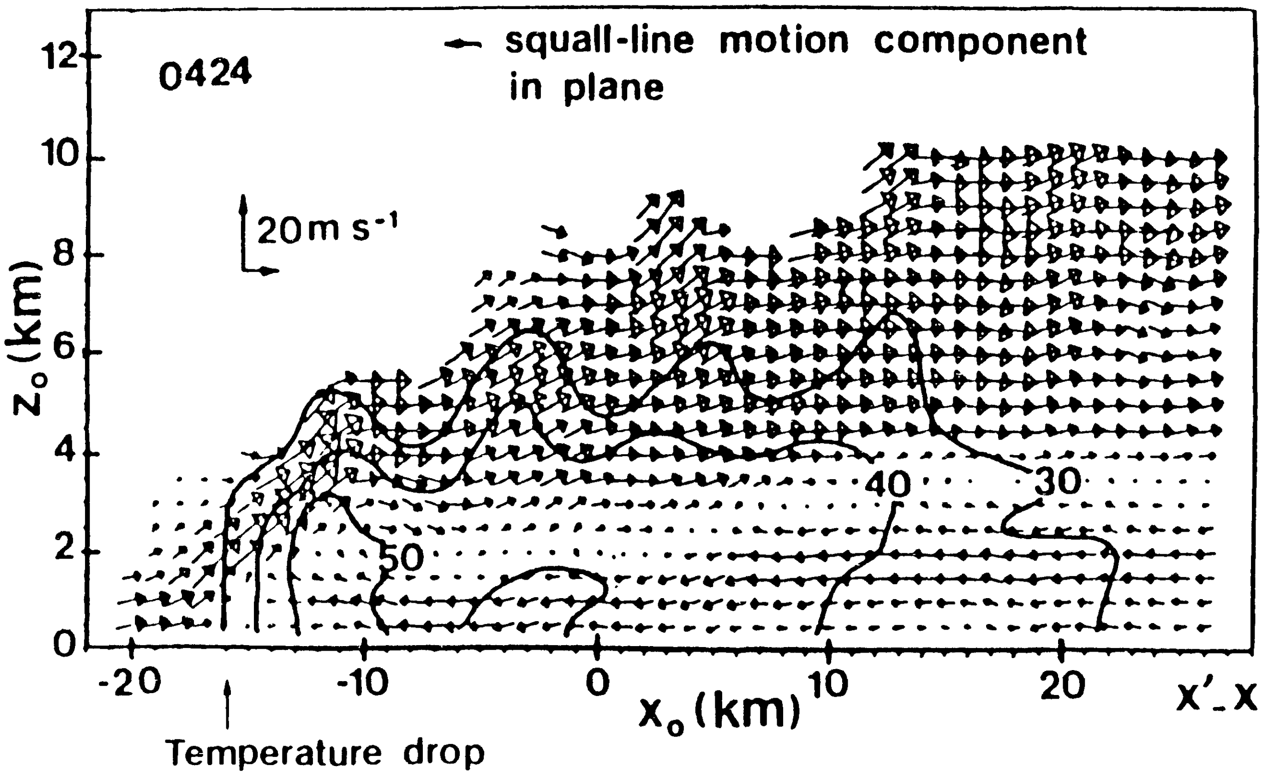

FIG 5.2.5a Observed vertical cross-section of squall line relative wind field and radar reflectivity factor contours

The propagation speed of the squall line calculated from the model result is 16m/s relative to the ground which is close to the observed value of 16.5-17m/s(estimated from the radar picture in fig 5.1.1b).

One significant difference found between the simulation and observation is the level of the anvil top. In the simulation, the anvil extends vertically from 4 to 9 km whereas it is observed that it extend from 4 to 12 km. One explanation is that the warm air in the anvil induces a low pressure at the AEJ level(suggested by the internal solutions of the free boundary problems with buoyant updraughts in chapter 3) which in turn induces a circulation in a plane parallel to the squall line; this circulation brings forth mass convergence in the third spatial dimension, increasing the mass flux into the anvil and raising its maximum height.

5.3 SIMULATION WITH AN IDEALISED WIND PROFILE

It is interesting to investigate how much the mature regime depends on the initial wind profile in a numerical simulation. Some dependence of the propagation speed of the convective cells embedded in the updraught on the relative inflow speed at about 500mb was suggested in 5.2.3.1. To understand further the role of the wind profile, another simulation is performed using exactly the same thermodynamic sounding and initialisation procedure but a different wind profile. The wind profile below 750mb is unchanged but above this level the shear is linear with pressure (fig 5.1.1d). Its general form is that of a broadened jet with its maximum near to the surface. The resulting regime is quite different from the previous simulation. The updraught is much more upright and the cold density current is absent. Another prominent difference is that the cellular structures of the updraught is replaced by a steady deep single cell. The simulation, named as S03 for future reference, was run for 6 hours and the system was quasi-steady from 150 minutes onward. The initial wind profile is very similar to that of the P(-5) simulation of TMM which however produced a more cellular structure.

5.3.1 Updraught Structure

Since the thermodynamic profile is the same as that used in SL06(the first simulation), again the boundary layer air is stably stratified in the lowest 3km and the pressure field is responsible for the initial ascent (fig 5.3.1d). The potential temperature perturbation reaches a minimum of -1K in the initial ascent but rises to a maximum of 3K in the free convective section of the updraught. The streamline plots of fig 5.3.1a,b,c show again the jump structure of the updraught. Its maximum vertical velocity is 10-12m/s. There is no forward anvil outflow to the west so that an observer on the ground would receive little warning.

It is evident from the streamline plots that the updraught is very upright. Consequently, rain forming in the upper section of the updraught falls into the lower section causing a rainfall drag on some of the ascending boundary layer air which is negatively buoyant already (fig 5.3.1e,f,g). This drag is sufficiently strong to divert a proportion of the ascending air parcels from the updraught core to form a descending branch flowing towards the east at low level and out of the simulation domain. Therefore a substantial portion of the

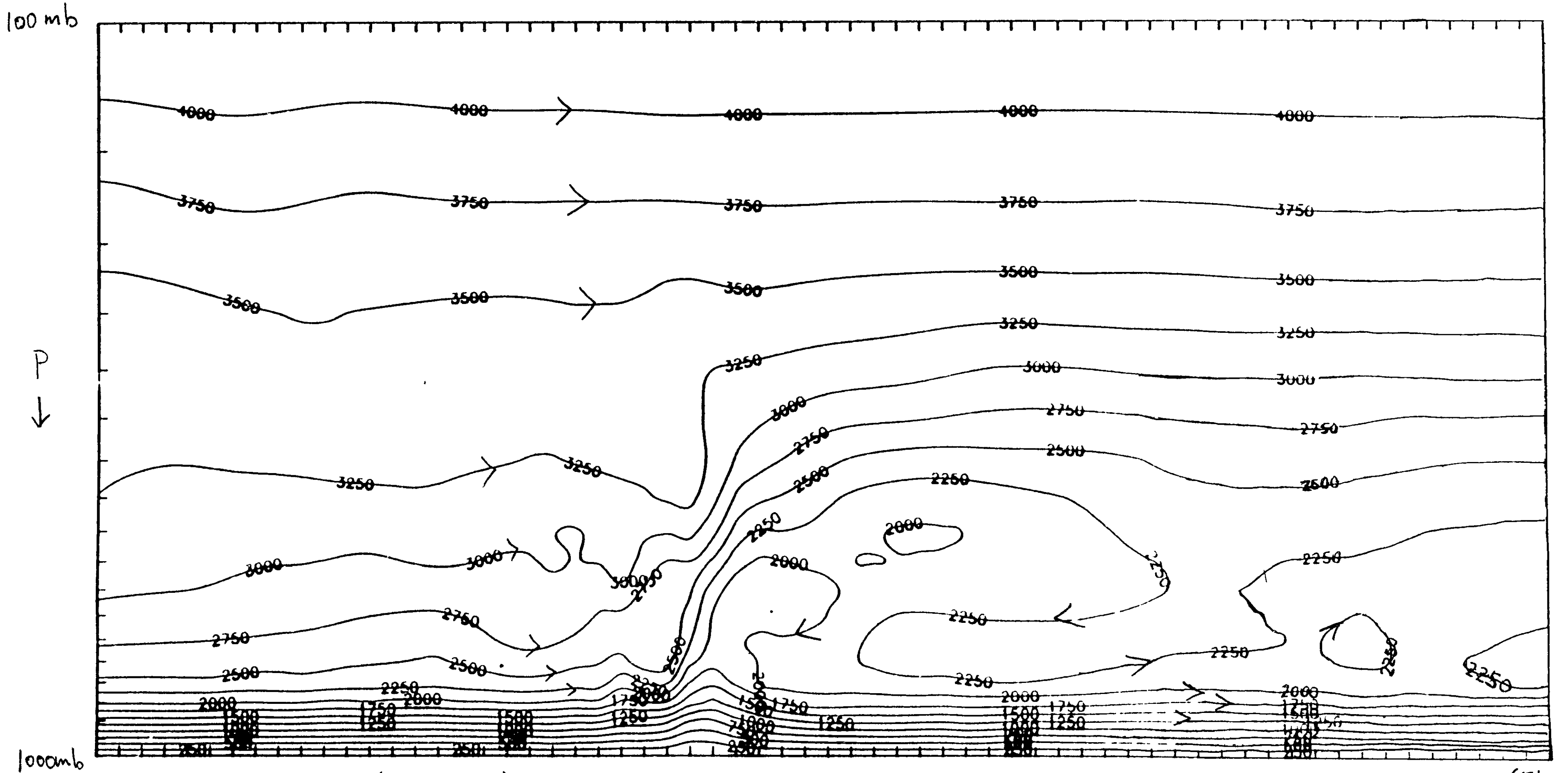

ψ – STREAM FUNC. (mb.m.s^{-1})

FIG 5.3.1a RUN SO3 Time150.0 min

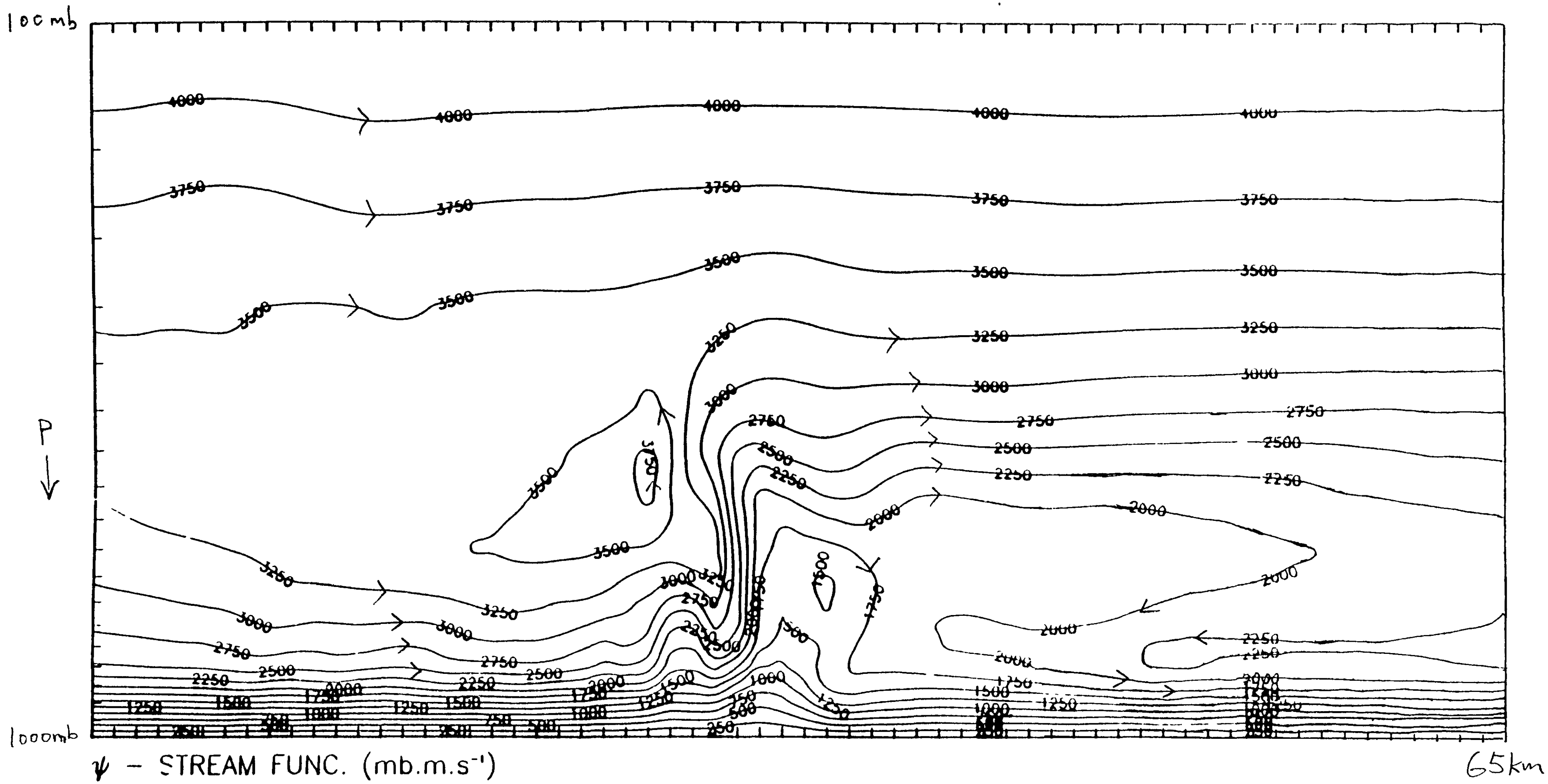

ψ - STREAM FUNC. (mb.m.s^{-1})

FIG 5.3.1b RUN SO3 Time180.0 min.

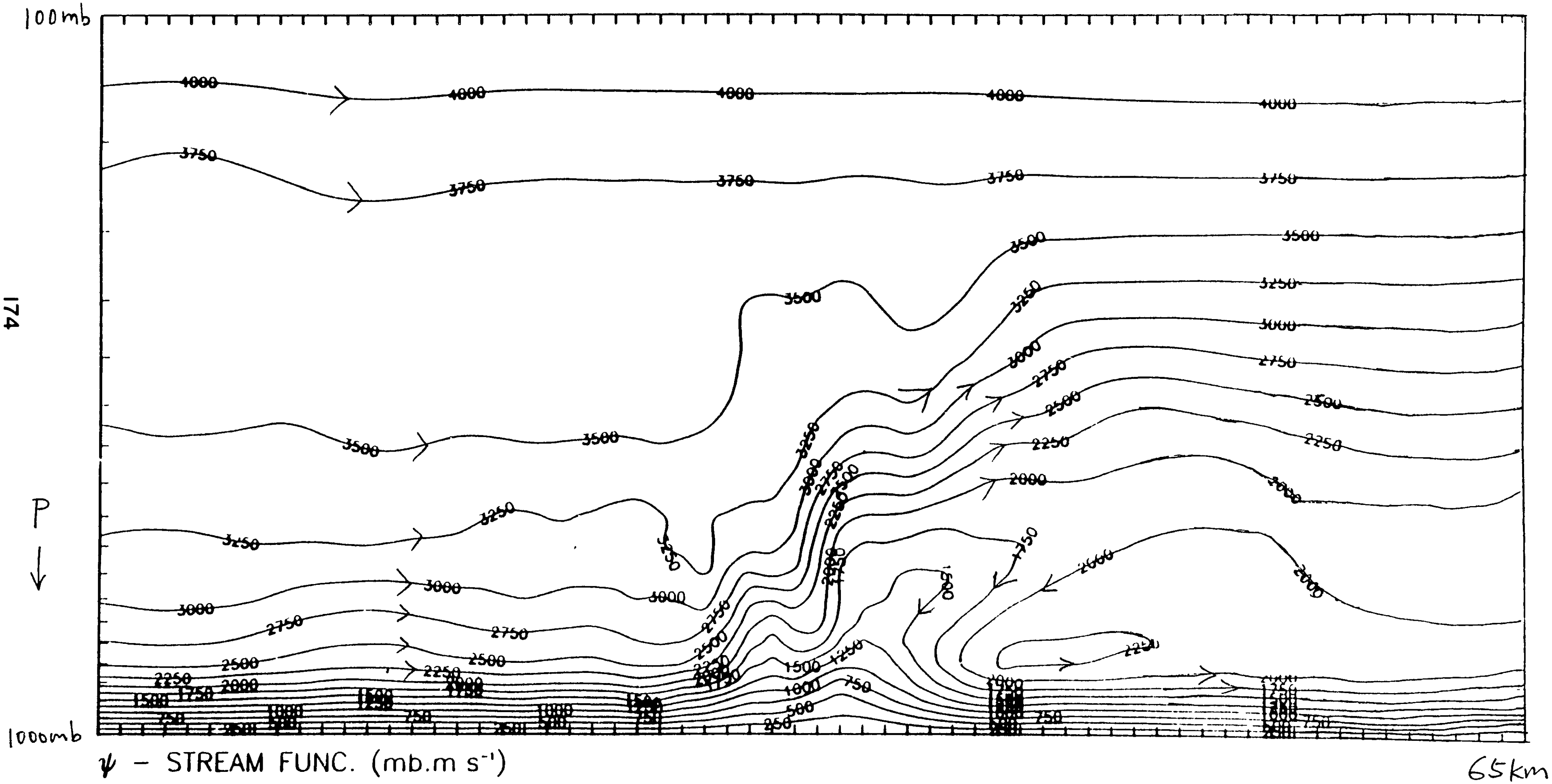

ψ – STREAM FUNC. (mb.m s^{-1})

FIG 5.3.1c RUN SO3 Time240.0 min

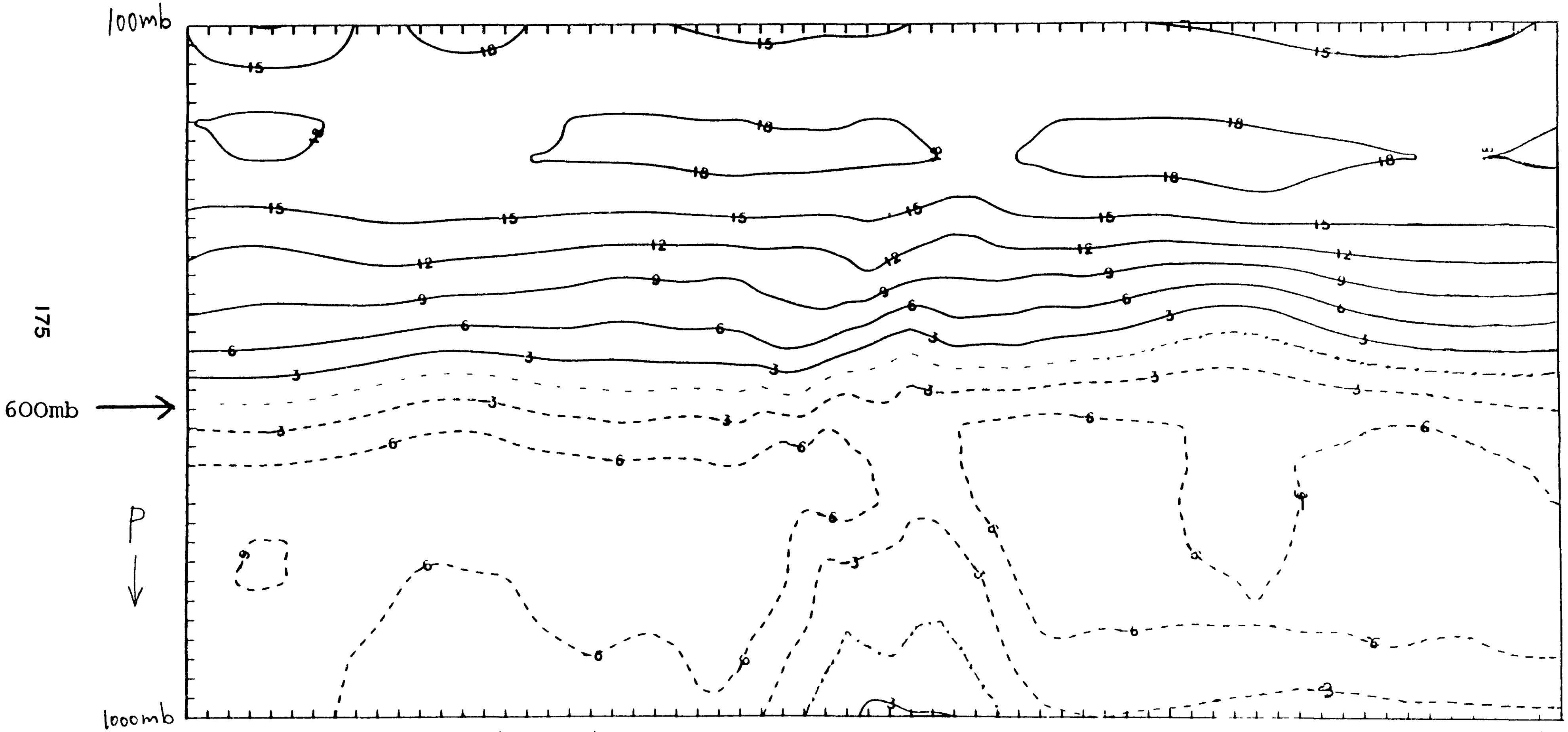

h' - HEIGHT DEVIATION (metres)

FIG 5.3.1d RUN SO3 Time240 0 min.

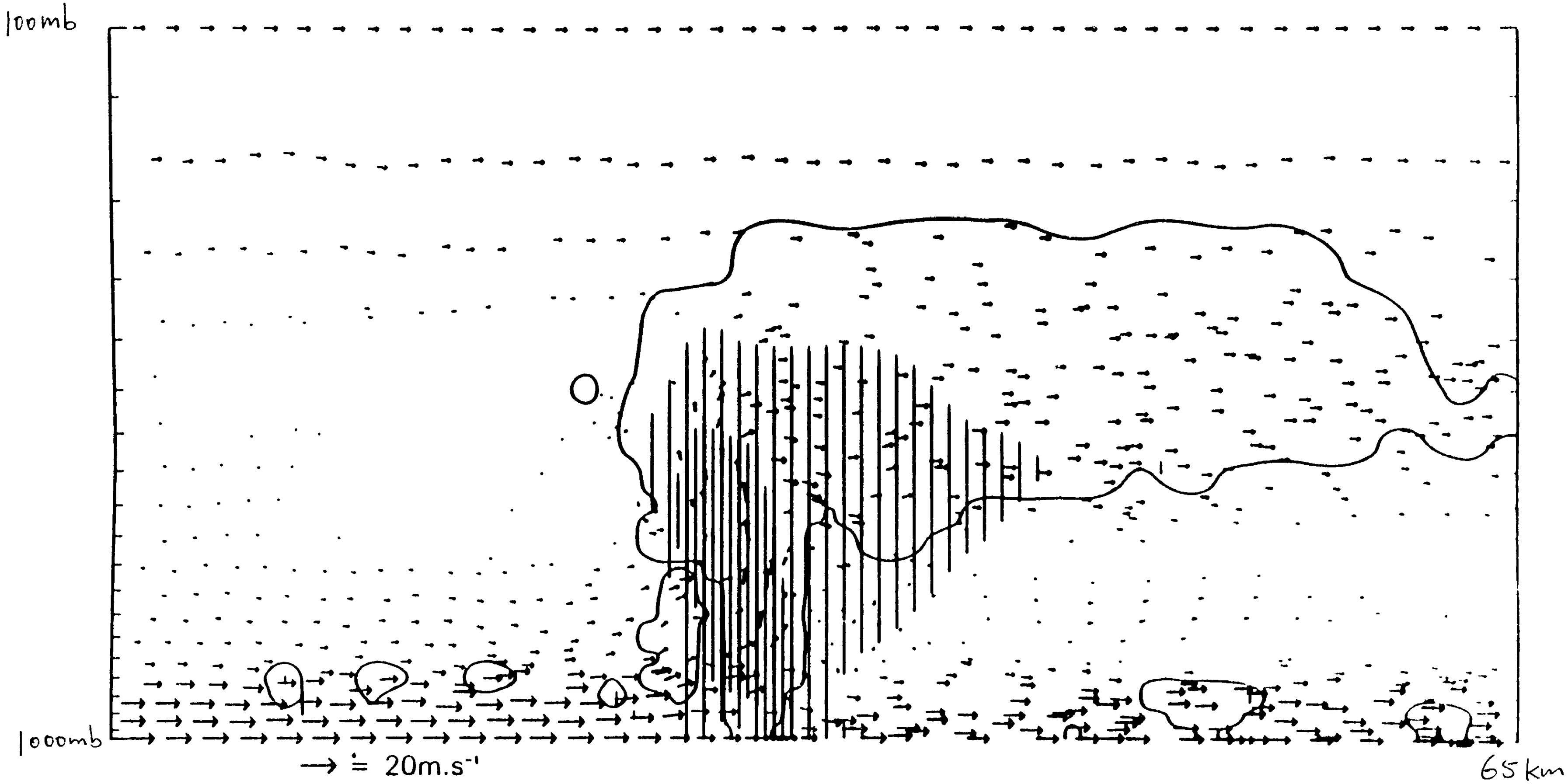

RUN SO3 Time 180.0 min.

FIG 5.3.1e cloud contour value 0.1g/kg
dense hatching : rainwater content > 2g/kg
less dense hatching : rainwater content > 0.1g/kg

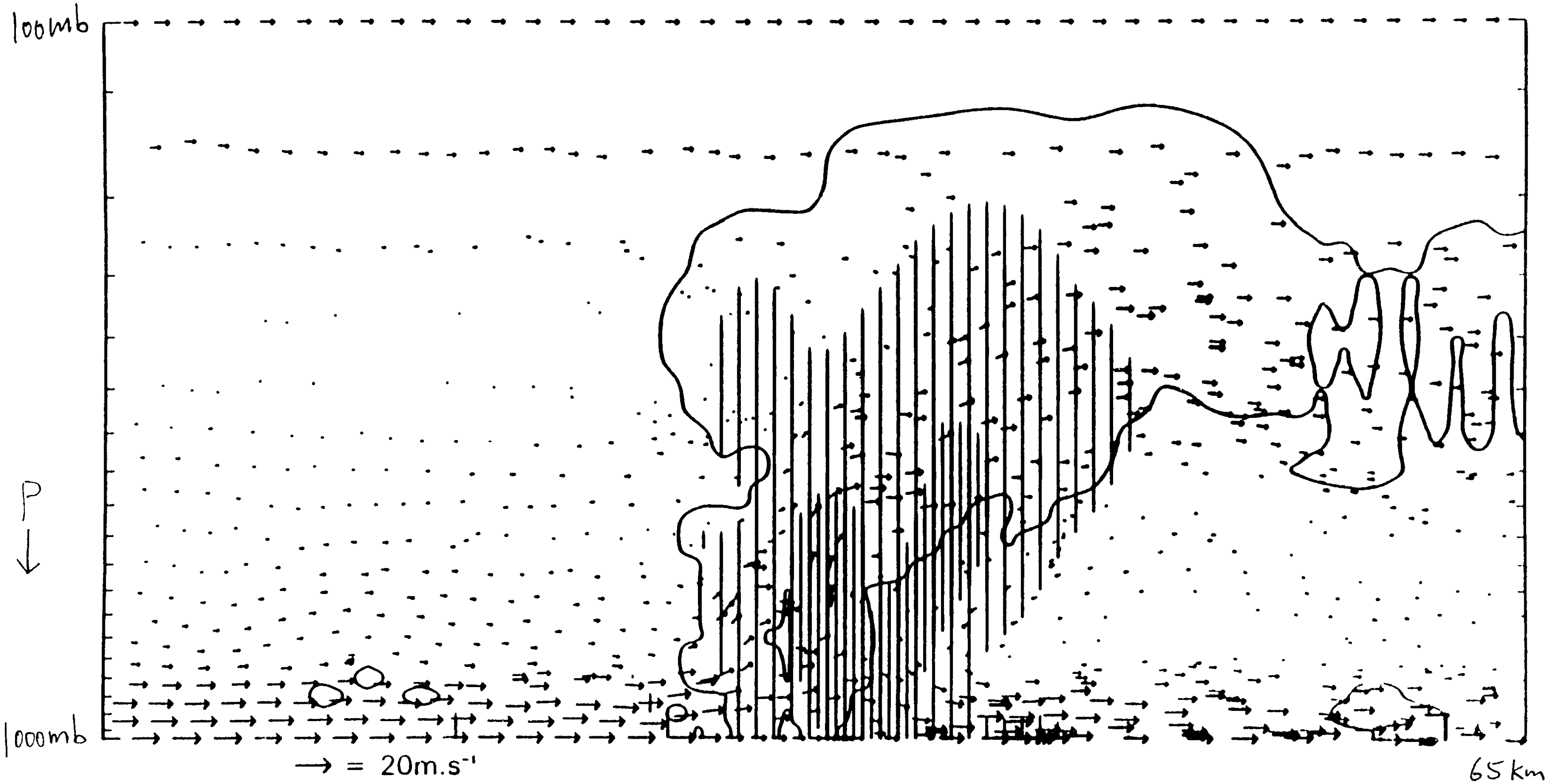

FIG 5.3.1f

RUN SO3 Time240.0 min.

(as FIG 5.3.1e)

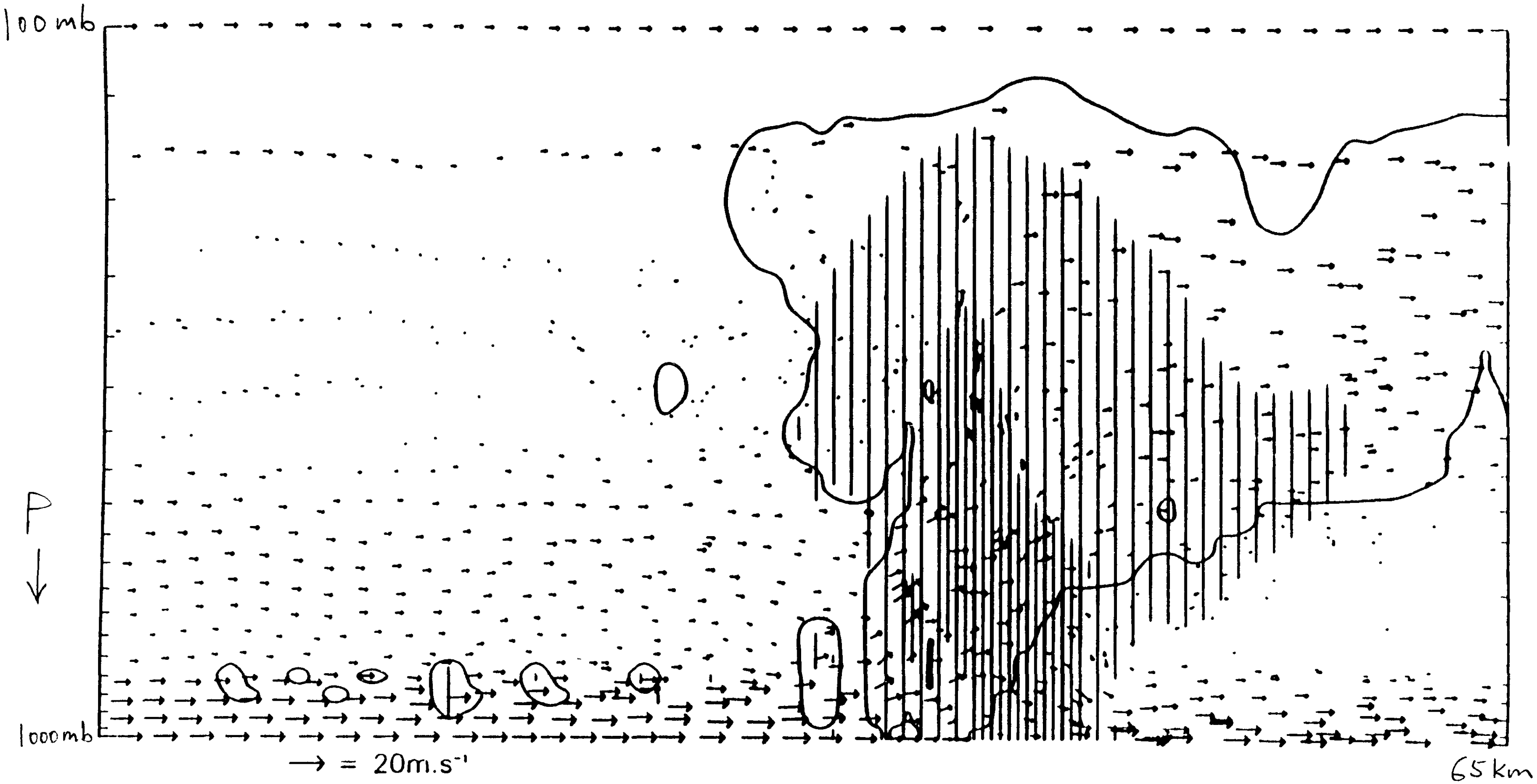

FIG 5.3.1g

RUN SO3 Time300.0 min.
(as FIG 5.3.1e)

potentially unstable convective boundary layer air does not ascend above the lowest 300mb and the latent heat is not released.

The cloud patterns in fig 5.3.1e,f,g are dominated by the large single cell (unicell) structure whose top is located at 150mb(about 13km high). The anvil is short and its base is located at 450mb(about 7km high). There is no convective cells being advected downstream and this could be explained in the following manner. Most of the ascent of the boundary layer air is accomplished in a matter of 15km horizontal distance near the front and beyond that the parcels travel horizontally. As the updraughts of convective cells are localised regions of maximum ascent, the horizontal motion to the rear of the front does not support such convective cells. In other words, most of the convective potential energy has been released over a short horizontal distance and little is left to support any convective cells downstream.

The question of steep updraught slope has yet to be answered. Figure 5.3.1d shows the pressure gradient in the updraught region is small between 1000mb and 600mb so the buoyancy force works to increase the vertical momentum. The upward motion is retarded above 600mb where the environmental mass flux is greater. The overall rapid ascent at the front explains the steepness of the updraught.

The stronger downward pressure gradient above 600mb may be explained by the fact that the updraught impinges on the strong environmental inflow above 300mb which serves as a cap to the ascending updraught air (fig 5.3.1h). In SL06, a strong environmental inflow at 500mb inhibits free and rapid ascent at the front, hence the gentler slope of the updraught in that simulation.

Again, the forced initial ascent implies $\frac{\partial\theta}{\partial x} < 0$ which is evident in fig 5.3.1i especially above 650mb. The consequent generation of positive vorticity reduces the negative vorticity from inflow to near zero at outflow (fig 5.3.1j).

The localised ascent exclusive to the front region implies a localised formation of cloud and rain which results in a narrow surface rainfall area of only 15km wide with high maximum surface rainfall rate of about 100mm/hr (fig 5.3.1k,l,m).

5.3.2 Downdraught Structure

The downdraught is not evident in either the streamline plot of fig 5.3.1c or the wind,cloud and rain picture of fig 5.3.1f. Nevertheless, it can be broadly identified as a weak downward overturning flow extending from 800-500mb, or 2-6km,beneath the updraught. The downdraught air does not reach the 1000mb surface but it overlies a layer of surface air of 200mb deep (or 2km deep) which has partially ascended at the base of the updraught but was forced back to the surface by rainfall drag. The mass flux within the downdraught is small and the maximum downward velocity is only about 2m/s. As seen from fig 5.3.1d,f,i, the downward motion at the transistion area between the updraught and downdraught (called also the front for the sake of simple terminology) cannot be accounted for

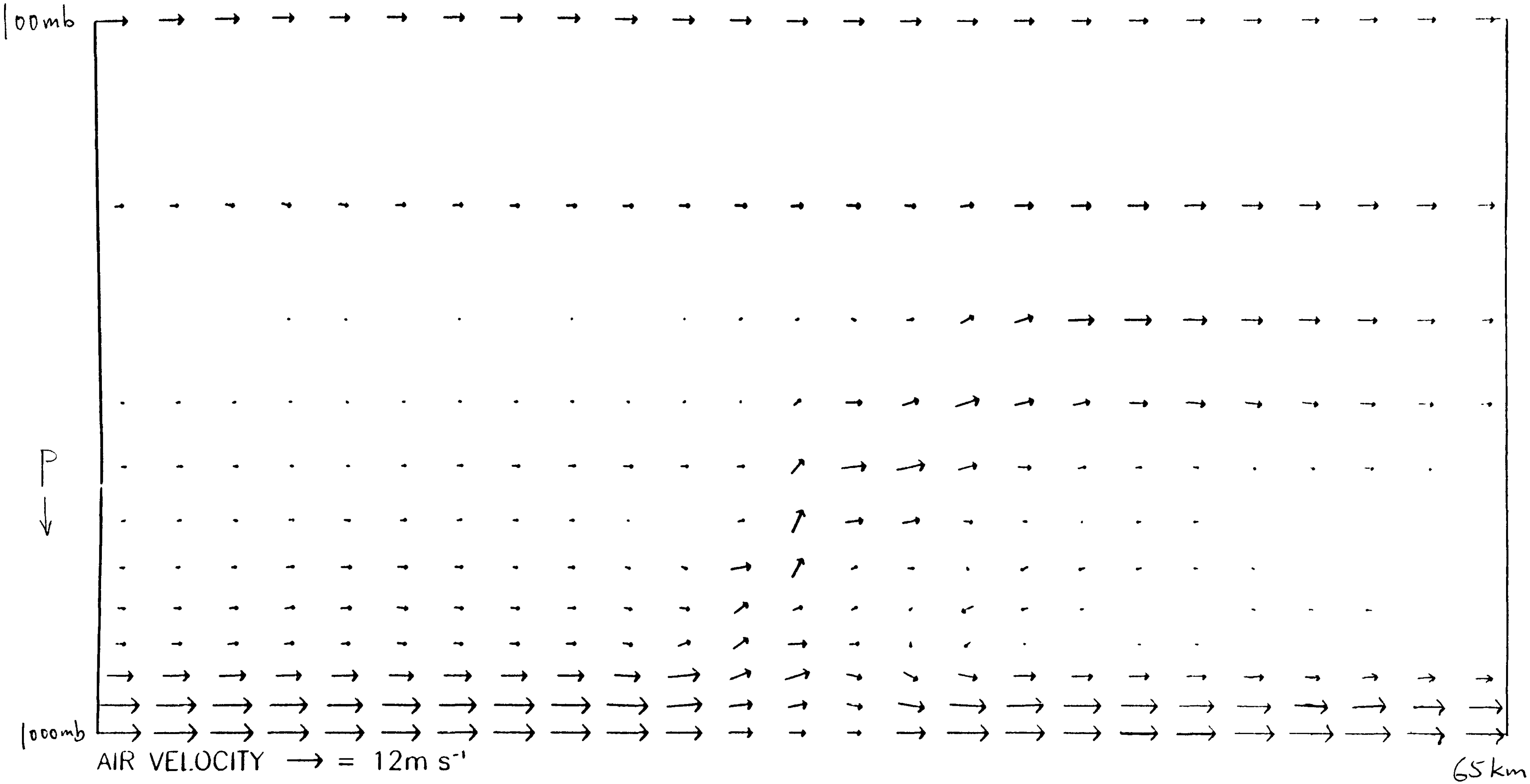

FIG 5.3.1h RUN SO3 Time240.0 min.

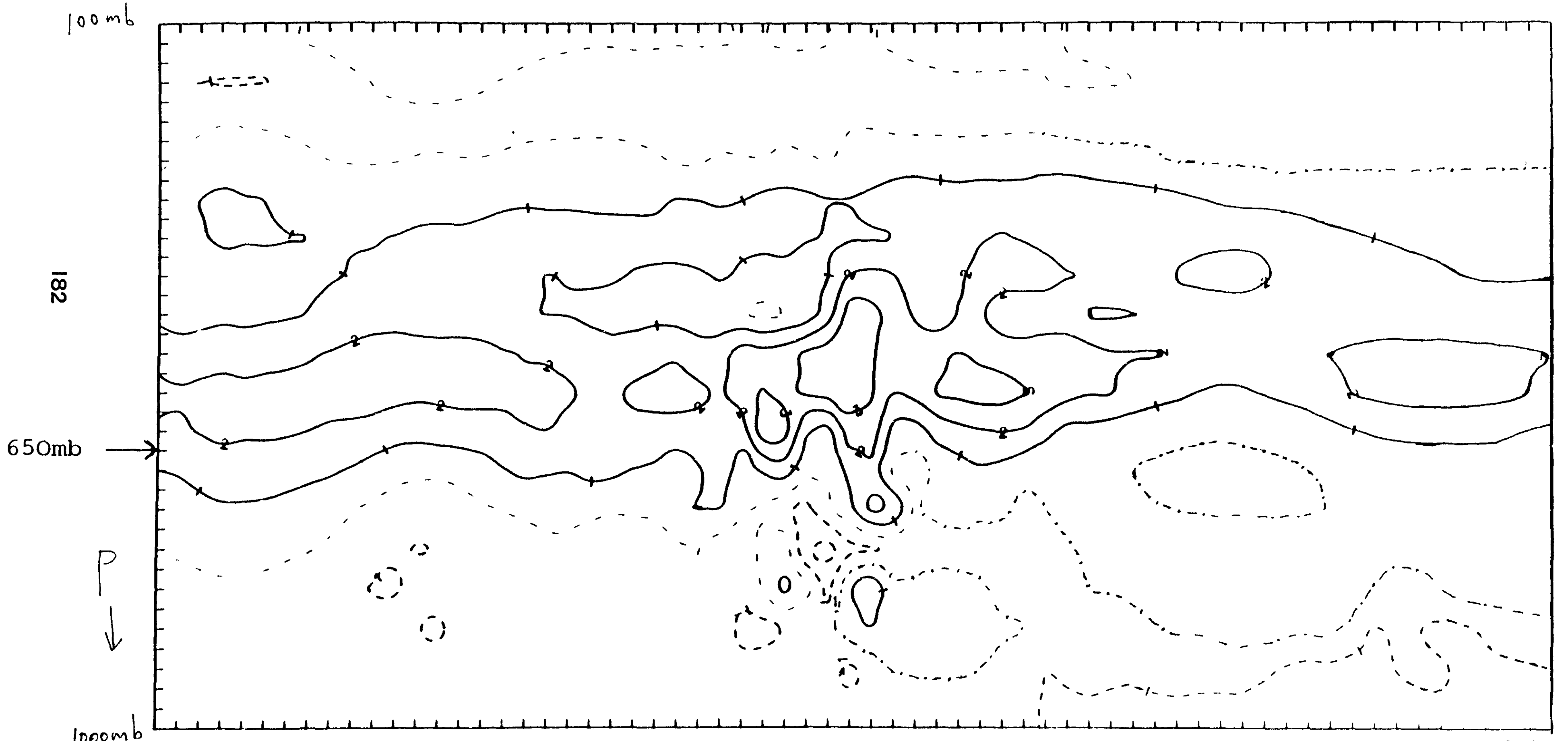

ϑ' – TEMP. DEVN (deg K)
FIG 5.3.1i

RUN SO3 Time240.0 min

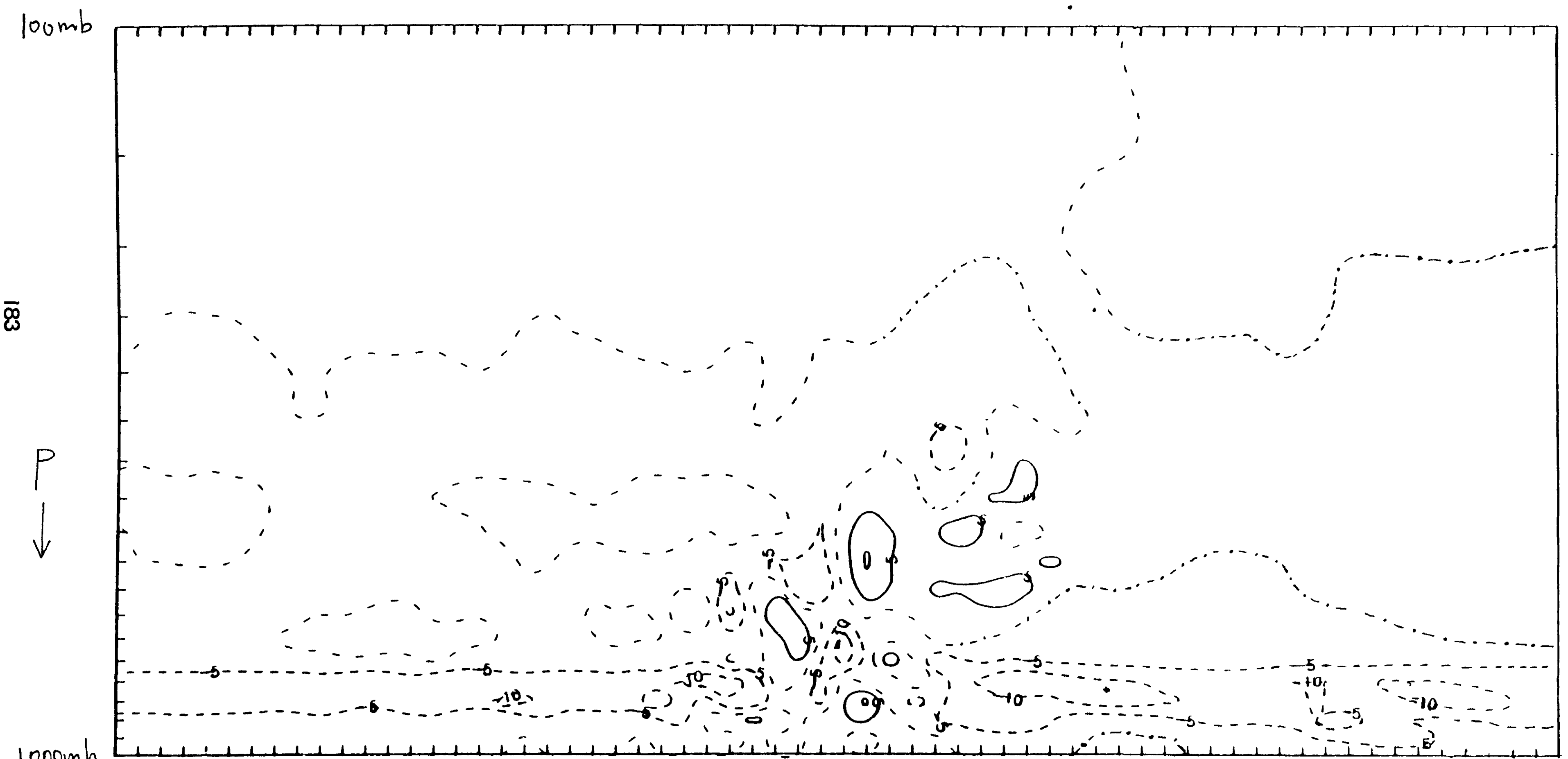

$\eta \times 10^3$ – VORT×1000 (s^{-1}) 65km

FIG 5.3.1j

Time240.0 min.

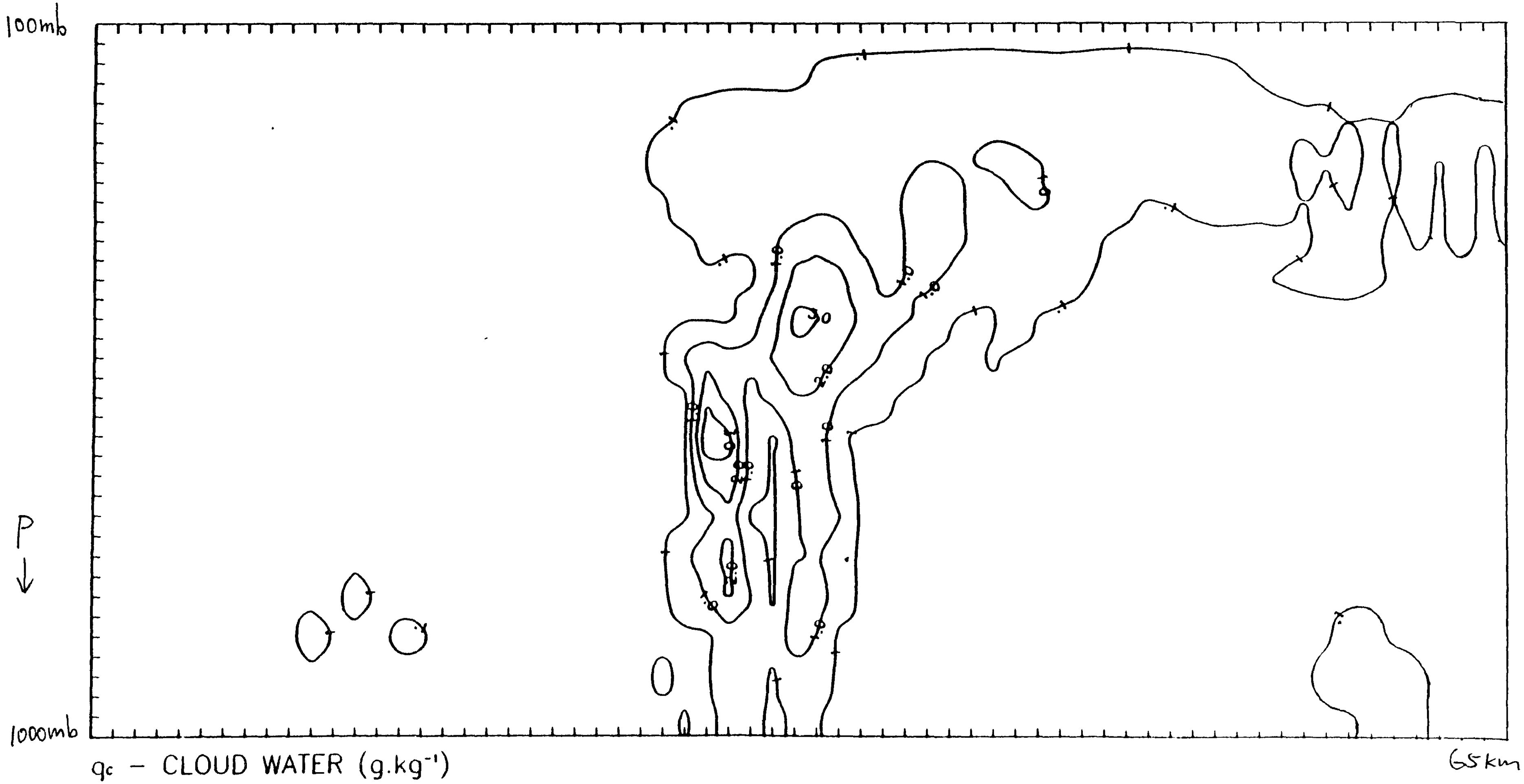

q_c – CLOUD WATER ($g.kg^{-1}$)

FIG 5.3.1k RUN S03 Time240 0 min

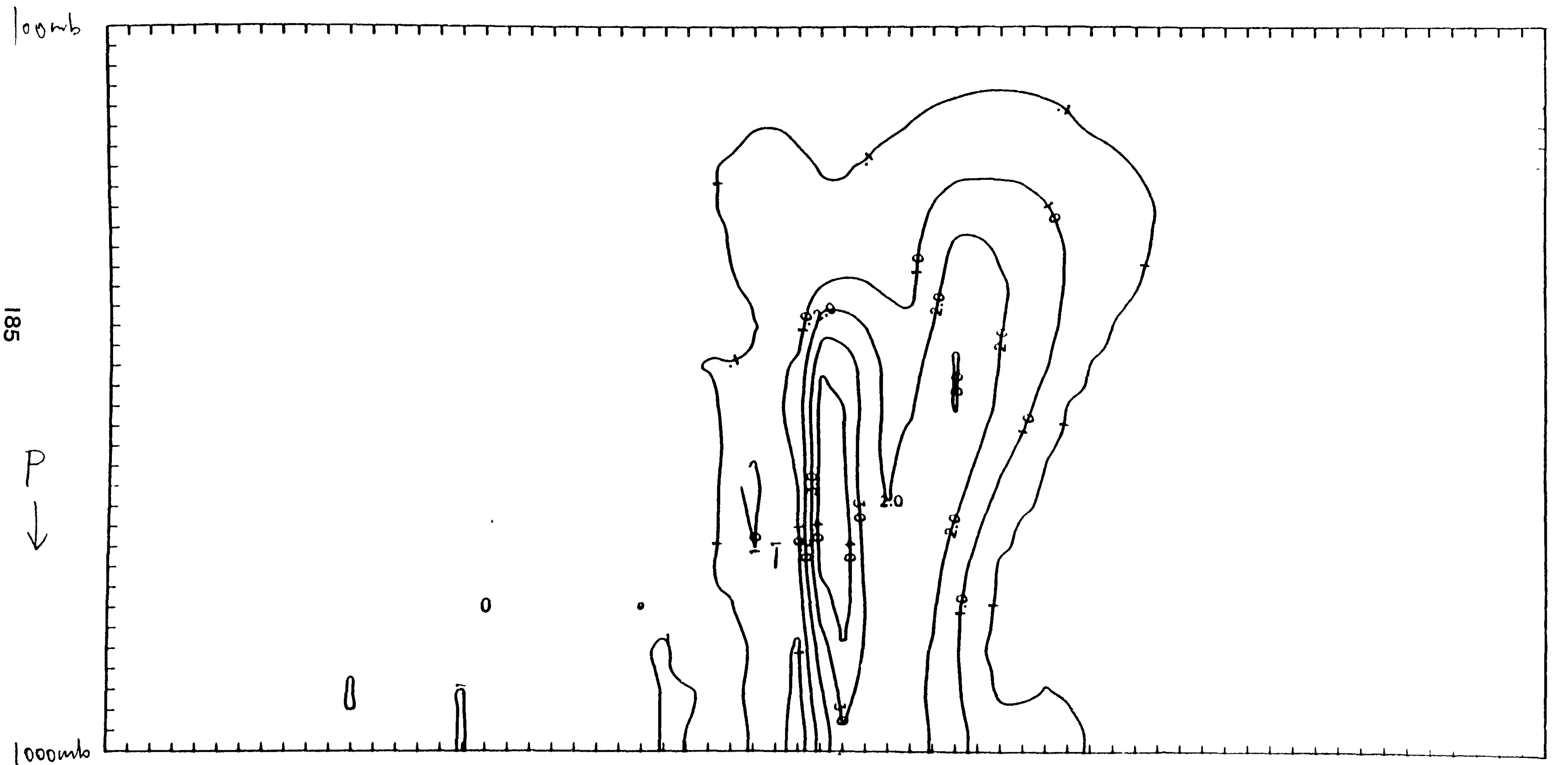

q_R – RAIN WATER ($g.kg^{-1}$)

FIG 5.3.1 1 RUN SO3 Time240 0 min.

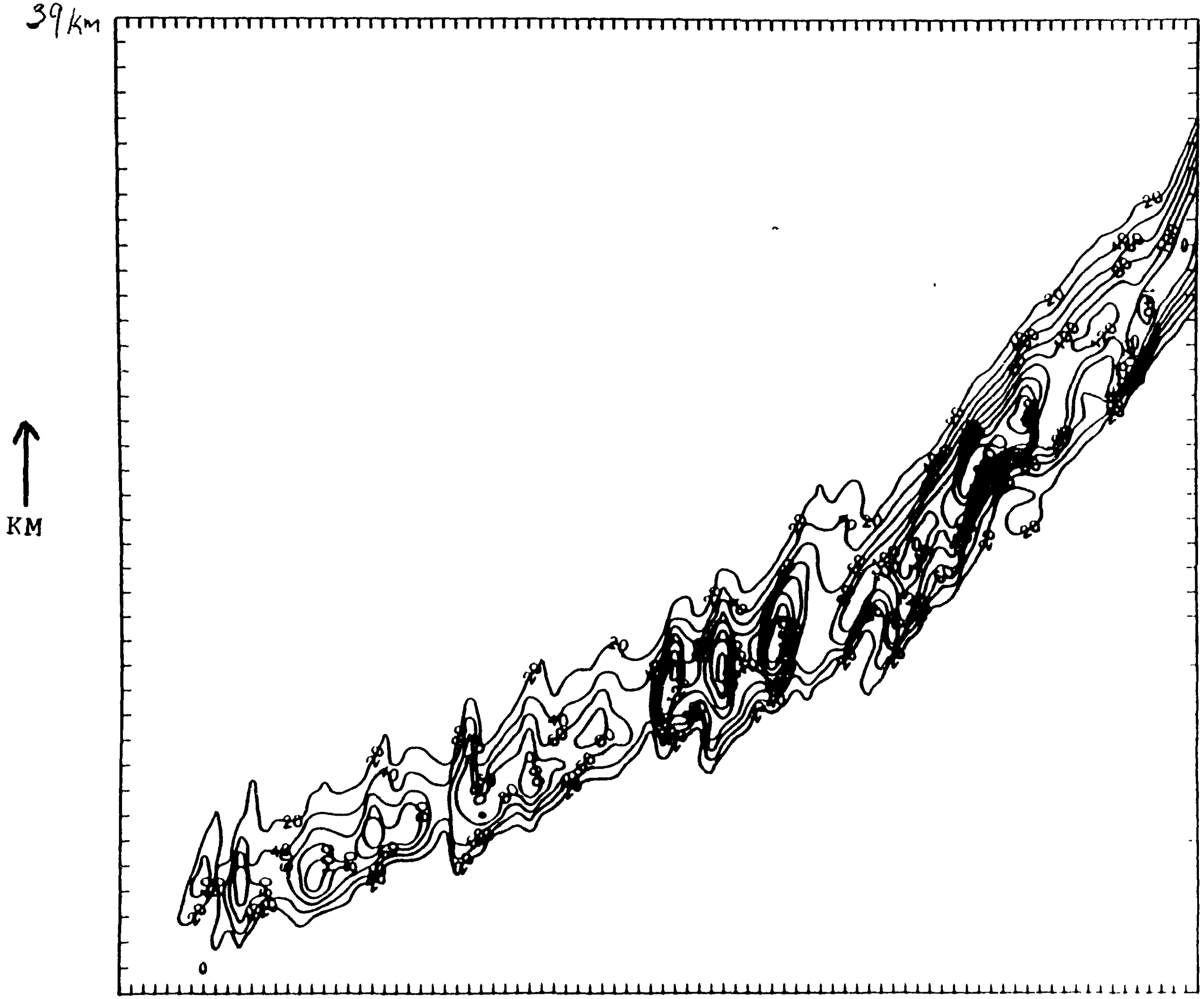

SO3 SURFACE RAINFALL MM PER HOUR 0-6 **HOUR**

FIG 5.3.1m

Time →

by the pressure force because it is acting upward, or the buoyancy force because the air is neutrally buoyant. The only driving force for the downward motion is therefore the rainwater loading which amounts to 2g/kg. The temperature perturbation throughout the downdraught is nearly zero and attains its minimum value of only -1K at 800mb at the rear of the system. The small temperature deficit could be explained by the fact that the localised rainfall at the front only allows a short time interval in which rain evaporation can work to cool the descending air.

In fig 5.3.1d we can identify a high pressure area at the surface corresponding to a hump in the streamline plot. It is this high pressure area which forces the updraught air to ascend and its presence deserves some explanation. The quantity $\frac{1}{2}v^2 + gh' + \int_{P_0}^{P}\left(\frac{\theta_v'}{\theta_{vs}} - \ell\right)\frac{dP}{\rho_0}$ where ℓ represents the liquid water content, is conserved in a steady motion. Large h' and therefore high pressure can be obtained by having small velocity(dynamical) and negative value for the integral in pressure(thermodynamical). For a descending flow, negative buoyancy or large liquid water content will give rise to a negative value for the integral. This condition and the condition of small velocity are met at the front region and hence the high pressure there.

Vorticity at inflow to the downdraught is near zero but negative generation of vorticity at the front , again by liquid water drag, decreases the vorticity to a minimum of $-10 \times 10^{-3} s^{-1}$ at outflow (fig 5.3.1j).

It has been seen that the liquid water drag plays very important roles in maintaining the flow regime. It diminishes the mass flux into the updraught by bringing some ascending air back to the surface and it is responsible for the downward overturning of the downdraught. Furthermore, it also helps to create a high pressure area near the ground to maintain the initially forced updraught.

5.4 COMPARISON BETWEEN SIMULATIONS SL06 AND S03

Although the initial conditions of the two simulations are the same except the wind profiles above 750mb, two different regimes of organised convection are nevertheless produced. A marked contrast between the two is that in S03 one large cell dominates and persists for hours whereas in SL06 many cells develop at the front and propagate to the rear of the squall line. SL06 will be referred as the multicell case and S03 the unicell case. Figure 5.4a shows the two surface rainfall areas associated with two cells in the multicell case and fig 5.3.1f shows only one surface rainfall area but with a higher rainfall rate. The anvil of the unicell is short compared with the multicell anvil where it covers about 70km of horizontal distance in the model.

Another marked contrast is the slope of the updraughts at the fronts, i.e. the much steeper updraught of the unicell case than the multicell case. The steeper updraught slope of S03 inhibits total separation of boundary layer air from the ground and therefore the potential energy of the boundary air returning to the surface is not released whereas in SL06 the 'peeling' of boundary layer air off the

FIG 5.4a (as FIG 5.3.1e) RUN SL06 Time216.0 min.

ground into the updraught core has meant greater potential energy release and a more vigorous system. This is related to the difference in wind profiles and will be discussed in the next section. The more active multicell squall line travels 3.5m/s faster than the unicell system.

The downdraught structures of the two cases are very different. The cold density current structure in the multicell case is not found in the unicell case where only a weak but deeper overturning flow can be identified. The small mass flux in the weak downdraught is the result of the small environmental wind component at 500mb which is the level of inflow to the downdraught. The idealised flow patterns of the simulations are shown in fig 5.4b for comparison.

Finally, the upward overturning flow ahead of the front is absent in the unicell case as a result of the westerly environmental inflow at the upper level.

5.4.1 Role Of The Mid-level Wind Profile

In SL06, a distinctive westerly jet is identified in fig 5.1.1d between 400-600mb. Its maximum velocity is 8.8m/s compared with only 3.3m/s in the unicell case. The gentle updraught, separation of flow at the ground, cellular pattern and the cold density current can be explained in terms of this jet.

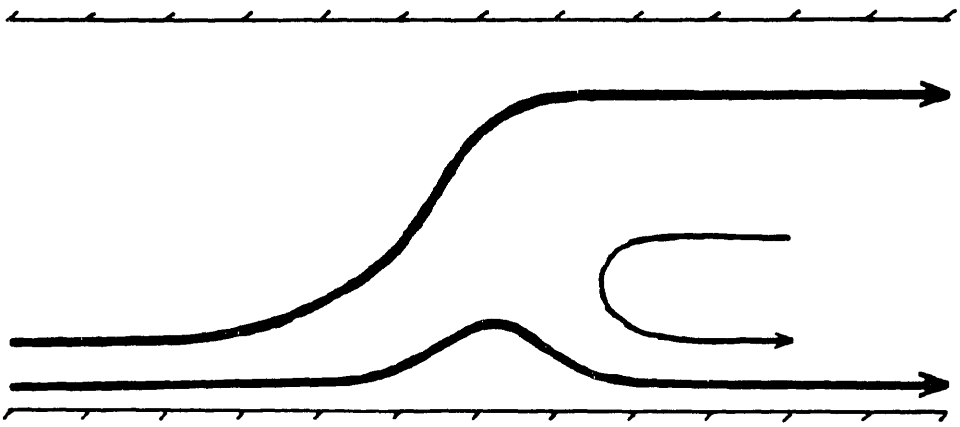

SO3

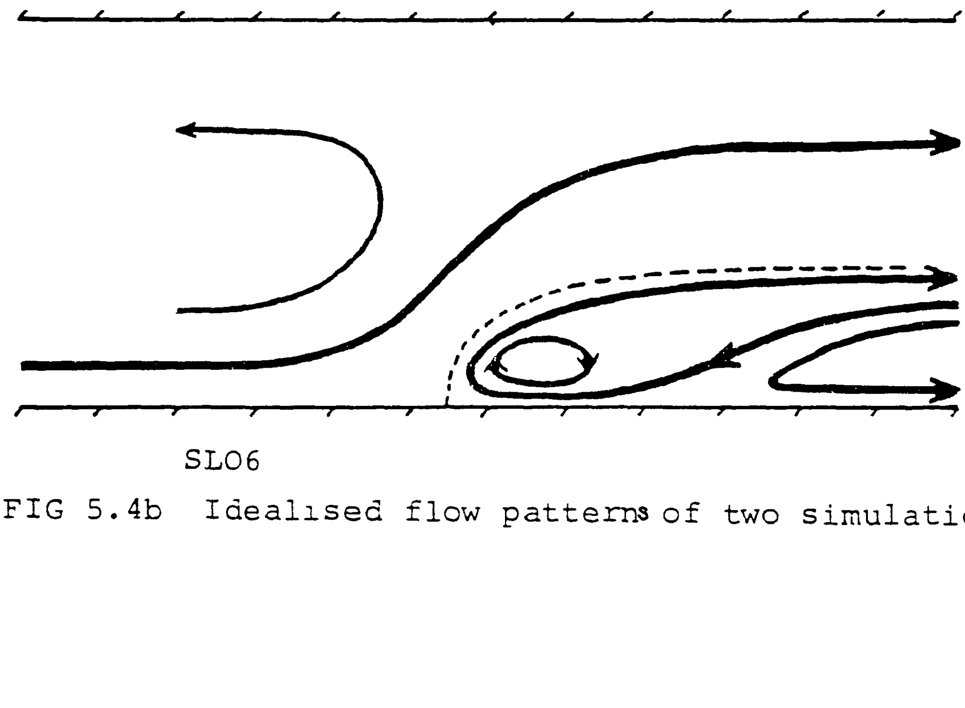

SLO6

FIG 5.4b Idealised flow patterns of two simulations

This horizontal jet converges with the updraught air from the surface at 500mb and suppresses the upward motion of the updraught air by inducing a downward pressure gradient force. However, the buoyant updraught parcels gradually rise to their respective maximum level at the rear of the system. Therefore the overall updraught at the front is more gentle than in the unicell case where only at 150mb the environmental wind (5.5m/s) is strong enough to inhibit further upward motion. The gentle updraught slope means that only a small amount of rain falls into the base of the updraught causing only a relatively small drag on the ascending parcels and so the separation of boundary layer air from the ground was totally accomplished, resulting in full utilisation of potential energy of the boundary layer air. This is not true in the unicell case. As previously explained, ascent also takes place at the rear of the front and the local maximum ascents correspond to convective cells. Therefore much of the area behind the front (about 100km) receives rainfall and the downdraught air is evaporatively cooled for several hours before it leaves the domain. Most of the air in the rotor at the front is trapped and therefore saturated and cooled by evaporation to 4K below the pre-squall temperature. The overall temperature drop in the density current implies higher density and enhanced hydrostatic pressure at the front and this helps to 'peel' boundary layer air off the ground as well.

In Thorpes,Miller and Moncrieff(1982), storm P(-10), P(-5) and P(0) were simulated with different wind profiles above 750mb. P(0) with no mid-level inflow has the most upright updraught and is the most steady and long lasting storm. P(-5) and p(-10) have progressively larger mid-level inflow; the updraught slopes are progressively more gentle and the storms are progressively multicellular and unsteady. Therefore,the discussion above on the role of the mid-level wind profile agrees with the simulation results of TMM.

All these simulations show that the updraughts slope backward over the downdraught and it is suggested that this is an effective organisation for convection ; the mid-latitude storm P(0) and the West African(tropical) squall line simulation are variants of this type of organisation.

A deduction about single cell and multicell convective systems in three dinensions could be drawn here. Where the updraught is upright as a result of weak mid-level environmental mass flux, ascent of updraught parcels and release of latent heat are accomplished in one localised area, giving rise to one convective cell only. Multicellular systems are associated with stronger mid-level flow and gentler updraught slope.

5.5 CONCLUSIONS

The West African squall line observed on 22June1981 was successfully simulated by a meso-scale model and the structure of the squall line can be examined. The propagation speed of the squall line in the simulation is close to the observed value and it is also near to the African Easterly Jet speed. The downdraught within the density current , the rotor and the updraught are reproduced in the simulation. The updraught vorticity fields can be explained in terms of the time-dependent vorticity equation 4.3d. The cold convective scale downdraught and the warm meso-scale downdraught were identified and the latter is a response to the former. The warm subsidence was explained in terms of negative vorticity generation. This suggests that in three-dimensional squall lines, the convective scale downdraught plays an important role in maintaining meso-scale subsidence.

The dependence of mature regimes on the initial wind profiles is demonstrated by the second simulation with an idealised initial wind profile. The simulation shows the importance of rain water loading in maintaining the weak downdraught and the high pressure at the frontal convergence zone.

The differences between the two simulations, particularly the steep updraught and unicellular nature of S03 and the gentle updraught and multicellular nature of SL06 have been explained in terms of the pressure induced by a mid-level jet. An implication for three-dimensional cloud systems is that multicellular regimes may be associated with strong mid-level relative inflow.

CHAPTER 6

CONCLUSIONS AND SUGGESTIONS FOR FURTHER WORK

The study of density models in a neutrally stratified atmosphere suggests in sections 2.2.1.4 and 2.2.2.4 that two-dimensional mid-latitude and tropical squall lines are perturbations of neutrally buoyant density models. It is worth investigating whether classification of squall lines based on these neutrally buoyant models is indeed satisfactory. The analysis in section 2.1.1.2 points out the shortcomings of the formula, $C = \sqrt{2\hat{g}h}$, for predicting density propagation speed, i.e. the pressure drop across the domain and the surface flow of the density current should be taken into account. An alternative formula is proposed and its counterpart in pressure coordinates is given by eqn 5.2.4a.

The attempt to solve the free boundary problems in chapter three was successful but considering the human effort and the computing time involved, problems with only one free boundary were tackled. The internal solutions show that the density current interface is convex in shape with the tangent at the stagnation point making an angle of about 60° with the bottom boundary. Also, a low pressure area is located beneath a buoyant updraught and this could induce a circulation in the third dimension. The method of solution could find useful application in treating similar free boundary problems. The work in chapter two is a digression from chapter three.

The analysis in chapter four has progressed the understanding of the vorticity equation and consequently the outflow thermodynamical profile and wind profile. The dependence of the dynamical flow structure on $\frac{\gamma - B}{u_0}$ (evaluated at inflow) rather on CAPE implies that this inflow parameter and the cloud top height should play more important roles than CAPE in parameterising heat and momentum transport in global circulation models. The analysis could be extended to three dimensions so that the proposition in the last sentence can be affirmed and the parameterisation technique improved accordingly. Models with suitably chosen inflow shear can be solved analytically while previously constant or zero inflow shear has to be assumed. Deriving the vorticity equation in pressure coordinates has meant that the gross variation of mean density with height, i.e. the compressibility of the atmosphere, can be included in the analytic models. Also , the results in chapter four can be re-interpreted in pressure coordinates. It is possible that the form of the interface in the mid-latitude squall line model studied by Moncrieff(1978) is dependent on the values of $(\gamma - B)$ at various heights. It is interesting to see if a model with $(\gamma - B)$ as a function of height would produce a thermodynamically consistent flow with the interface tilting upshear.

CONCLUSIONS AND SUGGESTIONS FOR FURTHER WORK

The simulations in chapter five demonstrated once again the updraught and downdraught interaction which maintains quasi-steady convective systems. The vorticity fields were explained in terms of temperature gradient and the time-dependent vorticity equation was found useful in this explanation. The meso-scale downdraught was interpreted as a response to the convective scale downdraught which is driven by negative buoyancy. Again vorticity was a useful quantity to consider in this interpretation. It is worthwhile to see if vorticity can be used to elucidate the relationship between convective scale and meso-scale downdraughts in three-dimensional squall lines. Such work will involve three-dimensional simulations and comparisons with observations. The multicellular squall line was found to be associated with strong mid-level inflow and a deep unicellular system associated with weak mid-level inflow. Further investigation will show whether this is true of three-dimensional convective systems.

As the general structures of the density current models and squall line considered in this thesis are similar to that of a cold front, it is conceivable that this work can be extended (by including the Coriolis parameter and the y-component velocity) for the study of cold front dynamics.

References

Abbreviations:
QJ = Quarterly Journal of the Royal Meteorological Society
JAS = Journal of Atmospheric Sciences

Benjamin,T.B. 1968
Gravity currents and related phenomena.
J. Fluid Mechanics, 31, p209-248

Betts,A.K., Grover,R.W. and Moncrieff,M.W. 1976
Structure and motion of tropical squall-lines over Venezuela.
QJ, 102, p395-404

Bluestein,H.B. and Jain,M.H. 1985.Formation of mesoscale lines of precipitation:severe squall lines in Oklahoma during the spring.
JAS 42 p1711

Bolton,D. 1981
Generation and propagation of African squall lines.
Ph.d thesis, Atmospheric Physics Group, Imperial College, Univ. of London.

Browning,K.A. 1977
The structure and mechanism of hailstorms.
Hail:a review of hail science and hail suppression, Met. Monog. no. 38, ed Foote,G.B. and Knight,C.A., Amer. Met. Soc., p1-43

Browning,K.A. and Ludlam,F.H. 1962
Air flow in convective storms.
QJ, 89, p117

Charba,J. 1974
Application of gravity current model to analysis of squall-line gust front.
Monthly Weather Review, 102, p140

Dudhia,J. 1984
A numerical study of tropical band convection.
Ph.d thesis, Atmospheric Physics Group, Imperial College, Univ. of London.

Elliot,C.M. and Ockendon,J.R. 1982
Weak and variational methods for moving boundary problems
Published by Pitmans Book Limited.

Fernandez,W. 1982
A review of downdraughts at the rear of tropical squall lines.
Bull. Amer. Met. Soc., Nov.1982, p1285-1293.

Fernandez,W. and Thorpe,A.J. 1979
An evaluation of theories of storm motion using observations of tropical convective systems.
Monthly Weather Review, 107, p1306-1319.

Flugge,S. and Truesdell,C. 1960
Encyclopedia of Physics, Vol IX, Fluid Dynamics III
Published by Springer-Verlag, Berlin.

Green,J.S.A. and Pearce,R.P. 1962
Cumulonimbus convection in shear.
Tech. Note No. 12, Dept. of Met., Imperial College, London.

Houze,R.A. Jr. 1977
Structure and dynamics of a tropical squall-line system.
Monthly Weather Review, 105, p1540

Karman,T.Von 1940
The engineer grapples with non-linear problems.
Bull Amer. Math. Soc., 46, p615.

Kessler,E. 1969
On the distribution and continuity of water substance in atmospheric circulations.
Met. Mon. (Amer. Met. Soc.), 10, no.32

Lindzen,R.S. 1974
Wave-CISK in the tropics.
JAS, 31, p156-179

Ludlam,F.H. 1980
Cumulonimbus convection.
Chapter 8, Clouds and storms, published by Penn. State. Univ. Press.

Miller,M.J. 1978
The Hampstead storm:a numerical simulation of a quasi-stationary cumulonimbus system.
QJ, 104, p413-427

Miller,M.J. and Betts,A.K. 1977
Travelling convective storms over Venezuela.
Monthly Weather Review, 105, No. 7.

Miller,M.J. and Pearce,R.P. 1974
A three-dimensional primitive equation model of cumulonimbus convection.
QJ, 133, p133-154.

Miller,M.J. and Thorpe,A.J. 1981
Radiation conditions for the lateral boundaries of limited-area numerical models.
QJ, 107, p615-628.

Moncrieff,M.W. 1970
Cumulonimbus convection in shear.
Ph.d thesis, Dept. of Met., Imperial College, Univ. of London.

Moncrieff,M.W. 1978
The dynamical structure of two-dimensional steady convection in constant vertical shear.
QJ, 104, p543-567.

Moncrieff,M.W. 1985
Steady convection in pressure coordinates.
QJ, 111, p857-866.

Moncrieff,M.W. and Green,J.S.A. 1972
The propagation and transfer properties of steady convection overturning in shear.
QJ, 98, p336-352.

Moncrieff,M.W. and Miller,M.J. 1976
The dynamics and simulation of tropical cumulonimbus and squall lines.
QJ, 102, p373-394.

Schlesinger,R.E. 1975
A three-dimensional model of an isolated deep convective cloud: preliminary results.
JAS, 32, p934-957.

Raymond,D.J. 1976
Wave-CISK and convective mesosystems
JAS, 33, p2392-2398

Sommeria,G. and Testud,J. 1984
COPT81: A field experiment designed for the study of dynamics and electrical activity of deep convection in continental tropical regions.
Bull. Amer. Met. Soc., 65, p4-10.

Steiner,J.T. 1973
A three-dimensional model of cumulus cloud development.
JAS, 30, p414-435.

Simpson,J.E. 1969
A comparison between laboratory and atmospheric density currents.
QJ, 95, p758-765

Simpson,J.E., Mansfield,D.A. and Milford,J.R. 1977
Inland penetration of sea-breeze fronts.
QJ, 103, p47-76.

Tepper,M. 1950
A proposed mechanism of squall lines: the pressure jump line.
Journal of Met., 7, p21-29.

Thorpe,A,J. and Miller,M.J. 1978
Numerical simulations showing the role of the downdraught in cumulonimbus motion and splitting.
QJ, 104, p873-893.

Thorpe,A.J., Miller,M.J. and Moncrieff,M.W. 1980
Dynamical models of two-dimensional downdraughts.
QJ, 106, p463-484.

Thorpe,A.J., Miller,M.J. and Moncrieff,M.W. 1982
Two-dimensional convection in non-constant shear: a model of mid-latitude squall lines.
QJ, 108, p739-762.

Zipser,E.J. 1977
Mesoscale and convective-scale downdraughts as distinct components of squall-line structure.
Monthly Weather Review, 105, p1568.

Acknowledgements

I would like to thank my supervisor, Dr. M.W. Moncrieff, who applied a N.E.R.C. research studentship grant for me in July 1982 through an appeal procedure. I am also grateful for his continual interest in my work and his readiness to discuss and advise. Thanks are also due to Dr. J. Dudhia, our research assistant, who patiently and frequently discussed the work with me. He also ran simulation SL06 and provided me with the figures for that simulation. Dr's J. Marshall, R. Brugge and Miss Toni Lee read and commented on drafts of the various chapters of this thesis.

It is a pleasure to acknowledge the fellowship with Mike Brown and David Gregory (research students) during our time together at the Atmospheric Physics Group.

Finally, I must express my thanks to God who, through Jesus Christ, has sustained and inspired me throughout the years.